Grant Agreement no. *241321-2*

Geothermal Engineering Integrating Mitigation of Induced Seismicity in Reservoirs

Project Acronym: GEISER

D3.3 Guidelines for techniques/methodologies for seismological investigations to be applied in future EGS operations, developed on the basis of successful analyses of past sequences

Due date of deliverable: 30.06.2013
Actual submission date: 12.09.2013

Start date of project: 1.1.2010 Duration: 42

Participant short name: AMRA, ETHZ, EOST, GFZ, ISOR, NORSAR

NAMES INVOLVED: A. Zang, V. Oye, J. Albaric, N. Deichmann, B. Goertz-Allmann, M. Calò, C. Dorbath, K. Ágústsson, O. Flóvenz, M. Bohnhoff, G. Kwiatek, A. Zollo, O. Amoroso, V. Convertito, A. Emolo, N. Maercklin, E. Matrullo, A. Orefice, N. Sharma

Revision: 1

Dissemination Level		
PU	Public	
PP	Restricted to other programme participants (including the Commission Services)	
RE	Restricted to a group specified by the consortium (including the Commission Services)	x
CO	Confidential, only for members of the consortium (including the Commission Services)	

Contents

1. EXECUTIVE SUMMARY

Guidelines for techniques/methodologies for seismological investigations to be applied in future EGS operations, developed on the basis of successful analyses of past sequences.

Enhanced Geothermal System (EGS) operations are usually related to engineering of hot, low permeability rock. Similar operations are common, and will be applied in the future to a large extent in conventional fracture dominated geothermal systems. The reason for this is that geothermal energy can only be extracted from a small volume of hot rock surrounding the fracture systems. Permeability enhancement in boreholes and creation of artificial fracture for production, therefore, are considered crucial for future development of the reservoirs. The same applies to the re-injection wells in fracture-dominated reservoirs. The fluid injected must go either into open fractures that are a part of a tectonic fault system, or into new fractures that must be created. In general, the basic knowledge on design and safe operation of fluid injection is based on a geologic map with fault/fracture distribution, tectonic movements, stress field, and natural seismicity with estimates of the moment magnitude of the largest seismic event to be expected in the area of interest.

Seismological investigations

Our WP3 recommendation, in particular, is based on the analysis of induced seismicity in past sequences from geothermal areas located in different tectonic settings. The geothermal sites investigated include Basel (Switzerland), Berlin (El Salvador), Campi Flegrei (Italy), Krafla, Hengill and Reykjanes peninsula (Iceland), Paralana (Australia), Soultz-sous-Forets (France), and The Geysers, CA (USA). As a general note we strongly recommend to do a quality assessment of the recorded waveforms, and thereafter to apply four different techniques/methodologies for seismological investigations. We recommend to apply (1) a relocation method to reveal small-scale patterns in the induced event location clouds, (2) a spectral ratio technique to improve induced event source parameters, (3) a stress-inversion techniques to relate reservoir hydraulics to the stress field in situ, and (4) a passive continuous ambient seismic noise analysis for imaging changes in mechanical reservoir parameters during and after shut-in. These methods will provide the basis for the secondary well to be drilled. The costs for a thorough analysis of the waveform data practically is negligible when comparing to the costs of a borehole, which should be placed optimally.

Numbers suggested

Magnitude threshold (M= -1 to M= 0) as compared to the magnitude of completeness (Mc= 1, e.g. The Geysers); location accuracy (decameters); source parameters for event magnitudes down to (M= -1 to M= 0); magnitude of completeness should be two orders of magnitudes lower than the maximum acceptable/expected magnitude in the area. If tomography is planned for seismicity located at depth shallower than 5 km, a seismic network >16 stations in 6 x 6 km^2 area with test injection is recommended. Source parameters like location, orientation, length, displacement, moment, rupture velocity, stress drop (apparent, dynamic, static) and seismic efficiency are the very foundation to (1) constrain mechanisms of M= 0

fluid-induced seismicity, (2) monitor near-well changes in reservoir stress, and (3) lead to more efficient reservoir management.

In terms of instrumentation, pre-site investigation should gather information on the velocity structure. This should include near-surface attenuation and noise studies for surface network design, and ray modeling for testing event location performance. After drilling a first well, Vp/Vs logging and in situ stress needs to be determined. This is important for interpretation of located seismicity and related source parameters. Data from borehole and surface stations allow to detect Vp/Vs-variations. For larger source-receiver distances (>3 km), a 3D velocity model is required. For this, seismic reflection lines and well-logs are needed.

Technical

Implement borehole and surface real time 4D systems (3D tomography at repeated times) for detection of shallow depth fluid migration paths based on (1) active mini-vibroseis trucks, and (2) continuous, ambient seismic noise analysis. For the passive seismic monitoring we recommend to use sensors adjusted to expected magnitude and frequency range. Field operator is advised to provide raw seismic data with no downscaling, high sampling rate and broad frequency band. This is a pre-requisite for applying the methods mentioned above (relocation, spectral ratio, stress inversion, ambient seismic noise).

Distinguish between location accuracy of hypocenters relative to the injection borehole (absolute locations), and relative to each other (relative locations). A calibration shot is necessary prior to the start of the first stimulation. Based on the findings that more than half of the events occurred as sequences of events with almost identical waveforms, high-precision relative locations can help identifying orientation and length of faults activated during stimulation. This requires signal cross-correlation, master event and double-difference techniques. Combined with focal mechanisms, this information is essential to determine the stress state in the reservoir. Stress inversion from induced events, however, needs to be validated against stress analysis from wellbore measurements (borehole breakouts, hydraulic fracturing, extended leak-off tests).

Site specific issues

Distinguish between the injection into fractured, fault-free reservoir, and injection into fractured reservoirs with fault zone. In the first case, low anomaly of P-waves are expected in the zone of seismicity during injection. A cloud of induced events during injection is expected, and designated structures in the post-shut-in phase. The sudden release in flow rate will result in disappearance of velocity anomalies. The reasons for this are not pressure diffusion but large aseismic events. In the second scenario (reservoir with faults), no compact extended cloud of events will be expected, but seismicity will align along pre-existing faults. Monitoring by seismic noise tomography is recommended if no wells are available, VSP when first well is available.

Recommendations

Use hypoDD relative relocation to be performed for the located induced seismic events. This improves precision of hypocenters to allow for sharp images of fluid path ways and stress directions in response to multiple injections. Use spectral ratio technique to improve source parameters of the original seismic catalogue at geothermal sites. Refined source parameters

are useful for interpretation of subtle interaction between pore pressure perturbations, fluid flow and fracture reactivation. Stress inversion from fluid-induced seismic events can help to relate stress field changes to hydraulic response of the reservoirs, and mechanical processes in the subsurface, in general.

Critical aspects

Although much was learned about the processes underlying the stimulation boreholes at single sites, one must be careful to generalize these results. Indeed, comparisons with other geothermal sites, show that the seismic response to stimulation is very variable. Thus progress in our general understanding of the physical processes that lead to unwanted seismicity during stimulation of an EGS will only be made through systematic and comparable seismological investigations in the course of future projects. Based on our experience gained in GEISER, the parameters that need to be determined in future EGS projects include: (1) In-situ stress analysis based on stress-induced borehole failures, and stress inversions from fluid-induced seismic events (i.e. focal mechanisms and moment tensors using both first-motions and waveform amplitudes); (2) accurate absolute (error < 100 m) and relative hypocenter locations (error < 10 m), based on a velocity model that has been calibrated beforehand with check shots or sensors in the injection well; (3) reliable moment magnitudes (seismic moments); (4) spatial and temporal variations of stress drop, using procedures that correct reliably for path and site effects; and (5) spatial and temporal variations of b-values.

Interface issues

In case no seismic catalogue is available for the geothermal site of interest, we advice to use synthetic catalogues based on physical model approaches (WP4). Different stimulation scenarios for one and the same reservoir and fracture geometry should be used in order to find safer injection strategies. In this context, we recommend to connect these models to probabilistic seismic hazard assessment (WP5). In particular we advise to use the method of Forward Induced Seismic Hazard assessment (FISHA) based on zero a priori seismicity information as opposed to the conventional probabilistic seismic hazard assessment (PSHA) applied to induced seismic events obtained real-time.

Conclusion

As the combination of all observables ((1) in-situ stress, (2) hypocenter locations, (3) seismic moments, (4) stress drop and (5) b-value) allows direct estimates of the spatial and temporal evolution of pore pressure in the stimulated rock volume, every effort should be made to perform such investigations during or immediately after a stimulation. Thus, semi-automatic methodologies need to be developed to determine these parameters in near-real-time. The last three points, if available in real-time, constitute also essential input to advanced, dynamic traffic-light systems that are based on probabilistic seismic hazard assessments during ongoing stimulation.

2. AMRA

Introduction

The research group of the Department of Physics at the University of Naples Federico II, participated as partner of AMRA, to the European Union project GEISER on Enhanced Geothermal Systems (EGSs) and induced-seismicity. Most of our work was devoted to two geothermal fields that are The Geysers in California (USA) and Campi Flegrei caldera (Italy). On the basis of our three-year experience, we are able in providing suggestions guidelines in four main topics, i.e., insights on seismic networks to be used for monitoring, source parameters to be inferred from data analysis, monitoring of medium mechanical properties, and seismic hazard analysis.

Seismic network

Our experience on the analysis of The Geysers (USA) and Campi Flegrei (ITA) geothermal fields suggest to improve the seismic network capability to detect and analyze induced/natural microseismicity down to the lowest magnitude thresholds, possibly negative. For this task the actual networks seems to be inadequate to study and track the space-time evolution of seismicity during field operations.

As from The Geyser case study, a surface seismic network consisting more than 40 stations deployed on a surface of about 20x20 km^2 with an average station spacing of 3 km, has a completeness magnitude threshold of ML about 1, where completeness is intended in terms of locatable events.

The main goals of a high resolution seismic monitoring network are:

- to estimate the lateral and in-depth extension of microseismicity with respect to the wells (location errors of tens of meters);

- to analyze source characteristics of extremely low magnitude events, possibly linked to the water injection activities (source mechanisms, rupture sizes, stress-drops, energies, etc.)

We propose the implementation of a surface/borehole, real-time, 4D (e.g. in space and time) observing system for shallow fluid migration and state changes, by combining and integrating innovative seismic techniques based on repeated 3D active/passive seismic surveys, for the detection, location and tracking of seismic transients which are generated by fluid diffusion in the EGS site.

Our solution involves both the use of active sources and continuous ambient noise recordings. The waveform signals generated by a large number of mini-vibroseis sources can be collected at a dense three-component seismic array installed at the surface or adjacent borehole of the pilot site. A minivib truck and related equipments can be used to generate active sources.

Reservoir monitoring can be realized by a regular repetition of the active seismic experiment over the operation period, keeping unchanged the acquisition lay-out. Medium mechanical property changes can be revealed and tracked in space and time by the cross-correlation analysis of seismic waveforms generated at the same stations by different repeated sources. This approach is similar to the one based on the analysis of repeated earthquake waveforms to detect time-varying properties of seismic scatter in active fault zones (Niu et al., 2003).

Depending on the available number and spatial density of active sources/receivers, time-varying properties of the medium embedding the EGS site can be investigated by 4D seismic tomography approaches (3D seismic tomography repeated at regular time intervals), where a decameter accuracy of detected anomalies can be achieved by double-difference, arrival time pickings measured by waveform cross-correlation (Zhang and Thurber, 2003; Satriano et al., 2008).

In addition, the contemporary acquisition of ambient noise at mutually combined, couples of stations allows for the determination of the Green's function representing the impulsive elastic response of the medium between stations (Shapiro and Campillo, 2004). Combining the information provided by Green's function acquired from different station couples, images of the subsoil structure are achievable through ambient noise tomography even at a very small scale (Brenguier et al., 2008). Several methods have been proposed to reveal changes in the elastic properties of the medium through the comparison of noise-extracted green's functions acquired at different times at the same station couple. Recently, Cros et al. (2011) successfully applied the “Stretching” (Sens-Shonefeld and Weger, 2006) and “Instant Phase variation” methods (Corciulo et al., 2012) to detect time changes of the velocity structure of the geyser Old Faithful in California, USA. The analysis of ambient noise recordings acquired during the repeated active source experiments, can be a powerful tool to track temporal changes in the medium possibly induced by EGS activity.

Since spatial and temporal changes of the medium elastic properties are expected to occur during the exploitation period, we suggest the implementation of 4D seismic imaging surveys (as 4D time lapse tomography) to be performed using active/passive sources.

Analysis and mapping of fracture properties can be an useful information to monitor stress/deformation state of the reservoir during stimulation. For this aim we need accurate estimate of microfracture source parameters, e.g. location, fracture surface orientation and size, moment & dislocation, rupture velocity, static/dynamic/apparent stress release, seismic efficiency. Given the possible small size and location of induced earthquakes, a dense seismic array (very high resolution antenna) at the surface of the EGS site and a borehole seismic array are the optimal observing system operating in continuous (real-time) acquisition mode. For the example-antennas to be deployed at Campi Flegrei, preliminary estimations give a decrease of the magnitude detection threshold (from the actual threshold magnitude M~2 to M=0 or smaller) for events occurring at about 3 km depth beneath the off-shore caldera, combining the high sensor spatial density of SNAKE with the application of refined waveform cross-correlation (Gibbons and Ringdal, 2006) and stacking techniques of data processing (Rost and Thomas, 2002).

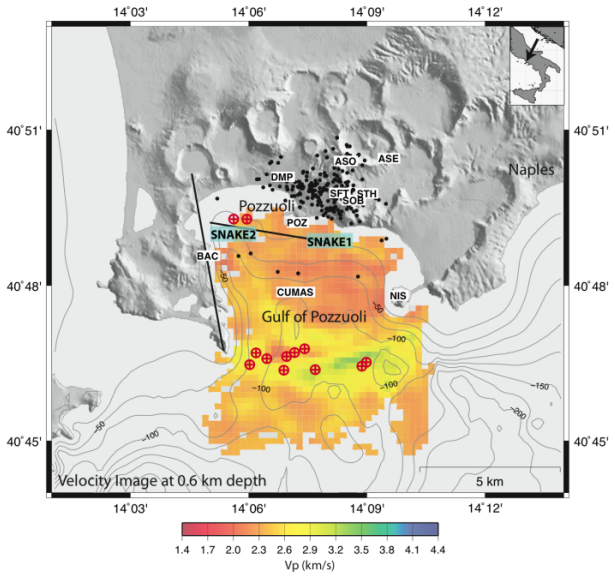

Figure 1. The Campi Flegrei Caldera in Southern Italy. The color map is a slice at 0.6 km depth of the tomographic velocity model obtained by Dello Iacono et al. (2009), evidencing the buried rim of the caldera. Two of the major known faults for the area are indicated by black lines, while the symbols ⊕ denote known fumaroles. Black dots represent selected earthquakes locations (high quality) from the 1982-84 uplift event. Existing onland INGV stations and the CUMAS underwater module (Iannacone et al., 2010) are shown. Finally two possible locations for ta chilometric-size, high resolution seismic antennas (SNAKE1 and SNAKE2) are evidenced. Bathymetry is indicated by isolines. The maximum depth of Pozzuoli Gulf is 100 m.

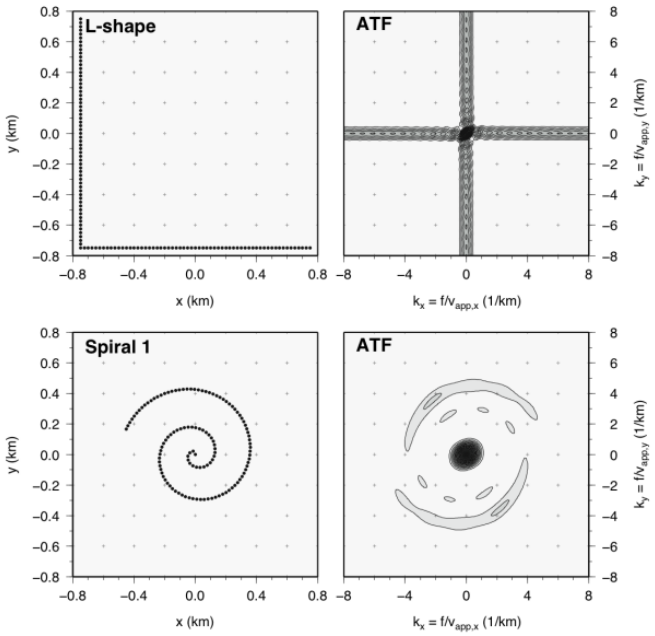

Figure 2. Examples of possible geometries for SNAKE arrays in Figure 1. Left: Map view of an OBC array with a cable length of 3 km and 25 m sensor spacing. Each dot represents one sensor. Right: Corresponding array response for incoming monofrequency, plane waves as a function of the wave number in x- and y-directions. Dark regions represent the wave numbers that yield a constructive stack in the beam forming process. An optimum array is characterized by a narrow central peak and vanishing side lobes.

Earthquake source parameters

The analysis and mapping of fracture properties can be an useful information to monitor stress/deformation state of the reservoir of a geothermal system, during its stimulation. Field operations include fluid extraction and injection which perturb the natural stress/strain conditions of the crust and causes failure of strength of rocks, thus resulting in earthquakes. We believe that source information about induced micro-earthquakes can help to constrain the possible mechanisms of the induced micro-seismicity, allowing for a more efficient reservoir management.

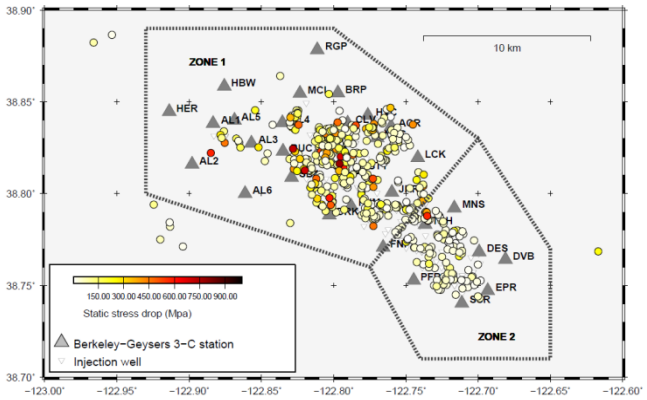

Figure 3. Induced seismicity map at The Geysers in the 2007-2011 time period. Circles correspond to earthquake epicentres and their colour is proportional to the stress-drop according to 484 the colour-scale in the figure. The grey triangles indicate the seismic stations of the Lawrence Berkeley National Laboratory (LBNL) Geysers/Calpine seismic network used in this study.

To this aim, we need

- accurate estimate of microfracture source parameters,

e.g., seismic moment, corner frequency and γ, i.e. the high-frequency spectral fall-off rate. The selection of source model which can differ from the standard model (γ=2) may be justified by the fact that the triggering mechanism of the induced seismicity, that, for instance, at The Geysers is likely ascribed to a temperature contrast, can modify the spectral fall-off. The corner frequency provides information about the dimension of fractured area which, together with seismic moment, allows to estimate the static stress-drop.

If S-waves are also analyzed, information about

- seismic efficiency can be obtained.

Estimates of the seismic efficiency, which mainly depends on the degree of lubrication of fractures induced by the fluids percolation, can be inferred from the comparison between the static stress release and apparent stress.

- The stress-drop (and eventually, the seismic efficiency)

can be used as a proxy to infer the space-time variation of fluids (fluids migration). In fact, the variability of the stress release suggests the presence of heterogeneities in the friction

distribution and fluid pressure, and normal stress and elastic properties variability in the fault zone.

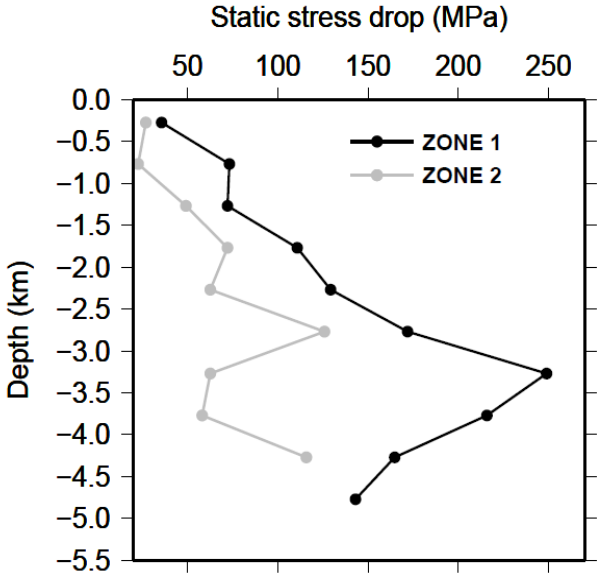

Figure 4. Static stress-drop versus depth for the analyzed earthquakes, distinct for ZONE1 (black line) and ZONE2 (grey line).

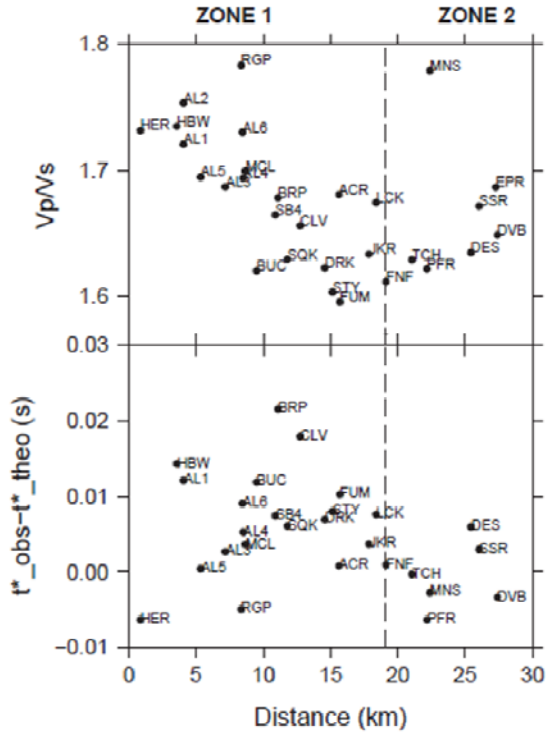

Figure 5. Spatial variation along a NW-SE profile of the single station Vp/Vs (top), and station residuals for P-wave attenuation parameter t (bottom). Dashed lines roughly outline the boundary between the two seismic source zones (ZONE 1 on the left and ZONE2 on the right). Stations codes are reported in all panels.*

As an example, we provide hereinafter some information about The Geysers geothermal field. Our studies on the earthquake source parameters confirm and refine the subdivision of the geothermal field into two distinct zones (ZONE1 and ZONE2), exhibiting significantly different medium and seismic source properties. In particular we observe a spatial variation of stress-drop, moving from ZONE1 to ZONE2 along the NW-SE direction, with larger stress-drop in the ZONE1. This can explain the difference in the seismogenic potential among the two zones and in particular the observation proposed by Beall et al. (2010) concerning the occurrence of the larger event ($M \geq 4$) in the ZONE1. We interpret the relatively high stress-drop values as associated with the dominant fluid fault lubrication effect which strongly reduce the friction level during microfractures. Moreover, we observe a difference in the depths distribution of the induced earthquakes occurring in the two zones. In particular, ZONE1 is characterized by a peak of the seismicity at depths ranging between 2 and 3 km while in ZONE2 the peak is at about 2 km. This feature is correlated with a known difference in the depth of the reservoir which is deeper in the ZONE1 with respect to ZONE2 (Beall et al., 2010).

The source information can be used as a proxy to monitor the pore pressure if

- the anelastic parameter t*,

which depends on the travel time T the quality factor Q in the medium, is known well. Highly attenuating media are characterized by small values of Q, and conversely, high values of Q correspond to weakly attenuating media. Analyzing both P- and S-waves, it is possible to estimate the ratio between S- and P-wave quality factors. According to laboratory measurements, $Qs/Qp > 1$ is a marker for a partially fluid-saturated crust, while $Qs/Qp < 1$ is expected for dry or full-saturated rock layers (Winkler and Nur, 1970; Toksoz et al., 1979). In practice, quality factor ratio behaves similar to compressional to shear velocity ratio, for which around 1.8 or slightly larger, suggest partially fluid-saturated materials (Ito et al., 1979). Comparing the P-attenuation characteristic residual time t* with respect to the single-station Vp/Vs ratio, both represented as function of the distance along the profile NW-SE, we infer relatively high values in ZONE1 for both quantities, consistently with Vp/Vs seismic tomography images. This suggests the presence of a low velocity, strongly attenuating, fluid saturated volume in the northern sector of The Geysers.

Finally,

- focal mechanisms and/or moment tensor

can be useful to infer information about the actual stress regime. In particular, for The Geysers, the fault-plane solutions obtained show a dominant strike-slip and normal faulting mechanisms, with P and T axes coherently oriented as expected for the regional stress field.

Monitoring of the medium mechanical properties

We analyzed a seismic waveform dataset of more than 15000 events ($1.0 < M_L < 4.5$) recorded at The Geysers geothermal field by a dense surface seismic array during August 2007 to October 2011. The obtained results provided interesting issues concerning the investigated area characteristics, but above all, they highlighted very important general indications about the importance in geothermic contexts of seismological analyses for characterizing the medium mechanical properties. In particular,

- the identification of strong seismic velocity variations by 3D P- and S-wave seismic tomography analyses

represents an effective means for the localization of the reservoir portions characterized by high temperature. Furthermore,

- tomographic images of the P- and S-wave seismic velocity ratio (Vp/Vs)

are valuable tools for identifying the presence of fractured rocks and the discrimination between their saturation level in terms of fluid or gas. Besides the velocity, also

- the anelastic attenuation should be taken into consideration.

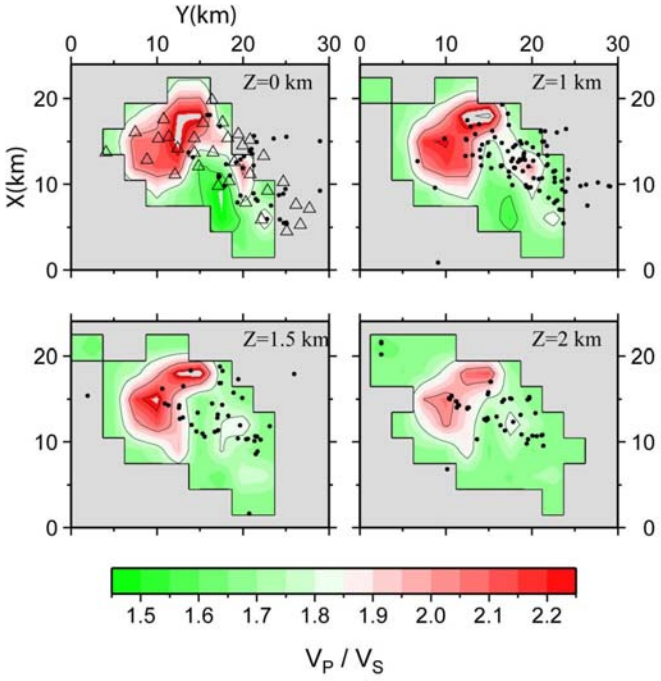

Figure 6. Map view showing the Vp/Vs ratio inferred from the 3-D tomography, at 0, 1, 1.5 and 2 km depth, at The Geysers.

In fact, the experience of The Geyser study showed that the strong variation in P-wave velocity and Vp/Vs are closely related to a variation of the attenuation. In turn, all these parameters have been found consistently with the subdivision of The Geyser field in two sub-regions characterized by significantly different medium and fracture source properties.

A further important issue related to the availability of high resolution 3D velocity models is that they would be very important for improving the earthquakes location, and thus for obtaining a better reconstruction of the fractures orientation and dimension.

Finally, the seismic monitoring should be maintained throughout the whole geothermal field exploitation, being the repetition of tomographic analyses on regular bases in time (i.e. 4D tomography) a very useful strategy for keeping under control the variations in time of the medium mechanical properties, especially following prolonged periods of EGS operations.

Seismic hazard

Fluid injection and/or withdrawal, gas storage or any other filed operation that perturbs the stress condition of the earth crust can induce seismicity. The induced earthquakes, due to their magnitude and relatively short source-to-site distance, may have adverse consequences ranging from people nuisance to structural damage to the buildings. In order to mitigate the seismic risk of the induced seismicity a reliable approach for evaluating seismic hazard is mandatory. The key points for computing seismic hazard from induced seismicity should consider:

Compilation of a seismic catalog containing earthquakes magnitude and hypocentral parameters recorded in the study area. Based on the available network configuration and its performance the minimum magnitude of completeness Mc should be as smaller as possible. Ideally, a negative Mc would be required.

Time dependent estimates of the b-value of the Gutenberg-Richter relationship. The b parameter is indeed correlated to the pore-pressure decay (in near-field) and anti-correlated to stress-drop. Thus it can be used to monitor the time-evolution of the seismicity.

The same catalog should be used to identify the number and the extension of the seismogenic areas to be used as input for hazard analysis.

Compilation of a time-evolving tables of measured ground-motion measures to infer empirical ground-motion prediction equations and/or seismic source and attenuation parameters (e.g. seismic moment, corner frequency, stress-drop, the quality factor Q, the surface amplification factor k) to set-up a stochastic model. The ground-motion parameters of interest should be identified on the basis of the target (e.g. a particular structure typology or people perception) but at least peak-ground acceleration, peak-ground velocity and spectral ordinates at a set of structural periods must be considered.

Analysis of the recorded seismicity and its correlation with field operations to identify the most suitable seismicity model to be used for predicting future events. Those models can be parametric (e.g. Poisson, Poisson non-homogeneous, ETAS, etc.) or non-parametric and should account for the spatio-temporal distribution of the events. The reliability of the models must be tested for example through a retrospective approach on an existing catalog or by using the current catalog.

Time-dependent seismic hazard analysis. The result should be always expressed in probabilistic terms and must concern the expected ground-motion value in the next future.

Identification of critical hazard levels that should not be exceeded and should be used to conduct safe field operations.

Implementation of fragility curves for different structural typologies to be used for risk analyses. In addition, nuisance fragility curves that provide the probability that a felt ground-motion is unacceptable should be investigated.

Testing the hazard estimates on the actual recorded seismicity and re-calibration of both the input parameters and the previously selected protection levels.

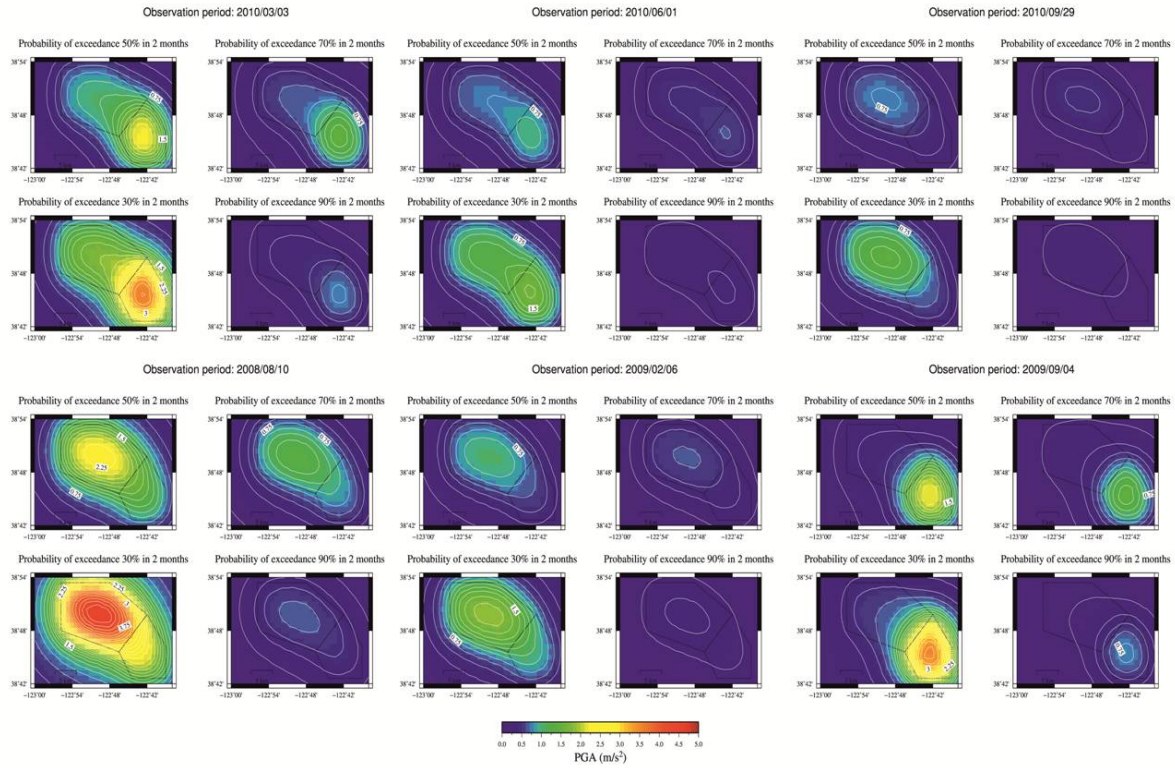

Figure 7. Seismic-hazard maps for The Geysers geothermal area. The reported PGA values are expressed in m/s^2 and represent the peak-ground-motion values having the probability of exceedance reported on the top of each map. Each date corresponds to the central time of a one-month window centered on that date. The dashed lines outline the two seismic zones.

3. NORSAR

Involved in the work package WP3, *Analysis of Induced Seismicity*, NORSAR has focused on the analysis of data from two sites, (1) Paralana, in South Australia, a new enhanced geothermal system (EGS) where the first main stimulation occurred in July 2011 and (2) Basel, in Switzerland, an EGS which was stopped during the stimulation phase in 2003 due to the occurrence of a large magnitude event (LME).

From the analysis of the Paralana data, we propose several critical points that should be taken in consideration for the seismological investigation of any future EGS.

In terms of instrumentation, it is necessary to build a seismic network composed of both, surface (or shallow borehole) and deep borehole stations. Closer to the source, borehole stations allow to detect very small events. Even if the site has a low level of noise, such as Paralana, built in the middle of the desert, the signal-to-noise ratio (SNR) likely decreases rapidly with distance. In addition, a broad area needs to be covered with seismic stations, and due to economic reasons surface stations are often prioritized before a network of downhole stations. However, the costs for downhole stations need to be considered carefully, taking into account the trade-off between costs and quality of the recorded data. At Paralana, for example, most of the surface stations have recorded seismic phases arriving between the direct P- and S-wave phases (Fig. 1), which reveal the complexity of the medium, mainly towards shallower structures. Such phases, often S-to-P conversions on high-impedance layers, are relatively often observed on surface stations and can create difficulties for automatic processing. Having obtained data from surface and borehole stations, we were also able to detect variations in the Vp/Vs ratio by comparing surface and borehole seismic signals.

Another important point concerns the velocity model, to which absolute locations, and consequently relocations, are very sensitive. Event locations are generally computed using a homogenous or a 1D velocity model, corrected with calibration shots. However, these approximations are no longer valid in the case of a complex medium, particularly for larger source-receiver distances (> 3 km); hence a 3D velocity model should be used. We used seismic reflection lines and well-log information to build a 3D velocity model. We used it not only for the location purpose but also to perform 3D ray modeling and identify the converted phase we observed in-between the P and S phase. Our recommendation for future EGS is therefore to conduct as good as possible a pre-site investigation and to gather information on the seismic velocity structure. This should include near-surface attenuation studies and noise studies for the network design. Ray-modeling for testing of the event-location performance with different feasible network designs is also a cheap method to conduct before any drilling/instrumentation. Once drilling is conducted, the whole well should be logged at least for Vp, Vs, and density to correlate with the reflection/refraction seismic data, if available. In addition, information about in-situ stresses in the well should be investigated, using borehole breakouts, extended leak-off-tests and/or formation integrity tests, preferably at several depths. This will be important for the interpretation of the located microseismicity and the related source parameters.

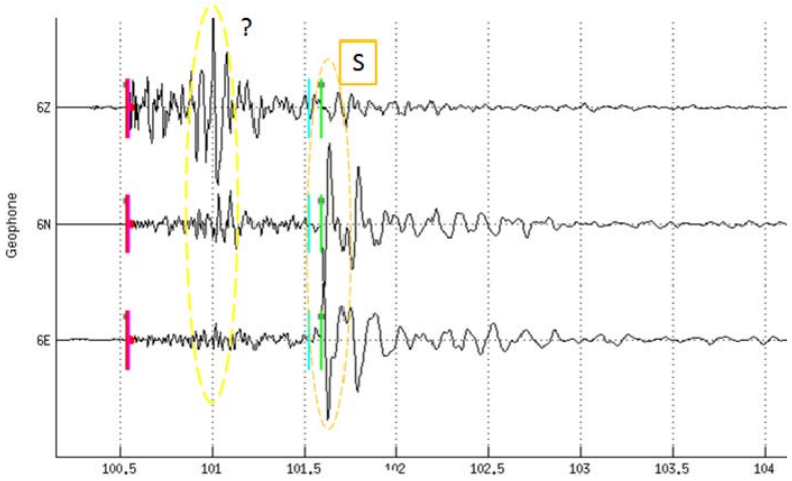

Figure 1. Seismogram recorded at a shallow-borehole station (40 m below surface). A converted phase can be observed between the direct P- and S-wave phases.

EGS operations induce generally several thousands of microearthquakes. Because manual picking takes a lot of time and can lead to inconsistent picks (Diehl et al., 2009), automatic processing is required for this type of study. In addition, automatic picking generally allows to lower the detection threshold, that is to take into account very small events. However, the uncertainty of automatic picks might be larger, if for example the data are noisy or if several events occur at the same time. A careful check of the picks, based for example on location error and residual values, is of course a first step for improving the data base. Another step to refine phase picks is to perform waveform cross-correlations for pairs of earthquakes recorded at the same station (Rowe et al., 2002). Improving onset picking is particularly important if one wants to perform double-difference relocation or tomography (e.g. hypoDD, Waldhauser and Ellsworth, 2000; tomoDD, Zhang and Thurber, 2003) as the error made on the absolute pick is increased in differential picks. Our approach at Paralana was first to process the data automatically with MIMO (Oye and Roth, 2003), to assess the quality of the automatic picks using a reference subset of events picked manually, and to cross-check the database manually (for events with magnitude larger than one and for the large residuals). Then, we improved the travel-time differences with waveform cross-correlation (Fig. 2) and relocated the events using the double-difference algorithm (Waldhauser and Ellsworth, 2000).

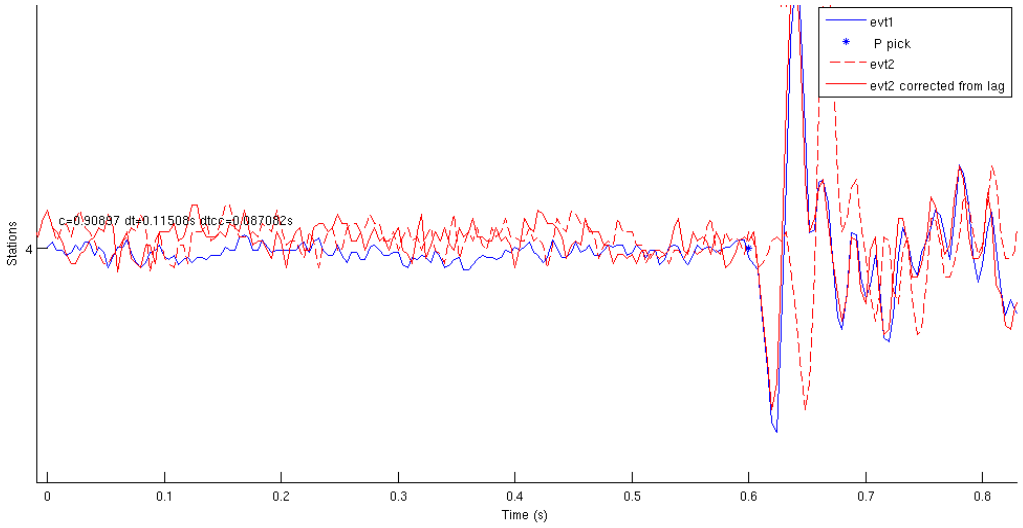

Figure 2: Seismograms of two events (1 and 2, blue and red, respectively) recorded at a surface station. Waveforms are aligned according to the automatic P-picks (blue star): wrong P-picks for event 2 is then highlighted by the gap between the waveforms (blue line and red dashed line). After waveform cross-correlation, the waveform of the event 2 is correctly aligned (red line) with event 1 and the travel-time difference can be corrected.

4. ISOR

Recommended guidelines for Iceland:

Iceland is located at the diverging boundaries of the North American and Eurasian plates, where volcanic and earthquake activities occur when the crust moves apart due to plate tectonic movements. Geothermal systems in Iceland are (mostly) conventional fractured systems. The permeability is a consequence of the fissures and fractures created in earthquakes. The areas are subdivided into high and low temperature fields. The high temperature fields are associated with volcanic activity and the seismic activity is due to plate motions and magma movement. The low temperature fields are generally in seismically active areas with high regional temperature gradients and large earthquakes can occur in these areas. The natural activity is variable in time.

The first phase when injection is planned is a preliminary project evaluation. In that the main focus is on legislation framework, natural seismic activity and vulnerability of the society. When the preliminary project evaluation is finished and a decision has been made to proceed with a specific injection plan, the next step is to acquire the necessary knowledge for design and the safest operation of injection. Usually, necessary information depends on local conditions. However, following are some main topics which should be available in all cases:

a) Geological map
b) Tectonic movements in the area before geothermal production started
c) Natural seismicity
d) Map showing fractures and fissures, stress field and largest earthquakes to be expected
e) Velocity and acceleration in earthquakes

These five topics are discussed in the following:

Geological map

A geological map, where visible fractures, faults and eruptive magma conduits have been mapped with care, is a required fundamental document. The map should contain necessary information on tectonic movements in the area along with an analysis of the tectonic evolution, including the age or relative age of fractures and faults. The results will be used for a further analysis of fractures and the tectonic stress field in the area.

Tectonic movements

Production of geothermal fluid and injection affects the natural background process. Therefore, it is important to measure tectonic movements in geothermal areas, preferably before the start of production, but at least before the start of injection. This is generally carried out with GPS and gravity measurements.

The preliminary project evaluation is to examine whether sufficient information is available on tectonic movements in the area, and whether adequate measurements are in progress. If not, additional measurements, and, where appropriate, installation of continuous GPS-stations should be carried out for improvement. Tectonic movements due to injection are generally

small, and therefore it is important that sufficient time series of measurements exists, before the start of injection. As a result, continuous GPS measurements need to be carried out at least 12 months in advance of the injection, to be able to evaluate seasonal natural movements for example.

Report is written on previous and existing tectonic movements before injection, including geological data on previous tectonic movements. The results would be used to assess the actual impact of the injection on tectonic movements and the tectonic stress field.

Natural seismicity

Exploration of natural seismicity provides information on the frequency and magnitude of natural earthquakes in the area, in advance of operations at the site. It also provides information on active fractures, displacements on faults and the principal stress field.

The exploration includes an analysis of available data on earthquakes, and the installation of a local seismic network.

Seismic monitoring should be commenced as soon as an injection site is selected. It should be comprehensive enough to allow complete spatial coverage of seismicity over an area that is at least twice the radius of the anticipated stimulated reservoir volume. The regional seismic monitoring network of the Icelandic Meteorological Office (SIL) provides information on large-magnitude events and a historical background, but a more sensitive array of seismic instruments is needed to be able to detect small-magnitude events (preferably magnitudes -1.0 to 0.0), and to improve location and depth accuracies. Current experience indicates that such a local seismic networks records up to ten times the number of earthquakes compared to the regional network. The duration of seismic monitoring of the injection area can be short, but it is generally recommended to be at least six months. Moreover, it is recommended that at least six seismic stations collect data in the area. While data is collected by the local seismic network, available data on earthquakes and focal mechanisms in the area should be analyzed, both available measurements and evaluation of historical data.

Report is written on natural seismicity, stating frequency of events, periodic behavior, magnitude distribution of earthquakes, analysis of seismically active fractures, their direction and dip, and a calculation of the tectonic stress field that creates earthquakes. The report would be the basis for a fracture map, the choice of injection site and an estimation of the probability of induced seismicity and its consequences.

Fracture map, stress field and maximum earthquakes to be expected

Results from geological mapping, and measurements and interpretation of tectonic movements will be used to create a comprehensive fracture map of the area, and to assess the tectonic stress field at the anticipated injection site. A proposal for an injection site based on this information should then be made, by taking into account the tectonic stress field, probable permeability and the probability of induced seismicity. Moreover, an evaluation would be made on the maximum earthquakes to occur inside the injection site, based on the fracture map and measurements of natural seismicity.

Recommendations are made on several potential injection sites, where the advantages and disadvantages of each site selection are explained. Those include probable permeability, probability of induced seismicity and corresponding magnitudes, and an evaluation on the maximum possible induced earthquake.

Ground velocity and acceleration

Geological conditions in populated areas, possibly affected by induced seismicity, need to be mapped. Sedimentary thicknesses and shear wave velocities are particularly interesting. Appropriate prediction model has to be made on peak ground acceleration (PGA) and peak ground velocity (PGV) for tectonic earthquakes, considering the earthquake source, magnitude and decay of impact with distance, besides assessing the earthquake impact on people, equipment and structures. If needed, an accelerometer should be installed in the affected community to explore ground vibrations and tremor in advance of operations.

Report is written on possible impact of different magnitude earthquakes on structures and people in the affected communities.

Risk estimate

Based on the outcome of the preliminary evaluation a thorough risk analysis is made and decision is made on whether the planned injection project is realised or not.

Injection

When decision on the injection is made the project is planned in detail. That includes the drilling, test injections and monitoring pressure rate and associated activity.

5. ETH

Lessons learned from the Basel EGS

The stimulation of the Basel EGS in 2006 induced about 3500 seismic events, which occurred during the injection phase and the following months, and which were locatable by the six-station borehole network (Häring et al., 2008). Close to 200 of the strongest events were also recorded by various surface networks (Deichmann and Ernst, 2009; Deichmann and Giardini, 2009). Preliminary hypocenter locations and magnitudes were obtained from manually picked arrival-times and amplitudes. This information was sufficient to map the overall orientation and dimension of the stimulated rock volume in near real-time. More detailed insights into the physical processes were obtained only through systematic re-evaluation of the data set by various groups of scientists over the following years: hypocenter locations were refined in several stages by the application of various methods; magnitudes were re-evaluated and seismic moments were calculated by different groups; focal mechanisms and moment tensors were determined; b-values and stress-drops were mapped in space and time; pore pressure evolution was estimated.

Hypocenter locations and identification of activated faults

Accurate hypocenter locations of the induced seismic events are undoubtedly the most important and fundamental data for all subsequent investigations. Poorly calibrated seismic velocity models and arrival-time errors lead to a more or less amorphous appearance of the so-called seismic cloud, which in addition can be systematically mislocated and misshaped (Kraft and Deichmann, 2013). In fact, a large component of the observed scatter of the initial hypocenter locations was due to faulty or inconsistent arrival time picks made under time pressure by inexperienced analysts. In the context of seismicity induced by water injection into a potential geothermal reservoir, it is useful to distinguish between the location accuracy of the hypocenters relative to the injection borehole (e.g. relative to the casing shoe) and of the hypocenters relative to each other or relative to a chosen master event. In the first case we speak of their absolute location and in the second case of their relative location.

P- and S-wave velocities are usually not known with a sufficient resolution and accuracy to obtain reliable absolute locations. However, given that the expected seismicity is concentrated in a restricted volume separated by some distance from the recording stations, accurate absolute locations can be obtained even with a simple and poorly constrained velocity model, provided that travel-time corrections to each station have been determined from some kind of calibration procedure. In the case of the Basel EGS, the operators had planned a check-shot at the base of the injection borehole. For technical reasons this was not possible. Instead, a seismometer installed close to the casing shoe was operated during the first two days of the stimulation. The signals recorded by this sensor constrain the hypocenters of the very first seismic events induced by the stimulation to lie in the immediate vicinity of the open hole section, so that these events could be used to determine station corrections for locating all subsequent events (Dyer et al., 2008). In practice, this procedure amounts to locating all hypocenters relative to a chosen master-event and was the key to reliable absolute hypocenter locations during the stimulation of the Basel EGS. Other calibration procedures are also possible, such as check-shots near the surface stations, that are recorded prior to the start of the stimulation by one or more seismometers installed temporarily in the injection well.

Such a well-calibrated velocity model, while ensuring the proper location of the seismic cloud as a whole relative to the injection well, is not sufficient to resolve individual faults activated by the stimulation. The average errors of the P- and S-arrival times determined by eye are too large. However, the observation that more than half of the events occurred as sequences of events with almost identical signals (e.g. Asanuma et al., 2008; Deichmann and Giardini, 2009; Deichmann et al., 2013; Dyer at al., 2008, 2010; Häring et al., 2008; Kahn, 2008; Kraft and Deichmann, 2013; Mukuhira et al., 2013) implies that the events pertaining to a particular sequence are located close to each other and have the same focal mechanism. In other words, their hypocenters lie on the same fault. Thus, high-precision relative locations of earthquake hypocenters in sequences with similar events can image the orientation and dimensions of faults activated during stimulation; this requires relative arrival times determined by signal cross-correlation and a relative location algorithm (master-event method or double-difference). Combined with a representative focal mechanism for each sequence, this information is essential to determine the state of stress in the reservoir. The excellent match between the orientation of the stress field derived from focal mechanisms and from borehole failure analyses (Deichmann and Ernst, 2009; Terakawa et al., 2012; Valley and Evans, 2009) demonstrates that such borehole analyses undertaken before the start of stimulation can provide reliable insight into the state of stress of the potential reservoir.

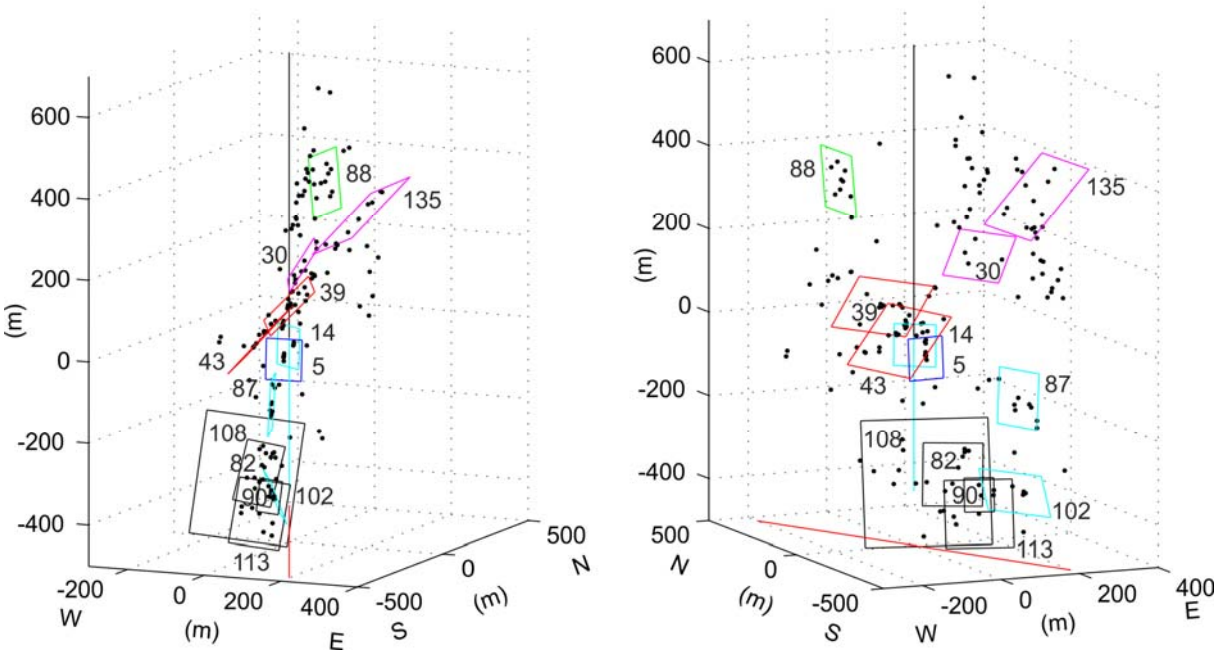

Figure 1. Perspective plots of the identified faults, viewed at 10 degrees from above and towards the NNW (azimuth 336 degrees, left) and towards the NNE (azimuth 24 degrees, right). The black dots are the master-event locations for the 165 events recorded in December 2006 by both the borehole and the surface networks. The different colors differentiate between the different faults as follows: normal faults (red), oblique strike-slip/normal fault (magenta), N-S strike-slip (green), E-W strike-slip (blue), approximately NW-SE strike-slip (cyan), ML 3.4 mainshock cluster (black). The numbers next to the planes identify each cluster (the mainshock cluster is identified by four planes corresponding to events 82, 90, 108 and 113). The vertical line denotes the location of the borehole (black, the cased section, and cyan, the open hole) and the red line shows the overall orientation of the seismic cloud (from Deichmann et al. 2013).

To map possible flow paths that have been opened during stimulation, and thus to constrain geo-mechanical models of permeability enhancement, estimates of the dimensions of the activated faults are also necessary. This requires reliable measures of seismic moment or moment magnitude (not just local magnitude) and, if possible, stress drops (Bethmann et al., 2011; Goertz-Allmann et al., 2011). The detailed analysis of the sequences associated with the larger magnitude events ($M_w > 2$) induced during the stimulation of the Basel EGS showed that the activated faults have dimensions on the order of several 100 m and are often oriented obliquely to the overall orientation of the microseismic cloud (Deichmann et al., 2013). These results reveal a complex internal structure of the flow paths in the rock volume stimulated by the water injection and imply that geo-mechanical models consisting of a single throughgoing structure are too simplistic.

Stress drop

Although the dimensions of the faults activated by the stimulation of the Basel EGS were estimated on the assumption of a constant stress-drop (Deichmann et al., 2013), the analysis by Goertz-Allmann et al. (2011) shows that stress-drop varies over a wide range and tends to increase systematically with distance from the injection point. Due to its model dependence and because it is strongly affected by attenuation effects along the path between source and observer that often are difficult to quantify and correct, the absolute stress-drop values are subject to large uncertainties. However, relative stress-drop differences calculated in a consistent manner are usually robust. For the induced seismicity of Basel, Goertz-Allmann et al. (2011) applied a sophisticated stacking technique to calculate stress-drops from the corner frequencies of the recorded seismograms. The results obtained by Goertz-Allmann et al. (2011) are shown in Figure 2. The mean and median stress drops are around 2.3 MPa. However, given the large uncertainty, not much can be concluded from this value. More significant are the systematic variations of stress drop as a function of hypocenter location: as shown in Figure 2c, close to the injection well, stress drops are low, while at the periphery of the seismic cloud, they are high. Significant for the long-standing earthquake-scaling debate is the observation that there does not seem to be any systematic variation of stress drop with magnitude (Fig.2b).

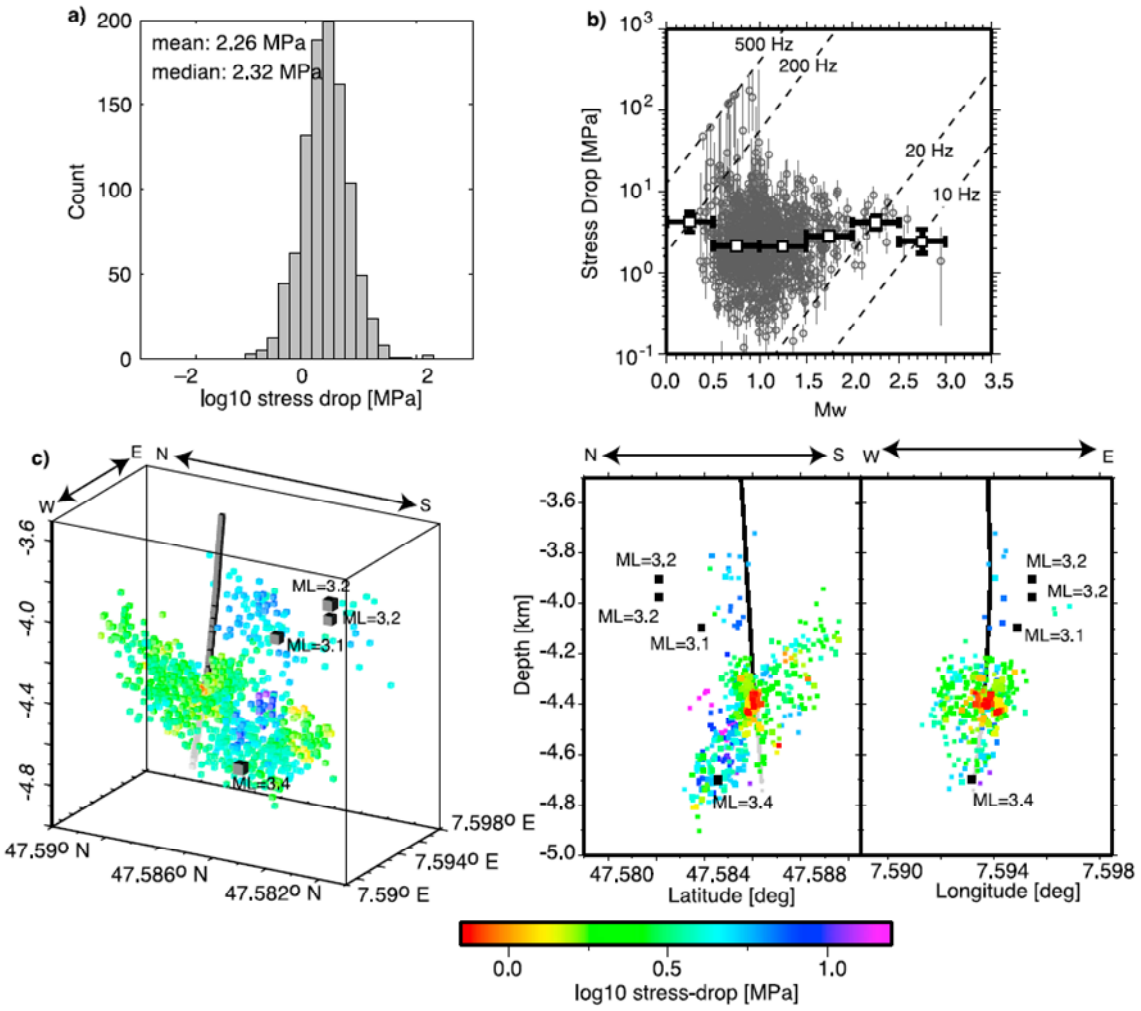

Figure 2. (a) Histogram of log stress drop for 1000 events. (b) Stress drop versus moment magnitude. Thin bars indicate the estimated uncertainty of the stress drop from the uncertainty of the corner frequencies. White squares show median stress drop per magnitude bin with standard errors (vertical) from bootstrap resampling. Horizontal bars mark the bin width. Dashed lines show constant corner frequencies as marked. (c) Lateral stress-drop variations as 3-D view and two cross sections of all events within 100 m of a plane through the injection point. The trace of the borehole is shown in black down to the casing shoe and in gray for the open hole section. The four largest events are marked by black squares and identified by their magnitudes. (From Goertz-Allmann at al., 2011).

Estimates of pore pressure

One of the key questions regarding the stimulation of a geothermal reservoir is how the pressure perturbation due to the injected water propagates through the rock and how this effect can be monitored during the stimulation process. Goertz-Allmann et al. (2011) propose to use earthquake stress-drops as a proxy for pore pressure. Their hypothesis relies upon an apparent inverse correlation between stress-drop and modeled pore pressure, based upon a dependence of both on the distance from the injection well. That stress-drop seems to increase with distance from the well was already seen in the hypocenter plots in Figure 2. Assuming that the temporal evolution of the pore pressure can be captured to first order by a linear diffusion model and following the procedure suggested by Dinske and Shapiro (2010), they compute the pressure perturbation due to the injection as a function of time and distance. As

expected, at any point in time, pore pressure decreases with increasing distance from the injection well. Given this distance dependence of both stress-drop and pore pressure perturbation, it is not surprising to find that stress-drop decreases with increasing pore pressure. The physical link between the two is the differential stress: both low stress-drops and high pore pressures are thought to be symptomatic of low differential stress. Although the inverse correlation between stress-drop and pore pressure is convincing, it is important to realize that the absolute pore pressure levels shown in the article by Goertz-Allmann et al. (2011) are constrained only by the assumption that the spatial and temporal evolution of the pore pressure during water injection can be predicted by a linear diffusion model.

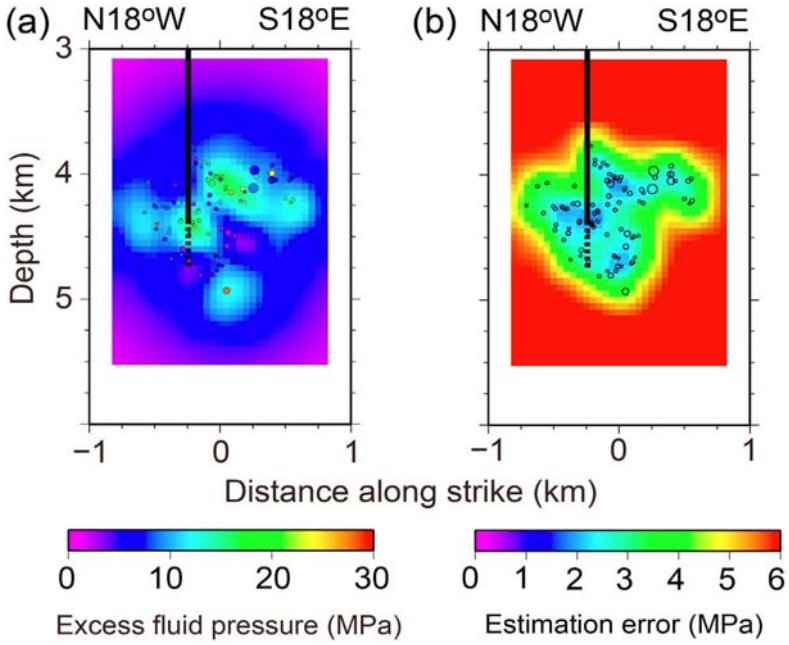

Figure 3. The distribution of pore fluid pressures formed by the fluid injection in Basel. (a) The excess pore fluid pressure field projected onto the macroscopic plane defined by the overall hypocenter distribution. The circles show hypocenters of events projected on the plane, whose excess pore fluid pressures are included in the analysis to estimate the pore fluid pressure field. (b) The distribution of estimation errors of pore fluid pressures. (From Terakawa et al. 2012).

An alternative approach to obtain direct observational estimates of pore pressure within the stimulated reservoir was taken by Terakawa et al. (2012). It is based on the fact that the potential fault-planes seen in the focal mechanisms of the induced earthquakes show large variations in strike, dip and sense of slip. Assuming that the stress field is more or less homogeneous over the stimulated rock volume, many of the activated faults are not optimally oriented. This means that the shear stress acting on a given non-optimally oriented fault is not high enough to cause the fault to fail, unless the fault is sufficiently weakened by an increase of the pore pressure within it. Consequently, if one knows the orientation and magnitude of the principle axes of the stress field and assumes that it is homogeneous over the volume of rock under consideration, and if one extrapolates laboratory measurements of the coefficient of friction to natural faults, then for each earthquake with a known focal mechanism one can calculate the pore pressure in excess of hydrostatic that is needed to trigger the event. In the case of the induced seismicity of Basel, the orientation of the stress field and a ratio of stress

differences is available from the inversion of the observed focal mechanism. The vertical stress is given by the weight of the overburden (the lithostatic pressure). In addition, Terakawa et al. (2012) make the assumption that slip on faults optimally oriented with respect to the average stress field occurs at hydrostatic pressures. The latter assumption is equivalent to the hypothesis that the Earth's crust is critically stressed and that optimaly oriented faults are on the verge of failure. With all these observations and assumptions it is possible to fully characterize the average stress field and to calculate the shear stress on each fault and the fluid pressure necessary to induce failure. Terakawa et al (2012) resolve the ambiguity between the two possible fault-planes in each focal mechanism by choosing the plane that is more favourably oriented as the active fault-plane. The interpolated and smoothed pore pressure field obtained by Terakawa et al. (2012) from this procedure and the corresponding error estimates are shown in Figure 3. Although overall the fluid pressures decrease towards the periphery of the stimulated volume, the pressure field within this volume is characterized by several patches of higher and lower pressures. More important is, however, that according to the results of this analysis the fluid pressures needed to trigger many of the observed earthquakes are in the range of 10 to 20 MPa even out to several 100 m from the injection well. This result is obtained totally independently of the applied injection pressures but is entirely consistent with these pressure values. Moreover the in-situ fluid pressures estimated by this method are one to two orders of magnitude larger than those predicted by linear diffusion models.

b-values

One of the key discoveries of the research performed on the seismicity induced by the Basel EGS concerns the relative size distribution of earthquakes (Bachman et al., 2012). The cumulative number of earthquakes, N, in a given volume generally follows a power law distribution (called the Gutenberg-Richter relation) and can be expressed as $\log N = a - bM$, where a and b are constants that describe the productivity and the relative size distribution, respectively. Higher b-values indicate more small events relative to larger events and vice versa. The Gutenberg-Richter relation and slight modifications thereof are used in essentially all seismic hazard studies, as it allows extrapolation from the number of observed smaller events to the occurrence of infrequent larger ones. Studies of micro-earthquakes on faults have shown that the b-value, when mapped with high quality data at high resolution, varies in the Earth's crust over distances of a few kilometers or less. These studies, combined with the analysis of regional and global focal mechanism data as well as laboratory work indicate that the b-value is inversely proportional to the differential stress and thus may qualitatively be used as a stress meter at depth in the Earth's crust, where generally no direct measurements are possible. Bachmann et al. (2012) apply high-resolution b-value mapping to induced seismicity, in order to obtain information on the stress regime and possibly the pore-pressure evolution in space and time inside the stimulated rock volume.

The key findings of Bachmann et al. (2012) are summarized in Figure 4, which shows the strong and highly systematic spatial heterogeneity of the b-values for the seismicity induced by the Basel EGS. Unusually high b-values shown in red are found near the injection point and earlier in the sequence; further out, b-values tend to be closer to the normal tectonic average of around 1.0. Bachman et al. (2012) and in even more detail Goertz-Allmann and Wiemer (2012) have developed a geo-mechanical model that explains these observations and that offers a framework for improved forecasting of induced seismicity. The fact that the largest events in induced seismicity often – but not always – occur after shut-in is well-explained by this model.

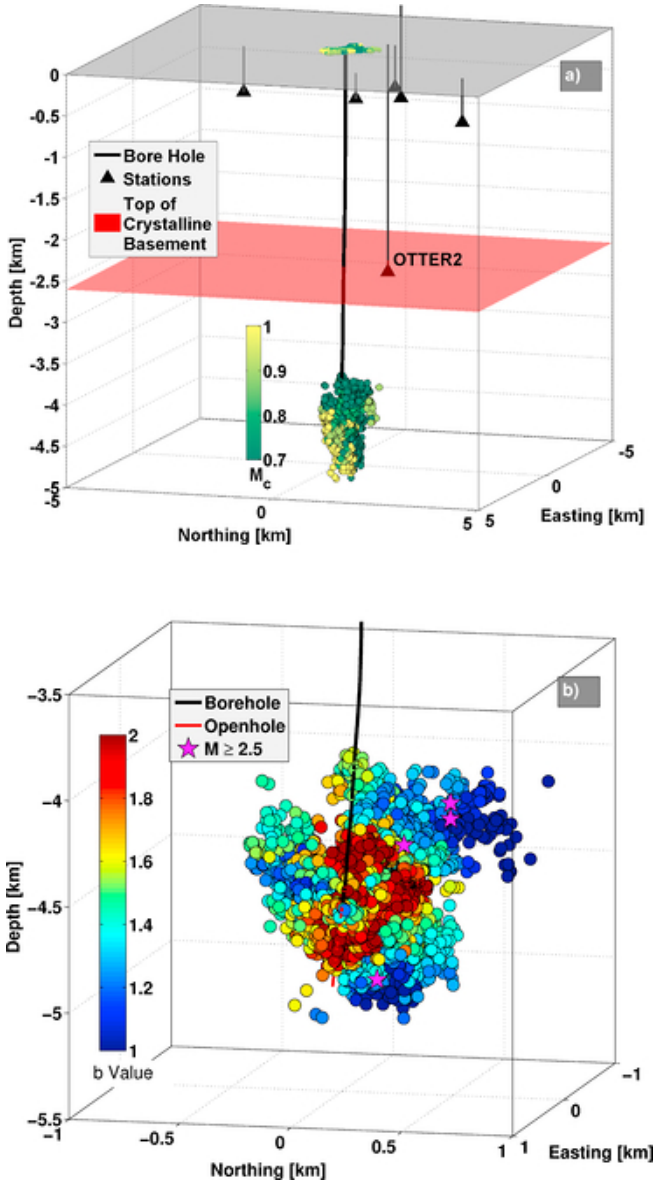

Figure 4. (a) Overview of the Basel induced seismicity showing the depth of the 3560 located events (circles) and the location of the seismic stations (triangles). The red plane marks the top of the crystalline basement, within which all events occurred. The color scale indicates the recording completeness ranging from Mw 0.7 to 1 (Mc). (b) Close-up of the events with the overall b-value distribution based on all events. While values range from Mw 0.8 to 3.5, the color bar is limited from 1 to 2 for a clearer visibility. (From Bachmann et al., 2012).

Conclusions

Although much was learned about the processes underlying the stimulation of the Basel EGS, one must be careful to generalize these results. Indeed, comparisons with other geothermal sites, some of which were studied in the context of the GEISER project, show that the seismic response to stimulation is very variable. Thus progress in our general understanding of the physical processes that lead to unwanted seismicity during stimulation of an EGS will only be made through systematic and comparable seismological investigations in the course of future projects.

Based on the experience gained from the analysis of the Basel EGS, the parameters that need to be determined in future EGS projects include:

- In-situ stress analysis based on stress-induced bore-hole failures.
- Accurate absolute (error < 100 m) and relative hypocenter locations (error < 10 m), based on a velocity model that has been calibrated beforehand with check shots or sensors in the injection well.
- Focal mechanisms and moment tensors using both first-motions and waveform amplitudes.
- Reliable moment magnitudes (seismic moments).
- Spatial and temporal variations of stress drop, using procedures that correct reliably for path and site effects.
- Spatial and temporal variations of b-values; this requires sufficient network sensitivity to achieve a magnitude of completeness that is at least two magnitude values lower than the maximum expected or acceptable event magnitude.

As the combination of all of these observables allows direct estimates of the spatial and temporal evolution of pore pressure in the stimulated rock volume, every effort should be made to perform such investigations during or immediately after a stimulation. Thus, semi-automatic methodologies need to be developed to determine these parameters in near-real-time. The last three points, if available in real-time, constitute also essential input to advanced traffic-light systems that are based on probabilistic seismic hazard assessments during ongoing stimulation.

6. EOST

The work completed by the research group of the EOST, in the framework of the GEISER project, allowed to provide some important guidelines: 1) on the study of the induced seismicity associated with the hydraulic stimulations in geothermal fields; 2) on the use of passive methods as the seismic noise correlation for detecting and monitoring geothermal reservoirs; 3) on the exploitation of the active Vertical Seismic Profiling (VSP) for constructing seismic velocity models highly resolved near to the wells.

The EOST crew took advantage of the large amount of data gathered by the Soultz EGS scientific project to develop a seismological methodology and obtained a reliable knowledge of the deep structures developing reliable methods that can be applied at various scales and different moments of the development of geothermal projects.

Study of the induced seismicity.

Our experience on the study of the induced seismicity observed at the geothermal power plant of Soultz-sous-Forêts gives evidence that the seismic tomography, and especially the double-difference one (Zhang and Thurber, 2003), represents a powerful technique to image the seismic patterns and to describe their temporal and spatial evolution. Since we focused our attention on the study of the temporal variations of the elastic parameters through the 4D seismic tomography, we can state that these methods are very useful for the understanding of the mechanical behavior of the geothermal reservoirs, when used with rigorous assessment tests and post-processing procedures (e.g. the Weighted Average Model method; Calo' et al., 2009, 2011, 2013a) to avoid misunderstanding due to the presence of bias in the models. The WAM method consists in an algorithm that unifies several velocity models of the same area, with a weighting technique determining an average model statistically independent from the input parameters that normally could affect the "classic" tomographies. It results a powerful tool to strongly reduce to presence of artifacts in the models.

The main goals that should be achieved with the implementation of the 4D tomography methods are:

- to describe the behaviors of the geothermal reservoir in terms of seismic velocity variations during and after the injections;
- to increase the resolution of the seismic patterns by re-locating the events using 3D velocity models that result more appropriate than the 1D models used for routine locations;
- to infer on the transient stress perturbation during the injections;
- to use the obtained seismic velocity models for inferring on the change of some important mechanical properties of the reservoir (e.g. crack extension and evolution of the seismic anisotropy (Adelinet et al., 2013), formation of damage zones (Shalev et al., 2103), etc.

To study the temporal changes of the seismic velocities during the stimulation periods, the recorded events should be divided into temporal subsets that explore periods defined with

respect to the injection scheme. Particular attention should be given to changes in injected flow rates, periods of stationary injection conditions, and post injection periods.

In our studies, we show that injections tests performed in regions of the Soultz reservoir that are initially poorly connected to large faults (e.g. the case of GPK2) are characterized by a low anomaly of the P-wave velocity mainly located around the zone where microseismic activity develops (Figure 1). Seismicity appears as a compact cloud without internal structures during the stimulation whereas some well-identified segments are noticeable in the post-injection periods (Figure 2). In some specific periods (i.e. when the injected flow rate was suddenly increased) the velocity anomaly disappears suggesting that the velocity variations within the reservoir (and consequently the related variations of effective stress) are not associated with simple water diffusion from the injection well, but rather reflect the occurrence of large-scale aseismic events in the reservoir.

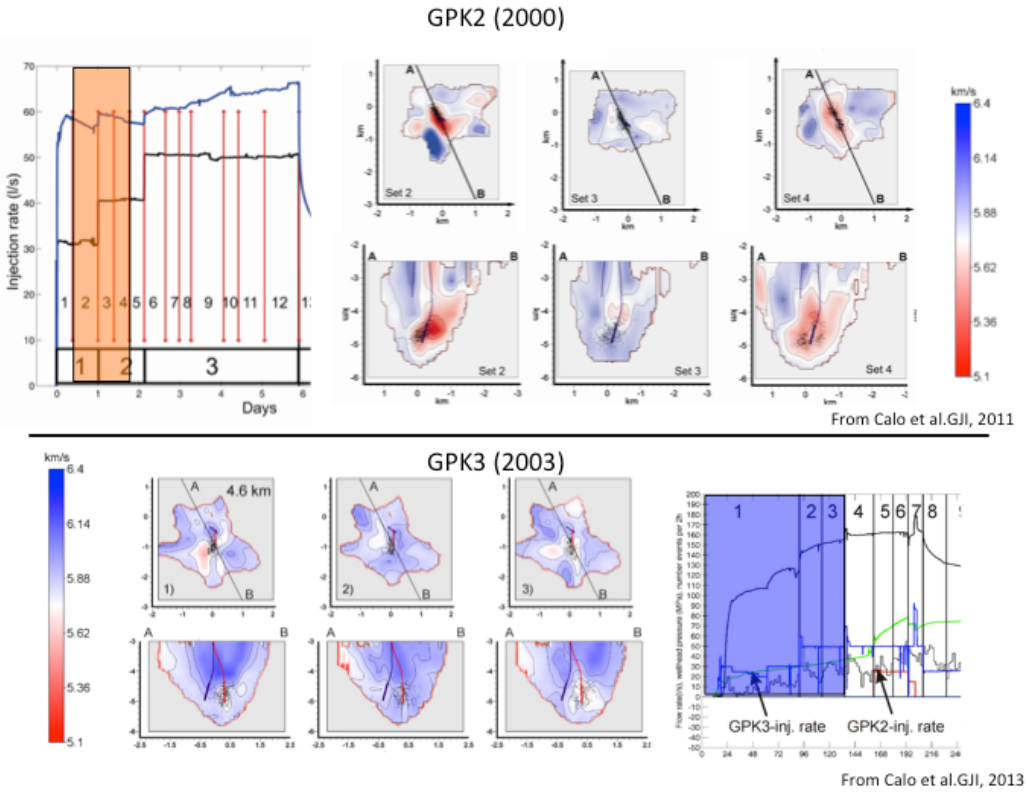

Figure 1. Evolution of the P-wave seismic velocity at 4.6 km depth during the stimulation tests of the well GPK2 in 2000 (top) and of GPK3 in 2003 (bottom).

In regions where pre-existing faults are well documented (e.g. for the GPK3 well) the accumulation of effective stresses close to the well is avoided probably because the structures represent the main paths of the injected water. This results in a lack of large low Vp anomalies during the stimulation (Figure 1) and in the occurrence of the induced seismicity located along the major structures (Figure 2).

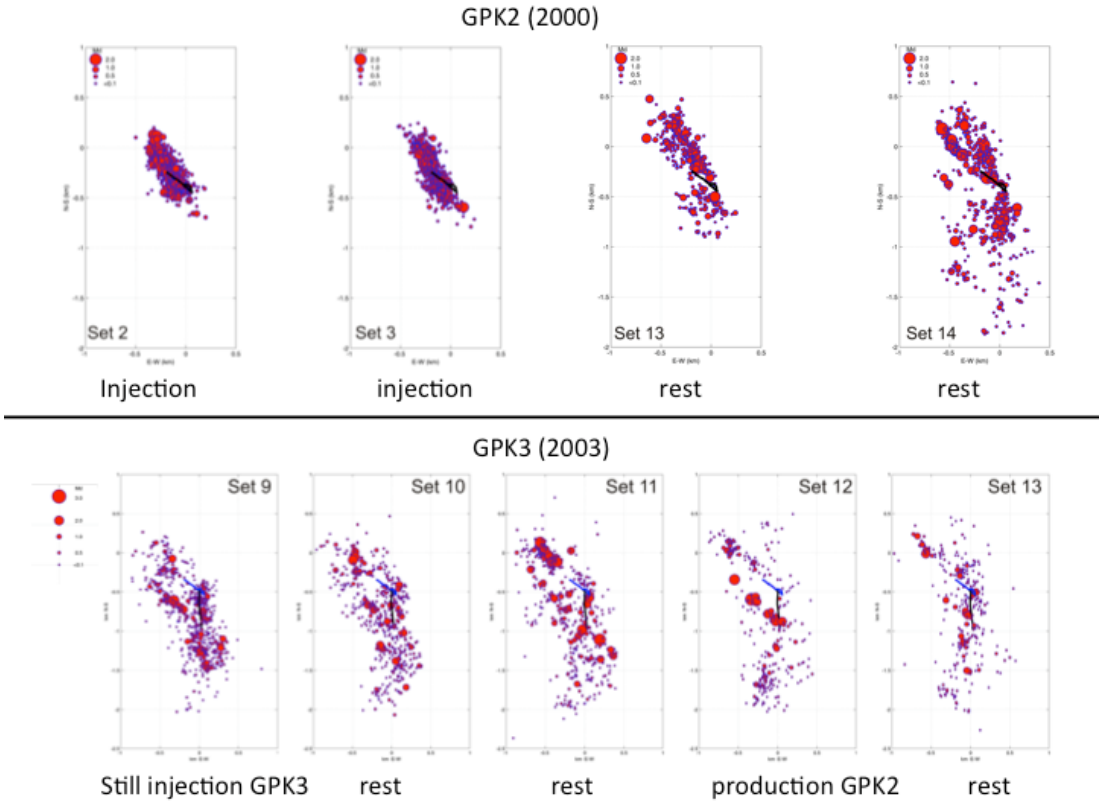

Figure 2. Horizontal projection of the seismic cloud relative to the stimulation tests of the well GPK2 in 2000 (top) and of GPK3 in 2003 (bottom).

When the lack of data occurs, due to poor station coverage or reduced microseismic activity, the double difference method (Waldhauser, 2001) should be used to refine the preliminary locations. This technique was meaningfully applied to data collected at Soultz during minor stimulation tests, acidified injections, and circulation tests (Calò et al., 2013c), highlighting the necessity to improve the event relocation methods for characterizing the seismic response of the reservoirs.

However seismic tomography and event re-locations are subject to some constraints that are common to the use of these methods therefore the recommendation that we suggest for employing these techniques in geothermal areas are:

- to install a dense seismic network (at least 17-20 stations) in a restricted area (less than 6x6 km^2) for local geothermal monitoring especially if seismic tomography is planned. The seismic network should be optimized for the studied reservoir and installed before, during and after the stimulation periods.
- to separate the microseismicity in chronological subsets to study the temporal evolution of the activity. The subset separation should take into account the changes of injected flow rates, periods of stationary injection conditions, and post injection periods, and of the variations of the fluid pressure monitored during the stimulation.
- to evaluate accurately the possibility to apply 3D and 4D tomography with respect to the local conditions by performing preliminary tests to assess the expected resolution and reliability of the models.

- to carry out severe assessment tests and post-processing of the velocity models to reduce the presence of artifacts in the the obtained models.

Exploration and monitoring of geothermal reservoirs using seismic noise correlation

The EOST team tested the ability of the noise cross correlation tomography method to image 3D structures of the Soultz-sous-Forêts EGS at small scale (about 1x1 km^2) and we propose the guidelines to apply it in regions characterized by high geothermal potential, and densely anthropized, as is the case of the upper Rhine valley (Calò et al., 2013b).

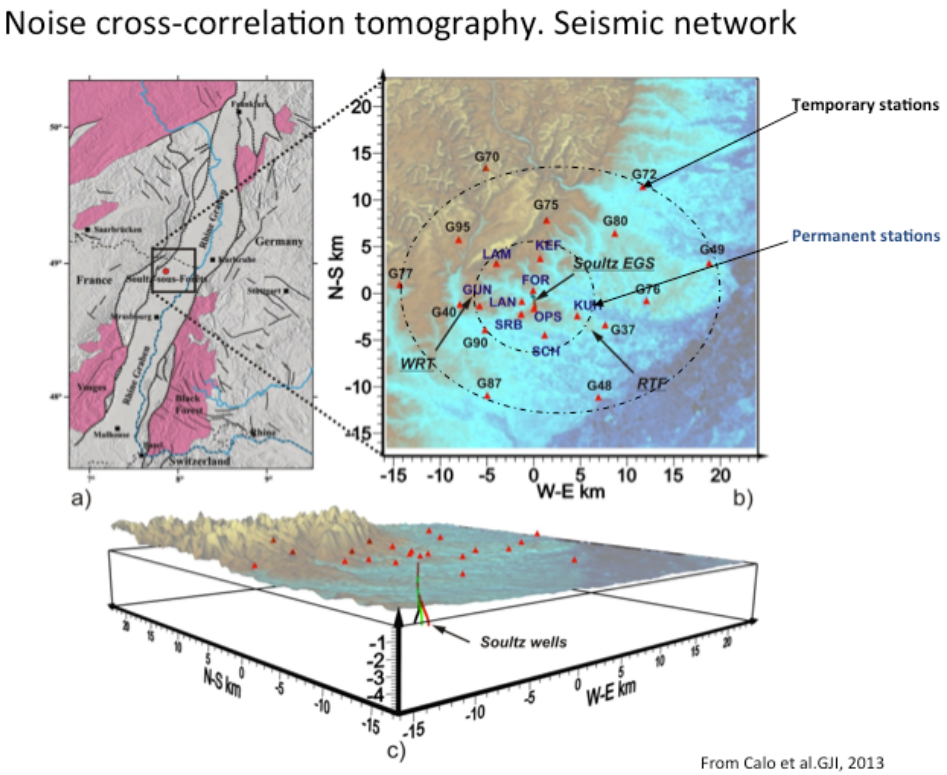

Figure 3. a) Location of the Soultz-sous-Forêtes in the Rhine Graben. Outcropping crystalline rock is in pink (from Dorbath et al., 2009). Black square is the target area; b) permanent (blue) and temporary (black) stations used in this work. In the map are reported also the position of the Woerth (WRT) and Rittershoffen (RTF) towns; c) 3D view of the study area with the position of the seismic stations and of the wells of the Soultz EGS.

In the early phases of a project for the exploitation of a geothermal reservoir, traditional seismic tomography methods can often not be performed because of the lack of an intense natural or induced microseismicity. Similar problems can occurs during the exploitation periods of the geothermal reservoirs, when a constant circulation of fluids at low flow-rate (and reduced pressure) avoids the occurrence of the induced seismicity.

The technique of the noise cross-correlation consists in using the ambient noise recorded at seismic stations and collected during several months. After filtering and normalization, data corresponding to some days are cross-correlated for each station pair, leading to reconstructed Rayleigh waves. Then it is possible to perform a tomographic inversion of the arrival-time

measurements deduced from the group velocity measurements at each period. Therefore the use of seismic noise cross-correlation method should be a useful technique to image the seismic features of the reservoir when the traditional seismic sources (natural/induced seismicity or active sources) do not supply enough information for constructing reliable models.

We tested the noise correlation method to reconstruct the geometrical features of the Soultz-sous-Forêts EGS. We inverted Rayleigh waves reconstructed from cross-correlations of 15 months of ambient seismic noise recorded by 23 seismological stations (nine permanent and thirteen temporary stations installed around the Soultz-sous-Forêts geothermal power plant). All the stations use the same equipment, which allows to make inter-stations measurements without dealing with the problem of instrumental corrections. By correlating noise records between 22 receivers, we reconstructed Rayleigh waves with sufficient signal-to-noise ratio for 231 inter-station paths. The reconstructed waveforms were used to measure group velocity dispersion curves at periods between 1.0 and 5.0 s. The obtained measurements were inverted for two-dimensional group velocity maps and finally for a 3-D S-wave velocity model of the Soultz region from 0 to 5.2 km depth.

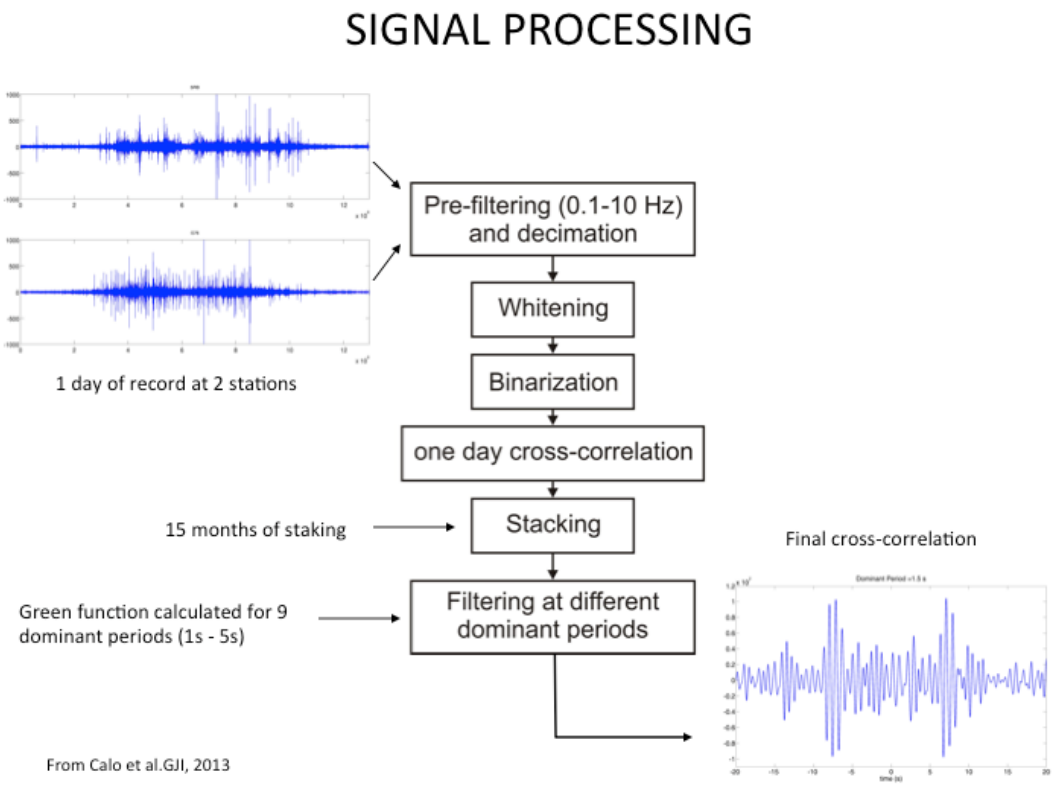

Figure 4. Flow chart showing the procedure applied to the Soultz data for retrieving the Rayleigh waves from cross-correlation of the seismic noise.

Our results clearly show a crystalline basement marked by low velocity bodies below the Soultz power plant at depth of 4-5 km, and other low velocity zones at shallower depth (2.5-3.5 km) beneath the Rittershoffen and Woerth towns. The position of the anomalous body associated with the Soultz geothermal reservoir suggests that the actual boreholes intercept marginally the main anomaly. This inference should be taken into account for future

improvement of the power plant. The site of Rittershoffen is already known in the region and a project for the exploitation of intermediate-deep geothermal energy started in 2012. Conversely the velocity anomalies imaged beneath Woerth were not documented before and should be object of further investigations for geothermal exploitation in this area.

The observations, in agreement with the previous studies, confirm that the procedure applied is suitable for geothermal exploration. Moreover, this procedure can easily be implemented for geothermal explorations in other regions.

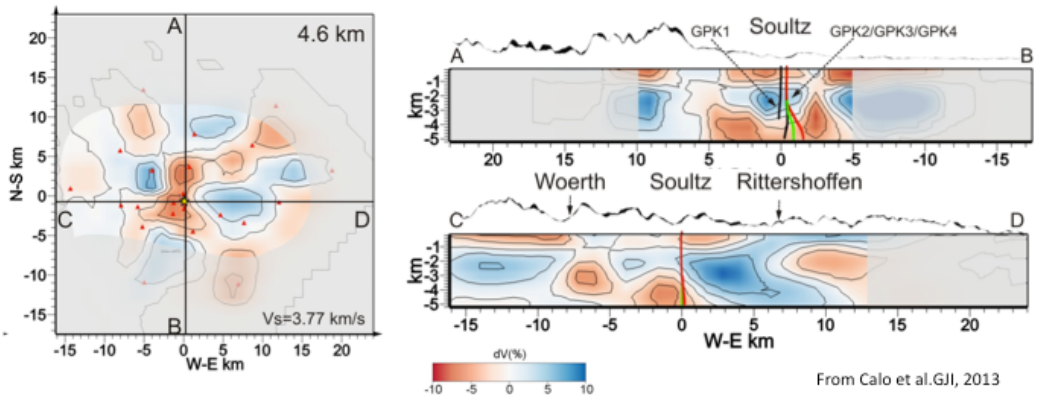

Figure 5. Horizontal slice at 4.6 km of the 3D reconstructed model and vertical sections (AB and CD), in the N-S and E-W directions of the 3D model. The model is represented as variations in percentage with respect to the 1D reference velocity model. Parts of the model not resolved are masked.

The procedure applied at Soultz should be considered as a guideline to follow for a reliable employment of this technique for the 3D imaging of the geothermal reservoirs (Calò et al., 2013b). Furthermore cross-correlation of ambient noise should be also applied to develop geothermal monitoring systems. Duputel et al. (2007) and Brenguier et al. (2011) showed that in the volcano Piton de la Fouranise it was possible to detect very small velocity changes (0.1%) with a time resolution as small as one day using noise cross-correlations analysis. These small variations were interpreted as the result of the change of the rock properties associated with dike intrusions and volcanic eruptions. Strong seismic velocity variations were already observed in the Soultz reservoir during injection tests (Calò et al., 2011; Calò and Dorbath, 2013a). These transient variations are interpreted as a result of sudden changes of the stress field due to large aseismic slips re-accommodating the stress perturbations. Adelinet et al. (2013) show that these variations may be related to changes of the aspect ratio of the fractures in agreement with variations of the S-wave anisotropy observed during the injections. However temporal seismic velocity variations should also occur during circulation tests. Often, induced seismicity is weak in these periods and making difficult a reliable assessment of the variation of the elastic parameters. Furthermore, small variations such as of 0.1% will be difficult to observe with the traditional tomographic methods. Therefore the use of the noise correlation method will result a useful tool for monitoring these possible changes of the elastic properties in order to understand the behaviour of a geothermal reservoir during the exploitation periods.

We recommend the application of this method:

- to reconstruct the shape of the deep and shallow geothermal reservoirs;

- to detect presence of new potential reservoirs;
- for continuous monitoring of the physical changes in the reservoirs.

Seismic tomography using VSP data

When drilling injection wells for EGS exploitation, VSP measurements are commonly performed. In Soultz well GPK1, VSP dataset were recorded in 1988 and 1993. A new VSP campaign was performed in GPK3 and GPK4 in 2008, mainly between 4000 and 5000 m depth. The main goal of this experiment was to get a better knowledge of the main permeable fractures that correspond to the major circulation paths of the geothermal water in the reservoir.

The precise positions of the 26 seismic sources are known by GPS measurements, and precise locations of the recording tool in the wells are known by trajectory. These sources didn't have moved during a full well log phase (2 vibrating trucks operating with two tools, one in GPK3, and one in GPK4). The offset of the sources is between 0 and 5 km from the vertical of the logged interval.

It seems particularly interesting to adapt the local seismic tomography techniques to the VSP scale travel-time data in order to obtain a velocity model in the close vicinity of the documented drillings. In this case, on the contrary to induced seismicity, the location and origin time of the source are known, thus we have four unknown parameters less per event. Furthermore, the possibility to constrain the tomography with others data obtained during the wells drillings allows realizing a robust geophysical model.

The preliminary results are extremely promising. Both independent approaches performed on the VSP data, that is the “classical” reconstruction of structures by reflection and the velocity model obtained from travel-times, are in good agreement. The main well-known reservoir scale fault is identified as a clear limit between higher and lower Vp zones. The main result is the evidence of a new structure clearly underlined by reflections and a well-marked high velocity anomaly. This structure is located between the wells GPK3 and GPK4 and could explain the low connection between these two wells already observed by hydrologists.

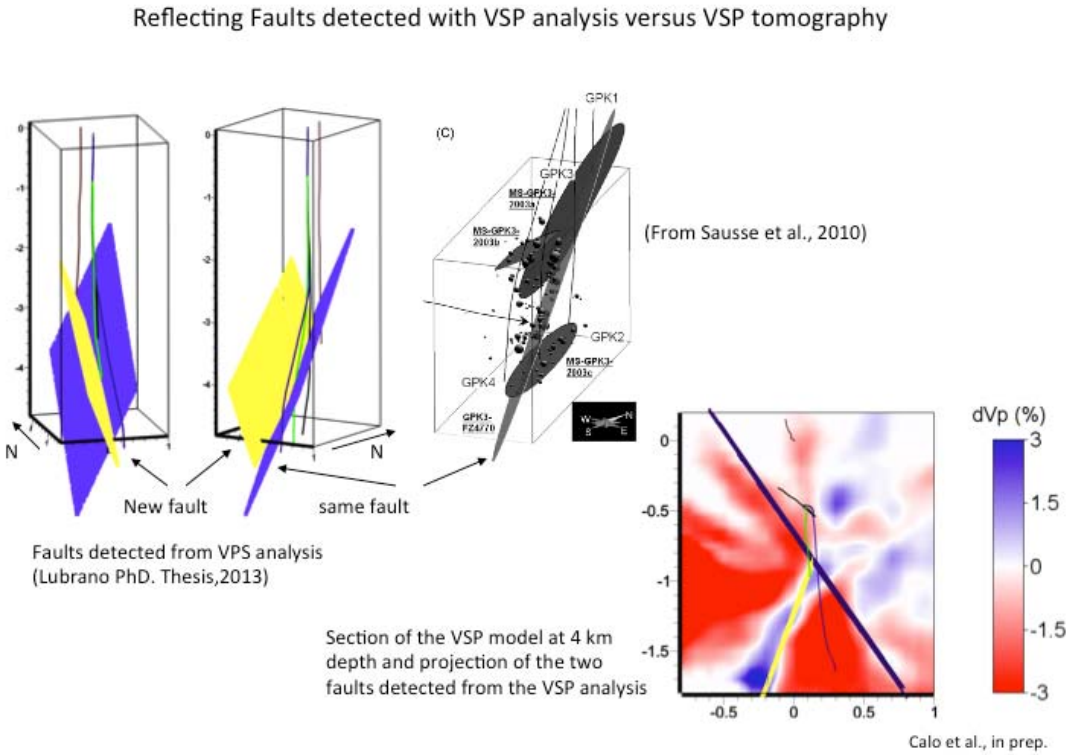

Figure 6. Top: 3D view of the reflecting faults detected from the VSP analysis (blue and yellow, from Lubrano PhD thesis, 2013) and sketch of the known faults reported by Sausse et al., 2010). Bottom: Horizontal slice at 4.0 km of the model of the VSP tomography. The model is represented as variations in percentage with respect to the 1D reference velocity model. Blue and yellow lines are the projections of the faults detected with the VSP analysis.

Final recommendations

Soultz EGS site provided the opportunity to test and assess all the methods described above and which can be directly applicable to the survey of new EGS sites.

The EOST team strongly recommends the use of the geophysical methodologies above described in an easy and well-defined path that can be applied from the exploration to the exploitation steps of a geothermal project.

First, a large-scale seismic noise tomography may be performed in any target area. On the first well drilled, VSP data can be recorded; stimulation may induce microseismic events that can be used to obtain 3D and 4D seismic tomography. Precise relocation of this microseismicity will give information on the circulation paths of water in the medium and on the location of faults. This knowledge will give an important constraint on the location of next drillings. Monitoring of the induced seismicity and of the changes of the seismic velocities through seismic noise analysis should be performed with the same network of stations providing useful information during the exploitation periods. Important additional information, which is requested, should be available, mainly structural pictures from borehole imagery and fractures identification transfer of stress due to hydraulic activities.

7. GFZ

The research group at GFZ German Research Center for Geosciences was focused on analysis of seismic data from Berlín Geothermal Field, El Salvador and The Geysers geothermal field in California, USA. We firstly present a short review of studies performed at these sites, which were related to the high resolution reservoir characterization using induced seismicity data and state of the art waveform processing techniques. In the following the guidelines are provided together with the list of contributions (references).

Review

In our studies we presented the application of three state-of-the-art algorithms, namely the *Double-Difference (hypoDD) re-location technique*, the *Spectral Ratio (SR) technique* and the *Stress Inversion (SI)* method in analyzing IS generated by fluid injection and steam production at The Geysers and Berlín geothermal fields in California and El Salvador, respectively. We show how hypoDD significantly improves the precision of hypocenters allowing imaging the fluid path and propagation in response to multiple injections with unprecedented detail. In addition, the application of the SR technique provides refined source parameters that can later be used to interpret the subtle interactions between pressure perturbations, fluid flow and fracture (re-)activation within the reservoir. Finally, we show how the SI technique can contribute towards monitoring geomechanical processes occurring in the reservoir in response to short-term injection and long-term production activities.

Double-Difference relocation

The double-difference (DD) relative re-location technique (hypoDD) (Waldhauser and Ellsworth, 2000) uses differential travel times of body waves to improve the hypocenter location accuracy (Figure 1). The differential travel times are determined for station-specific P and S wave arrivals of closely-spaced pairs of events. This allows suppressing poorly known velocity models in and around the reservoir, since the differential travel times are not sensitive to the path effects between the sources and receivers. Eliminating path effects allows improving hypocenter precision by a factor of typically more than 10 compared to absolute locations thereby achieving a much finer internal resolution of the seismicity clusters. Additionally, the waveform cross-correlation techniques may be used to revise the relative arrival times and provide even more precise hypocenter (re-)locations.

Spectral ratio method

The spectral ratio method (SR) is again a relative technique that can be used to significantly decrease the uncertainties of seismic source parameters such as the seismic moment as a measure for the energy released during an induced earthquake, corner frequency as a measure for its fault size and static stress drop or apparent stress for assessing the damaging potential of a seismic event. Consequently, the refined source parameters may provide additional information on processes induced by human activity but usually not detected in standard analysis. Recently, it has been suggested that the SR-refined static stress drops of IS may serve as a proxy for modeling the pore pressure perturbations related to fluid injections (Goertz-Allmann et al., 2011; Kwiatek et al., 2013).

The SR method also takes advantage of the similar source-receiver travel paths between the seismic events within the same cluster. Assuming that the seismogram of event *i* recorded at a sensor *k* is a convolution of seismic source $\Omega_i(f)$, path $G_{ik}(f)$, site $S_k(f)$ and sensor $T_k(f)$ effects:

$$u_i(f) = \Omega_i(f)\, G_{ik}(f)\, S_k(f)\, T_k(f)$$

a *spectral ratio* between suitable pairs of seismic events from the same cluster may be formed fulfilling certain criteria (for details, see e.g. Kwiatek et al., 2011). Forming a spectral ratio between two events $u_i(f)/u_j(f)$ results in cancelling of the site ,sensor, and propagation effects ($G_{ik}(f) \approx G_{jk}(f)$) once the distance between pairs of earthquakes is much smaller than the distance to the sensor. Many spectral ratios may be formed between events contained in a spatial seismicity cluster. The bulk inversion for source parameters, typically seismic moment and corner frequency, of all events can be performed using Monte-Carlo techniques resulting in very precise source parameters due to suppressed path and sensor-related effects.

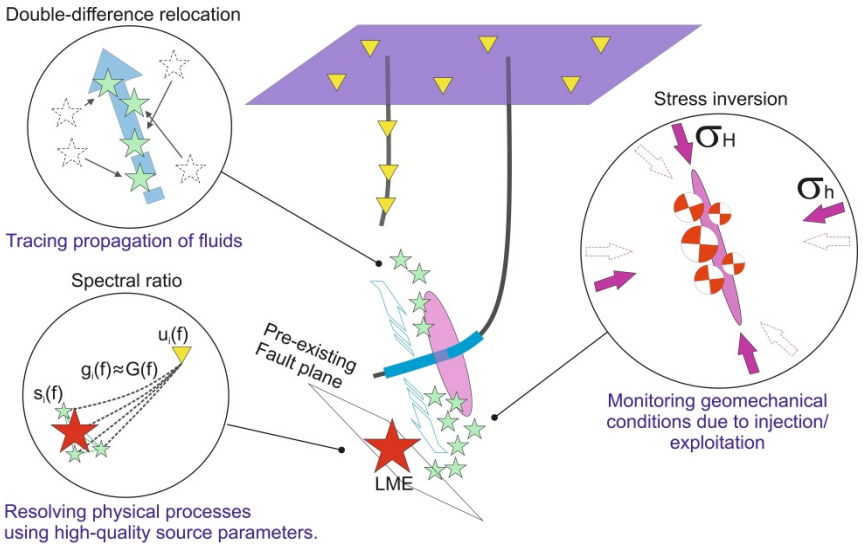

Figure 1. Schematic presentation of the three methods applied in the study.

Stress inversion

The crustal stress field orientation can be determined directly from borehole data (borehole breakouts, drilling induced fractures, in-situ stress measurements), but also indirectly by inverting earthquake focal mechanisms by applying a stress inversion (SI). The latter has proven to be a robust and effective technique to study fault mechanics or spatiotemporal rotations of stress axes in response to large earthquakes along plate boundaries. At the reservoir scale, the direction of the principal stress axes provides important information for planning the stimulation operations. Another important application of SI concerns seismic hazard assessment. For example, knowledge of stress orientations allows estimating the fault re-activation potential from reservoir stimulation. Finally, the changes in the stress tensor orientation may be a proxy to determine geomechanical processes occurring in the reservoir on the short-term (massive fluid injection) or on the long-term (reservoir depletion). Various SI schemes have been developed to determine the orientation of the stress field from focal mechanisms (e.g. Michael, 1987). However, SI has not yet been extensively applied to

seismicity induced in geo-reservoirs. A few existing studies focus on detecting variations of the stress with depth, possibly providing insights in potential stress changes within the reservoir (e.g. Bohnhoff et al., 2004).

Data

We applied the techniques described above in characterizing IS and geomechanical processes at two geothermal reservoirs, the Berlín Geothermal Field (BGF) in El Salvador and The Geysers (TG) in California. While these are selected case studies we believe that these methods can be applied to any data set of IS with a reasonably good quality of the recorded waveforms obtained from a sufficient monitoring network.

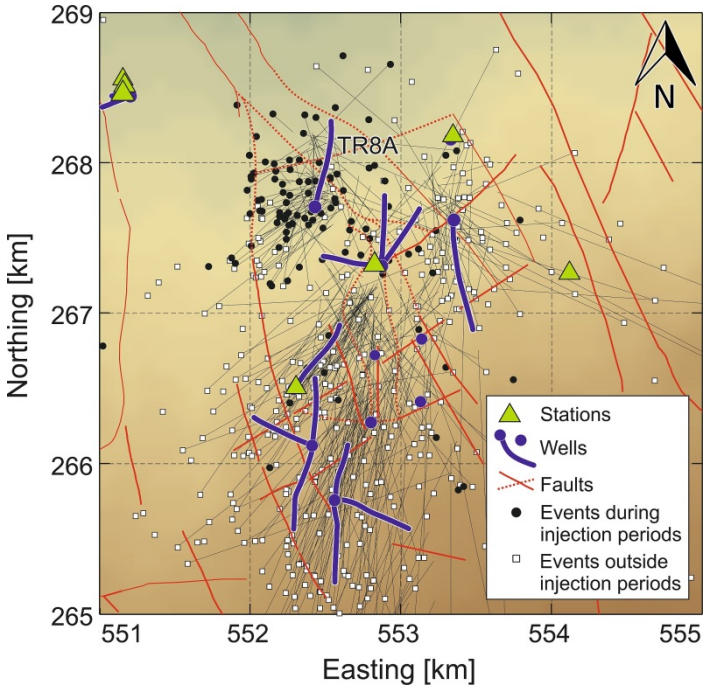

Figure 2. BGF: Spatial distribution of 581 seismic events recorded between Oct-2002 and Jan-2004 (locations provided by BGF operator). Thin gray lines display shifts in earthquake locations towards the center of the BGF due to the application of DD relocation technique (cf. Figure 4).

BGF is located at the northern flank of the Cerro Tecapa volcano. The power plant produced 54 MW (as of 2006) from eight production wells with the fluid being extracted at a temperature of 183°C and disposed via re-injection through a total of ten wells (Bommer et al., 2006). The seismic and production/injection data provided by the BGF operator covers three stimulations (each lasting between 18 and 21 days) performed between Jun-2003 and Jan-2004 in the injection well TR8A located in the northern part of the main production zone (Figure 2) (Kwiatek et al., 2013). The stimulations aimed at increasing the permeability around the well and extending the production zone further to the north. The local seismic network composed of 13 borehole sensors was installed to monitor the evolution of the microseismicity and therefore the potential expansion of the reservoir. The original industrial hypocenter catalogue contained 581 events with magnitudes ranging from -0.5 to 3.7 recorded between Oct-2002 and Feb-2004 (Figure 2). Only 134 events framing the stimulation

campaigns in the well TR8A had been analyzed in terms of the spatial and temporal evolution and source parameters using DD and SR methods.

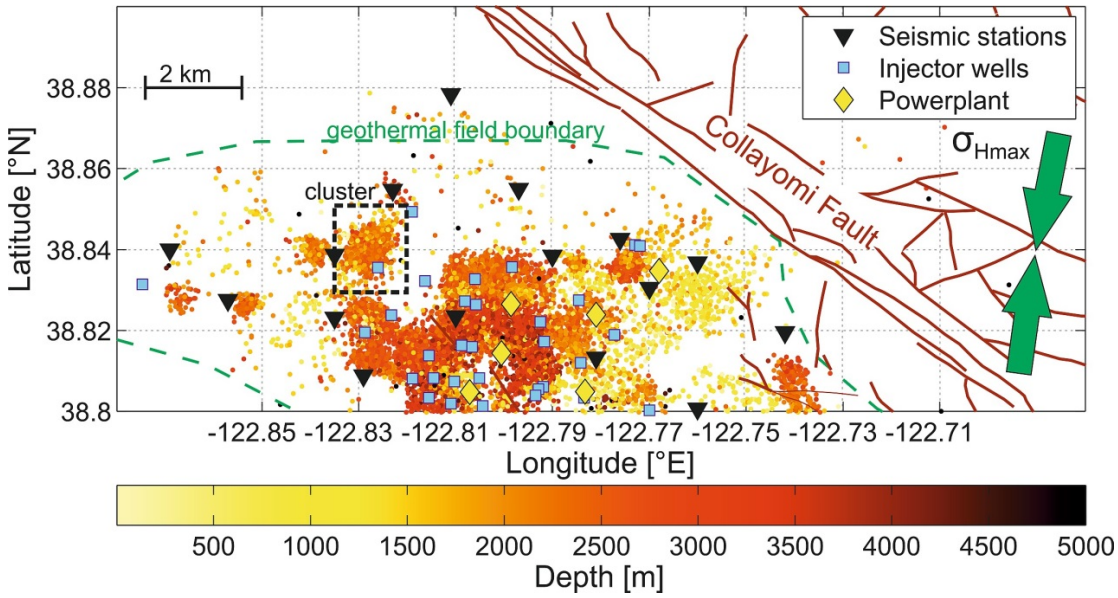

Figure 3. TG: Spatial distribution of the seismicity recorded between Sep-2007 and Jul-2012 in the north-western part of TG. The dashed rectangle shows a cluster containing 742 earthquakes used to perform the SI.

TG is the largest geothermal field in the world in terms of steam production, with 1517 MW active installed capacity and average production of 955 MW. It has also the largest existing dataset of IS consisting of more than 500,000 located microseismic events since the beginning of operation in the 1960s. Since 2007, the installed local seismic network was operated by the Lawrence Berkeley National Laboratory. The network consists of 31 short period 3-component geophones recording more than 3000 events with magnitudes M≥1 annually. The occurrence of seismic events is directly related to the injection of water into the reservoir and vapor production. We selected a subset of seismic data induced by injection campaigns performed between Oct-2007 and Jun-2012 in two wells located in the northern part of the reservoir (Figure 3). A total of 742 earthquake focal mechanisms with magnitudes ranging from 1.0 to 3.1 were analyzed aiming at investigating potential changes in the stress field related to injection using two different SI methods (Martínez-Garzón et al., 2013).

Discussion

The original seismicity catalog from BGF reflects the typical location quality for absolute hypocenter locations at these monitoring conditions (Figure 2). The hypocenter distribution does not allow identifying any specific spatio-temporal pattern related to the multiple injections into the well TR8A. Instead the events form a scattered cloud of seismicity around the injection well. This is well-explained by using a simplified isotropic model and standard quality phase arrival picks. Therefore, to improve the quality of the initial dataset we applied the DD re-location algorithm along with refined P and S wave arrival times derived from waveform cross-correlation and using the 1D-velocity model available for BGF. The average precision of the absolute locations was typically 150 m (previously >300 m). Applying re-location then resulted in lowering the average relative hypocentral location misfit of a total of

393 events down to ~10 m, which is in the range of the source size. Figure 4 displays the substantial improvement in the hypocenter locations now allowing for a detailed analysis of spatio-temporal behavior of the seismicity and its relation to fluid injections into well TR8A. In a second step, events were divided into nine families based on waveform similarity obtained from waveform cross-correlation. The source parameters of events belonging to the same family were then recalculated and refined using the SR technique (see Kwiatek et al., 2011 for details). The results of the refinement are presented in Figure 5. It is clearly seen that the original source parameters are significantly affected by high attenuation observed in the investigated area. No events with higher corner frequencies ($f > 60$ Hz) are observed despite a broad recording bandwidth of the sensors up to 1500 Hz and a high signal-to-noise ratio. Initial stress drop values covered a broad range exceeding 3 orders of magnitude reflecting rather strong uncertainties in estimated source parameters. However, the SR method effectively cancelled path effects resulting in a significant improvement of source parameters estimation.

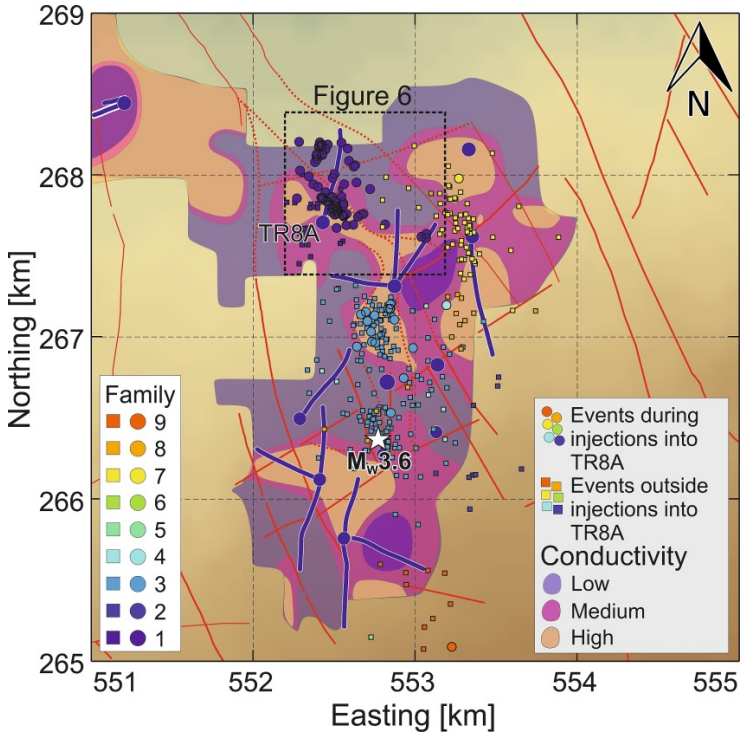

Figure 4. BGF: Spatial distribution of 393 events relocated with DD technique. The accumulation of events in the highly permeable zones and along the faults is clearly visible.

Both DD and SR methods provided significantly refined hypocenter locations and source parameters. This allowed investigating the interactions between fluid injections into TR8A and the observed patterns of induced microseismicity. This in-depth analysis could not have been performed given the initial dataset due to its insufficient quality. To summarize our observations (c.f. Figure 6):

1. We found seismic activity displaying clear spatial and temporal patterns that could be easily related to the injections into the well TR8A. The migration of seismicity away from the injection point is observed for injections 1+2 ([1] in Figure 6) while the injection rate is increasing. Migration of events continues until shut-in of the well. The

clustering of seismicity at the injection well is found at greater depth during injection 3 ([2] in Figure 6).

2. The locations of migrating seismic events are related to the existing fault system F1. The DD-relocated hypocenters systematically align along different faults mapped at the surface or imaged at depth.
3. Events with larger magnitudes typically occur right after the shut-in of the well concentrating in undamaged parts of the fault system, a well-known phenomenon from various previous studies of seismicity induced by massive fluid injection. ([3] in Figure 6).
4. Continuing stimulation episodes require increased injection rate levels (and thus increased reservoir pressure) to induce seismic activity in previously active volumes which is interpreted to reflect a crustal memory ("Kaiser") effect first observed during laboratory studies in the 1960s.
5. We observe that static stress drop values increase with distance from the injection point, possibly related to pore pressure perturbations introduced by stimulation of the respective part of the reservoir.
6. We find that seismic activity concentrates in highly conductive parts of the reservoir. However, a larger magnitude event M_w 3.6 (Bommer et al., 2006) rather occurred in an area of a gradient in conductivity with the aftershock sequence being located in an area of low electrical conductivity (cf. Figure 4).

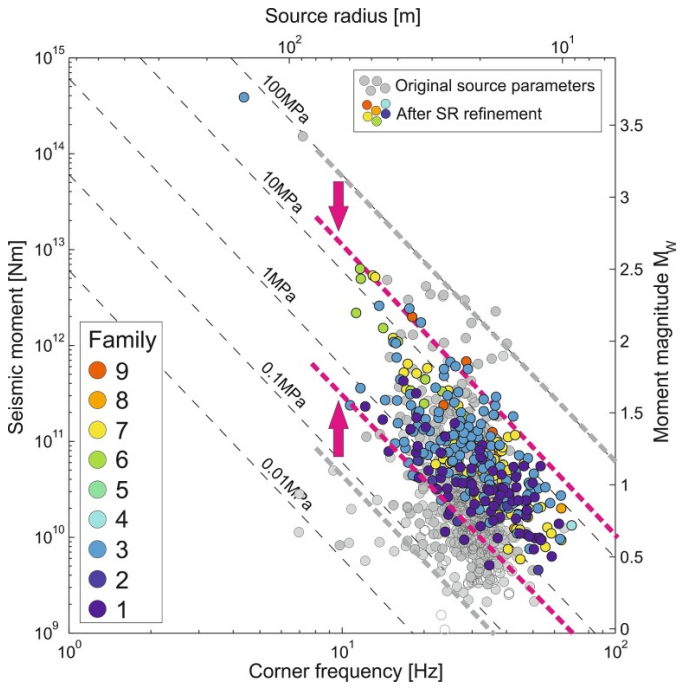

Figure 5. BGF: Comparison of original (grayed circles) and SR-refined source parameters (color-coded circles reflecting the family number). A decrease in the scatter of static stress drops is observed (purple-dashed lines and arrows) and application of SR-technique.

SI was applied to 742 earthquake focal mechanisms from the TG geothermal field (Figure 3) that occurred at depths ranging between 2000-3000 m in response to five years of ongoing injections performed in two wells (Martínez-Garzón et al., 2013). The seismicity data

includes a sufficiently high number of focal mechanisms which allows investigating potential changes of stress field orientation in response to changes in flow rate. The selected time interval covered two injection campaigns performed between Oct-2007 and Jun-2012. Creating moving windows of 55 events, we performed a stress inversion of focal mechanism using a modified version of the SATSI software package (Hardebeck and Michael, 2006). In addition we performed a bootstrap resampling uncertainty assessment.

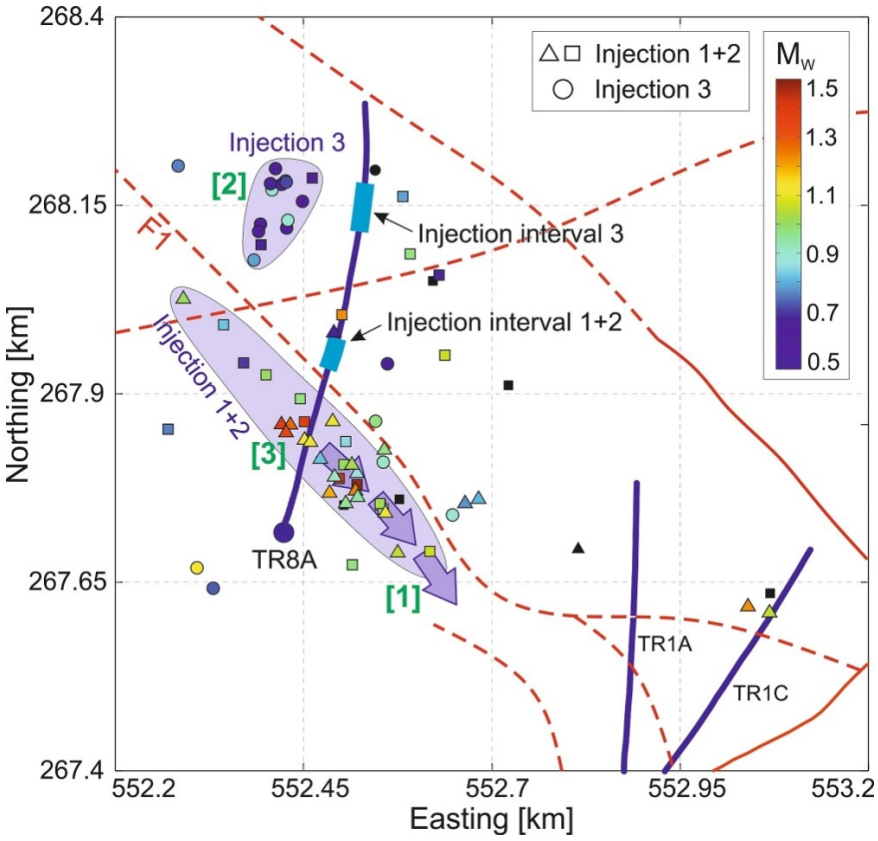

Figure 6. BGF: A detailed map view of the area of TR8A injector well. Spatial and temporal changes of seismicity in response to multiple injections are visible (see text for details).

The results summarized in Figure 7 clearly show a statistically significant systematic rotation of the principal stress axes during periods of massive fluid injection at the 95% confidence level. This suggest that variations in the stress tensor orientation might serve as a proxy for detecting and monitoring changes in the stress state of geo-reservoirs directly related to fluid injection, which is observed directly for the first time. While this process is reversible we also notice the decrease in stress rotation with repeated injections. The rotations of the stress tensor are interpreted in terms of re-activation of pre-existing local faults and fractures well-oriented according to regional stress field orientation. Alternatively, the results might as well suggest that the massive fluid injection aiming at increasing the permeability of the reservoir (Enhanced Geothermal System) allowed for the creation and opening of small fractures oriented in the direction of maximum horizontal stress.

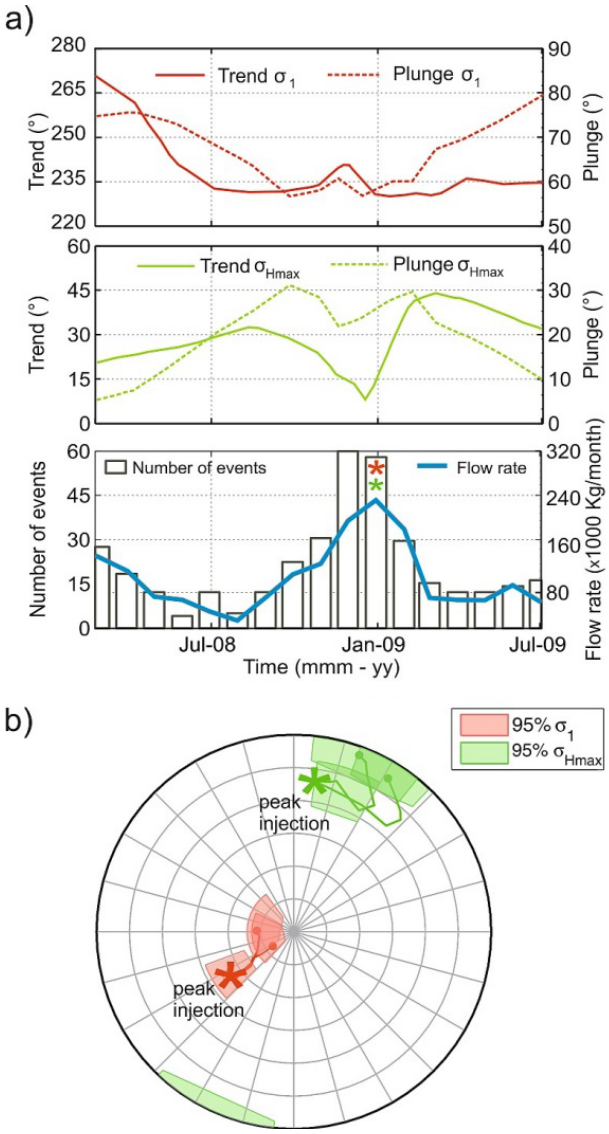

Figure 7. TG: Example of the relation found between peak injection and a temporal variation of the stress field orientation. a): Changes in S1 and SHmax together with flow rate and number of recorded events. b): variation in stress axes orientation over time.

Conclusions

Applying state-of-the-art seismological approaches to geo-reservoir characterization has a huge potential. In this study we presented applications of seismological techniques rarely used in reservoir characterization allowing a better understanding of injection related processes occurring in geo-reservoirs. In particular we find that high-precision relative DD re-locations are of fundamental importance for detecting and investigating fluid paths and progressing pressure perturbations. We show how additional information on physical processes, previously not visible due to high uncertainties, may be obtained from source parameters refined using the SR technique. Finally, it is well known that development of geo-reservoirs is significantly affected by the stress state in the earth crust. We presented the stress inversion technique using focal mechanism of earthquakes and notice that SI may be an efficient tool to determine the crustal stress field changes at depth due to field operations.

High precision hypocenter determination, spectral ratio refinement of source parameters as well as the stress tensor inversion can substantially improve the understanding of physical

processes occurring in any type of geo-reservoir. The proposed methods can be applied if appropriate microseismic monitoring is performed and if the data quality and quantity is sufficient, but they also may be used to re-investigate already collected data previously processed with conventional methods.

Guidelines

We proposethe use of relative relocation (hypoDD) to be performed for the located induced seismic events. HypoDD significantly improves the precision of hypocenters allowing imaging the fluid path and propagation in response to multiple injections with unprecedented detail.

We propose spectral ratio technique as a way to improve the quality of the source parameters of the original seismic catalog recorded at the geothermal sites. The application of the SR technique provides refined source parameters that can later be used to interpret the subtle interactions between pressure perturbations, fluid flow and fracture (re-)activation within the reservoir.

We suggest the stress inversion technique can contribute towards monitoring and comprehensive understanding of the geomechanical processes occurring in the reservoir in response to short-term injection and long-term production activities.

Concerning our experiences and extreme difficulties in analysis of data from industrial catalog from Berling Geothermal field, we suggest the passive seismic monitoring should be performed using sensors adjusted to the expected magnitude and frequency range. This can be easily checked by e.g. by investigating the scaling relations plot (moment magnitude-corner frequency, see e.g. Kwiatek et al., 2011, for details) assuming the relatively low stress drop values (0.1-1 MPa assuming Madariaga source model). Also, the field operator is advised to provide the raw seismic data with no downsampling, with as high sampling frequency and as wide frequency recording band as it is possible. Such data are of very high value for hypocenter relocation using double-difference algorithm as well as for the spectra ratio technique source parameters refinement.

List of Contributions

Here is the list of contributions (papers, conference proceedings, reports) (co-)funded by GEISER between 2012 and July 2013. Bold are papers published in (peer reviewed) journals.

Davi, R., V. Vavryčuk, E.-M. Charalampidou, and G. Kwiatek (2012), Accurate moment tensor inversion of acoustic emissions, in Proceedings of AIM 3rd Advanced Industrial Monitoring Workshop on Induced Seismicity, October 10-13rd, 2012, Smolenice Castle, Czech Republic.

Harrington, R. M., and G. Kwiatek (2012a), Volcanic Seismic Earthquakes at Mount St. Helens Exhibit a Constant Seismically Radiated Energy per Unit Size, Seismol. Res. Lett., 83(2), 400.

Harrington, R. M., and G. Kwiatek (2012b), Volcanic Seismic Earthquakes at Mount St. Helens Exhibit a Constant Seismically Radiated Energy per Unit Size, in Geophys. Res. Abstr., vol. 14, pp. EGU2012–2731, European Geosciences Union.

Kwiatek, G., F. Bulut, M. Bohnhoff, and G. Dresen (2013), High-Resolution Analysis of Microseismicity Related to Hydraulic Stimulation in the Berlín geothermal field, El Salvador, in Proceedings of 4th EAGE Passive Seismic Workshop, Amsterdam, The Netherlands.

Kwiatek, G., M. Bohnhoff, R. Harrington, F. Bulut, T. Goebel, and G. Dresen (2013), The spectral ratio method as a tool to investigate the source scaling relations from km- to cm-scale (M< 4 to -6) earthquakes: Experiences from induced seismicity, volcanic-hybrid earthquakes and laboratory experiments, Seismol. Res. Lett., 84(2), 353.

Kwiatek, G., E.-M. Charalampidou, S. Stanchits, and G. Dresen (2013), An improved method for seismic moment tensor inversion of acoustic emissions: The effect of incidence angle, sensor coupling and damage evolution, Seismol. Res. Lett., 84(2), 353.

Kwiatek, G., G. Dresen, M. Bohnhoff, R. M. Harrington, E.-M. Charalampidou, F. Bulut, and T. Goebel (2013), Is earthquake rupture process self-similar between km- and cm- scale (M< 4 to -6)? Experiences from induced seismicity, volcanic-hybrid seismic events and laboratory experiments, in Proceedings of the 73.Jahrestagung der DeutschenGeophysikalischenGesellschaft, Leipzig, Germany.

Kwiatek, G., E.-M. Charalampidou, and G. Dresen (2013), An improved method for seismic moment tensor inversion of acoustic emissions: The effect of incidence angle, sensor coupling and damage evolution, in Proceedings of the 73. Jahrestagung der DeutschenGeophysikalischenGesellschaft, Leipzig, Germany.

Kwiatek, G., F. Bulut, M. Bohnhoff, and G. Dresen (2012), High-resolution analysis of microseismicity related to hydraulic stimulations in the Berlín geothermal field, El Salvador, in Proceedings of AGIS Workshop on Induced Seismicity, November 26-28th, Karlsruhe, Germany.

Kwiatek, G., F. Bulut, M. Bohnhoff, and G. Dresen (2012a), High-resolution Analysis of Seismicity Induced at Berlín Geothermal Field, El Salvador, in Geophys. Res. Abstr., vol. 14, pp. EGU2012–2235, European Geosciences Union.

Kwiatek, G., F. Bulut, M. Bohnhoff, and G. Dresen (2012b), High-resolution Analysis of Seismicity Induced at Berlín Geothermal Field, El Salvador, in Abstract S43E-2518 presented at 2012 Fall Meeting, AGU, San Francisco, Calif., 3-7 Dec.

Kwiatek, G., F. Bulut, M. Bohnhoff, and G. Dresen (2012c), High-Resolution Analysis of Seismicity Induced at Berlín Geothermal Field, El Salvador, in Proceedings of the 72. Jahrestagung der DeutschenGeophysikalischenGesellschaft, Hamburg, Germany.

Kwiatek, G., and Y. Ben-Zion (2012), Assessment of Radiated P and S Wave Energy from Shear and Tensile Picoseismicity in the Mponeng Deep Gold Mine, South Africa, in Geophys. Res. Abstr., vol. 14, pp. EGU2012–12042, European Geosciences Union.

Martínez-Garzón, P., M. Bohnhoff, and G. Kwiatek (2012), Relation Between Crustal Stress Field Changes and Fluid Injection at The Geysers Geothermal Field, California, in Abstract S43E-2511 presented at 2012 Fall Meeting, AGU, San Francisco, Calif., 3-7 Dec.

Martínez-Garzón, P., M. Bohnhoff, and G. Kwiatek (2013), Stress tensor changes related to fluid injection at The Geysers geothermal field, California, Seismol. Res. Lett., 84(2), 353.

Martínez-Garzón, P., M. Bohnhoff, G. Kwiatek, and G. Dresen (2013), Stress tensor changes related to fluid injection at The Geysers geothermal field, California, in Proceedings of the 73. Jahrestagung der DeutschenGeophysikalischenGesellschaft, Leipzig, Germany.

References

Adelinet M., Dorbath C., Calò M., Dorbath L., & Le Ravalec M., 2013, Crack features and shear-wave splitting associated with dilatancy during hydraulic stimulation of the geothermal reservoir in Soultz-sous-Forêt, *Geophysical Journal International*, In review.

Asanuma H., Kumano Y., Niitsuma H., Schanz U., & Haring M., 2008, Interpretation of reservoir structure from super-resolution mapping of microseismic multiplets from stimulation at Basel, Switzerland in 2006, *Transactions of the Geothermal Resources Council* **32**, 65-70.

Bachmann C.E., Wiemer S., Woessner J., & Hainzl S., 2011, Statistical analysis of the induced Basel 2006 earthquake sequence: introducing a probability-based monitoring approach for Enhanced Geothermal Systems, *Geophysical Journal International* **186**, 793-807.

Bachmann C.E, Wiemer S., Goertz-Allmann B.P., & Woessner J., 2012, Influence of pore-pressure on the event-size distribution of induced earthquakes, *Geophysical Research Letters* **39**, L09302, doi:10.1029/2012GL051480.

Beall J.J., Wright M.C., Pingol A.S., & Atkinson P., 2010, Effect of high rate injection on seismicity in The Geysers, *GRC Transactions, Geothermal Resources Council* **34**, Geothermal Resources Council, Davis, California, pp. 1203-1208.

Bethmann F., Deichmann N., & Mai M., 2011, Scaling relations of local magnitude vs. moment magnitude for sequences of similar earthquakes in Switzerland, *Bulletin of the Seismological Society of America* **101**(2), 515-534, doi:10.1785/0120100179.

Bohnhoff M., Baisch S., & Harjes H.P., 2004, Fault mechanisms of induced seismicity at the superdeep German Continental Deep Drilling Program (KTB) borehole and their relation to fault structure and stress field, *Journal of Geophysical Research* **109**, B02309.

Bommer J.J., Oates S., Cepeda J.M., Lindholm C., Bird J., Torres R., Marroquin G., & Rivas J., 2006, Control of hazard due to seismicity induced by a hot fractured rock geothermal project, *Engineering Geology* **83**(4), 287-306.

Brenguier F., Shapiro N., Campillo M., Ferrazzini V., Duputel Z., Coutant O., & Nercessian A., 2008, Towards forecasting volcanic eruptions using seismic noise, *Nature Geoscience* **1**(2), 126-130.

Brenguier F., Clarke D., Aoki Y., Shapiro N.M., Campillo M., & Ferrazzini V., 2011, Monitoring volcanoes using seismic noise correlations, *Comptes Rendus Geoscience* **343**(8-9), 633-638, doi: 10.1016/j.crte.2010.12.010.

Calò M., Dorbath C., Luzio D., Rotolo S.G., & D'Anna G., 2009, Local Earthquakes Tomography in the southern Tyrrhenian region: geophysical and petrological inferences on subducting lithosphere, In: *Subduction Zone Geodynamics, Frontiers in Earth Sciences*, S. Lallemand and F. Funiciello (eds.), Springer-Verlag Berlin Heidelberg, 85-99, doi: 10.1007/978-3-540-87974-9.

Calò M., Dorbath C., Cornet F.H., & Cuenot N., 2011, Large-scale aseismic motion identified through 4-D *P*-wave tomography, *Geophysical Journal International* **186**, 1295-1314, doi: 10.1111/j.1365-246X.2011.05108.x.

Calò M., & Dorbath C., 2013a, Different behaviours of the seismic velocity field at Soultz-sous-Forêts revealed by 4D seismic tomography: case study of GPK3 and GPK2 injection tests, *Geophysical Journal International*, doi: 10.1093/gji/ggt153.

Calò M., Kinnaert X., & Dorbath C., 2013b, Procedure to construct 3-D models of geothermal areas using seismic noise cross-correlations: application to the Soultz-sous-Forêts enhanced geothermal site, *Geophysical Journal International*, doi: 10.1093/gji/ggt205.

Calò M., Dorbath C., & Frogneux M., 2013c, Injection tests at the EGS reservoir of Soultz-sous-Forêt, Seismic response of the GPK4 stimulations, *Geothermics*, Accepted for Publication.

Calò M., Lubrano P., Dorbath C., & Marthelot J.M., 2013, Seismic velocity structures and faults imaged by Vertical Seismic Profiling data at Soultz-sous-Forêts Enhanced Geothermal Site, In preparation.

Corciulo M., Roux P., Campillo M., & Dubucq D., 2012, Instantaneous phase variation for seismic velocity monitoring from ambient noise at the exploration scale, *Geophysics* **77**, Q37-Q44.

Cros E., Roux P., Vandemeulebrouck J., & Kedar S., 2011, Locating hydrothermal acoustic sources at Old Faithful Geyser using matched field processing, *Geophysical Journal International* **187**(1), 385-393, doi: 10.1111/j.1365-246X.2011.05147.x.

Davidsen J., Kwiatek G., & Dresen G., 2012, No Evidence of Magnitude Clustering in an Aftershock Sequence of Nano- and Picoseismicity, *Physical Review Letters* **108**, 038501, doi: 10.1103/PhysRevLett.108.038501.

Davidsen J., & Kwiatek G, 2013, Earthquake interevent time distribution for induced micro-, nano- and picoseismicity, *Physical Review Letters* **110**, 068501, doi: 10.1103/PhysRevLett.110.068501.

Deichmann N., & Ernst J., 2009, Earthquake focal mechanisms of the induced seismicity in 2006 and 2007 below Basel (Switzerland), *Swiss Journal of Geosciences* **102**(3), 457-466, doi: 10.1007/s00015-009-1336-y.

Deichmann N., & Giardini D., 2009, Earthquakes induced by the stimulation of an Enhanced Geothermal System below Basel (Switzerland), *Seismological Research Letters* **80**(5), 784-798, doi:10.1785/gssrl.80.5.784.

Deichmann N., Kraft T., & Evans K.F., 2013, Identification of faults activated during the stimulation of the Basel geothermal project from cluster analysis and focal mechanisms of the larger magnitude events. Submitted to Geothermics Special Issue on Induced Seismicity.

Dello Iacono D., Zollo A., Vassallo M., Vanorio T., & Judenherc S., 2009, Seismic images and rock properties of the very shallow structure of Campi Flegrei caldera (southern Italy), *Bulletin of Volcanology* **71**, 275-284.

Diehl T., Kissling E., Husen S., & Aldersons F., 2009, Consistent phase picking for regional tomography models: application to the greater Alpine region, *Geophysical Journal International* **176**, 542-554.

Dinske C., & Shapiro S., 2010, Interpretation of microseismicity induced by time-dependent injection pressure, *Society of Exploration Geophysicists Expanded Abstracts*, pp. 2125-2129.

Duputel Z., Ferrazzini V., Brenguier F., Shapiro N.M., Campillo M., & Nercessian A., 2009, Real Time Monitoring of Relative Velocity Changes Using Ambient Seismic Noise on the Piton de la Fournaise Volcano (La Reunion) from January 2006 to June, *Journal of Volcanology and Geothermal Research*, doi: 10.1016/j.jvolgeores.2008.11.024.

Dyer B.C., Schanz U., Ladner F., Häring M.O., & Spillmann T., 2008, Microseismic imaging of a geothermal reservoir stimulation, *The Leading Edge* **27**, 856-869.

Dyer B.C., Schanz U., Spillmann T., Ladner F., & Häring M.O., 2010, Application of microseismic multiplet analysis to the Basel geothermal reservoir stimulation events, *Geophysical Prospecting* **58**, 791-807, doi: 10.1111/j.1365-2478.2010.00902.x.

Gibbons S.J., & Ringdal F., 2006, The detection of low magnitude seismic events using array-based waveform correlation, *Geophysical Journal International* **165**, 149-166.

Goertz-Allmann B.P., Goertz A., & Wiemer S., 2011, Stress drop variations of induced earthquakes at the Basel geothermal site, *Geophysical Research Letters* **38**, L09308, doi: 10.1029/2011GL047498.

Goertz-Allmann B.P., & Wiemer S., 2012, Geomechanical modeling of induced seismicity source parameters and implications for seismic hazard assessment, *Geophysics* **78**(1), 25-39, doi: 10.1190/GEO2012-0102.1

Häring M.O., Schanz U., Ladner F., & Dyer B.C., 2008, Characterization of the Basel 1 Enhanced Geothermal System, *Geothermics* **37**, 469-495, doi: 10.1016/j.geothermics.2008.06.002.

Iannaccone G., Vassallo M., Elia L., Guardato S., Stabile T.A., Satriano C., & Beranzoli L., 2010, Long-term seafloor experiment with the CUMAS module: performance, noise analysis of geophysical signals, and suggestions about the design of a permanent network, *Seismological Research Letters* **81**(6), 916-927, doi: 10.1785/gssrl.81.6.916.

Ito T., Matsui T., & Hong W.Y., 1979, Design method for the stability analysis of the slope with landing pier, *Soils and Foundations* **19**(4), 43-57.

Kahn D.S., 2008, Hydro-fractured reservoirs: A study using double-difference location techniques, Ph.D. Thesis, Dept. of Earth and Ocean Sciences, Duke University, 163 pp.

Kraft T., & Deichmann N., 2013, High-precision relocation and focal mechanism of the injection induced seismicity at the Basel EGS, Submitted to *Geothermics*.

Kwiatek G., Plenkers K., & Dresen G., 2011, Source Parameters of Picoseismicity Recorded at Mponeng Deep Gold Mine, South Africa: Implications for Scaling Relations, *Bulletin of the Seismological Society of America* **101**(6), 2592-2608.

Kwiatek G., Bulut F., Bohnhoff M., & Dresen G., 2013, High-Resolution Analysis of Microseismicity Related to Hydraulic Stimulation in the Berlín geothermal field, El Salvador, In *Proceedings of 4th EAGE Passive Seismic Workshop, Amsterdam, The Netherlands*.

Kwiatek G., Bohnhoff M., Martínez-Garzón P., Bulut F., & Dresen G., 2013,. High-resolution reservoir characterization using induced seismicity and state of the art waveform processing techniques. *First Break* **31**(7), 81-88.

Kwiatek G., & Ben-Zion Y., 2013, Assessment of P and S wave energy radiated from very small shear-tensile seismic events in a deep South African mine. *Journal of Geophysical Research* [in press].

Martínez-Garzón P., Bohnhoff M., Kwiatek G., & Dresen G., 2013, Stress tensor changes related to fluid injection at The Geysers Geothermal Field, California, *Geophysical Research Letters*, in press, doi: 10.1002/grl.50438.

Michael A.J., 1987, Use of focal mechanisms to determine stress: A control study, *Journal of Geophysical Research, Solid Earth* **92**(B1), 357-368.

Mukuhira Y., Asanuma H., Niitsuma H., & Häring M.O., 2013, Characteristics of large-magnitude microseismic events recorded during and after stimulation of a geothermal reservoir at Basel, Switzerland, *Geothermics* **45**, 1-17.

Niu F.L., Silver P.G., Nadeau R.M., & McEvilly T. V., 2003, Stress-induced migration of seismic scatters associated with 1993 Parkfield aseismic transient event, *Nature* **426**, 544-548.

Oye V., & Roth M., 2003, Automated seismic event location for hydrocarbon reservoirs, *Computers & Geosciences* **29**, 851-863.

Rost S., & Thomas C., 2002, Array seismology: methods and applications, *Reviews of Geophysics* **40**(3), doi: 10.1029/2000RG000100.

Rowe C.A., Aster R.C., Borchers B., & Young C.J., 2002, An Automatic, Adaptive Algorithm for Refining Phase Picks in Large Seismic Data Sets, *Bulletin of the Seismological Society of America* **92**, 1660-1674.

Satriano C., Lomax A., & Zollo A., 2008, Real-time evolutionary earthquake location for seismic early warning, *Bulletin of the Seismological Society of America* **98**(3), 1482-1494, doi: 10.1785/0120060159.

Sausse J., Dezayes C., Dorbath L., Genter A., & Place J., 2010, 3D model of fracture zones at Soultz-sous-Forêts based on geological data, image logs, induced microseismicity and vertical seismic profiles, *Comptes Rendus Geosciences* **342**, 531-545.

Sens-Shonefeld C., & Weger U., 2006, Passive image interferometry and seasonal variations of seismic velocities at Merapi volcano, Indonesia, *Geophysical Research Letters* **33**(21), L21302.

Shalev E., Calò M., & Lyakhovsky V., 2013, Formation of Damage zone and seismic velocity variations during hydraulic stimulation: numerical modeling and field observations, *Geophysical Journal International*, In Revision.

Shapiro N., & Campillo M., 2004, Emergence of broadband Rayleigh waves from correlations of the ambient seismic noise, *Geophysical Research Letters* **31**, L07614, doi: 10.1029/2004GL019491.

Toksoz M.N., Johnsont D.H., & Timur A., 1979, Attenuation of seismic wave in dry and saturated rocks-1, Laboratory experiments, *Geophysics* **44**, 681-690.

Valley B., & Evans K.F., 2009, Stress orientation to 5 km depth in the basement below Basel (Switzerland) from borehole failure analysis, *Swiss Journal of Geosciences* **102**/3, doi: 10.1007/s00015-009-1335-z.

Waldhauser F., & Ellsworth W.L., 2000, A Double-Difference Earthquake Location Algorithm: Method and Application to the Northern Hayward Fault, California. *Bulletin of the Seismological Society of America* **90**(6), 1353-1368.

Winkler K.W., & Nur A., 1970, Pore fluids and attenuation in rocks, *Geophysical Research Letters* **6**, 1-4.

Zhang H., & Thurber C.H., 2003, Double-difference tomography: method and application to the Hayward fault, California, *Bulletin of the Seismological Society of America* **93**(5), 1875-1889.

List of Attachments

Attachment 1:

Calò M., Kinnaert X., Dorbath C., 2013a, Procedure to construct three-dimensional models of geothermal areas using seismic noise cross-correlations: application to the Soultz-sous-Forêts enhanced geothermal site, *Geophysical Journal International* Advance Access published June 26, 2013, doi: 10.1093/gji/ggt205

Attachment 2:

Calò M., Dorbath C., 2013b, Different behaviours of the seismic velocity field at Soultz-sous-Forêts revealed by 4-D seismic tomography: case study of GPK3 and GPK2 injection tests, *Geophysical Journal International* Advance Access published May 15, 2013, doi: 10.1093/gji/ggt153

Attachment 3:

Deichmann N., Kraft T., Evans K.F., 2013, Identification of faults activated during the stimulation of the Basel geothermal project from cluster analysis and focal mechanisms of the larger magnitude events. Submitted (December 29, 2012) to the *Geothermics Special Issue on Induced Seismicity*.

Attachment 4:

Martínez-Garzón P., Bohnhoff M., Kwiatek G., Dresen G., 2013. Stress tensor changes related to fluid injection at The Geyssers geothermal field, California, *Geophysical Research Letters*, Vol.40, 2596-26041, doi:10.1002/grl.50438

Attachment 5:

Zang A., Yoon J.S., Stephansson O., Heidbach O., 2013, Fatigue hydraulic fracturing by cyclic reservoir treatment enhances permeability and reduces induced seismicity, *Geophysical Journal International* Advance Access published August 28, 2013, doi: 10.1093/gji/ggt301

Geophysical Journal International

Geophys. J. Int. (2013) doi: 10.1093/gji/ggt205

Geophysical Journal International Advance Access published June 26, 2013

Procedure to construct three-dimensional models of geothermal areas using seismic noise cross-correlations: application to the Soultz-sous-Forêts enhanced geothermal site

Calò Marco,[1] Kinnaert Xavier[1,3] and Dorbath Catherine[1,2]

[1]*EOST Institute, 5 rue René Descartes,* 67084 *Strasbourg cedex, France. E-mail: calo@unistra.fr*

[2]*IRD-UR*234 *(GET), Toulouse, France*

[3]*KIT Institute of Applied Geosciences, Geothermal Research, Adenauerring* 20*b,* 76131 *Karlsruhe, Germany*

Accepted 2013 May 16. Received 2013 May 15; in original form 2013 February 22

SUMMARY

The aim of this work is to assess the feasibility of the noise-cross correlation tomography method for imaging and detecting potential geothermal reservoirs even in highly urbanised areas. We tested the noise correlation method to reconstruct the shape of the Soutlz-sous-Forêts enhanced geothermal system (northern Alsace, France). We inverted Rayleigh waves (RWs) reconstructed from cross-correlations of 15 months of ambient seismic noise recorded by a seismic array installed around the Soutlz geothermal power plant. By correlating noise records between 22 receivers, we reconstructed RWs with sufficient signal-to-noise ratio for 231 interstation paths. The reconstructed waveforms were used to estimate group velocity dispersion curves at periods between 1.0 and 5.0 s. The results were inverted for 2-D group velocity maps, and finally for a 3-D *S*-wave velocity model from 0 to 5.2 km depth. Our results clearly show the presence of low velocity bodies in the crystalline basement below the Soultz power plant at depth of 4–5 km, and at shallower depth (2.5–3.5 km) beneath the Rittershoffen and Woerth villages. These observations, in agreement with some previous studies, confirm that our procedure is suitable for geothermal exploration. Furthermore, the model presented here provides some suggestions to improve the existing geothermal power plant and inferences for further explorations in the area.

Key words: Interferometry; Hydrothermal systems; Seismic tomography; Crustal structure.

INTRODUCTION

The Rhine Valley runs along the rift structure between Basel and Frankfurt with an average width of 35 to 40 km and a length of around 300 km (Fig. 1a) and offers particularly favourable conditions for geothermal energy development. The opening of the rift was achieved through a massive fracturing of the upper crust (Brun *et al.* 1991) characterized by large-scale normal faults striking more or less parallel to the Rhine Graben axis. A sedimentary cover, comprising mainly sandy marls with oil-bearing sand channels, overlies the granitic basement. The several profiles carried out (Elsass *et al.* 1995) have provided a detailed description of the tectonic structures in the sedimentary cover and in the upper part of the basement down to a depth of 2–2.5 km.

Some passive seismic tomographies, using regional and teleseismic data (Lopez-Cardozo & Granet 2005), provided a general view of the deeper structures. Nevertheless, the resolution of these velocity models is estimated to be 10–50 km resulting inadequate for investigating structures suitable for geothermal exploration, which requires to define bodies 1–5 km large. Furthermore, although active seismic imaging can provide the requested resolution, it is often difficult to reach the target depth for exploitation and the costs are often prohibitive for small and medium business companies.

In the last decades, several projects have been approved for the exploration and exploitation of intermediate and deep (2–5 km depth) geothermal resources (e.g. Soultz, Basel, Landau, Insheim). The site of Soutlz-sous-Forêts is the oldest one, and the most important from the scientific point of view. Several studies based on geophysical, geological and geochemical methods allowed describing the main features of this geothermal reservoir (e.g. Sanjuan *et al.* 2006; Dezayes *et al.* 2008; Dorbath *et al.* 2009 and references therein). Right now, the geothermal power plant of Soultz-sous-Forêts consists of three boreholes (GPK2, GPK3, GPK4) reaching a depth of about 5 km and one well (GPK1) drilled down to a depth of 3870 m. All the wells were stimulated throughout hydraulic injections in order to connect efficiently the boreholes to the fracture network and to improve the global permeability of the reservoir. Transient variations of the elastic parameters of the reservoir were observed applying 4-D seismic tomography techniques during some stimulations tests (Charléty *et al.* 2006; Cuenot *et al.* 2008; Calò *et al.* 2011; Calò & Dorbath 2013). However, it was possible to apply the tomographic method only during the injection periods, i.e. when an

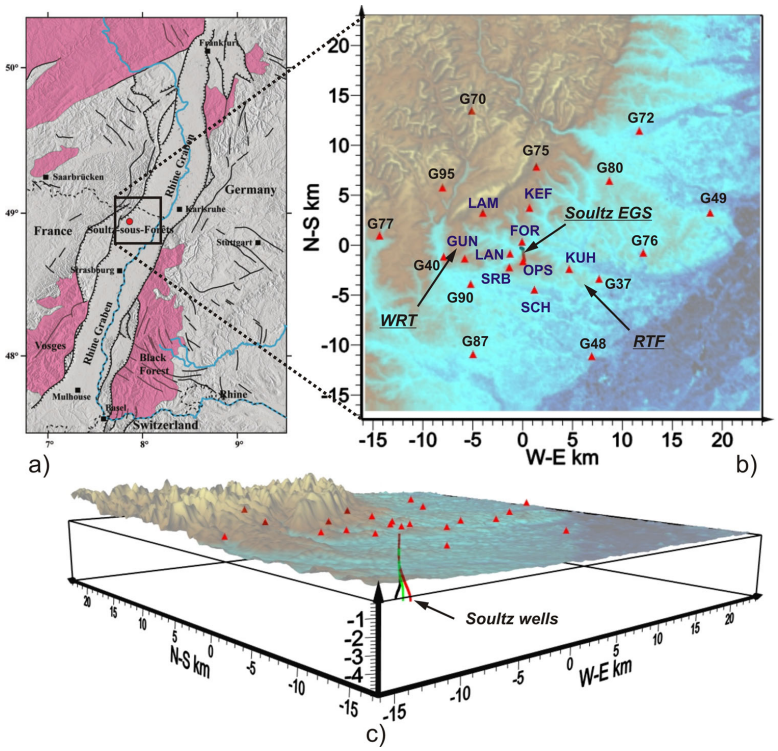

Figure 1. (a) Location of the Soultz-sous-Forêtes in the Rhine Graben. Outcropping crystalline rock is in pink (from Dorbath *et al.* 2009). Black square is the target area; (b) permanent (blue) and temporary (black) stations used in this work. In the map are reported also the position of the Woerth (WRT) and Rittershoffen (RTF) towns; (c) 3-D view of the study area with the position of the seismic stations and of the wells of the Soultz EGS.

intense induced seismicity was recorded. Unfortunately, no information is available during the periods of rest because of the lack of an intense natural seismicity.

Recently, regional-scale noise cross-correlation tomography resulted as a powerful method to image crustal and upper-mantle seismic velocity structure without using 'natural' or 'human' seismic sources (Shapiro & Campillo 2004; Sabra *et al.* 2005; Shapiro *et al.* 2005; Campillo 2006). Since then, considerable researches on ambient noise tomography have been reported (e.g. Villaseñor *et al.* 2007; Yang *et al.* 2007; Bensen *et al.* 2008; Saygin & Kennett 2010; Stankiewicz *et al.* 2010; Li *et al.* 2012). Brenguier *et al.* (2007) showed for the first time the possibility to apply this technique at small scale by imaging the 3-D structures of the volcano Piton de la Fournaise. Recent studies have shown the possibility to retrieve signals from the noise cross-correlation at higher frequency ranges (1–30 Hz) and for different phases (e.g. the *P* waves; Roux *et al.* 2005) extending the reliability of the method also to image shallow structures of a few dozen of meters (Gouédard *et al.* 2012; Mordret *et al.* 2013).

In this work, we test the ability of the noise cross-correlation tomography method to image 3-D structures at small scale (about 1 × 1 km^2), and we propose the guidelines to apply it in regions characterized by high geothermal potential, and densely anthropized, as is the case of the upper Rhine valley.

DATA PROCESSING

The seismic network used in this work is composed of 22 short period seismometers (Mark Products L4C 1 Hz). We used a homogeneous network in order to avoid the instrumental corrections. Nine stations are permanent sensors installed for the monitoring of the Soutlz-sous-Forêts enhanced geothermal system (EGS) site (Fig. 1b, in blue), while 13 sensors were installed in the framework of the European project GEISER from March 2011 to May 2012 (Fig. 1b, in black). Some preliminary studies were performed using only the permanent stations highlighting the necessity to enlarge the interstation distance for retrieving signals able to image the seismic features at depth of the Soutlz Geothermal reservoir. Therefore, the temporary array was installed for 15 months. The seismic noise at the range of the frequencies considered in this work is essentially due to the strong human activity existing in the region then subjected to high variability. We observed also a daily azimuthal variation on the direction of the noise sources. However, the heterogeneity of the sources and their variability makes the sources of noise almost homogeneously distributed when a whole day of noise record is used to calculate the cross-correlation functions. This study uses only the vertical component signals of the stations and the seismic data were continuously recorded and sampled at 150 Hz.

We tested two procedures for the reconstruction of the Green's Functions (GF). The first procedure is similar to that described by Bensen *et al.* (2007) where the data are windowed in 1-d segments, then bandpass filtered between 0.1 and 10 Hz and decimated to 37.5 samples per second. Subsequently, spectral whitening and one-bit normalization is applied to the records. The cross-correlation functions are then computed between signals of all possible pairs of stations. Finally, the traces are staked day per day over 15 months and the GF filtered at different dominant periods. An example of reconstructed Rayleigh wave (RW) at 1.5 s dominant period is shown in Fig. 2a. Since we observed a satisfactory symmetry of the traveltimes picked on the causal and anticasual part of the signals, the final RW reconstruction was obtained averaging the two parts of the cross-correlation functions. An example of the final RW

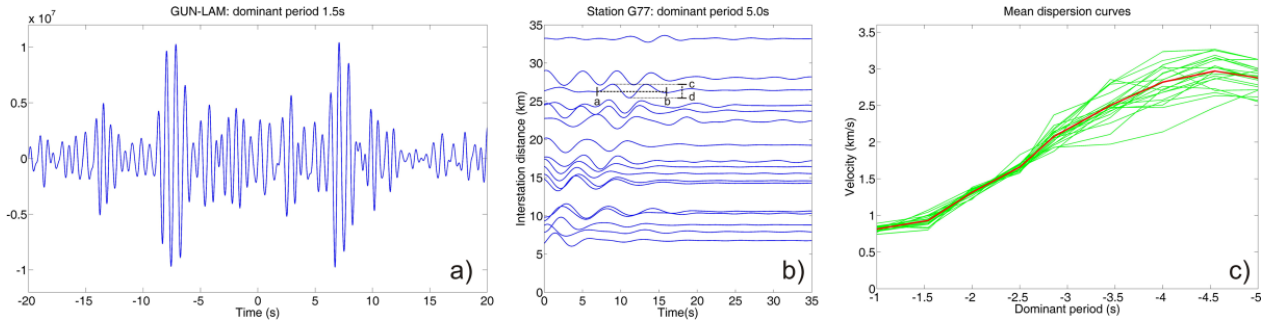

Figure 2. (a) Causal and anticausal reconstructed Rayleigh waves for a dominant period of 1.5 s; (b) folded cross-correlation functions between the station G77 and the rest of the network for the period of 5 s. a-b and c-d are the parameters used to calculate the factor form described in the text; (c) twenty-two average dispersion curves relative to the station used (green curves). The red curve is the average dispersion curve used as initial value for the tomographic inversions.

reconstructed between the station G77 and the rest of the network for the period of 5 s is reported in Fig. 2b. The second approach consisted on a preliminary filtering of the records using a narrow passband window centred on a dominant period followed by the spectral whitening, one-bit normalization and stacking of the cross correlated signals. Since the signals filtered at the same period obtained by the two procedures resulted equivalent, we selected the first one because less time consuming.

Therefore, we estimated a group velocity dispersion curve for each trace using a semi-automatic traveltime picking procedure. The traveltimes were estimated as the maximum of the envelope of the time derivative of the noise cross-correlation (Shapiro & Campillo 2004; Sabra *et al.* 2005). The envelope is computed by using the Hilbert transform.

For each considered period, the semi-automatic procedure is based on a preliminary manual picking of the clearest GF retrieved for some pair of stations in order to estimate an initial group velocity, and in a subsequent automatic research of the maxima for the other traces using the mean group velocity previously calculated. Then we selected only the traveltimes picked on the maxima of the GF that respect a factor form calculated on the clearest GF manually picked. The factor form is calculated for each dominant period considered and is computed using the time length (a-b in Fig. 2b) of the GF and the distance between the maximum and the minimum of the signal (c-d in Fig. 2b). We finally eliminated the traveltimes of stations that have interdistance less than two times the considered dominant period.

By using these traveltimes and the distance between the stations, the group velocity for each station pair is computed for nine dominant periods equal to 1, 1.5, 2, 2.5, 3, 3.5, 4, 4.5 and 5 s. Finally, we averaged the dispersion measurements for each station in order to obtain 22 dispersion curves (green in Fig. 2c) and we calculated an average reference dispersion curve of the region by averaging the 22 dispersion curves previously calculated (red in Fig. 2c). The average 1-D dispersion curve is used as initial velocity model to compute the 2-D dispersion maps.

2-D TOMOGRAPHIC INVERSION

We applied the 2-D tomographic inversion technique of Barmin *et al.* (2001) for estimating the group velocity variations derived from the dispersion measurements. This method treats the surface waves as rays that sample an infinitesimal zone along the great circle linking two stations (source and receiver) and the regularization is based on minimizing a penalty function composed of a linear combination of data misfit and model smoothness. We optimized the damping and smoothing parameters performing a series of tests using different combinations of these parameters considering data misfit, model resolution and model norm and by constructing the empirical trade-off curves (Hansen 1992; Evans & Achauer 1993). Since the amount of ray paths used to calculate the dispersion maps ranges between 198 and 85 for the periods of 1 and 5 s, respectively, the damping of the resolution matrix was optimized for each considered period. The 2-D model consists of $37 \times 27 = 999$ cells of size $1 \times 1\,\mathrm{km}^2$. To be consistent with previous studies, we chose GPK1 wellhead (48.93537 N, 7.86535 E, altitude 153 m) as the geographical origin for the inversion grid.

In Fig. 3 are reported the distributions of RW group velocities as anomalies with respect to the reference velocity values at 1, 3 and 5 s. The dispersion maps at these periods most likely refer to the seismic velocity field in the sedimentary cover (1 s), in the upper part of the geothermal reservoir (3 s) and in the lower one (5 s). The separation in depth of the reservoir is marked by a petrographic facies variation (Genter *et al.* 2000) and by the fact that the lower reservoir is much more fractured due to the deep stimulation tests conducted between 2000 and 2005. However, the tomographic maps clearly show the changing of the velocity pattern with the increasing of the dominant period considered, suggesting the presence of seismic velocity heterogeneities both in the horizontal and vertical directions.

To assess the reliability of the velocity pattern imaged, we built a synthetic model characterized by a low cross-shaped velocity anomaly of –10 per cent with respect to the initial 1-D velocity model (black line in Fig. 3). The cross is centred on the EGS Soultz site. With the same configuration of the stations as in the real inversion, we calculated synthetic traveltimes for the nine periods considered. The inversion of the synthetic data shows that the anomaly is well located and its shape is adequately reconstructed in the well-resolved area (Fig. 3). Considering the parts of the model recovered using the synthetic data, the well-resolved area was estimated of $30 \times 15\,\mathrm{km}^2$ in E–W and N–S directions, respectively. It is worth noting that the decreasing of the restoration with the increasing of the dominant period is related to the decreasing of the number of traveltimes available.

DEPTH INVERSION AND 3-D S-VELOCITY MODEL CONSTRUCTION

To obtain a 3-D model, we computed the tomographic dispersion maps for the nine considered periods using the same cell configuration. For each cell, we constructed a dispersion curve and we fitted these curves by polynomial functions in a least-squares sense. In the

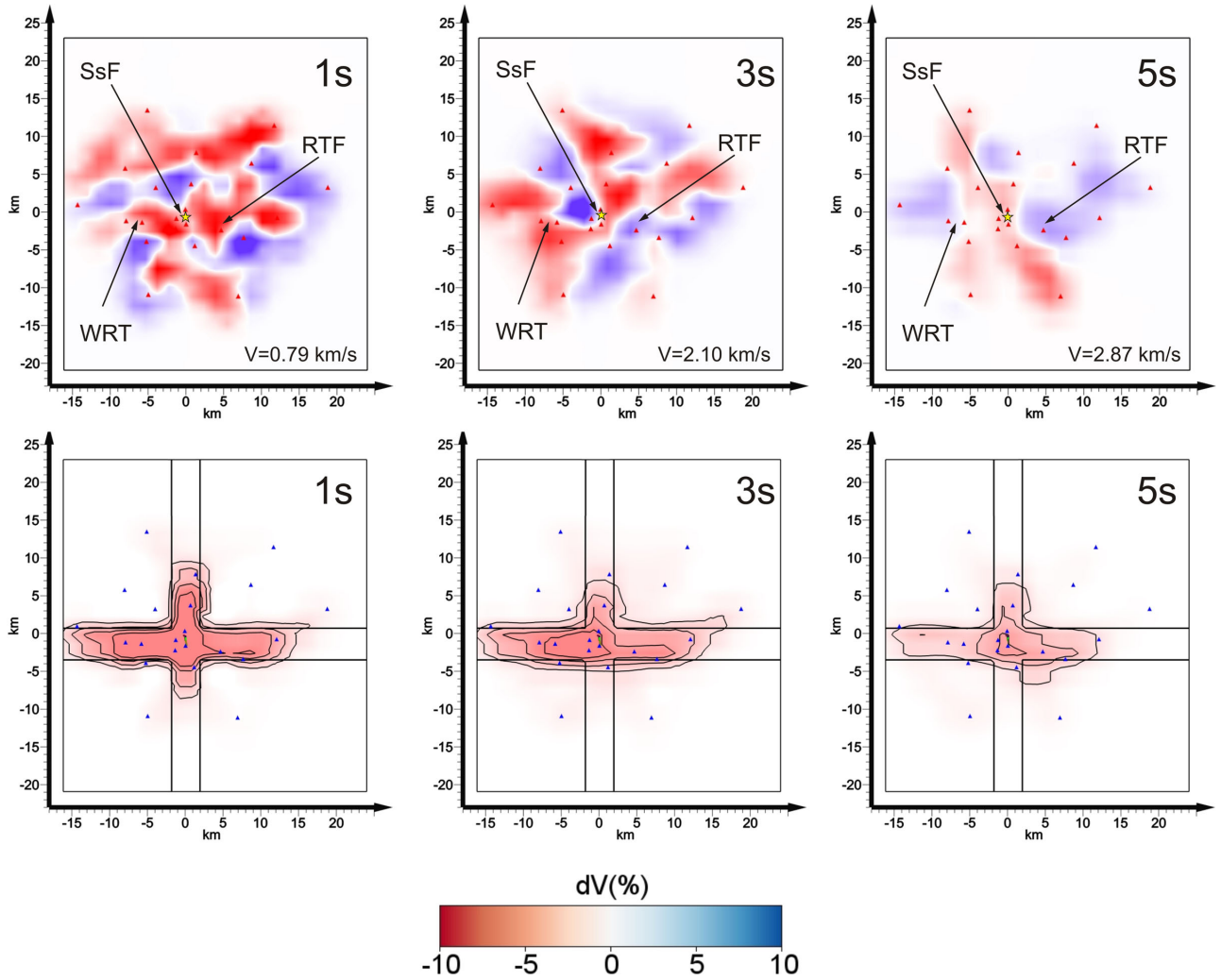

Figure 3. Top panels: Rayleigh group velocity map reported as anomaly with respect to the reference velocity values at 1, 3 and 5 s. Bottom panels: results of the test performed using synthetic traveltimes calculated in a model characterized by a low cross-shaped velocity anomaly of −10 per cent with respect to the reference velocity for the periods of 1, 3 and 5 s. Black lines mark the shape of the cross-shaped true model.

inversion, only shear wave velocities are inverted. *P*-wave velocity and density are maintained fixed at values derived from geophysical logs performed in the Soutlz-sous-Forêts boreholes (Beauce *et al.* 1991; Grecksch *et al.* 2003). The initial 1-D model has 13 layers, which are on average 0.4 km thick and match with the main change of the Vp model in depth. We thus obtained a Vs versus depth velocity profile for each cell by applying the method of Herrmann & Ammon (2002) that use an iterative damped least-square approach. We performed several tests using different configurations of the input parameters (e.g. damping, smoothing and number of iterations) to assess the stability of the results. In Fig. 4 is reported an example of the depth inversion result for one of the dispersion curves. The mean *SD* between the 999 observed and calculated dispersion curves is 0.35 s. Finally, the 1-D profiles are combined into 3-D shear wave velocity model. We spatially smoothed the 3-D velocity distribution in order to avoid sharp horizontal velocity gradients (Brenguier *et al.* 2007).

In Fig. 4, we present two horizontal slices of the model, at 3 and 4.6 km, and two vertical sections (A–B and C–D), in the N–S and E–W directions. The model is represented as variations in percentage with respect to the 1-D reference velocity model. Parts of the model poorly resolved are shadowed. The horizontal slice at 3 km shows the velocity pattern in the upper part of the crystalline basement. At this depth, the EGS site of Soutlz does not seem to be characterized by particular velocity structures. Low seismic velocities are mostly located in the northern part, and in the southern and western part of the geothermal power plant. At greater depth, a 6–8 km low Vs body elongated in the N–S direction involves the deep geothermal reservoir. The deepest wells of the geothermal power plant (GPK2, GPK3, GPK4, Fig. 4 section AB) reach this low seismic anomaly while the shallower one (GPK1) stops at its top. In section C–D (Fig. 4), the low Vs anomaly is 2–4 km wide and mainly located west of the EGS boreholes. This section presents also two low velocity anomalies shallower than the one associated with the Soutlz reservoir. A low Vs region (2.5–4 km deep) is located approximately beneath the village of Woerth and another one, less marked but much larger, located at a depth of 1.5–3.5 km, slightly at NE of the Rittershoffen village. High velocity regions separate the bodies at lower seismic velocity. Finally, both vertical sections report shallow seismic velocity anomalies

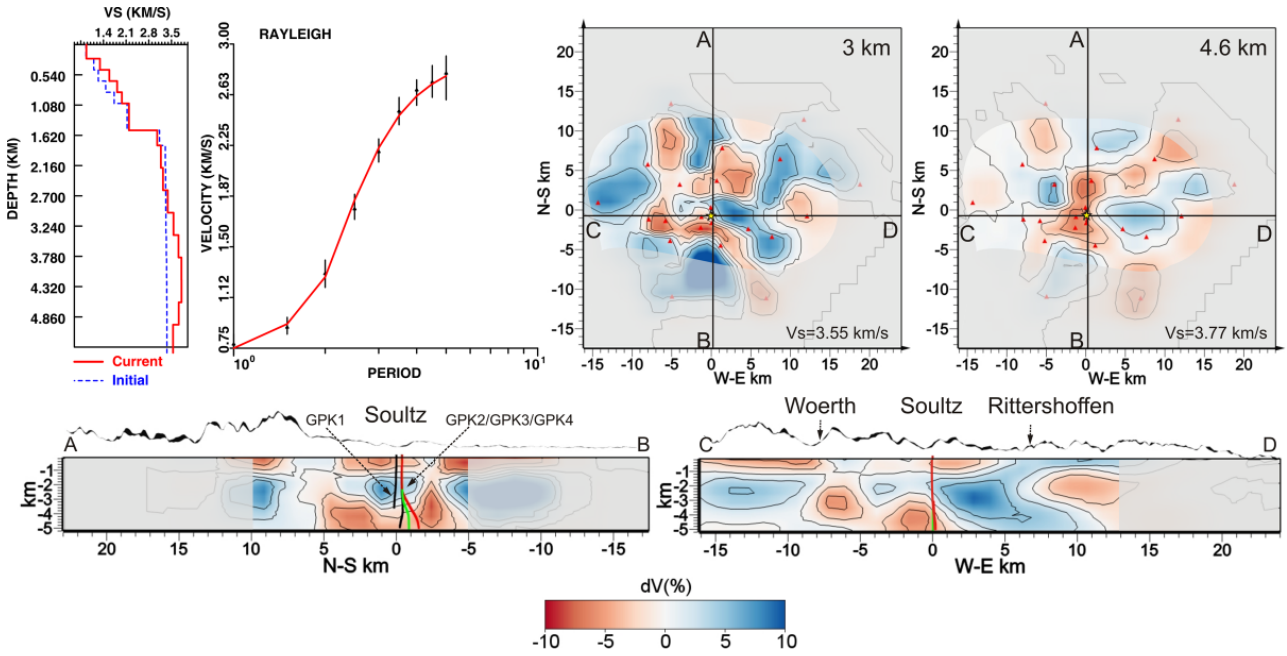

Figure 4. Top panels: example of the depth inversion of one cell dispersion model and horizontal slices at 3 and 4.6 km of the 3-D reconstructed model. Bottom panels; vertical sections (AB and CD), in the N–S and E–W directions of the 3-D model. The model is represented as variations in percentage with respect to the 1-D reference velocity model. Parts of the model not resolved are masked.

(0–1.6 km), which are related to the sedimentary layers of the Rhine Graben.

DISCUSSION AND CONCLUSIONS

This study confirms the suitability of the seismic noise cross-correlation tomography for characterising geothermal reservoirs, also in densely populated regions such as is the case of the Rhine valley, where seismic noise sources are mostly originated by the human activity.

We used 15 months of seismic noise recorded by 22 stations deployed in the Soutlz-sous-Forets region to retrieve RW between each pair of seismic sensors. Nevertheless, we tested that the emergence of the RW from cross-correlation with sufficient signal-to-noise ratio was observed after a stacking of only few days and therefore it is worth considering to perform a similar study using shorter temporal records. We used these waveforms to perform a RW tomography and invert dispersion curves extracted from nine group velocity maps in order to build a 3-D *S*-wave velocity model of the Soutlz region. Synthetic tests allowed assessing the resolution and the reliability of the seismic velocity anomalies observed in the experimental velocity model.

We can relate the low velocity anomalies located in the crystalline basement to the presence of deep and intermediate geothermal reservoirs giving also inferences on their volumetric size.

Our results agree with other studies based on geochemical analyses and ground water circulation that suggest the presence of 'hot-spot' geothermal reservoirs in the crystalline basement of the Rhine Valley (Schellschmidt & Clauser 1996; Pribnow & Schellschmidt 2000; Clauser *et al.* 2002). The position of the anomalous body associated with the Soutlz geothermal reservoir suggests that the actual boreholes intercept the main anomaly at its boundary. Nonetheless, we have to recall that the site of Soultz-sous-Forêts has been object of huge stimulations in the past and we cannot exclude that the low seismic velocity anomaly is the result of these injections. However, Schellschmidt & Clauser (1996), in a study of modelling of the thermal regime in the region, have already shown a similar pattern but at a depth of 800 m. This suggests that the velocity pattern observed in our model at greater depth is probably related to the seismic structure of the reservoir. This inference should be taken into account for future improvement of the power plant. The site of Rittershoffen is already known in the region and a project for the exploitation of intermediate-deep geothermal energy started in 2012. The lower amplitude of the anomaly imaged beneath Rittershoffen with respect to that of Soultz is in agreement with the thermal modelling proposed by Guillou-Frottier *et al.* (2012). Conversely, the velocity anomalies imaged beneath Woerth were not documented before and should be object of further investigations for geothermal exploitation in this area.

The procedure applied here should be considered as a guideline to follow for a reliable employment of this technique for the 3-D imaging of the geothermal reservoirs. Furthermore, cross-correlation of ambient noise should be also applied to develop geothermal monitoring systems. Duputel *et al.* (2009) and Brenguier *et al.* (2011) showed that in the volcano Piton de la Fouranise it was possible to detect very small velocity changes (0.1 per cent) with a time resolution as small as 1 d using noise cross-correlations analysis. These small variations were interpreted as the result of the change of the rock properties associated with dike intrusions and volcanic eruptions. Strong seismic velocity variations were already observed in the Soultz reservoir during injection tests (Calò *et al.* 2011; Calò & Dorbath 2013). These transient variations are interpreted as a result of sudden changes of the stress field due to large aseismic slips reaccommodating the stress perturbations. Adelinet *et al.* (2013) show that these variations may be related to changes of the aspect ratio of the fractures in agreement with variations of the *S*-wave anisotropy observed during the injections. However, temporal seismic velocity

variations should also occur during circulation tests. Often, induced seismicity is weak in these periods and making difficult a reliable assessment of the variation of the elastic parameters. Furthermore, small variations such as of 0.1 per cent will be difficult to observe with the traditional tomographic methods. Therefore, the use of the noise correlation method will result a useful tool for monitoring these possible changes of the elastic properties in order to understand the behaviour of a geothermal reservoir during the exploitation periods.

In conclusion, this preliminary study demonstrates that the noise cross-correlation tomography is a convenient technique for studying geothermal reservoirs. We were able to image the main features of the Soutlz EGS and we gave inferences for improving the exploitation of the geothermal reservoir. Some low seismic anomalies infer on the presence of new geothermal reservoirs although further investigations are necessary for a proper assessment on the exploitation possibilities.

Finally, the procedure that we have applied in this work can easily be implemented in other regions for geothermal explorations.

ACKNOWLEDGEMENTS

This work was funded by the European project GEISER (FP7: 241321). We sincerely thank M. Campillo for the fruitful and constructive discussions. We thank Helene Jund and Hervé Wolding for the technical support and also we thank all the people who allowed the installation of the temporary network on their gardens. We thank the GEIE for the density borehole data.

REFERENCES

Adelinet, M., Dorbath, C., Calò, M., Dorbath, L. & Le Ravalec, M., 2013. Crack features and shear-wave splitting associated with dilatancy during hydraulic stimulation of the geothermal reservoir in Soultz-sous-Forêt, *Geophys. J. Int.,* in revision.

Barmin, M., Ritzwoller, M. & Levshin, A., 2001. A fast and reliable method for surface wave tomography, *Pure appl. Geophys.,* **158**(8), 1351–1375.

Beauce, A., Fabriol, H., Le Masne, D., Cavoit, C., Mechler, C. & Chen, X., 1991. Seismic studies on the HDR site of Soultz-sous-Forets (Alsace, France), *Geotherm. Sci. Technol.,* **4,** 239–266.

Bensen, G.D., Ritzwoller, M.H., Barmin, M.P., Levshin, A.L., Lin, F., Moschetti, M.P., Shapiro, N.M. & Yang, Y., 2007. Processing seismic ambient noise data to obtain reliable broad-band surface wave dispersion measurements, *Geophys. J. Int.,* **169,** 1239–1260.

Bensen, G.D., Ritzwoller, M.H. & Shapiro, N.M., 2008. Broadband ambient noise surface wave tomography across the United States, *J. geophys. Res.,* **113,** doi:10.1029/2007JB005248.

Brenguier, F., Shapiro, N.M., Campillo, M., Nercessian, A. & Ferrazzini, V., 2007. 3-D surface wave tomography of the Piton de la Fournaise volcano using seismic noise correlations, *Geophys. Res. Lett.,* **34,** L02305, doi:10.1029/2006GL028586.

Brenguier, F., Clarke, D., Aoki, Y., Shapiro, NM, Campillo, M. & Ferrazzini, V., 2011. Monitoring volcanoes using seismic noise correlations, *Comptes Rendus Géosc.,* **343**(8–9), 633–638.

Brun, J.P. & Wenzel, F., the ECORS-DEKORP Team, 1991. Crustal scale structure of the southern Rhine Graben from ECORS-DEKORP seismic reflection data, *Geology,* **19,** 758–762.

Calò, M., Dorbath, C., Cornet, F.H. & Cuenot, N., 2011. Large-scale aseismic motion identified through 4-D *P*-wave tomography, *Geophys. J. Int.,* **186,** 1295–1314.

Calò, M. & Dorbath, C., 2013. Different behaviours of the seismic velocity field at Soultz-sous-Forêts revealed by 4D seismic tomography: case study of GPK3 and GPK2 injection tests, *Geophys. J. Int.,* doi:10.1093/gji/ggt153.

Campillo, M., 2006. Phase and correlation in 'random' seismic fields and the reconstruction of the Green function, *Pure appl. Geophys.,* **163,** 475–502.

Charléty, J., Cuenot, N., Dorbath, C. & Dorbath, L., 2006. Tomographic study of the seismic velocity at the Soultz-sous-Forêts EGS/HDR site, *Geothermics,* **35,** 532–543.

Clauser, C., Griesshaber, E. & Neugebauer, H.J., 2002. Decoupled thermal and mantle helium anomalies: implications for the transport regime in continental rift zones, *J. Geophys. Res.,* **107**(B11), doi:10.1029/2001JB000675.

Cuenot, N., Dorbath, C. & Dorbath, L., 2008. Analysis of the microseismicity induced by fluid injection in the Hot Dry Rock site of Soultz-sous-Forêts (Alsace, France): implications for the characterization of the geothermal reservoir properties, *Pure appl. Geophys.,* **165,** 797–828.

Dezayes, C., Genter, A., Thinon, I., Courrioux, G. & Tourlière, B., 2008. Geothermal potential assessment of Clastic triassic reservoirs (upper Rhine Graben, France), in *Proceeding of the Thirty-Second Workshop on Geothermal Reservoir Engineering Stanford University,* Stanford, California, January 28–30, 2008.

Dorbath, L., Cuenot, N., Genter, A. & Frogneux, M., 2009. Seismic response of the fractured and faulted granite of Soultz-sous-Forêts (France) to 5 km deep massive water injections, *Geophys. J. Int.,* **177,** 653–675.

Duputel, Z., Ferrazzini, V., Brenguier, F., Shapiro, N.M., Campillo, M. & Nercessian, A., 2009. Real time monitoring of relative velocity changes using ambient seismic noise on the Piton de la Fournaise volcano (La Reunion) from January 2006 to June 2007, *J. Volc. Geotherm. Res.,* **184,** 164–173.

Elsass, P., Aquilina, L., Beauce, A., Benderitter, Y., Fabriol, H., Genter, A. & Pauwels, H., 1995. Deep structures of the Soultz-sous-Forêts HDR site (Alsace, France), in *Proceedings of the World Geothermal Congress,* Florence, Italy, pp. 2543–2647.

Evans, J. & Achauer, U., 1993. Teleseismic velocity tomography using the ACH method: theory and application to continental-scale studiesin, *Seismic Tomography: Theory and Practice,* pp. 319–360, Chapman & Hall, London.

Genter, A., Traineau, H., Ledésert, B., Bourgine, B. & Gentier, S., 2000. Over 10 years of geological investigations within the HDR Soultz project, France, in *Proceedings of the World Geothermal Congress 2000 Kyushu - Tohoku,* Japan, pp. 3707–3712.

Gouédard, P., Yao, H., Ernst, F. & van der Hilst, R.D., 2012. Surface wave eikonal tomography in heterogeneous media using exploration data, *Geophys. J. Int.,* **191,** 781–788.

Grecksch, G., Ortiz, A. & Schellschmidt, R., 2003. HDR project Soultz – thermophysical study of GPK2 and GPK3 granite samples. GGA Internal report, ENK5-CT-2000–00301.

Guillou-Frottier, L., Carre, C., Bourgine, B., Bouchot, V. & Genter, A., 2012. Hydrothermal convection beneath an inclined basement-sediment interface: application to the Rhine Graben and its Soultz-sous-Forets temperature anomaly, in *Proceedings of the AGU Fall Meeting,* San Francisco, V13C-2856. 3–7 December.

Hansen, P.C., 1992. Analysis of discrete ill-posed problems by means of the L-curve, *SIAM Rev.,* **34,** 561–580.

Herrmann, R.B. & Ammon, C.J., 2002. Computer Programs in Seismology: Surface Waves, Receiver Functions and Crustal Structure, St. Louis Univ., St. Louis, MO.

Li, H., Li, S., Song, X.D., Gong, M., Li, X. & Jia, J., 2012. Crustal and uppermost mantle velocity structure beneath northwestern China from seismic ambient noise tomography, *Geophys. J. Int.,* **188,** 131–143.

Lopez-Cardozo, G. & Granet, M., 2005. A multi-scale approach to study the lithospheric structure of the southern Upper Rhine Graben; from seismic tomography through reflection seismics to surface geology, *Int. J. Earth Sci.,* **94,** 615–620.

Mordret, A., Landès, M., Shapiro, N.M., Singh, S.C., Roux, P. & Barkved, O.I., 2013. Near-surface study at the Valhall oil field from ambient noise surface wave tomography, *Geophys. J. Int.,* **193,** 1627–1643.

Pribnow, D. & Schellschmidt, R., 2000. Thermal tracking of upper crustal fluid flow in the Rhine Graben, *Geophys. Res. Lett.,* **27**(13), 1957–1960.

Roux, P., Sabra, K.G., Gerstoft, P., Kuperman, W.A. & Fehler, M.C., 2005. P-waves from cross-correlation of seismic noise, *Geophys. Res. Lett.,* **32,** L19303, doi:10.1029/2005GL023803.

Sabra, K.G., Gerstoft, P., Roux, P., Kuperman, W.A. & Fehler, M.C., 2005. Surface wave tomography from microseism in southern California, *Geophys. Res. Lett.,* **32,** L14311, doi:10.1029/2005GL023155.

Saygin, E. & Kennett, B.L.N., 2010. Ambient seismic noise tomography of Australian continent, *Tectonophysics,* **481,** 116–125.

Sanjuan, B. *et al.*, 2006. Tracer testing of the geothermal heat exchanger at Soultz-sous-Forêts (France) between 2000 and 2005, *Geothermics,* **35**(5–6), 622–653.

Schellschmidt, R. & Clauser, C., 1996. The thermal regime of the Upper Rhine Graben and the anomaly of Soultz, *Z. Angew. Geol.,* **42**(1), 40–44.

Shapiro, N.M., Campillo, M., Stehly, L. & Ritzwoller, M., 2005. High resolution surface-wave tomography from ambient seismic noise, *Science,* **307,** 1615–1618.

Shapiro, N.M. & Campillo, M., 2004. Emergence of broadband Rayleigh waves from correlations of the ambient seismic noise, *Geophys. Res. Lett.,* **31,** L07614, doi:10.1029/2004GL019491.

Stankiewicz, J., Ryberg, T., Haberland, C., Fauzi & Natawidjaja, D., 2010. Lake Toba volcano magma chamber imaged by ambient seismic noise tomography, *Geophys. Res. Lett.,* **37,** L17306, doi:10.1029/2010GL044211.

Villaseñor, A., Yang, Y., Ritzwoller, M.H. & Gallart, J., 2007. Ambient noise surface wave tomography of the Iberian Peninsula: implications for shallow seismic structure, *Geophys. Res. Lett.,* **34,** L11304, doi:10.1029/2007GL030164.

Yang, Y., Ritzwoller, M.H., Levshin, A.L. & Shapiro, N.M., 2007. Ambient noise Rayleigh wave tomography across Europe, *Geophys. J. Int.,* **168,** 259–274.

SUPPORTING INFORMATION

Additional Supporting Information may be found in the online version of this article:

Figure S1. Upper part of the figure reports the diagonal elements of the covariance matrix calculated for the dispersion maps at 1, 3 and 5 s. Figures display that the central parts of the investigated area are enough resolved even for the period at 5 s. Lower part of the figure reports the empirical curves constructed for the empirical optimization of the damping for the dispersion maps at 1, 3, and 5 s. Each inversion was obtained with a different damping value. Arrows indicate the values of data variance and model length of the inversion selected (http://gji.oxfordjournals.org/lookup/suppl/doi:10.1093/gji/ggt205/-/DC1).

Please note: Oxford University Press are not responsible for the content or functionality of any supporting materials supplied by the authors. Any queries (other than missing material) should be directed to the corresponding author for the article.

Geophysical Journal International

Geophys. J. Int. (2013) doi: 10.1093/gji/ggt153

Geophysical Journal International Advance Access published May 15, 2013

Different behaviours of the seismic velocity field at Soultz-sous-Forêts revealed by 4-D seismic tomography: case study of GPK3 and GPK2 injection tests

Calò Marco[1] and Dorbath Catherine[1,2]

[1] *Ecole et Observatoire des Sciences de la Terre, EOST, University of Strasbourg, Strasbourg Cedex, France. E-mail: calo@unistra.fr*
[2] *GET (IRD-UMR234)*

Accepted 2013 April 12. Received 2013 April 11; in original form 2012 October 19

SUMMARY

The geothermal power plant of Soultz-sous-Forêts in Northeastern France consists of three boreholes (GPK2, GPK3, GPK4) reaching a depth of about 5 km. All the wells were stimulated through hydraulic injections. In this study, we present the results of a time-dependent (4-D) seismic tomography obtained with the *P*-wave arrival times of seismic events recorded in 2003 during the stimulation of the GPK3 well. The method combines double-difference tomography with the Weighted Average Model post-processing that corrects for parameter dependence effects. In light of additional processing of the continuous seismic records of 23 surface stations, some 4728 precisely located events were selected and separated into 13 subsets to examine periods defined with respect to the injection scheme. Particular attention is given to changes in injected flow rates, periods of stationary injection conditions, periods of dual stimulation with the GPK2 well and post-injection periods. Results confirm that significant structures crossing the well have controlled the evolution of the seismicity and have played a fundamental role in the distribution and amplitude of the seismic anomalies. Furthermore, the evolution of the seismic velocity field, together with the representation of the relocated seismicity, have been compared with the results of the 4-D tomography of the GPK2 well, which is located at only 600 m from the stimulated well.

Key words: Tomography; Seismic tomography; Rheology and friction of fault zones.

1 INTRODUCTION

At the EGS geothermal field of Soultz-sous-Forêts shown in Fig. 1(a) three wells (GPK2, GPK3, GPK4) reach a depth of about 5000 m. All the wells are not cased in the last 500 m. To connect the boreholes to the fracture network efficiently and to improve the overall permeability of the reservoir, GPK2 was stimulated in June/July 2000, GPK3 in May/June 2003 and GPK4 in September 2004 and again in February 2005. The reservoir development has now been completed and heat is exploited for conducting electricity.

During the different stimulations, several thousands events were detected and located (Cuenot *et al.* 2005, 2006, 2008; Charléty *et al.* 2006). Dorbath *et al.* (2009) observed different seismic responses during the stimulation tests of the three wells, particularly between GPK2 and GPK3, although the horizontal distance between the open sections is ∼600 m (Fig. 1b). During the seismic sequence of GPK2, 718 earthquakes had a magnitude equal or greater than 1.0 and the largest a magnitude of 2.5. The b-value result of the Gutenberg–Richter law was higher than 1.2 (Cuenot *et al.* 2008; Dorbath *et al.* 2009), and the injectivity has been increased by a factor of 20 (Nami *et al.* 2007). These characteristics indicate that the stimulation reactivated a 3-D dense network of fractures. The stimulation of GPK3 only induced approximately 250 events with a magnitude greater than 1.0 but with a greater number of large events (between 2 and 2.9). The hypocentres form clear structures identified as large faults, the b-value is about 0.9 and the large events ($M > 2.0$) account for the greater part of the cumulative seismic moment (Charléty *et al.* 2006; Charléty *et al.* 2007; Dorbath *et al.* 2009). The injectivity of the well, which was already high before the stimulation, remained almost unchanged (Nami *et al.* 2007).

No borehole log data (Ultrasonic-Borehole-Image, Gamma ray, etc) are available for GPK2 below 3500 m depth, but the data collected in GPK3 give insights into the presence of large fractures crossing the well. In the open-hole section of GPK3, at about 4775 m, several fractures forming a fracture cluster striking 160°E on average and dipping between 40° and 70° are observed (Dezayes *et al.* 2004). During the drilling operation, most of the fluid was lost at this depth. Moreover, this zone corresponds to a loss of water of about 70 per cent during the 2003 stimulation and 60 per cent during a flow-log test 3 yr later with a 30 l s^{-1} flow rate (Nami *et al.* 2008). A similar total loss was also observed close to the bottom of the same well, during the drilling operations, corresponding to a fracture zone identified at 4957 m. Another fracture zone with significant loss of water during flow-log measurements (greater than

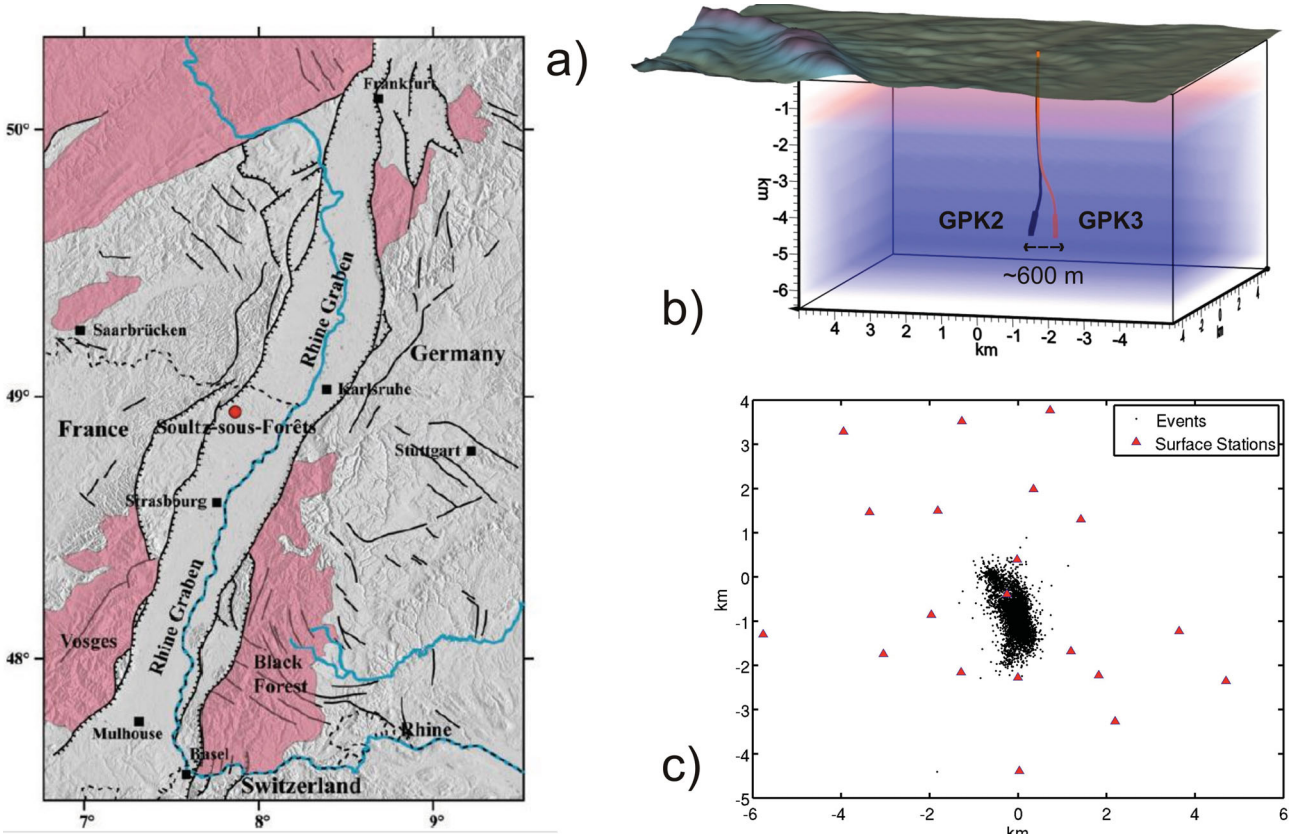

Figure 1. (a) Location of the Soultz-sous-Forêts EGS site in the Rhine Graben. Outcropping crystalline rocks are shown in pink; (b) Three-dimensional view of the GPK2 and GPK3 wells. The thick part of the boreholes corresponds to the open-hole sections of the wells; (c) Surface seismological stations (red triangles) installed during the 2003 stimulation test. Black dots are the epicentres of the events used for this study.

10 per cent) was found at 4905 m. The different seismic response of the reservoir to the GPK3 injection test compared with the GPK2 test was therefore interpreted as a consequence of such structures (Dorbath *et al.* 2009).

In this study, we present new results of a time-dependent (4-D) seismic tomography obtained by inverting *P*- and *S*-wave arrival times for seismic events recorded during the 2003 GPK3 stimulation. During this stimulation more than 7000 microearthquakes were recorded by the surface network (Charléty *et al.* 2006). Among them we have selected 4728 events detected by the seismic network which have magnitudes ranging from −0.9 to 2.9. As with Charléty *et al.* (2006), we performed the 4-D seismic tomography after dividing the main set into chronological subsets to describe temporal changes in the seismic velocity structure during the stimulation. This study differs from theirs in three main points: (i) the continuous seismic records were carefully reprocessed allowing a large increase of events selected for the tomography, (ii) the subsetting of the data has been performed by taking into account variations of injection parameters (i.e. injection flow rate, well-head pressure and down-hole pressure) and: (iii) the approach combines a double difference tomography method (tomoDD, Zhang & Thurber 2003) with an averaging process [Weighted Average Model (WAM), Calò *et al.* 2009, 2011] that adjusts for parameter dependence effects. A comparison of these results with those of the 4-D tomography obtained for the GPK2 injection test (Calò *et al.* 2011) offers insights into the different response of the reservoir for the two wells.

Finally, we discuss how the precise relocation of seismic events together with the temporal variations of the 3-D *P* velocity models facilitates the detection and description of some previously known features of the stimulated reservoir and to individuate large new structures.

2 GPK3 STIMULATION

2.1 Injection parameters

To improve the connectivity and the permeability of the reservoir, GPK3 was stimulated through a high-pressure water injection that lasted more than ten days. During this stimulation test, over 33 000 m^3 of fluids were injected in GPK3 and 4300 m^3 in GPK2. In contrast to the GPK2 stimulation, the GPK3 injection strategy was very complex (Fig. 2). We have divided the stimulation test into seven main phases according to the main variations of the injection parameters (Fig. 2). Phase 1 includes the first 60 hr of the stimulation where the injection flow rate was approximately constant at ∼30 l s^{-1}. Phase 2 consists of the early period of the stimulation when the injected flow rate of GPK3 was increased to 50 l s^{-1} for 72 hr. During this phase two 'shots' at 60 and 93 l s^{-1} were tested for a period of a few hours. Phase 3 includes a dual stimulation and the injected flow rate was at 50 l s^{-1} in GPK3 and 25 l s^{-1} in GPK2, respectively. The injection in GPK2 lasted 32 hr while a pick at 86 l s^{-1} was tested in GPK3 for a few hours. In Phase 4, the injection in GPK2 was stopped while the flow rate at GPK3 was decreased to about 25 l s^{-1}. Phase 5 is a period of rest with no injections. Phase 6 includes a production period in GPK2 of 120 hr where water was pumped at about 15 l s^{-1}. Phase 7 corresponds to the end of the stimulation test where all the wells were again at rest.

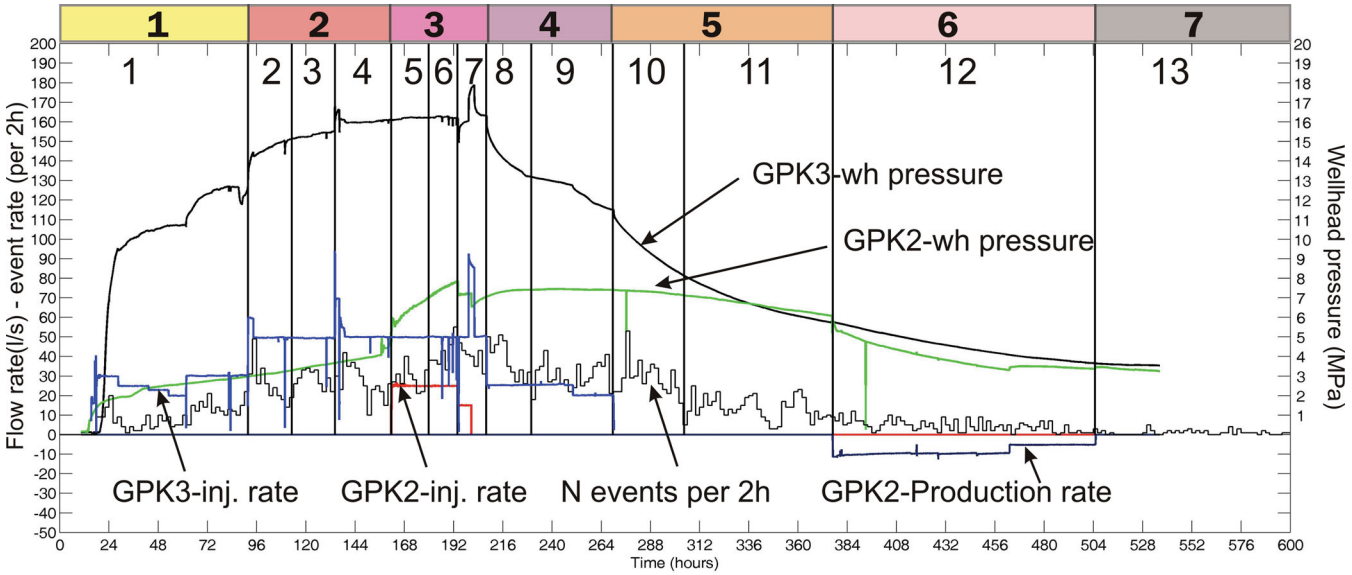

Figure 2. Injection rate (blue line for GPK3 and red line for GPK2) and overpressure (black line for GPK3 and green line for GPK2) measured at the well head. The event occurrence is also reported in the graph. The seven main phases are shown in the coloured rectangles and the subdivisions into 13 sets for the 4-D tomography are in black.

2.2 Data and method

As observed in the GPK2 injection test, intense microseismic activity was recorded during and after the GPK3 injection test. The seismic network installed by EOST, (University of Strasbourg) consisted of nine permanent surface stations supplemented by 14 temporary stations (Fig. 1c). They included 14 1C and nine 3C short period (1 Hz) seismological stations (Charléty *et al.* 2006). The area covered by the network is centred on the EGS and is $\sim 11 \times 9$ km^2.

The initial 1-D horizontally layered velocity model used for locating events was the same used to locate the events recorded during the GPK2 stimulation and derived from sonic logs and calibration shots performed in the GPK1 well (Beauce *et al.* 1991). To be consistent with previous studies, we chose GPK1 well-head (48.93537 N, 7.86535 E, altitude 153 m) as the geographical origin for this work.

Automatic processing of the data, based on an autoregressive algorithm (Leonard & Kennett 1999), detected and picked the arrival times (*P*- and *S*-phases) of about 7000 events. The method was set up and optimized for the Soultz region by Charléty (2007). However after some further improvements and optimizations of the code routine, we reanalyzed the whole sequence of the continuous seismic records to augment the present data set. About 7500 triggers were detected and among them we selected 4728 events located using at least eight *P*- and three *S*-arrival times and located with a root mean square (rms) lower than 0.04 s. The events were located using on average 15 *P* and 5 *S* phases. After the location procedure the mean rms resulted in 0.021 s.

The reliability of the automatic procedure for detecting and picking the seismic phases was tested by comparing the picking of the *P*- and *S*-arrival times of the 250 largest events with the phases hand-picked for the same events (Dorbath *et al.* 2009). The difference between the automatic and manually picked phases (1000 *P* and 300 *S*) was on average 0.01 s and resulted in an absolute random displacement of the hypocentre positions of 30 m and 50 m in the horizontal and vertical directions, respectively. Because these differences are lower than the hypocentre error estimations we can conclude that the automatic procedure does not significantly affect the reliability of the Soultz site data, at least for the larger events. Finally, we purposely included all the events collected by Charléty *et al.* (2006) in our data set and the resultant hypocentre locations are very close. However, the new data set incorporates 2476 events that were excluded from the database of Charléty *et al.* (2006). The main reason for this discrepancy is that we included events that occurred in a longer time period. The database collected by Charléty *et al.* (2006) contains events recorded until the end of the stimulation test (2003 June 17) while we included the events that occurred up to 2003 July 12. Furthermore, during the overlapping period, several additional events were included in our data set because they were located with lower rms or detected by a larger number of stations. Finally the optimization of the automatic routine allowed for the detection of some new events not picked in the previous data set. Therefore this data set represents a more complete catalogue.

Hence we decided to apply the tomographic method to 13 unevenly populated sets to observe the seismic velocity variations during the time. The sets were set up according to the seven main phases described above (Table 1; Fig. 2). To study the reservoir response in detail, we considered the main variations of the flow rate (Sets 1, 2, 5, 7, 8, 10, 12 and 13) and we added steps when the injection parameters were maintained constant for long time periods (Sets 3, 4, 6, 9 and 11). Each set was used to calculate *P*- and *S*-wave velocity models using the same procedure as described by Calò *et al.* (2011) to study seismic velocity variations during the GPK2 injection test. The approach combines a double-difference tomography method (Zhang & Thurber 2003) with an averaging process (WAM: Calò 2009; Calò *et al.* 2011) that corrects for parameter dependence effects. Reliability tests on the tomograms calculated with the data of the GPK3 stimulation (described in Appendix A) show that the data and method are able to uncover weak differences >1.5 per cent in *P*-velocity structures with respect to the initial model. Although the *S*-velocity models were also calculated, the lack of experimental data does not allow a reliable assessment of these results. Consequently, in this work we will discuss only the *P*-wave velocity models.

Table 1. Time period, number of events, absolute data (*P* and *S*) and differential data (*P* and *S*) for the 13 sets.

Subset	Time period	N. events	Abs. *P* phases	Abs. *S* phases	Diff. *P* data	Diff. *S* data
1	06/30 hr 19:15 07/01 hr 03:40	351	3131	1162	32 839	9167
2	07/01 hr 03:41 07/01 hr 18:39	273	6443	1874	65 316	15 351
3	07/01 hr 18:39 07/02 hr 03:50	300	5807	2105	59 163	17 907
4	07/02 hr 03:50 07/02 hr 12:57	376	6807	1782	43 582	14 809
5	07/02 hr 12:58 07/02 hr 21:39	262	2246	674	23 429	6324
6	07/02 hr 21:46 07/03 hr 10:04	291	4382	900	44 049	6402
7	07/03 hr 10:04 07/03 hr 18:06	283	5836	2040	59 341	17 470
8	07/03 hr 18:07 07/04 hr 10:25	423	5745	2068	58 460	17 391
9	07/04 hr 10:32 07/04 hr 20:11	611	7192	2545	71 515	22 830
10	07/04 hr 20:12 07/05 hr 04:45	496	4493	1344	47 121	12 977
11	07/05 hr 04:47 07/05 hr 20:06	483	6701	2469	63 488	20 140
12	07/05 hr 20:07 07/06 hr 16:10	286	8659	3440	81 361	20 140
13	07/06 hr 16:10 07/07 hr 04:18	293	3213	1328	28 826	11 296

2.3 Temporal evolution of the *P*-wave velocity field during GPK3 stimulation

Thirteen WAMs have been computed from the thirteen sets reported in Table 1 to observe the temporal evolution of V_P field in the geothermal reservoir. The V_P value of the initial 1-D model is 5.85 km s^{-1} at 4.6 km depth. Thereafter, we discuss the seismic velocity anomalies with values greater or lower to ± 0.08 km s^{-1} from the initial 1-D model (i.e. 1.5 per cent of the initial model) and with standard deviation (WSTD) < 0.03 km s^{-1} (see Appendix A).

The V_P models are shown in Fig. 3 (horizontal sections at 4.6 km depth) and Fig. 4 (vertical sections along the profile A–B in Fig. 3). In the figures, the red line represents the projection of GPK3 whereas the blue represents GPK2. The thick part of the GPK3 and GPK2 trajectories correspond to the open-hole section of the wells which are located within the 4.4 to 5 km depth interval. For all the sets, only the part of the model with Derivative Weight Sum (DWS; Toomey & Foulger 1989) greater than 10 is displayed. For each set we also report the projection of the events used to obtain the models. Black contours correspond to velocity iso-values equal to 5.77, 5.85 and 5.94 km s^{-1}.

Fig. 5 shows the final epicentre locations for the 13 sets whereas Fig. 6 shows the vertical projections along the NS direction. The size of the circle of each event is proportional to its magnitude. The mean rms is 0.014 s, and the mathematical uncertainty on the final locations is ~30 m and ~50 m for the epicentre and depth position, respectively.

Phase 1; Set 1

Set 1 shows the mean state of the reservoir during the first 3 days of the stimulation when the injection flow rate was almost always 30 l^{-1} (Fig. 2). At a depth of 4.6 km a low V_P area ($5.55 < V_P <$ 5.77 km s^{-1}) is noted to the west of GPK3, about 200 m from the well. Its main elongation is N–S, although a NE prolongation of the V_P anomaly affects GPK3 (Fig. 3.1). The seismicity is centred on the stimulated well. The corresponding vertical section (Fig. 4.1) shows that the slight V_P anomaly affects only the GPK3 open-hole section whereas the seismicity covers a much larger area. Figs 5.1 and 6.1 display the relocated events of Set 1 as a compact cloud without any visible internal organization.

Phase 2; Sets 2–4

Set 2 includes events that occurred during the first 24 hr of Phase 2, when the injection rate was 50 l^{-1}. Fig. 3.2 shows the presence of a very weak low V_P anomaly ($V_P \approx 5.7$ km s^{-1}) located NW of the seismic cloud. The vertical section does not show velocity anomalies around the wells (Fig. 4.2). Seismicity of this set (Figs 5.2 and 6.2) is mainly centred on the well, although a small cluster is observed approximately 600 m from the stimulation region (black arrow in Fig. 5.2 at X = −100 m, Y = 0).

In Set 3, when injection parameters are maintained constant, a low V_P anomaly is identified ($5.67 < V_P < 5.77$ km s^{-1}; Fig. 3.3) affecting the region around GPK3 and the western area where low velocities were already observed in Set 1. Its vertical extension is estimated to be 1 km (by taking as reference the iso-contour 5.77 km s^{-1}; Fig. 4.3) whereas the horizontal extension (along the W–E direction) increases to 1.4 km. Here the seismic cloud is still centred on GPK3 and the seismicity located in the northern region has disappeared (Figs 5.3 and 6.3).

Set 4 includes the events that occurred until the end of this phase and the beginning of the dual stimulation. Injection parameters are mostly the same as the previous set and the resulting velocity model is similar, showing low V_p (Figs 3.4 and 4.4) and seismicity (Figs 5.4 and 6.4) centred around the stimulated well.

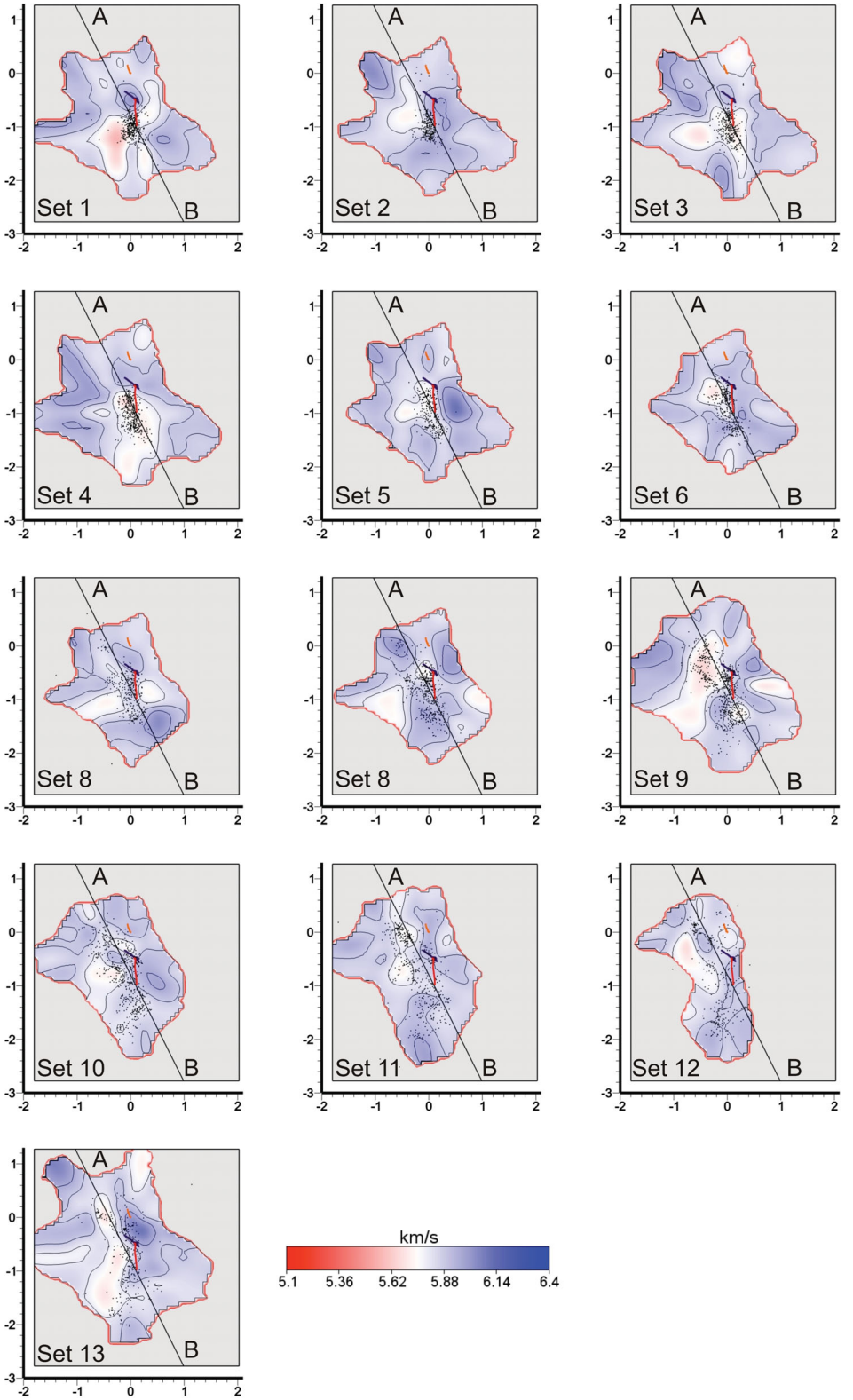

Figure 3. Evolution of the *P*-wave seismic velocity at 4.6 km depth during the 2003 stimulation test. Images are in chronological order from Set 1 to Set 13. The black dots are the projections of the events used to obtain the V_P models. Profiles A–B are the traces of the vertical sections reported in Fig. 4. Red and blue lines are the projections of GPK3 and GPK2, respectively.

Phase 3; Sets 5–7

Set 5 includes events recorded during the initial 16 hours of the dual stimulation test. The injected flow rate was 50 $1\,s^{-1}$ in GPK3 and 25 $1\,s^{-1}$ in GPK2. Horizontal and vertical V_P sections (Figs 3.5 and 4.5) report a low V_P region smaller than the previous set, and limited mostly to the region between the wells, whereas the seismicity remains located around GPK3 (Figs 5.5 and 6.5).

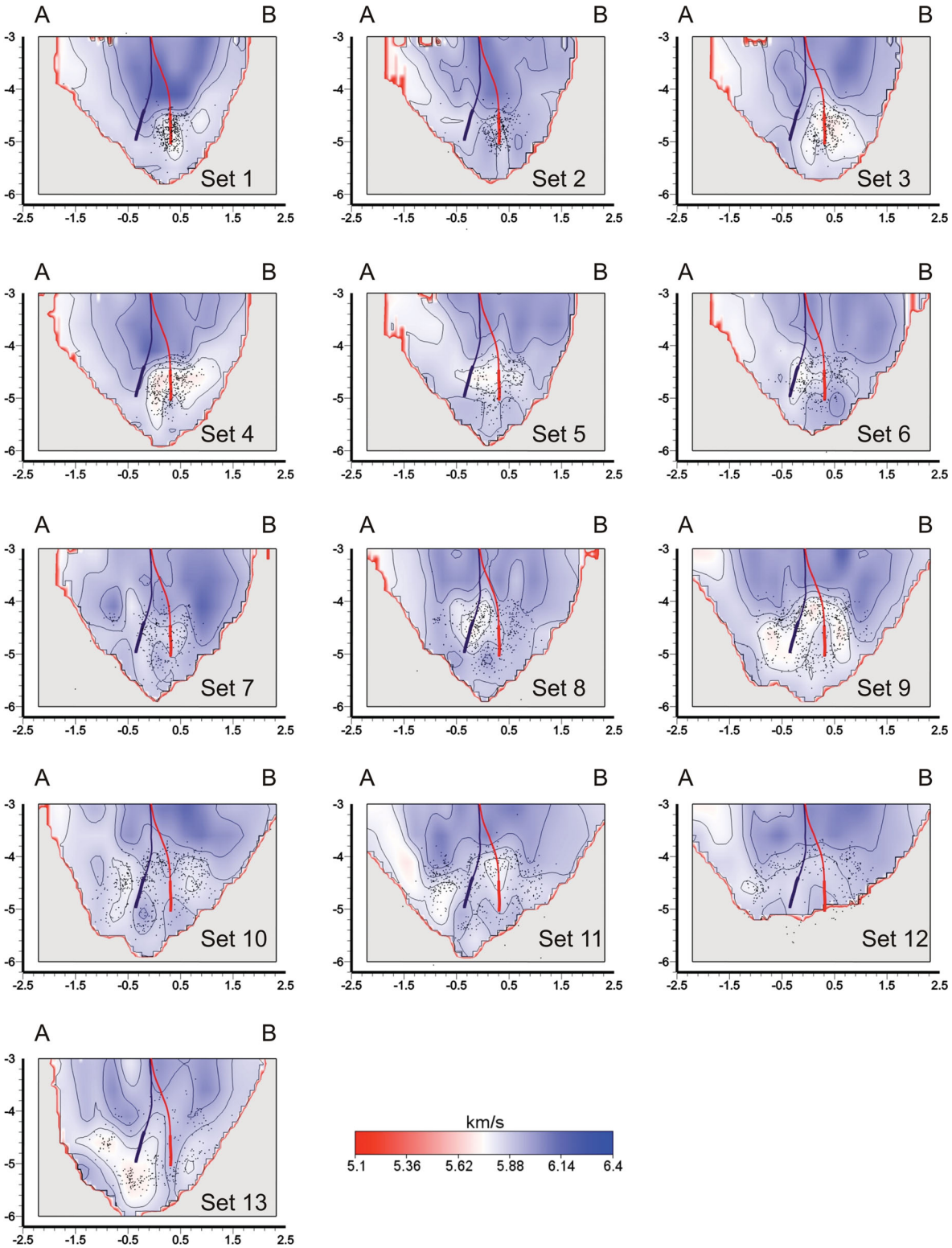

Figure 4. Vertical sections of the V_P models along traces A–B reported in Fig. 3. The black dots are the projections of the events used to obtain the V_P models. Red and blue lines are the projections of GPK3 and GPK2, respectively. The thick part of the borehole trajectories corresponds to the open-hole section of the wells.

In Set 6, the injection parameters remain constant. The area affected by the low V_P anomaly is more restricted and still located between the wells (Fig. 3.6). The vertical section shows that the weak low V_P anomaly is well centred on the open-hole section of GPK2 (Fig. 4.6). The seismicity is mainly located around GPK3 although a few events were recorded north of GPK2 (Figs 5.6 and 6.6) in the same area as observed in Set 2.

Set 7 contains the events recorded when the injection in GPK2 was stopped and a 'shot' at $\sim$80 l s^{-1} was tested in GPK3 for a few hours. Horizontal and vertical V_P sections are characterized by

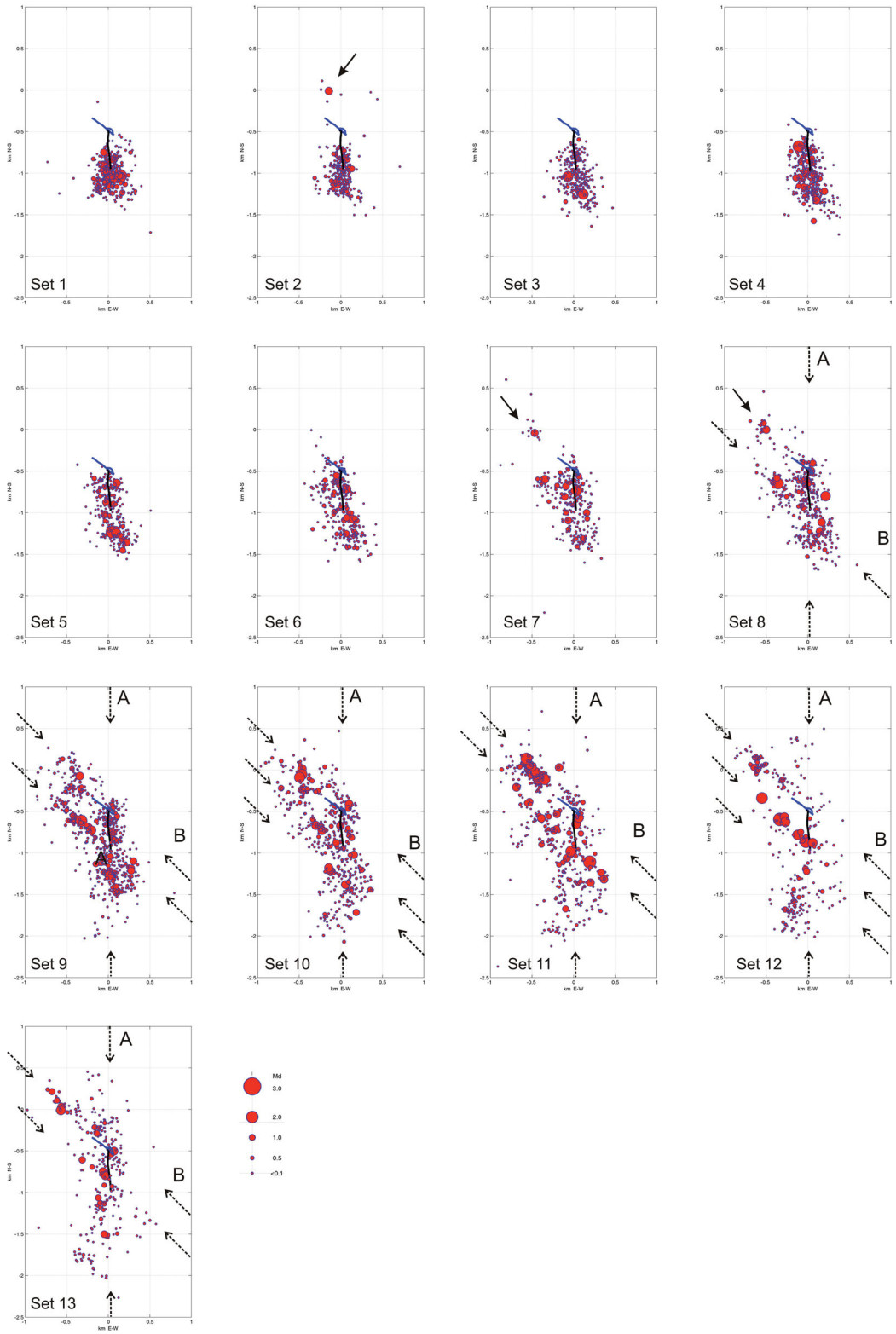

Figure 5. Evolution of the microseismic cloud. Each picture shows in chronological order the final epicentre positions after the computation of the local tomography. The radius of each circle is proportional to the magnitude and the projection of the injection well is indicated as a black line.

the quasi-total absence of velocity anomalies, showing only some patches in the eastern and western part of the larger seismic cloud (Figs 3.7 and 4.7). Seismicity is now organized into two main clouds instead, the larger located around the wells, the smaller located NW of GPK2 (X = −500 m, Y = 0 m; Figs 5.7 and 6.7).

Phase 4; Sets 8–9

Set 8 shows the mean state of the reservoir during the first 24 hr of Phase 4, when the injection rate in GPK3 was at 25 l s^{-1} (Fig. 2). A small low V_P anomaly ($V_P \approx 5.77$ km s^{-1}) is observed around GPK2 and a larger one at the western border of the resolved area. These

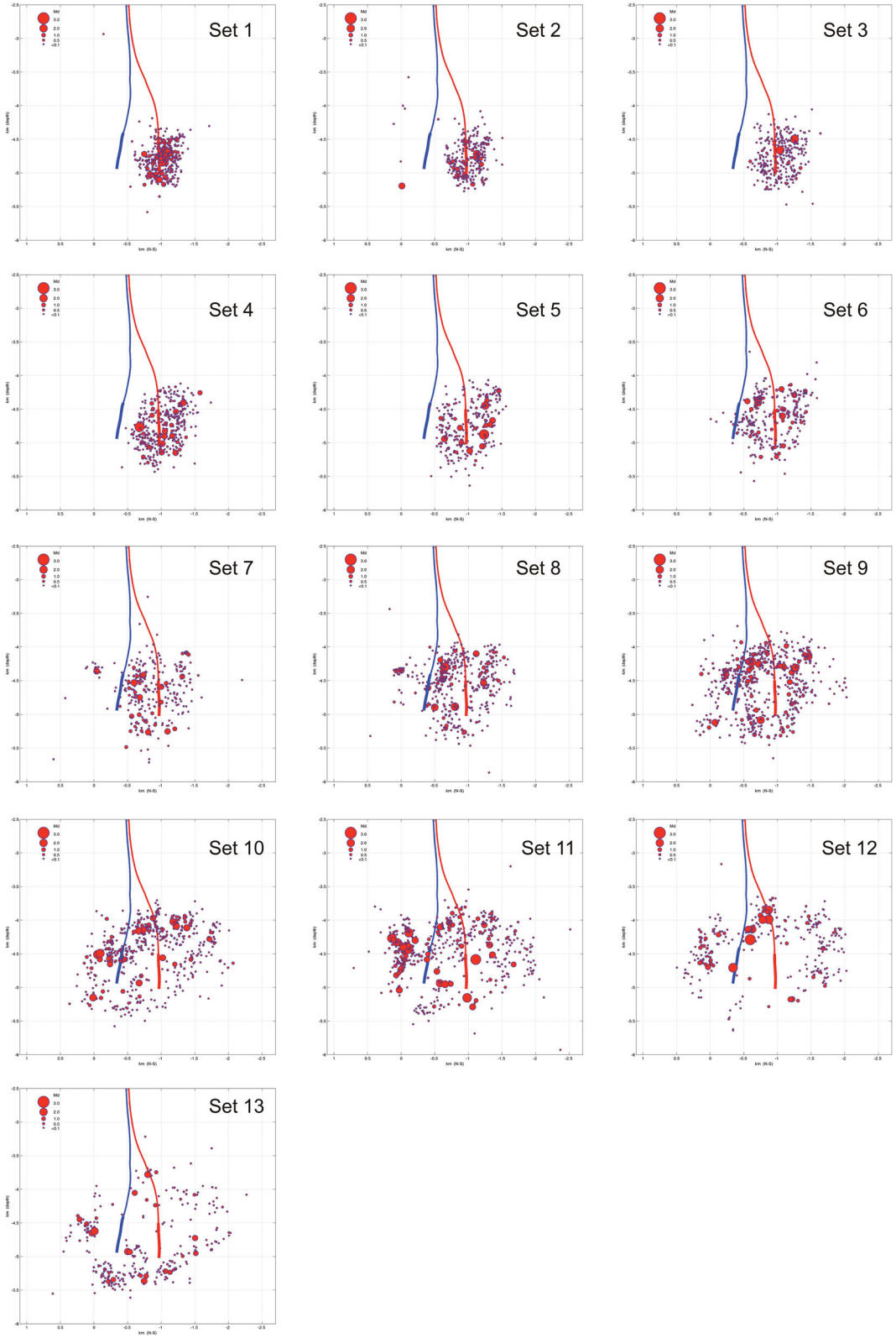

Figure 6. North–south vertical projections of the evolution of the microseismic cloud.

anomalies are not spatially correlated with the seismic clouds (Fig. 3.8). The vertical section of Fig. 4.8 shows the almost complete absence of V_P anomalies at depth of the stimulation, whereas a slight anomaly ($V_P \approx 5.77\,\mathrm{km\,s^{-1}}$) is observed around GPK2.

The two seismic clouds are apparent once again (Fig. 6.8) and the main cluster exhibits an internal organization of the seismicity, outlining at least two major active structures. The preferential directions are N–S (letter A in Fig. 5.8) and NW–SE (letter B in

Fig. 5.8). This internal pattern was discernible though hardly visible in the previous sets.

Set 9 shows a low V_P anomaly ($5.6 < V_P < 5.77\,km\,s^{-1}$) that develops NW of the seismic cloud (Fig. 3.9). In the vertical section (Fig. 4.9) the low V_P body depicts a particular shape from 4 to 5.4 km depth bordering the area around the open-hole part of GPK3. The two seismic clouds (Fig. 5.9) observed in the previous sets now nearly merge and involve an extensive area of $2.5 \times 1.5\,km^2$. Seismicity shows that the main direction of the major seismic cloud (A) is cut by two internal seismic structures with direction B (Fig. 5.9). Most of the largest events that occurred in this period are located in the shallow reservoir, between 4 and 4.5 km of depth (Fig. 6.9).

Phase 5; Sets 10–11

Sets 10 and 11 include events recorded during the four days following the shut in. Both models show very slightly low V_P anomalies ($5.73 < V_P < 5.77\,km\,s^{-1}$) at depth of the stimulation (Figs 3.10 and 3.11). Vertical sections highlight the absence of important anomalies, showing only small regions marked by low V_P north of GPK2 (Figs 4.10 and 4.11). The region affected by the seismicity is much larger than the low V_P anomalies mentioned above. However, the relocated seismicity (Figs 5.10, 5.11 and 6.10, 6.11) still depicts the internal seismic structures observed in the previous sets. In these sets at least three large seismic structures striking in the B direction are identified. In Set 11, the northern seismic cluster is characterized by intense activity and contains the largest magnitude event ($M_d = 2.9$) recorded during the whole injection test.

Phase 6; Set 12

Set 12 includes events that occurred when water was pumped at $15\ l\ s^{-1}$ from GPK2. At 4.6 km, depth only a slightly low V_P anomaly ($5.7 < V_P < 5.77\ km\ s^{-1}$) is present west of the wells (Fig. 3.12). The vertical section shows a total absence of anomalies (Fig. 4.12) and the seismicity occurs in the shallow part of the reservoir, between 4 and 4.6 km of depth. The horizontal projection of the seismicity displays at least three main structures along B, and one mainly oriented N–S (A, Fig. 5.12). The vertical projection of the hypocentres (Fig. 6.12) shows that most of the major events are located in the shallow part of the cloud at 3.6–4.3 km of depth.

Phase 7; Set 13

The last set includes the events recorded in the month following the stimulation test. A low V_P anomaly ($5.7 < V_P < 5.77\ km\ s^{-1}$) is observed at depth of the stimulation and mainly orientated N–S and NW–SE (Fig. 3.13). The vertical section shows a low V_P anomaly near GPK2 that develops northwards (Fig. 4.13). Notably, no low V_P residual anomalies are observed near GPK3, and the relocated seismicity (Fig. 5.13) depicts the same patterns observed in the previous sets.

3 COMPARISON OF THE GPK3 AND GPK2 STIMULATIONS

3.1 Summary of the tomography results of the GPK2 stimulation test

The time-lapse tomography of the GPK2 injection (Calò *et al.* 2011) has allowed us to identify temporal changes of the V_P velocity field during and after the stimulation test carried out in 2000. Fig. 7 indicates four representative sets of the 4-D tomography together with the relocated seismicity (Sets 2, 3, 4 and 14). Fig. 8(a) depicts the injection parameters recorded during the test along with the subset separation. In Appendix B, the 14 velocity models and the relocated seismicity obtained for the whole injection test are reported.

The main results of this 4-D tomography can be summarized by three main points (Calò *et al.* 2011):

(1) All the sets except Set 3 and Set 6 present highly similar features: a low-velocity anomaly mainly located around the zone where microseismic activity develops, but larger than the seismic cloud (Appendix B). Immediately after initiating the injection, the velocity anomaly is circular in shape as shown in Appendix B (Set 1). It elongates in the N145–N150°E direction during Set 2 (Fig. 7), and this direction remains constant over the whole injection period.

(2) Sets 3 and 6 represent the reservoir during the initial hours after an injection rate increase by $10\ l\ s^{-1}$, and show a return of the seismic velocity field to its initial value within the injection region (Fig. 7 and Appendix B).

(3) Relocated seismicity shows a seismic cloud centred on GPK2 striking in the NNW–SSE direction for the entire injection period, with only the post-injection seismicity (Fig. 7, Set 14) revealing some large internal structures.

The low V_P anomalies were interpreted as because of the presence of large rock mass volumes affected by changes in effective stresses, whereas the *P*-wave velocity variations within the reservoir (and consequently the related variations of effective stress) are not associated with simple water diffusion from the injection well, but rather reflect the occurrence of large-scale aseismic motions in the reservoir.

3.2 Comparison of the two stimulations

The different behaviours of the GPK2 (2000) and GPK3 (2003) stimulations have been noted and discussed by several authors (Dezayes *et al.* 2005; Nami *et al.* 2008; Dorbath *et al.* 2009). A direct comparison of GPK2 and GPK3 velocity model results is difficult to obtain for the following reasons: (i) in 2000 the water was injected at 5 km depth in an 'uncontaminated' rock volume whereas in 2003 a large part of the reservoir was already enhanced because of the previous stimulation of GPK2 at the same depth; (ii) the adopted 'injection strategy' was different.

However some trends relative to the two injections are quite similar, allowing a comparative analysis of the two V_P seismic evolutions. The main differences have been summarized in four main points, concerning the size, shape and intensity of the low seismic velocity anomalies and the induced seismicity location pattern.

(1) During the GPK2 injection test, a low V_P anomaly is always present near the well and assumes a well-defined shape. Seismicity is generally located in a smaller area inside the low V_P region. Conversely, during the GPK3 injection the low V_P anomaly changes shape continuously and the region affected by the seismicity often varies with respect to the position of the seismic velocity anomalies.

(2) The lowest values of velocity anomalies in the GPK2 tomography were 5.2–5.3 km s^{-1} (i.e. the 8–10 per cent of the velocity values of the reservoir at rest) whereas during most of the GPK3 stimulation the lowest values did not exceed 5.6–5.7 km s^{-1} (i.e. 3–5 per cent).

(3) The post-injection period of the GPK2 test (Fig. 7, Set 14) is characterized by a low V_P anomaly affecting a large area while for the corresponding period of the GPK3 injection seismic tomography (Figs 3 and 4, Set 13) shows a slightly low V_P body oriented NS

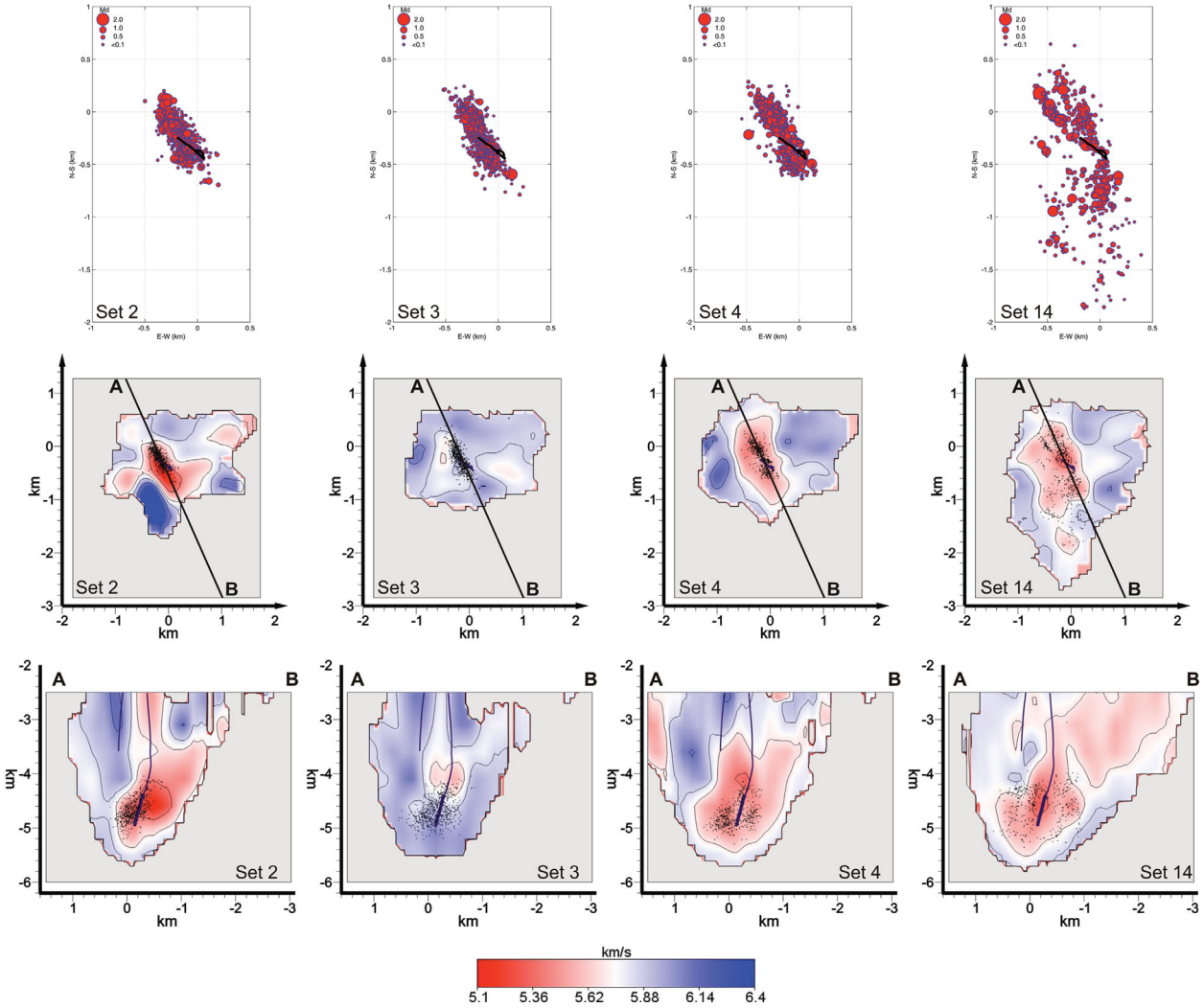

Figure 7. Evolution of the microseismic cloud (top) and of the *P*-wave seismic velocity models (bottom) of the GPK2 stimulation test performed in 2000 (after Calò *et al.* 2011). Set numeration is reported in Fig. 8a.

in the central and southern region, and oriented NNW–SSE in the northern region.

(4) The seismic clouds observed in GPK2 (Appendix B) are always dense and without internal structures until the shut in, and only the post-injection seismicity reveals some large structures (Fig. 7). On the contrary, seismicity recorded in 2003 underlines several seismic structures (directions A and B in Fig. 5) that are also evident during the stimulation period. Furthermore a small cloud clearly far from the stimulation region appears in a northern sector of GPK2 in the early phases of the injection.

Yet some interesting similarities are also revealed during the two stimulation tests, particularly concerning the temporal evolution of the velocity models. These similarities can be summarized in two main points.

(1) Tomograms of Sets 2, 3 and 4 relative to the GPK2 injection (Fig. 7) describe the seismic velocity variations when the injection rate was increased from 30 to 40 l s^{-1}. In Set 3, the very low anomaly observed in Set 2 disappears, only to reappear in Set 4. Set 3 shows the presence of a weak V_P anomaly ($V_P \approx 5.7$ km s^{-1}) located west of the stimulated well. In the tomography of GPK3, Sets 1, 2 and 3 (Figs 3 and 4) are comparable to a similar step, even though the injection flow rate was increased from 30 to 50 l s^{-1}. These three sets show that GPK3 behaved similarly to GPK2, even if the low V_P anomalies observed are much weaker.

(2) The post injection seismicity of both injection tests (Set 14 for GPK2 and Set 13 for GPK3) reveal similar patterns showing that the seismicity recorded in 2000 after the shut in (Fig. 7, Set 14) is located along the same active structures depicted by the seismicity recorded during the 2003 stimulation (Fig. 5, Set 13).

Finally, we also compared the relation between the occurrence of the largest earthquakes and the injection parameters of the two stimulations. Fig. 8 shows the well-head pressure and injected flow rate of the GPK2 and GPK3 injection tests, together with the occurrence of the earthquakes of magnitude greater than 1.7. In 2000, 89 events occurred during the stimulation but only 17 in the 5 d after the shut in (Fig. 8a). The largest events occurred during static conditions of the injection parameters (e.g. Sets 10 and 11). Conversely, in 2003 most of the events (31 of 56) occurred in the periods of rest or during the GPK2 production period (Fig. 8b). The largest events occurred in Sets 8, 11 and 12 corresponding to periods marked by sudden reductions of the injected flow rate or during production periods. Furthermore, no correlation between the largest events and the increasing of flow rates was observed in either stimulation test.

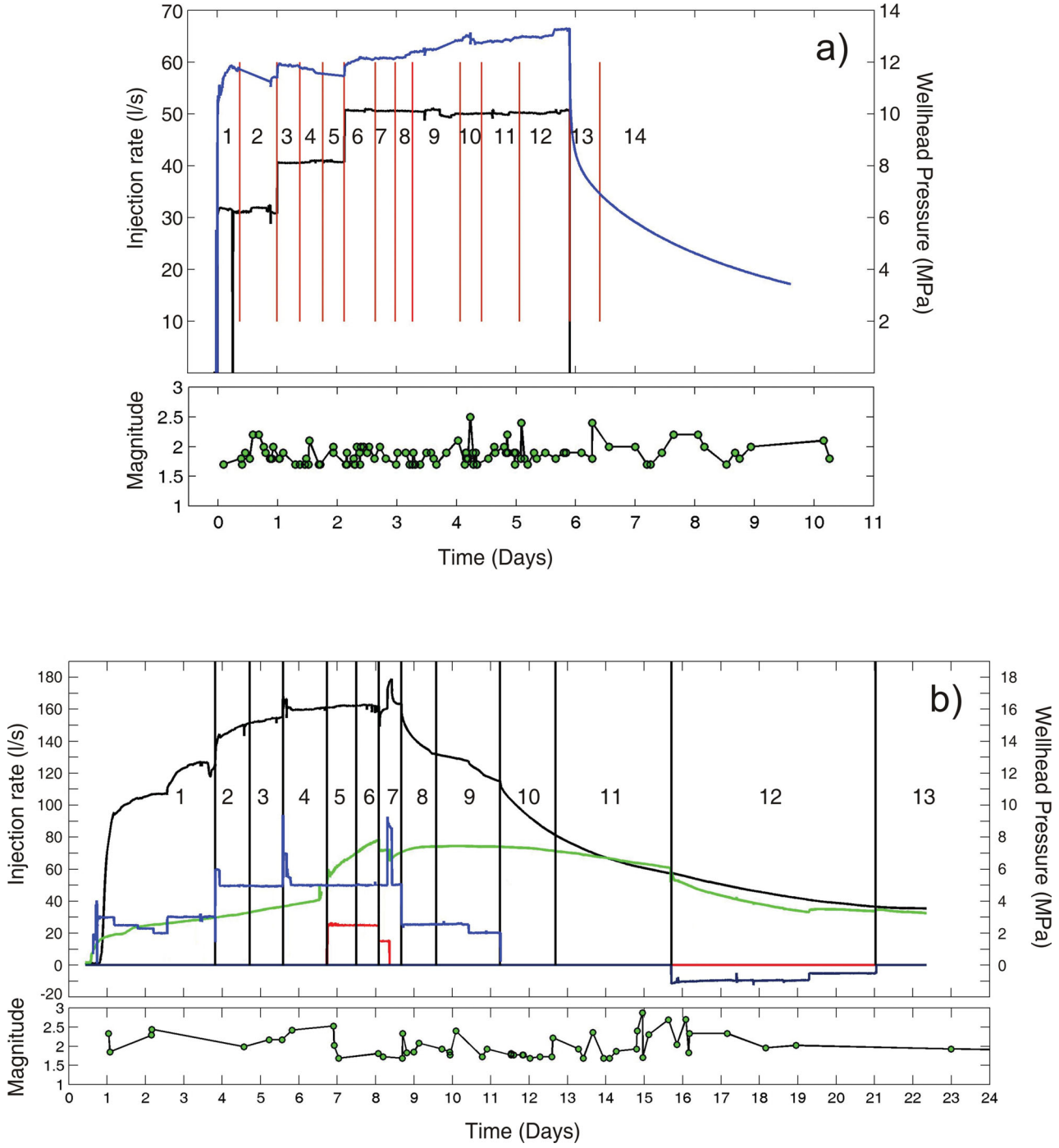

Figure 8. Injection parameters of the GPK2 (a) and GPK3 (b) injection tests. Also reported in the graphs are the temporal subsetting for the construction of the 4-D tomographies and the occurrence of the events with magnitude larger than 1.7 (green circles).

4 DISCUSSION

The 4-D seismic tomography of the GPK3 stimulation occurred in 2003 at Soultz-sous-Forêts, and comparing it with the 4-D tomography of the GPK2 stimulation test (Calò *et al.* 2011) highlights strong differences in the behaviour of the geothermal reservoir during the two injections.

Synthetic tests and spatial analysis of the WSTD (Appendix A) assessed the reliability of the tomograms, which reveals the possibility of imaging weak structures (1.5 per cent of the initial model) in the border regions as well. Julian & Foulger (2010) showed the risk of misinterpreting the artefacts related to the different ray path coverage of data collected in different epochs as temporal changes in the seismic velocity models. In the case of the Soutlz injections this problem is negligible because the seismicity occurs in a restricted area with respect to that covered by the seismic network; consequently the ray path coverage rarely varies during stimulation periods. This was already determined by synthetic tests presented by Calò *et al.* (2011). Another cause that could affect time domain tomography is the presence of high levels of random errors

in the data. This problem is greatly reduced by the application of WAM post-processing. Calò *et al.* (2009, 2012), using regional earthquakes, have demonstrated that the WAM method reduces the effect of random errors, along with those related to the optimization of the input parameter that needs to impose the set up of a seismic tomography at the outset. Therefore, the temporal variations of the seismic velocities imaged at Soultz can be related to the variations of the physical properties of the geothermal reservoir during the injection tests.

In the GPK2 stimulation, the low V_P anomalies were related to the increasing of effective stresses in the regions around the well. Schoenball *et al.* (2012), using a data set of 715 events ($M_d >$ 1) recorded during the stimulation of GPK2, suggested that the Coulomb failure stress (DCFS) by dislocation is only a minor contribution to the whole stress perturbation induced by stimulation, whereas it can be quite effective for rupture propagation along single large fault zones. Hence, the stress drop produced by the seismicity alone does not justify the variation of the seismic velocities. This consideration supports the occurrence of some mechanism (such as the aseismic slips) accommodating the transient stress perturbation.

During the GPK3 stimulation, such low velocities were not observed. Dezayes *et al.* (2003, 2004) identified a ∼10 m structure crossing GPK3 at depth of the stimulation. Flow-log tests determined that about 70 per cent of the water injected in GPK3 is absorbed by this fracture (Dezayes *et al.* 2004). As a consequence, the transmissivity of GPK3 after the stimulation test increased only by a factor of 1.6 (Nami *et al.* 2008; Schindler *et al.* 2008). Conversely, the increasing of transmissivity after the GPK2 injection test was by a factor 19 (Nami *et al.* 2008). Several seismic structures, some of them crossing the GPK3 well, are clearly revealed by the relocated seismicity (Fig. 5). It is therefore possible that the fluids moved quickly throughout these preferential paths, affecting regions more than 900 m from the injection point, while still in the early phases of the stimulation. This leaking of water resulted in low effective stress changes in the region close to the GPK3 open-hole section. The presence of small seismic clouds and low V_P in regions far from the stimulated well (Sets 1, 6 and 7) support this interpretation. Thus the absence of low V_P anomalies during the GPK3 stimulation is explained by most of the injected water rapidly moving far from the injection region, avoiding an increase in the effective stress near the well.

In the first phases of the stimulation the seismic cloud is dense and is mainly concentrated around the GPK3 open-hole section until Set 4 (Fig. 6). After this phase (Set 5, i.e. when dual stimulation started) the seismic pattern changed. The region close to GPK3 became progressively aseismic and the seismicity spread out and moved towards shallower depths (Fig. 6). This suggests that the opening of the preferential fluid paths occurs during well-defined time periods. Regions close to the well end up aseismic and they should be interpreted as regions where the pore pressure does not increase because the fracture system is sufficiently developed and/or oriented in favourable directions with respect the regional stress field. This behaviour is also known as the Kaiser Effect.

However, the main paths of water drainage should not only be the seismic structures imaged by the seismicity. In the GPK2 tomography we observed that large aseismic slips should occur during particular phases of the injection test, and we cannot exclude the possibility that similar processes also affected the reservoir during the GPK3 stimulation. Indeed in GPK3 a scenario similar to that described in the GPK2 stimulation was observed when the injection flow rate was increased. In both stimulations (2000 and 2003), the low V_P anomalies disappear only to reappear after a period of time, even if they differ in intensity and shape. This observation suggests that at such times a similar mechanism triggers some physical processes affecting the seismic velocity field. However, if in GPK2 the fading of V_P anomalies has been interpreted through the occurrence of large aseismic slips accommodating the increase in effective stress, the same cannot be assumed for GPK3 because the velocity variations observed are too weak.

The seismic velocity models were calculated using the data recorded during Phase 3 (Fig. 2), which allows observations of the interaction between the GPK3 and GPK2 wells during the dual injection. The sequence of Sets 4–6 (Figs 3 and 4) reports a gradual reduction of the slightly low V_P region and its migration from GPK3 to GPK2. The tomogram of Set 7 shows the total absence of V_P anomalies while they appear again in Set 8 in a region near GPK2. In Set 9, the low V_P grows and migrates towards GPK3 surrounding the open-hole section of the well (Fig. 4.9). The weakness of very low V_P values around GPK2 suggests that the presence of the dense fracture network is sufficiently developed (already present in 2000), allowing a rapid diffusion of the fluids at the flow rate tested in 2003. Despite the large amount of water injected at that time (a total of 75 l s^{-1}), the dense fracture network avoided the accumulation of effective stresses near the wells, which resulted in a complete absence of seismic velocity anomalies. This condition is generally expected in the periods of rest or when the stress field is transiently reported to the initial conditions, as it was observed in 2000 when the flow rate was suddenly increased.

Noteworthy is the pattern depicted by the seismicity recorded in 2000 and 2003. The post-injection events allowed for observation of well-defined structures which affect the whole geothermal reservoir and that are associated with the largest events that occurred in the northern part of the Soultz reservoir.

Finally, the relation between the occurrence of the largest events and the injection parameters (Fig. 8) shows that a network of pre-existing fractures plays a fundamental role in the repartition of the transient stress perturbations during massive hydraulic stimulations. In 2000, this network was not well developed and the largest events occurred during the injection, where the stress perturbation was expected to be the highest. In 2003, the largest events occurred in periods marked by sudden reductions of the injected flow rate or during production periods when a decreasing of the pore pressure was expected in the reservoir. Furthermore, for both stimulations the occurrence of the largest events seems independent of the sudden increasing of the injected flow rate.

5 CONCLUSION

We propose that a large network of faults, some of them crossing GPK3, affected the repartition of the effective stresses around the well during the stimulation test. The presence of these structures represented the main paths of the injected water, and avoided the accumulation of effective stresses in the reservoir close to the GPK3 well. This resulted in a lack of large low V_P anomalies during the stimulation. The injected water affected a large region activating structures far from the origin point of the stimulation. The presence of faults, some of them crossing GKP3, is revealed by the relocated seismicity and the weak variations of the V_P models are consistent with small stress perturbations of the reservoir near the injection well.

However a similar evolution occurred during the GPK3 and GPK2 stimulations when injected flow rates were suddenly varied. This suggests the occurrence of a similar mechanism for

accommodating the variation of the effective stress close to the wells when rapid variations of flow rate are imposed. Because this mechanism, while affecting the seismic velocities, cannot be related to the recorded seismic activity, we can assume that it represents a non-seismic event.

ACKNOWLEDGEMENTS

During this work M. Calò was funded by GEISER European Project (FP7: 241321). We thank the GEIE Exploitation Minière de la Chaleur for the hydraulic data. We also thank L. Dorbath for very fruitful and constructive discussions. Finally we very sincerely thank the editor and an anonymous reviewer who helped improve the quality of the manuscript.

REFERENCES

Beauce, A., Fabriol, H., Le Masne, D., Cavoit, C., Mechler, C. & Chen, X., 1991. Seismic studies on the HDR site of Soultz-sous-For○ets (Alsace, France), *Geotherm. Sci. Tech.,* **4,** 239–266.

Calò, M., Dorbath, C., Luzio, D., Rotolo, S.G. & D'Anna, G., 2012. Seismic velocity structures of southern Italy from tomographic imaging of the Ionian slab and petrological inferences, *Geophys. J. Int.,* **191,** 751–764.

Calò, M., Dorbath, C., Cornet, F.H. & Cuenot, N., 2011. Large-scale aseismic motion identified through 4-D P-wave tomography, *Geophys. J. Int.,* **186,** 1295–1314.

Calò, M., Dorbath, C., Luzio, D., Rotolo, S.G. & D'Anna, G., 2009. Local Earthquakes Tomography in the southern Tyrrhenian region: geophysical and petrological inferences on subducting lithosphere, in *Subduction Zone Geodynamics, Frontiers in Earth Sciences,* pp. 85–99, eds Lallemand, S. & Funiciello, F., Springer-Verlag, Berlin, Heidelberg.

Calò, M., 2009. Tomography of subduction zones using regional earthquakes:methodological developments and application to the Ionian slab, *PhD thesis,* EOST, University of Strasbourg, http://tel.archivesouvertes.fr/tel-00438598/en/2.

Charléty, J., 2007. Propriétés physiques du réservoir de Soultz-sous-Forêts à partir de l'analyse fine de la sismicit´e induite, *PhD thesis,* University of Louis Pasteur, Strasbourg, France.

Charléty, J., Cuenot, N., Dorbath, L., Dorbath, C., Haessler, H. & Frogneux, M., 2007. Large earthquakes during hydraulic stimulations at the geothermal site of Soultz-sous-Forêts, *Int. J. Rock Mech. Min. Sci.,* **44,** 1091–1105.

Charléty, J., Cuenot, N., Dorbath, C. & Dorbath, L., 2006. Tomographic study of the seismic velocity at the Soultz-sous-For○ets EGS/HDR site, *Geothermics,* **35,** 532–543.

Cuenot, N., Dorbath, C. & Dorbath, L., 2008. Analysis of the microseismicity induced by fluid injection in the Hot Dry Rock site of Soultz-sous-Forêts (Alsace, France): implications for the characterization of the geothermal reservoir properties, *Pure appl. Geophys.,* **165,** 797–828.

Cuenot, N., Charléty, J., Dorbath, L. & Haessler, H., 2006. Faulting mechanisms and stress regime at the European HDR site of Soultz-sous-Forêts, France, *Geothermics,* **35,** 561–575.

Cuenot, N., Charléty, J., Dorbath, L., Dorbath, C., Frogneux, M., Haessler, H. & Sahr, J., 2005. EOST contribution to the seismological studies at Soultz-sous-For○ets for the period 2001–2004, in *Proceedings of the EHDRA Scientific Conference,* Soultz-sous-For○ets, France, 17–18 March, p. 9.

Dezayes, C., Valley, B., Maqua, E., Syren, G. & Genter, A., 2005. Natural fracture system of the Soultz granite based on UBI data in the GPK3 and GPK4 wells, in *Proceedings of the EHDRA Scientific Conference,* Soultz-sous-Forêts, France, 17–18 March, p. 9.

Dezayes, Ch., Genter, A. & Gentier, S., 2004. Fracture network of the EGS geothermal reservoir at Soultz-sous-Forêts (Rhine Graben, France), in *Proceedings of the Geothermal Resource Council, Annual Meeting,* Vol. 28, pp. 213–218, Palm Springs, California, USA.

Dezayes, Ch., Genter, A., Homeier, G., Degouy, M. & Stein, G., 2003. Geological study of GPK-3 HFR borehole (Soultz-sous-Forêts, France), Open file Rep. BRGM/RP-52311-FR, 128 pp.

Dorbath, L., Cuenot, N., Genter, A. & Frogneux, M. 2009. Seismic response of the fractured and faulted granite of Soultz-sous-Forêts (France) to 5 km deep massive water injections, *Geophys. J. Int.,* **177,** 653–675.

Julian, B.R. & Foulger, G.R., 2010. Time-dependent seismic tomography, *Geophys. J. Int..,* **182,** 1327–1338.

Leonard, M. & Kennett, B.L.N., 1999. Multi-component autoregressive techniques for the analysis of seismograms, *Phys. Earth planet. Inter.,* **113,** 247–263.

Nami, P., Schellschmidt, R., Schlindler, M. & Tischner, T., 2008. Chemical stimulation operations for reservoir development of the deep crystalline HDR/EGS system at Soultz-sous-Forêts (France), in *Proceedings of the 33th Workshop on Geothermal Reservoir Engineering,* Stanford University, Stanford, CA, USA.

Nami, P., Schindler, M., Tischner, T., Jung, R. & Teza, D., 2007. Evaluation of stimulation operations and current status of the deep Soultz wells prior to power production, in *Proceedings of the EHDRA Scientific Conference,* Soultz-sous-Forêts, France, 28–29 June, p. 11.

Schindler, M., Nami, P., Schellschmidt, R., Teza, D. & Tischner, T., 2008. Summary of hydraulic stimulation operations in the 5 km deep crystalline HDR/EGS reservoir at Soultz-sous-Forêts, in *Proceedings of the Thirty-Third Workshop on Geothermal Reservoir Engineering,* Stanford University, Stanford, CA, USA, p. 9.

Schoenball, M., Baujard, C., Kohl, T. & Dorbath, L., 2012. The role of triggering by static stress transfer during geothermal reservoir stimulation, *J. geophys. Res.,* **117,** B09307, doi:10.1029/2012JB009304.

Toomey, D.R. & Foulger, G.R., 1989. Tomography inversion of local earthquake data from the Hengill Grensdalur central volcano complex, Iceland, *J. geophys. Res.,* **94**(B12), 17 497–17 510.

Zhang, H. & Thurber, C.H., 2003. Double-difference tomography: the method and its application to the Hayward fault, California Bull, *Seism. Soc. Am.,* **93,** 1175–1189.

APPENDIX A

To assess the reliability of our results and to show the resolution power of the data and method we build a synthetic model characterized by a low cross-shaped *P* velocity anomaly of −1.5 per cent with respect to the initial 1-D velocity distribution (Fig. A1a). The body is placed around the open-hole section of GPK3. Vertical section AB shows the velocity pattern at depth. With the same configuration of earthquakes and stations as in the real inversion, we calculate synthetic traveltimes for Set N 7. This set contains 283 events and represents one of the most representative sets in terms of shape of the seismic cloud. We simulate the possible picking errors by adding a vector of random errors with standard deviation equal to 0.01 s. The 1-D initial model is then used as starting velocity distribution for the inversion of the perturbed synthetic database.

Fig. A1(b) shows the results after the inversion of the synthetic data using only the tomoDD code. The low V_P anomaly is recovered in the region around the foci and the cross-shaped pattern is roughly recovered. This test highlights the fact that the double difference tomographic method applied to small and very concentrated data sets is able to recover the velocity structures in the regions near the events with satisfactory reliability.

Fig. A1(c) shows the velocity model obtained with the WAM method. We must bear in mind that this model is obtained by the weighted mean of 15 different velocity models previously obtained with tomoDD. Here the cross-shaped anomaly is well recovered also in the border areas. Also, the vertical section shows that the model exhibits no strong artefacts.

With this test we demonstrate that the method used (tomoDD plus WAM) is able to recover the velocity structures in the volume where DWS > 10.

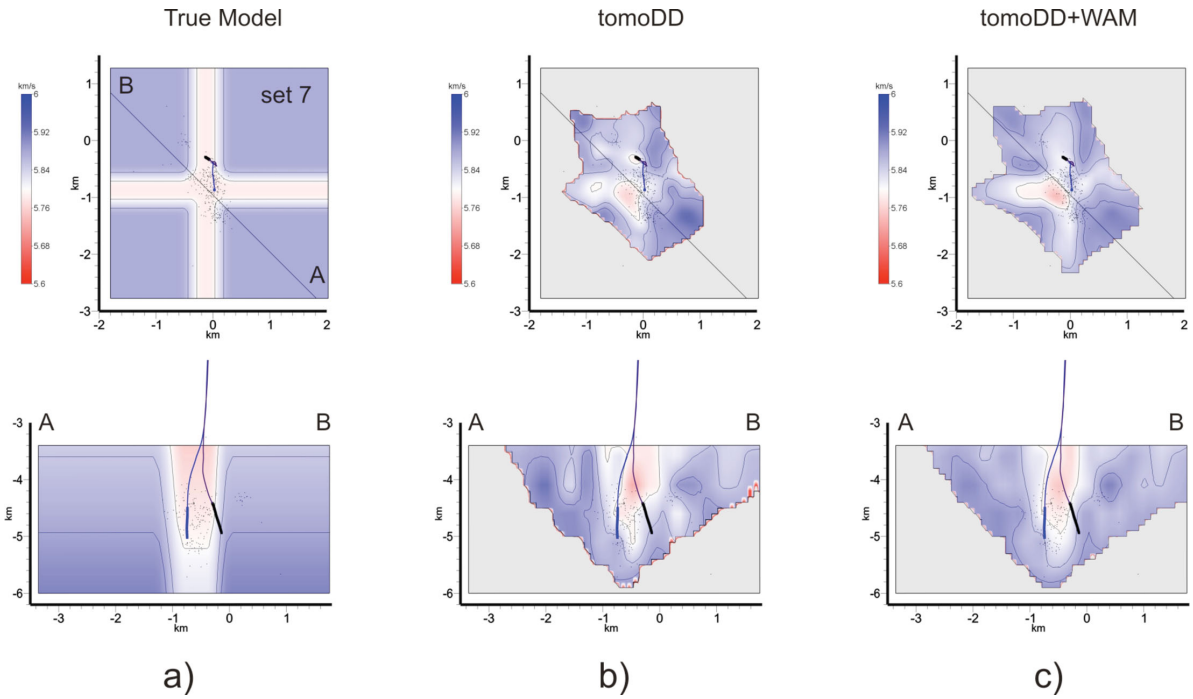

Figure A1. (a) Map view at 4.6 km depth and vertical section (AB) of the V_P model used to calculate the synthetic traveltimes; (b) map view and cross sections of the model obtained with tomoDD only for the Set N 7; (c) model obtained with the tomoDD method added to WAM.

The WAM method allows calculating a Weighted Standard Deviation (WSTD) of the velocity estimates. The WSTD is calculated directly using the velocity distributions used to build the WAM and with the same weighting scheme as to obtain the final velocity. It describes the variability of the models that have been used and it provides an estimation of the dependence of the single models to the input parameters. Here are reported the horizontal sections at 4.6 km depth (Fig. A2) and the vertical ones (Fig. A3) of the 13 WSTD distributions calculated for the corresponding seismic velocity models.

APPENDIX B

Evolution of the *P*-wave seismic velocity at 4.6 km depth (Fig. B1) and corresponding vertical sections (Fig. B2) during the 2000 stimulation test (after Calò *et al.* 2011). Images are in chronological order from Set 1 to Set 14. The black dots are the projections of the events used to obtain the V_P models. Profiles A–B are the traces of the vertical sections.

Fig. B3 reports the evolution of the microseismic cloud. The radius of each circle is proportional to the magnitude and the projection of the injection well is indicated as a black line.

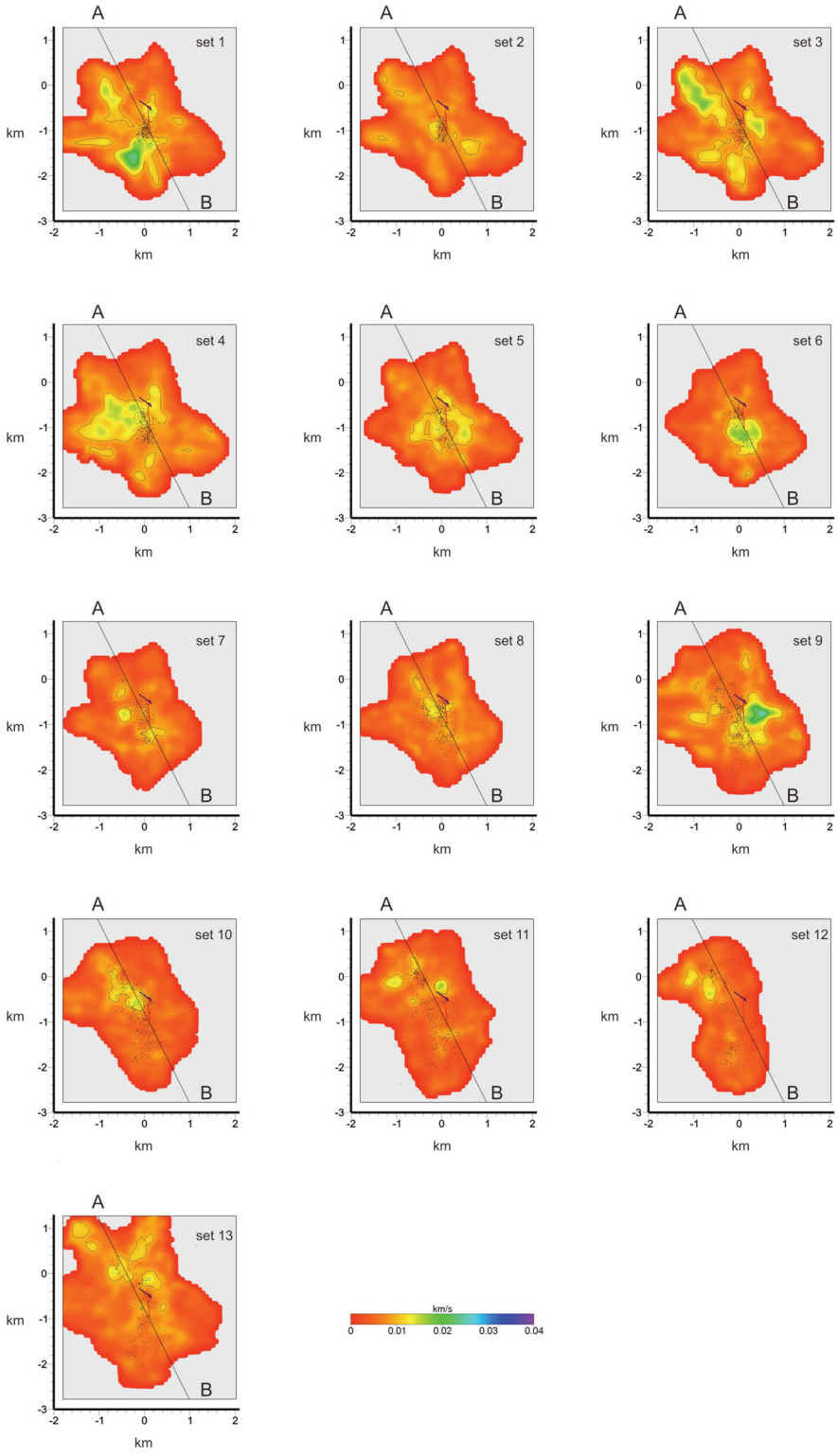

Figure A2. Horizontal slices at 4.6 km of depth of the WSTDs for the 13 tomograms.

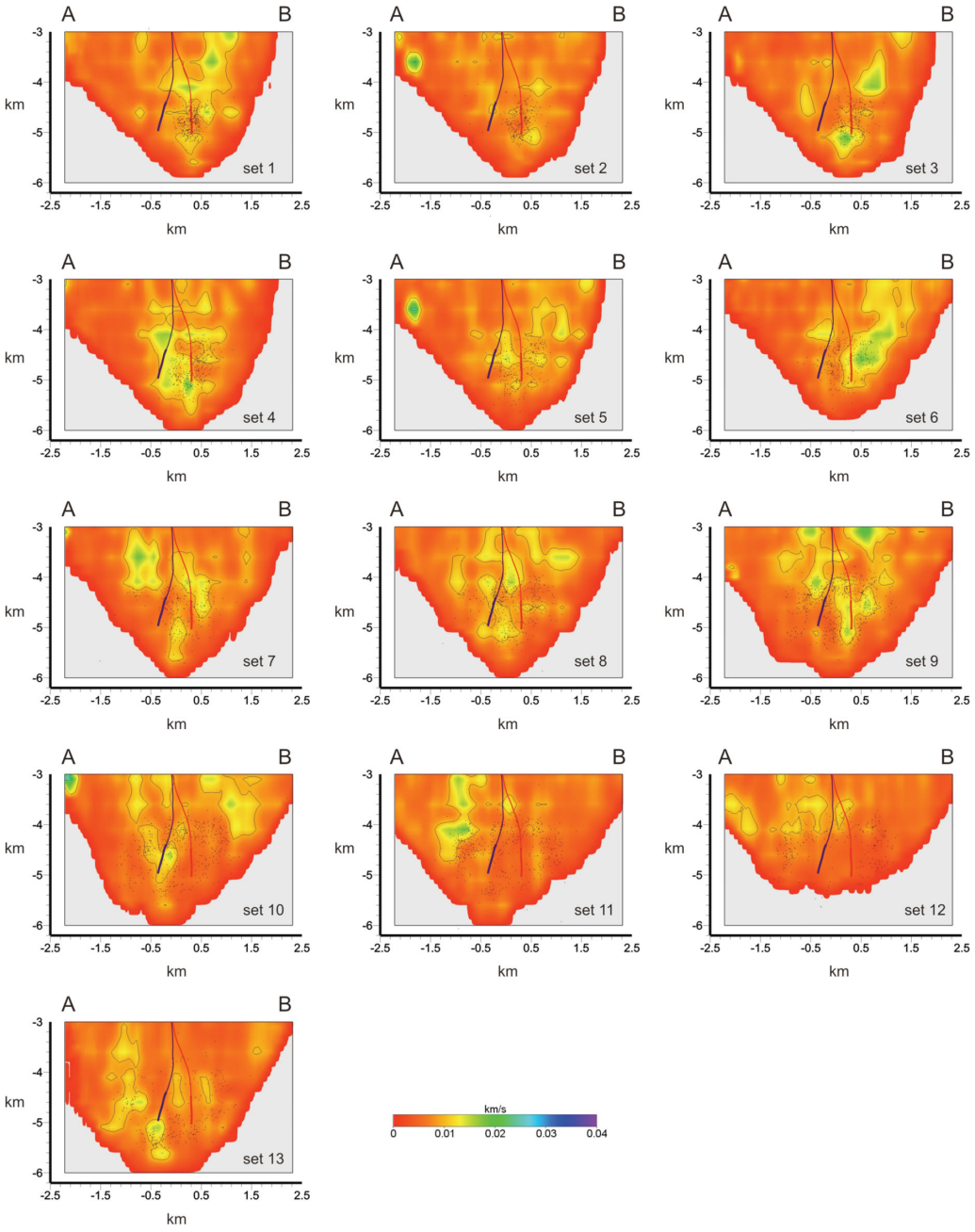

Figure A3. Vertical sections of the WSTDs for the 13 tomograms.

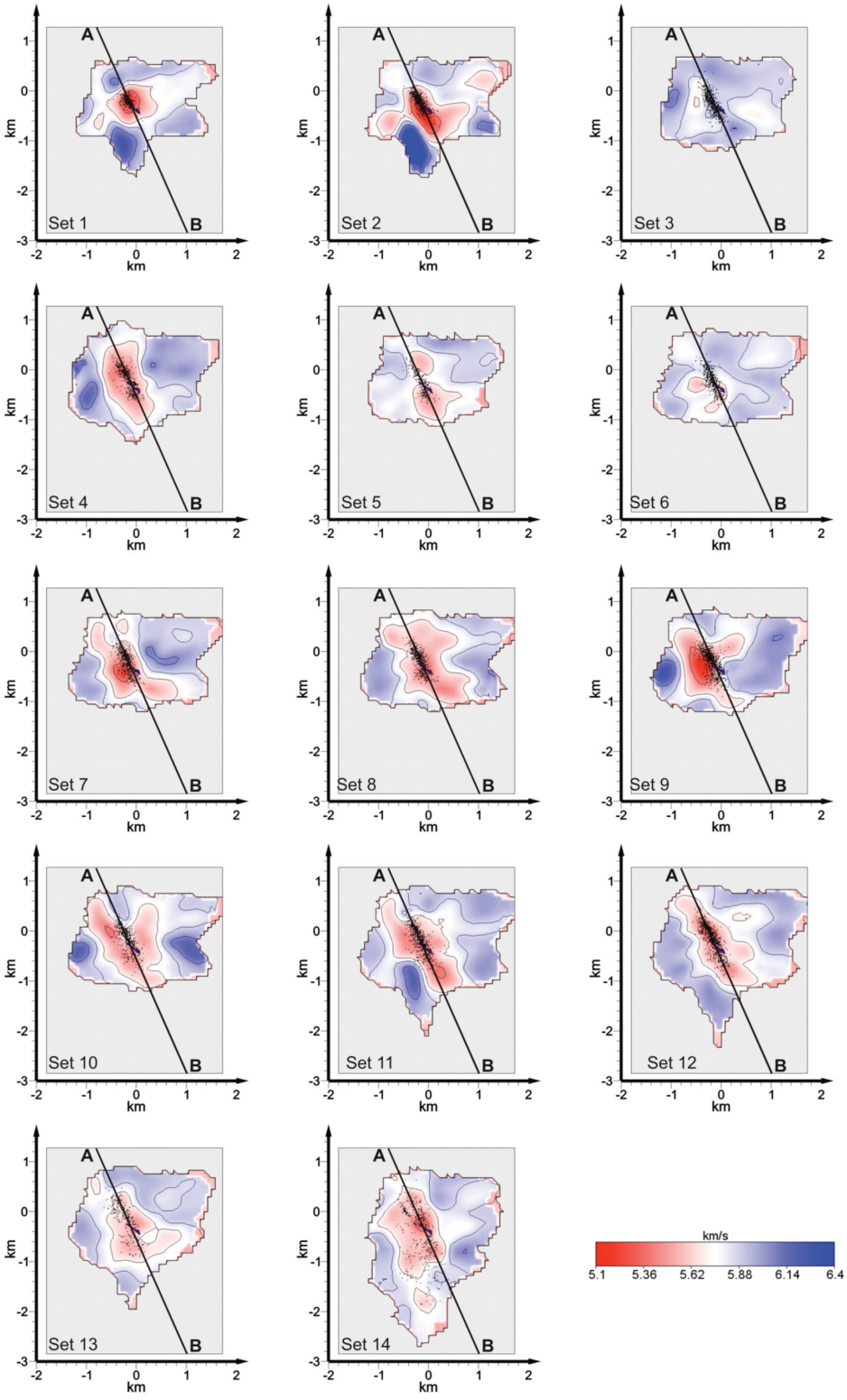

Figure B1. Evolution of the *P*-wave seismic velocity at 4.6 km depth during the 2000 stimulation test (after Calò et al. 2011).

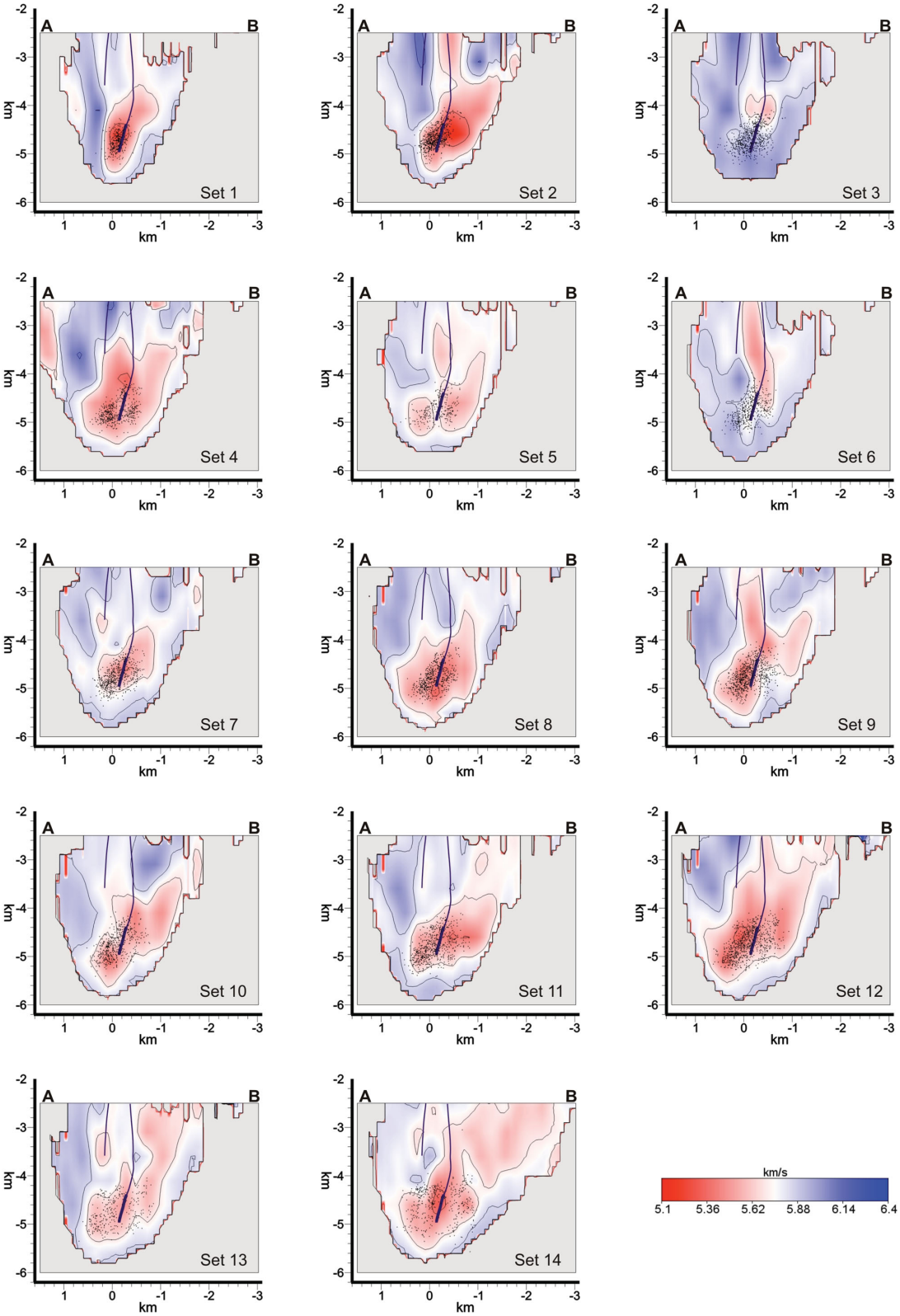

Figure B2. Vertical sections of the V_P models along traces A–B reported in B1 (after Calò et al. 2011).

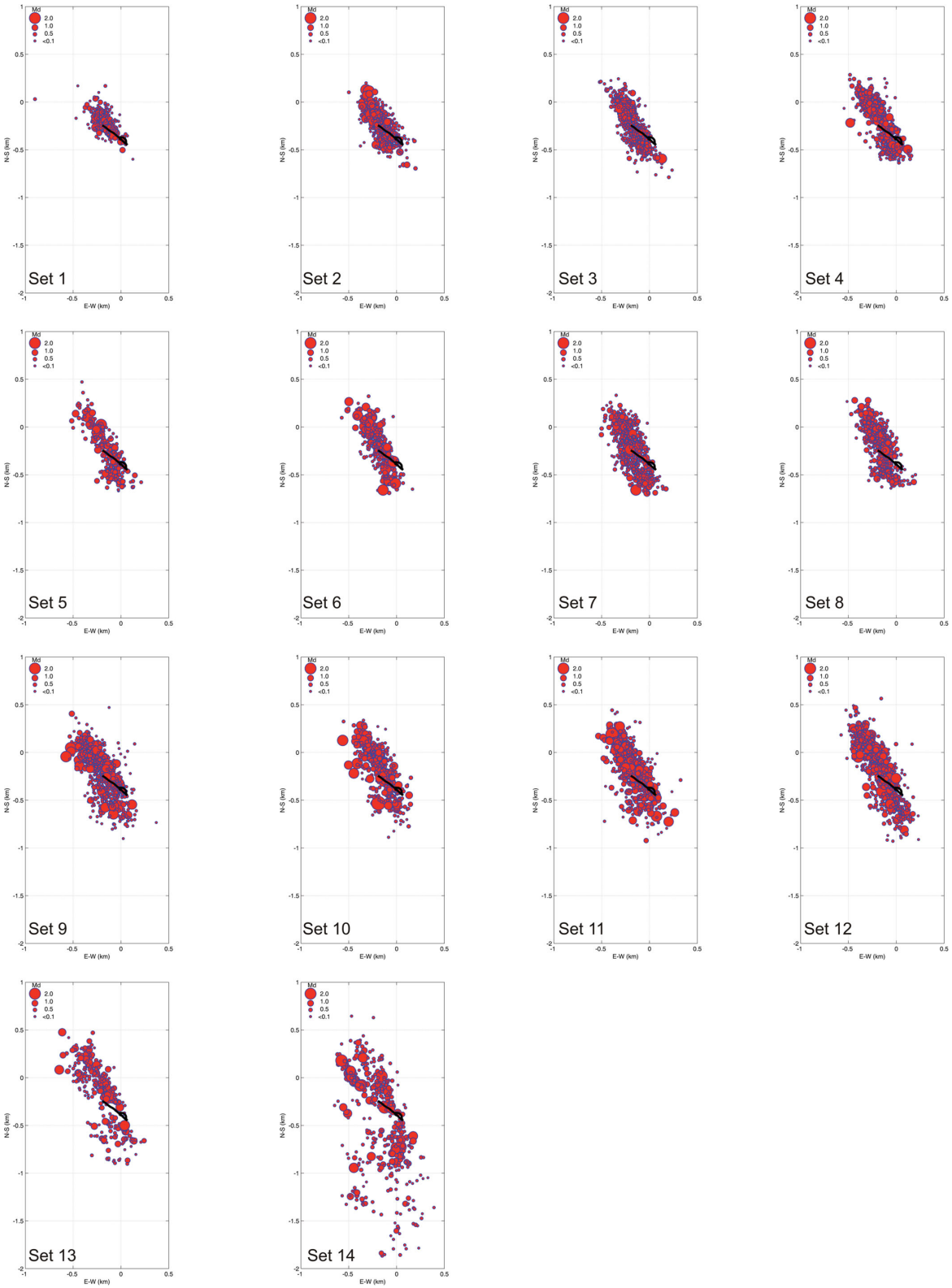

Figure B3. Evolution of the microseismic cloud recorded during the 2000 stimulation test (after Calò et al. 2011).

Identification of faults activated during the stimulation of the Basel geothermal project from cluster analysis and focal mechanisms of the larger magnitude events.

Submitted to the Geothermics special issue on induced seismicity, December 29, 2012

Revised, July 10, 2013

Nicholas Deichmann, Swiss Seismological Service, ETH Zürich, Sonneggstrasse 5, CH-8092 Zürich. deichmann@sed.ethz.ch

Toni Kraft, Swiss Seismological Service, ETH Zürich, Sonneggstrasse 5, CH-8092 Zürich. toni@sed.ethz.ch

Keith F. Evans, Engineering Geology, ETH Zürich, Sonneggstrasse 5, CH-8092 Zürich. keith.evans@erdw.ethz.ch

Key words: Enhanced Geothermal System (EGS); Induced Seismicity; High-Precision Hypocenter Locations; Activated Faults.

Abstract

High-precision relative location procedures of the stronger seismic events ($0.7 \leq M_L \leq 3.4$), based on cross-correlations of signals recorded by a six-sensor borehole network and numerous surface stations in the immediate epicentral area, show that clustering of hypocenters on different spatial scales is a dominant feature of the microseismicity induced by the stimulation of enhanced geothermal reservoir in Basel. In line with the fact that many of the observed earthquakes form clusters of similar events, several focal mechanisms are also nearly identical to each other. A comparison between the high-precision relative locations of the events within each cluster and the focal mechanisms often shows a good coincidence of the hypocentral distribution with one of the nodal planes of the focal mechanism. In some cases, the spatial extent of the individual clusters is limited to a few meters, which suggests that the corresponding events represent repeated slip with partial stress drop as pore pressures increase with time. In other cases, that include some of the stronger events ($M_L > 2$), the dimension of the individual clusters can amount to several 100 meters, and the activity within these clusters can extend over several days. Given that the orientation of many fault segments identified in this way deviates significantly from the overall orientation of the seismic cloud, these results reveal a complex internal structure of the flow paths in the rock volume stimulated by the water injection.

1. Introduction

To stimulate the reservoir for an Enhanced Geothermal System (EGS) initiated by a private/public consortium in the city of Basel, Switzerland, approximately 11,500 m^3 of water were injected at high pressures between December 2nd and December 8th 2006 into a 5-km-deep well below Kleinhüningen (Häring et al. 2008). Seismicity induced by the injections was monitored by regional networks of surface stations operated by national and state agencies, and by a dedicated six-sensor borehole network, installed by the operators. More than 10,500 seismic events were recorded during the injection and immediate post-injection phase. Hypocentral locations could be calculated for more than 3,000 of these events. The gradual increase in flow rate and wellhead pressure was accompanied by a steady increase in seismicity, both in terms of event rates and magnitudes. In the early hours of December 8th, after water had been injected at progressively higher flow rates up to 55 l/s and at wellhead pressures up to 29.6 MPa over a 16 hour period (Häring et al. 2008), a magnitude M_L 2.6 event occurred within the reservoir (Figure 1). This exceeded the safety threshold for continued stimulation, so that injection was stopped prematurely, and the well shut-in. In the afternoon and evening of the same day, two additional events of magnitude M_L 2.7 and 3.4 occurred within the same source volume. As a consequence, the well was opened and in the following days about one third of the injected water volume flowed back out of the well (Häring et al. 2008). Though the seismic activity declined rapidly thereafter, three more events with $M_L > 3$ occurred in January and February 2007, and sporadic lower-magnitude earthquakes are still being recorded in 2013.

This article presents the results of an ongoing analysis based mainly on the larger magnitude events that were induced by the stimulation of the reservoir. In this context, by "larger magnitude events" we mean all events that were recorded not only by the local borehole network installed by the project operators, but also by the regional seismometer and local surface accelerometer networks of the Swiss Seismological Service (SED) and the Landeserdbebendienst of Baden-Württemberg (LED). The goal is to examine the role that these larger events play in the stimulation process by mapping the faults on which they occurred. The temporal evolution of the seismic activity induced by the Basel geothermal project can be subdivided into three periods. The first from December 2nd to December 8th corresponds to the period of active stimulation and ends when the well was vented; 108 larger magnitude events, according to the definition given above, occurred in this first period. The second period, which lasted until the end of December 2006, is characterized by a steady decrease of activity, both in terms of magnitude and of number of events, as wellhead pressure declined due to the venting (Figure 1). Another 57 events occurred during this second period. The third began in January 2007 with a renewed increase in seismic activity that was followed by a gradual decline in spring and summer. By the end of November 2007, the regional networks had recorded a total of 195 seismic events with magnitudes between M_L 0.7 and 3.4 (Deichmann & Giardini, 2009). An additional M_L 0.6 event was recorded in 2010. Activity picked up again, with five more events with M_L between 0.9 and 1.2 in 2012 and an M_L 1.8 event on June 29th, 2013.

As already noted by several different authors (e.g. Asanuma et al. 2007, 2008, Dyer et al. 2010, Häring et al. 2008, Mukuhira et al. 2013), a substantial part of the seismicity induced by the stimulation of the Basel reservoir occurred in clusters of events with similar waveforms, or so-called families of similar events (also termed multiplets). This implies that the hypocenters of the events in each cluster must be located very close to each other and that

their focal mechanisms must be nearly identical. Very commonly, the hypocenters of events in such clusters are located on a plane that coincides with one of the nodal planes of their focal mechanism. In the present analysis, we take advantage of the high waveform similarity and apply a cross-correlation procedure between the signals of the different events to obtain precise relative arrival times. These arrival times serve as input for a master-event location technique to compute high-precision relative hypocenter locations that serve to resolve the structures such as planes on which the events are occurring. Planes identified in this way can be compared to the focal mechanisms of the events, which are based on first-motion polarities observed at both the local borehole seismometers and the regional surface networks.

2. Tectonic setting

Basel is located at the southern end of the Rhine Graben, where it intersects the fold and thrust belt of the Jura Mountains of Switzerland (Figure 2 and Figure 1 of Valley & Evans 2009). As such, it is an area that, in the geologic past, has seen both extension (rifting phase of the Rhine Graben) and thrusting (folding of the Jura Mountains). A recent comprehensive summary of the evolution of the Upper Rhine Graben and Jura Mountains through geologic time, together with an exhaustive reference list, can be found in Ustaszewski & Schmid (2007). The borehole itself is situated at the southern end of the Rhine Graben and reaches a depth of 5 km below the Earth's surface. As shown in the lithological section reproduced in Häring et al. (2008) and in Valley & Evans (2009), it penetrates a 2426 m thick sedimentary sequence before entering the crystalline basement.

Focal mechanisms in the Southern Rhinegraben, the Black Forest and northern Switzerland south of Basel, are dominated by strike-slip and normal faulting mechanisms (e.g. Kastrup et al. 2004, Plenefisch & Bonjer 1997). The average value for the direction of the regional maximum compressive horizontal stress, S_{Hmax}, calculated by Kastrup et al. (2004) from the focal mechanisms in the southern Rhinegraben region and in the central part of northern Switzerland, using two different inversion methods, is about 144 degrees. This value is identical to the average local S_{Hmax} in the crystalline basement derived from measurements in the 5 km deep Basel borehole by Valley & Evans (2009). Terakawa et al. (2012) obtain a strike-slip stress field from an analysis of 118 focal mechanisms of the seismicity induced by the Basel EGS with directions of the principle axes that match the borehole oservations of Valley & Evans (2009) to within a few degrees.

3. Seismic networks

The seismic data available for the Basel geothermal project and analyzed in this article were recorded by several different seismometer and accelerometer networks operated by three separate institutions: the Swiss Seismological Service (SED), Landeserdbebendienst Baden-Württemberg (LED) and Geothermal Explorers Ltd. (GEL). The locations of stations are shown in Figure 2. The network included a six-sensor borehole network installed by GEL around the project site at depths between 317 and 2,740 meters. Detailed documentation of the instruments and digital data acquisition systems can be found in the articles by Deichmann and Ernst (2009) and Deichmann and Giardini (2009). It should be noted that accelerometers at epicentral distances of a few kilometres installed at the Earth's surface in the middle of a noisy city such as Basel can provide good-quality data, even for events with magnitudes $M_L < 1$.

4. Data analysis

4.1 Magnitudes

The magnitudes of the events induced by the stimulation of the Basel reservoir have been determined by several different institutions and other special studies. A review of all of these different magnitudes is beyond the scope of this article. Here we document just those that are used in this study. The local magnitudes, M_L, were determined by the Swiss Seismological Service, SED, from the records of the Swiss national broad-band network, SDSNet, and are thus available only for the 202 events recorded by the regional networks. As discussed in detail by Deichmann and Giardini (2009), their individual uncertainty is about 0.2 magnitude units. Moment magnitudes, M_w, for the events recorded by the regional networks were calculated by Bethmann et al. (2011). These values are derived from fitting a theoretical far-field source spectrum to the displacement spectra of the P- and S-waves recorded at both the borehole- and surface stations following the method outlined in Abercrombie (1995). The spectra of events whose focal mechanisms were known at the time were corrected for the effects of the radiation pattern. The spectra of the other events were corrected with an average radiation coefficient. Taking into account the variability of all parameters that enter into the computation of M_w, the uncertainty of the individual M_w estimates is on the order of 0.25. We use these M_w values for all events that were recorded by the regional networks. A similar procedure was used by GEL to compute M_w for the entire dataset of locatable events. They applied the same spectral fitting method to P- and S-waveforms from four of the borehole sensors (OTER2, RIEH2, HALTI and MATTE) after rotating them into their principal component directions (T. Spillmann, personal communication). This is the procedure mentioned in the article by Dyer et al. (2008). For the subset of events used in this study that were recorded only by the borehole network, we use the median value of the GEL M_w estimates from the four stations. The resulting catalogue of moment magnitudes is also the basis for the statistical studies of Bachmann et al. (2011 and 2012), and was used to calibrate the absolute seismic moments for the stress drop mapping of Goertz-Allmann et al. (2011). A comparison of these M_w estimates derived from the four borehole sensors with those determined by Bethmann et al. (2011) from the regional network stations shows that on average they differ only by 0.03, with a standard deviation of 0.1.

4.2 Overall master-event relocation

The starting point for the present analysis is the set of hypocenter locations documented in the article by Deichmann and Giardini (2009). These locations are the result of a master-event technique based on visually determined arrival times, obtained mainly from the seismograms recorded by the six borehole seismometers. Although all these events were recorded also by the regional networks, we chose to restrict the input of the master-event relocations to the arrival times of the borehole network so as to ensure a maximum location consistency over the entire data set. In this procedure, the travel-time residuals of a chosen master-event are used as station corrections for locating the hypocenters of all other events. As master-event, we chose an event (2006/12/03 19:51 UTC, M_L 1.7) that was recorded also by a seismometer temporarily deployed close to the bottom of the injection borehole. The event location was fixed at the location obtained by GEL using a 1-D velocity model with station corrections (Häring et al. 2008). The mean standard deviations of the locations obtained in this way are on the order of 50 m horizontally and 70 m vertically (Deichmann and Giardini, 2009). Figure 3 shows an updated version of the resulting hypocenter locations. The changes to the earlier Figure 5 in Deichmann and Giardini (2009) are the following: (1) in the course of evaluating

additional fault-plane solutions, the arrival times of some of the events have been revised. However, in most cases, the shift in locations was less than the calculated uncertainties. A notable exception, discussed in more detail later in this article, is the deepest hypocenter in the original figure, which shifted upwards by 200 m; (2) for those events which have been identified as belonging to a cluster of similar events, we show the locations that were refined in the course of this study, as explained in the following sections; (3) the size of the circles is now scaled using the moment magnitudes (M_w) calculated by Bethmann et al. (2011), instead of converting the M_L values to M_w (for better comparison with the original figure, we have assumed the same stress drop of 10 MPa); (4) we have added the seven events recorded in 2010, 2012 and 2013. Note that the two events of February 26th 2010 and May 20th 2012 as well as the three events which occurred between December 12th and 15th 2012 and the event of June 29th 2013 are located in the same region as the events which occurred towards the end of 2007 (i.e. above the casing shoe, at the southern periphery of the seismic cloud), whereas the event of October 3rd 2012 is located about 400 m below the casing shoe and about 400 m to the east of the main microseismic cloud. Due to the removal of three of the borehole sensors, location uncertainties for the five events of 2012 and of the event of 2013 are about twice as large as for the earlier events. However, with computed standard deviations of 76 m (EW), 147 m (NS) and 67 m (Z), the outlier location of the event of October 3rd 2012 is well constrained.

In what follows, we concentrate our analysis on the 165 events recorded by the regional networks during the stimulation and immediate post-stimulation periods between December 2nd and December 31st, 2006. In addition, with these data we merge those events that were recorded only by the borehole network and that were identified by Kraft & Deichmann (2013) as belonging to one of the larger clusters.

4.3 Cluster definition

Figure 4 shows a typical example of similar seismograms of a set of events that belong to the same cluster, recorded on one channel of a borehole seismometer. A common procedure to identify seismic events that belong to a common cluster is based on an analysis of the cross-correlation coefficients between signals of different events recorded at a given station. However, both the threshold of the cross-correlation coefficient for including or excluding an event from a given cluster and the filters used to limit the frequency bandwidth for the cross-correlation are somewhat arbitrary. Higher signal frequencies and higher correlation coefficients are more restrictive than lower frequencies and a lower threshold. A restrictive choice finds only clusters with highly similar signals and thus with source locations that are so close to each other that within the obtainable location precision it can be impossible to identify a planar distribution of hypocenters. A less restrictive choice, on the other hand, tends to increase the spatial extent of the clusters, but entails the risk of associating events that actually do not share a common source structure. Consequently, the choice of the appropriate parameters depends on the goal of the analysis and should be made by an iterative trial and error procedure, based on visual inspection of the signals, on a comparison with the available focal mechanisms and on the resulting relative locations. For our purpose, we found that the correlation in the time domain of the signals recorded by the A-component of the borehole station OTER1 and a correlation coefficient threshold of 0.9 produced a useful initial cluster selection. The signals used for the cross-correlations included both the P- and the S-phase and were filtered with a causal 2nd order Butterworth band-pass filter between 1 and 20 Hz. In some cases, visual inspection of the signals and comparisons with the corresponding focal mechanisms showed that the clusters obtained in this way needed to be split into two or more

sub-clusters. In other cases, two families that were identified as being separate based on the chosen correlation threshold, in the end could be grouped under the same cluster. The results presented in this article concern 11 clusters containing a minimum of 3 and a maximum of 13 events recorded by the regional seismograph networks.

4.4 Relative locations of events within each cluster

The next step consists of choosing a master-event for each of the eleven identified clusters and of performing signal cross-correlations between all pairs of events in each cluster. As master we chose an event that is recorded by a large number of stations and with a signal frequency most similar to that of the other events in the cluster. Consequently, the magnitude of the master-event is roughly in the middle between the minimum and maximum magnitude in a given sequence. As shown in Figure 5, these correlations are performed separately for the P- and S-phases recorded at each station. The signal lengths used for the correlations are chosen long enough for a stable result and short enough to include only the direct P- or S-waves. For all the clusters documented in this report, we used signals recorded by the borehole sensors as well as by surface seismometers and accelerometers at epicentral distances out to 40 km. As explained in the Appendix to the article by Deichmann and Garcia-Fernandez (1992), the multiple and thus redundant cross-correlations constitute a quality check of the correlations and allow one to compute least-squares adjusted travel-time differences between the master-event and each other event in the given cluster. The relative timing precision obtained by means of this procedure is on the order of 1-2 ms. By nature of the algorithm, cross-correlations align the maxima and minima of two signals. For events with large magnitude differences and consequently with different dominant signal frequencies, the resulting alignment of the signals does not always correspond to the phase onsets. For the same reason, to guarantee consistency over all stations, acceleration traces must always be integrated to velocity before correlation.

The locations of the individual events within a given cluster relative to the corresponding master event are calculated with an algorithm proposed by Console and DiGiovambattista (1987). It is based on the fact that, for hypocenters which scatter over a volume that is very small relative to the distances to the recording stations, the angles at which the rays leave the source to each station are essentially the same for all events. As a consequence, the otherwise non-linear earthquake location problem becomes linear. Given a set of take-off angles for the master-event, the only seismic velocities that affect the results are the P- and S-velocities in the immediate source volume, and their uncertainties contribute only little to the final location error. With more than 20 travel-time differences for each event and a precision of 1-2 ms, the computed standard relative location errors are on the order of 2-6 m. However, it should be noted that for some of the stronger events, the actual error might be larger than this. As explained in the previous paragraph, the reason is that correlations, rather than representing differences in onset times, match the arrival times of the most energetic part of the P- or S-phase. Whereas the hypocenter is defined as the single point on the fault where the rupture initiates, the most energetic waves radiated during the rupture process emanate from a broader area, which for larger events is not necessarily the same for stations that see the fault from different directions. Such effects might lead to additional errors that are not accounted for in the standard errors computed by the location algorithm.

4.5 Focal mechanisms

All focal mechanisms in this study are determined from first-motion polarities observed both at the borehole stations and at the stations of the surface networks. The adopted procedure to calculate the take-off angles in the presence of the very heterogeneous seismic velocities below Basel is documented in detail in the publication by Deichmann and Ernst (2009). This earlier publication presents the focal mechanisms of the 28 strongest events. In contrast, the data set underlying the present study comprises more than 150 events and includes also events with $M_L < 1$. Of course, for these weaker events, the number of reliable first-motion data points is smaller than for the stronger events, so the range of possible nodal-plane orientations and consequently also the uncertainty of the mechanism are larger. In principle, we would consider a possible variability of more than 10 degrees in strike and dip of the nodal planes for a given distribution of first-motion points as too unreliable for an independently determined focal mechanism. However, in cases where these smaller events have essentially identical waveforms as a larger event with a well-constrained fault-plane solution, and are thus part of the same event family, the focal-mechanism parameters of the smaller event can be considered equal to those of the corresponding larger event. In this way we can assign a reliable focal mechanism to these small events as well. Note also that in the course of this study some of the previously published focal mechanisms have been revised, so that in some cases the corresponding parameters are slightly different.

5. Results

5.1 Identification of the activated faults

The locations and focal mechanism solutions of the events in each of the 11 clusters are listed in Table A.1 in the Appendix, that is included as online resource to this article. The clusters are named either after their strongest event or after the corresponding master event. As an example of the steps leading to the final result, we present details of the analysis of Cluster 14/15, illustrated in Figures 4 through 7. The initial cross-correlation of all seismograms recorded at station OTER1 actually identified the nine events of this cluster as pertaining to two separate event families, denoted as Clusters 14 and 15. In fact, as shown in Figures 4 and 6, at some stations the polarities of the P-onsets for Events 3 and 15 are opposite to the polarities of the other events. Moreover, in Figure 4, the amplitude of the P-phase of Event 8 is smaller than for the other events with downward polarity. In fact, Events 3, 8 and 15 constitute Cluster 15, while the others constitute Cluster 14. As a consequence, the SW-NE trending nodal planes of the focal mechanisms of the three events in Cluster 15 have a slightly different dip than the corresponding nodal planes of the events in Cluster 14 (see Figure 6 and Table A.1). However, the strike and dip of the SE-NW trending nodal plane is identical for all events in both clusters. Event number 1 in Figures 4 and 5 was chosen as the master event for the cross-correlations and for the computation of the relative locations of the hypocenters. The correlations provide precise travel-time differences for 29 to 33 P- or S-arrivals for each event, and the mean travel-time residuals calculated by the relocation algorithm are on the order of 1-2 ms. This is consistent with the mean relative arrival-time errors of 1-2 ms estimated from the least-squares adjustment of the travel-time differences determined by means of the signal cross-correlations (see Section 4.4). Based on these estimates of the relative arrival-time errors, the computed location uncertainties of the hypocenters relative to the master event are on the order of a few meters (single standard deviation). This has also been verified in numerous cases by so-called Monte Carlo simulations, in which the events were relocated several hundred times with the relative arrival times perturbed by the assumed timing errors. The results of the relocations are shown on an epicenter map and two vertical cross-sections in Figure 6. The hypocenters group into two distinct sub-clusters whose

members coincide precisely with Clusters 14 and 15, which exhibit the subtle differences in focal mechanism parameters described above. Within each sub-cluster, the hypocentral locations scatter over a very small volume. For sub-cluster 14, the scatter is +/-1 m in x-direction, +/-5 m in y-direction and +/-9 m in z-direction, whereas for sub-cluster 15, it is +/-1 m in x-direction, +/-2 m in y-direction and +/-4 m in z-direction. Thus, taken individually, it is not possible to resolve the active fault plane from the relative locations within the two sub-clusters. However, the two sub-clusters are displaced from each other by about 50 m along a line that matches the strike of the NW-SE striking nodal plane almost perfectly. If one assumes that the signal similarity of these events is evidence for their occurrence on a single common fault, then these events occurred as dextral strike-slip motion on an approximately NW-SE striking near-vertical fault.

An alternative way of visualizing the results for the example of Cluster 14/15 is shown in Figure 7. In this figure, we have supplemented the nine events of the cluster that were recorded by both surface and borehole stations (i.e. the events shown in Figures 4 through 6) with a further 15 events that were recorded only by the borehole network (see Table A.1). The latter were identified as being part of Cluster 14/15 on the basis of a similar analysis documented in Kraft & Deichmann (2013). In Figure 7, each event is represented by a circle with strike and dip of one of the nodal planes of the focal mechanism and a size equal to an estimate of its source radius. For an assumed circular fault patch that ruptures with a constant static stress drop, the latter is proportional to the cube-root of the seismic moment divided by the cube-root of the stress drop. The seismic moment of the events recorded by the regional networks was estimated from the moment magnitudes computed by Bethmann et al. (2011), whereas for the events recorded only by the borehole network we use the M_w values computed by Spillmann (personal communication), that are mentioned in Dyer et al. (2008). For the stress drop, we arbitrarily assume a constant value of 3 MPa for all events. This is close to the mean value obtained by Goertz-Allmann et al. (2011). Since the stress drop enters into the computation of the source radius as the cube root, actual deviations from these assumptions have only a relatively small effect on the source radius estimate. For example, adopting a value of 1 MPa would imply a source radius that is 1.4 times larger, and a value of10 MPa would yield a radius estimate that is 1.5 times smaller. So, despite the arbitrariness of the assumptions and the uncertainties of the actual values of seismic moment and stress drop, plots such as those in Figure 7 provide useful insight into the geometry of the potentially active structures.

In the case of Cluster 14/15 shown in Figure 7, the rupture areas of the NW-SE striking nodal planes with almost identical strike and dip of the nine events coalesce within one or two standard errors of the locations onto a single plane, while the alternative nodal planes would correspond to two or three separate faults up to 50 m apart. Given the two alternatives and in view of the fact that the seismograms recorded at most stations are almost identical for all nine events, it is more likely that their sources lie on the same fault (even though their rake is slightly different) rather than on two completely separate faults that happen to have exactly the right orientation to produce nearly identical signals. It is also highly unlikely that the events occurred on two or three separate faults with a rake such that the auxiliary nodal plane is common to all events and matches almost perfectly the planar distribution of their hypocenters. Thus in this case, the NW-SE striking nodal planes are considered to represent the fault that was activated during these events.

In Figures A.1 through A.8 in the Appendix included as online resource to this article, we show the evidence for the identification of the nodal planes that correspond to the activated faults of eight of the other nine clusters. The cluster, which includes the M_L 3.4 main-shock is

discussed in more detail at the end of this chapter (Figures 8, 9 and 10). The underlying criteria for choosing one nodal plane rather than the other as the active fault plane are, firstly, a nearly identical strike and dip for all events in the cluster and, secondly, the tightness of the cluster when viewed along the strike of the nodal planes.

For Cluster 14/15, discussed above, the scatter of hypocenters from the best-fitting plane oriented parallel to the chosen nodal plane is less than 10 m, whereas selection of the other nodal plane as the fault plane would lead to a scatter of about 50 m. Similar conclusions apply for clusters 43 and 87, shown in Figures A.1 and A.2. As can be seen in Figures A.3 through A.6, for Clusters 30, 39, 88 and 102, the chosen planes lie less than 20 m from all events, whereas the separation is more than 80 m for the alternatives. Thus for these six clusters, the criteria mentioned above clearly favor the chosen nodal plane rather than the other.

In the case of Cluster 5, shown in Figure A.7, the hypocenters extend over a volume of 5 x 8 m horizontally and 20 m vertically (including location uncertainties). This is so small that the distance over which the hypocenters scatter is the same in all directions. However, the distribution of the hypocenters with depth aligns more closely with the near-vertical E-W striking nodal plane than with the inclined N-S striking plane. So it is the former that is identified as the active fault plane.

As shown in Figure A.8, the nodal planes of the focal mechanisms of the events in cluster 135 strike either more or less E-W with a near-vertical dip or N-S with a dip of about 45 degrees to the W. Viewed along strike of the more or less E-W striking fault planes, the hypocenters scatter over more than 200 m. This would imply that practically each event occurred on a separate fault, which is highly unlikely considering the similarity of the signals. Viewed along the N-S striking nodal planes, the hypocenters extend down-dip for more 200 m and across dip over about 40 m. Though the latter is more than the expected location error, it is more likely that the N-S striking nodal planes correspond to the active fault. It is also possible that this cluster consists of two or three parallel en-echelon fault segments with offsets of 10-20 m.

Cluster 82, named after its master event, includes the M_L 3.4 main-shock of December 8th 2006. According to the relative locations of Deichmann and Giardini (2009), which are based only on cross-correlations of the six borehole stations, the active fault strikes WNW-ESE and dips with about 75 degrees towards the SSW. In the present study, this cluster was reanalyzed using also the data of the surface stations and including an additional event recorded by the regional networks (Event 113 in Table A.1) as well as seven events recorded only by the bore-hole sensors. Deichmann and Giardini (2009) already noted that the focal mechanisms of the events in this cluster are not identical. The focal mechanism differences, illustrated here in Figures 8 and 9, could be symptomatic of the fact that these events do not all lie on a single planar structure. Indeed, the results of the reanalysis suggest that this cluster, as shown in Figures 9b and 10a, consists of four more or less parallel faults that span a distance of about 50 m. Nevertheless, the fault-plane identified by Deichmann and Giardini (2009) is still judged to be the more likely fault, since, viewed along the strike of the alternative nodal plane, shown in Figures 9c and 10b, the scatter of the events is more than twice as large (125 m), so that even the events with the most similar signals do not come to lie on a common fault segment. A similar conclusion was reached by Kahn (2008) from the results of an overall double-difference relocation based on the records of the borehole stations alone.

The fault planes chosen for each cluster are shown in map-view in Figure 11 and in two perspective plots in Figure 12. For illustrative purposes, the individual faults are represented by a rectangle. The dimensions of each rectangle correspond to the down-dip and along-strike

extent of the cluster as a whole, as outlined by the sum of the rupture areas of all events in the cluster. The strike and dip of each plane are equal to those of the identified fault-plane from the focal mechanism of a representative event in each cluster and are listed in Table A.1.

5.2 Temporal evolution of the activity on each fault

The time of occurrence and the temporal evolution of each cluster are shown in Figures 13 and 14. For the sake of clarity, the two sub-clusters of Cluster 14/15 are shown separately, although the evidence implies they occurred on a single fault. Figure 13 shows the events not only as a function of time but also as a function of radial distance from the casing shoe. As expected from the temporal occurrence and spatial distribution of the entire sequence of induced events (e.g. Asanuma et al. 2007, Deichmann and Giardini 2009), the clusters closest to the injection well were active at the beginning of the injection (Clusters 14/15, 5 and 43), while those furthest away from the well became active towards the end of the injection (Clusters 88 and 102) or even after the beginning of bleed-off (Cluster 135). The increase in distance from the injection well with time is also visible as a general trend within several individual clusters (30, 39, 43, 82, 87 and 88). However it is noteworthy that in some clusters the occurrence of individual events is highly erratic, with consecutive events jumping back and forth between distinctly different locations on the fault (Clusters 39, 82, 102, 88 and 135). Both the overall growth of the cluster and the erratic activation in space and time are evidence of the fact that many of the events within a particular cluster represent rupture of different patches of a common fault rather than repeated slip of the same patch. On the other hand, the events in cluster 5, sub-clusters 14 and 15 as well as the early activity of cluster 43 seem to be concentrated in one spot and thus must correspond to repeated slip of the same fault patch. That such repeating-slip events seem to occur preferentially in the clusters close to the well and in the early phase of the injection makes sense: it is that part of the stimulated reservoir that experienced the greatest increase in fluid pressure. This last observation can be seen more clearly in Figure 14, where we plot the temporal evolution of each cluster together with the cumulative number of all events recorded by the bore-hole sensors as well as the time series of well-head injection pressure and flow rate. Thus repeated slip of the same fault patch can be explained by the occurrence of events that relieve only a fraction of the pre-existing shear stress (partial stress-drop events) and by a successive weakening of the fault as the effective stress decreases with increasing fluid pressure in the fractures. At larger distances from the well, the fluid pressure changes with time are expected to be smaller, so that conditions for repeated slip of the same patch are less favorable.

6. Comparison with previous studies

That a large proportion of the seismicity induced by the stimulation of the Basel EGS occurred in clusters and that the consequent signal similarity can be exploited to obtain high-precision relative hypocenter locations has been recognized in several previous studies (e.g. Asanuma et al. 2007, 2008, Dyer et al. 2010, Häring et al. 2008, Mukuhira et al. 2008, 2013) and is also the topic of the article by Kraft & Deichmann, (2013, this issue). A comparison between the different studies is difficult, because the degree of clustering found in each analysis depends strongly on the chosen signal processing parameters and similarity criteria that were employed for associating the individual events. This is illustrated in the article by Asanuma et al. (2008), who apply a coherence analysis over a low and a high frequency range and obtain very different cluster sizes and distributions. In practice, the choice of correlation parameters and filters is a function of what one is searching for: a high similarity threshold in

a high frequency range applied to all event and station pairs will produce many small clusters, whereas a low similarity threshold for low-pass filtered signals will produce fewer large clusters. Whether the chosen parameters make physical sense cannot be decided a priori, but requires additional information such as focal mechanisms. In addition, a direct comparison with other studies is also hampered by poor documentation of the actual seismic events that comprise the identified clusters.

In a preliminary analysis, Häring et al. (2008) found four multiplets that they associate with a then available focal mechanism. One of these matches one of the clusters analyzed in the present study. It is identified by the M_L 1.7 event of 2012/12/03 19:51, which corresponds to the master event of our cluster number 5. In their Figure10, they show a NNW-SSE trending alignment of epicenters, which they associate with this cluster and which they interpret as evidence for the activation of the N-S striking fault-plane of the corresponding focal mechanism. This is contrary to the results of our analysis. As shown in Figure A.7, the hypocenters of the seven events that we could associate to this cluster are restricted to a volume of 5 x 8 x 20 m and their relative locations are more compatible with the repeated activation of the E-W rather than of the N-S striking fault-plane. Unfortunately, Häring et al. (2008) specify neither what their estimate of their location uncertainty is, nor whether the relative arrival times were picked by eye or by some form of signal cross-correlation. Lacking information that identifies the other events in their cluster, it is not possible to determine whether they match the events that we have associated with our cluster number 5.

Dyer et al. (2010) present results of systematic signal cross-correlations of all events that could be located by the borehole network. The goal of their study was to find the smallest number of clusters that would cover most of the observed events and to improve the location precision of the events associated to their clusters. However, they treated each event as a point source without a magnitude-dependent rupture area and did not attempt to relate the clusters that they found to the published focal mechanisms. Without information about the actual events in each cluster, it is not possible to compare their results with ours. Nevertheless, the structure that dips towards the SW, mentioned by Dyer et al. (2010) and shown in their Figures 11 and 12, could correspond to the normal faults activated by our clusters 39 and 43.

The clustering properties of the seismicity induced by the stimulation of the Basel EGS have also been studied in some detail by the research group at Tohoku University. Most of the results of their work has been published in various conference proceedings (e.g. Asanuma et al. 2007, 2008; Mukuhira et al. 2008). More recently, results of their analysis of the larger-magnitude events have appeared as a research paper in Geothermics (Mukuhira et al. 2013). Asanuma et al. (2008) show two hypocenter plots of the multiplets that they found based on a coherence analysis in two different frequency ranges. From a plot of the occurrence in time of their clusters, similar to our Figure 14, they conclude that the clusters located close to the injection well were active only during the stimulation phase, while the more distant clusters were activated at a later stage and remained active after the well had been vented. However, they do not establish any link between their clusters and the focal mechanisms of the larger events, nor do they draw any conclusions from the distribution of their clusters regarding the orientation of the activated structures. Mukuhira et al. (2013) define larger-magnitude events as those with $M_w \geq 2$. Although Mukuhira et al. (2013) do not list which events meet this criterion, it is possible to identify them from Figure 3 in Mukuhira et al. (2008). According to them, only nine events have an $M_w \geq 2$. This is due to the fact that their M_w is an early version of the M_w calculated in the time-domain by Semore Seismic Ldt. and mentioned by Dyer et al. (2010, in connection with their Figure 9), and not the spectral M_w determined by Geothermal Explorers Ltd. and mentioned in Dyer et al. (2008 and 2010, in connection with

their Figure 2). On average over the nine events in Mukuhira et al. (2008), the time-domain Mw values are 0.31±0.32 units lower than the spectral M_w values. With the latter, 24 events would have an $M_w \geq 2$. The low M_w values used by Mukuhira et al. (2013) are one of several reasons for their abnormally low stress drops, compared for example to those of Goertz-Allmann et al. (2011).

7. Discussion and conclusions

The primary objective of this paper is to extract information relevant to defining the structures on which seismicity is occurring during the stimulation process from an analysis of waveforms of the "larger magnitude events" detected by the regional surface networks around Basel as well as the borehole stations. The analysis includes events as small as M_L 0.7.

Examination of waveform similarity revealed eleven earthquake clusters with at least three events each. These collectively include more than half of the events induced between December 2nd and 31st by the stimulation of the reservoir and recorded by the surface networks. Precise relative relocation of the events within each cluster allowed the geometry of the seismogenic volume to be constrained. This, combined with the well constrained focal mechanism solution that is available for all clusters, allowed the active fault plane to be identified with good confidence.

The spatial pattern of events for each cluster scatters closely about a plane. In most cases, the scatter is comparable to two standard deviations in the relative location error, which are on the order of 10 m. Thus, with the exception of Clusters 82 and 135, the analysis did not reveal any substantial thickness to the structures on which the seismicity was occurring, such as reported by Moriya et al. (2002) and Evans et al. (2005) from similar analyses of seismicity in the Soultz reservoir.

The locations together with rough estimates of source size for each event define faults with dimensions between less than 100 m and several hundred meters. Accepting that the microseismic cloud as a whole is near-vertical and has a predominant NNW-SSE orientation, we note that, except for Clusters 88 and 102, the strike or dip of the identified faults deviate more or less strongly from this overall orientation. The concept of a single fault zone with a more or less constant orientation is obviously too simplistic. This has important consequences for models of fluid migration during stimulation and thus for the process of permeability enhancement as well as for seismic hazard assessments.

Except in the case of Cluster 88, which was active for only 24 hours, activity in each individual cluster spans several days. The two sub-clusters 14 and 15 as well as cluster 5, which are the closest to the borehole, were active only in the first three days of the stimulation and included only smaller events (M_L between 0.8 and 1.7). Moreover the events in each of these three clusters are so closely co-located and their signals are so similar that they must represent repeated slip on exactly the same fault patch. This is only possible if each event releases merely a fraction of the total stress drop and each fault patch is repeatedly reactivated, as it is increasingly weakened due to the fluid pressures rising with time. Activity of other clusters is due to a combination of repeated slip on the same fault patches and activation of neighboring patches on the same fault. It is important to note that, of the 11 multi-event clusters analyzed in this study, only cluster 135 occurred entirely during the post-stimulation period. Moreover, among the 30 earthquakes recorded by the surface networks in 2007, the same selection criteria as applied to the events of December 2006 found only two event-doublets and not a single larger cluster. Evidently, the propensity of seismic activity to

occur as clusters of similar events is considerably enhanced by the injection of fluids at pressures that increase with time.

The evidence strongly suggests that the two sub-clusters of events in cluster 14/15 lie on a single fault plane. However, the focal mechanisms of the two sub-clusters imply that the rake of the slip direction differs by 15° (Table A.1). If the shear strength within the fault plane is isotropic, then this observation implies that the shear stress resolved in the plane of the fault differs by 15° in the region of the two clusters that are separated by about 50 m. The clusters were active at the same time (Figure 13), and so the difference in rake angles is interpreted as reflecting natural stress heterogeneity, rather than stress changes resulting from stress transfer.

The still ongoing detailed analysis of the seismicity induced by the stimulation of the Basel Enhanced Geothermal System will be expanded to include also the events that occurred in 2007 during the post-stimulation period.

Acknowledgements

A large part of this study was undertaken in the context of project GEOTHERM, funded by the Competence Center for Environment and Sustainability (CCES) of ETH, and constitutes an in-kind contribution to the GEISER project. Access to the borehole data of Geopower Basel, acquired by Geothermal Explorers Ltd. (GEL), is gratefully acknowledged. Special thanks to T. Spillmann (GEL) for computing the moment magnitudes based on the data from the borehole network. We are also grateful to W. Brüstle and S. Stange at the Landeserdbebendienst Baden-Württemberg in Freiburg for the seismic data recorded by their permanent network and temporary stations in southern Germany.

References

Abercrombie, R. 1995. Earthquake source scaling relationships from −1 to 5ML using seismograms recorded at 2.5 km depth. Journal of Geophysical Research, 100, 24015 – 24036.

Asanuma, H., Kumano, Y., Hotta, A., Niitsuma, H., Schanz, U., Haring, M., 2007. Analysis of microseismic events from a stimulation at Basel, Switzerland. Transactions of the Geothermal Resources Council 31, 265–270.

Asanuma, H., Kumano, Y., Niitsuma, H., Schanz, U., Haring, M., 2008. Interpretation of reservoir structure from super-resolution mapping of microseismic multiplets from stimulation at Basel, Switzerland in 2006. Transactions of the Geothermal Resources Council 32, 65–70.

Bachmann, C. E., Wiemer, S., Woessner, J., Hainzl, S. 2011. Statistical analysis of the induced Basel 2006 earthquake sequence: introducing a probability-based monitoring approach for Enhanced Geothermal Systems. Geophysical Journal International 186, 793–807.

Bachmann, C. E., Wiemer, S., Goertz-Allmann, B. P., Woessner, J. 2012. Influence of pore-pressure on the event-size distribution of induced earthquakes. Geophysical Research Letters 39, L09302, doi:10.1029/2012GL051480.

Bethmann, F., Deichmann, N., Mai, M. 2011. Scaling relations of local magnitude vs. moment magnitude for sequences of similar earthquakes in Switzerland. Bulletin of the Seismological Society of America 101, 2, 515–534, doi:10.1785/0120100179.

Console, R., DiGiovambattista, R., 1987. Local earthquake relative location by digital records. Physics of the Earth and Planetary Interior 47, 43–49.

Deichmann, N., Ernst, J. 2009. Earthquake focal mechanisms of the induced seismicity in 2006 and 2007 below Basel (Switzerland). Swiss Journal of Geosciences 102/3, 457-466, DOI: 10.1007/s00015-009-1336-y.

Deichmann, N., Giardini, D. 2009. Earthquakes induced by the stimulation of an Enhanced Geothermal System below Basel (Switzerland). Seismological Research Letters 80/5, 784-798, doi:10.1785/gssrl.80.5.784.

Deichmann, N., Garcia-Fernandez. M. 1992. Rupture geometry from high-precision relative hypocenter locations of microearthquake clusters. Geophysical Journal International 110, 501-517.

Dyer, B. C., Schanz, U., Ladner, F., Häring, M. O., Spillmann, T. 2008. Microseismic imaging of a geothermal reservoir stimulation. The Leading Edge 27, 856-869.

Dyer, B. C., U. Schanz, T. Spillmann, F. Ladner, and M. O. Häring, 2010. Application of microseismic multiplet analysis to the Basel geothermal reservoir stimulation events. Geophysical Prospecting, 58, 791–807, doi: 10.1111/j.1365-2478.2010.00902.x.

Evans, K.F., Genter, A., Sausse, J. 2005. Permeability creation and damage due to massive fluid injections into granite at 3.5 km at Soultz: Part 1 - Borehole observations. Journal of Geophysical Research 110, 19.

Goertz-Allmann, B. P., Goertz, A., Wiemer, S. 2011. Stress drop variations of induced earthquakes at the Basel geothermal site. Geophysical Research Letters 38, L09308, doi:10.1029/2011GL047498.

Häring, M. O., Schanz, U., Ladner, F., Dyer, B. C. 2008. Characterization of the Basel 1 Enhanced Geothermal System. Geothermics 37, 469-495, doi:10.1016/j.geothermics.2008.06.002.

Kahn, D. S. 2008. Hydro-fractured reservoirs: A study using double-difference location techniques. Ph.D. Thesis, Dept. of Earth and Ocean Sciences, Duke University, 163 pp.

Kraft, T., Deichmann, N. 2013. High-precision relocation and focal mechanism of the injection induced seismicity at the Basel EGS. Submitted to Geothermics.

Kastrup, U., Zoback M.-L., Deichmann, N., Evans, K., Giardini, D., Michael, A. J. 2004: Stress field variations in the Swiss Alps and the northern Alpine foreland derived from inversion of fault plane solutions. Journal of Geophysical Research 109/B1, doi:10.1029/2003JB002550B01402.

Moriya, H., Nakazato, K., Niitsuma, H., Baria, R. 2002. Detailed fracture system of the Soultz-sous-Forêts HDR field evaluated using microseismic multiplet analysis. Pure and Applied Geophysics 159, 517–541.

Mukuhira, Y., Asanuma, H, Niitsuma, H., Häring, M. O. 2013. Characteristics of large-magnitude microseismic events recorded during and after stimulation of a geothermal reservoir at Basel, Switzerland. Geothermics 45, 1-17, doi:10.1016/j.geothermics.2012.07.005.

Plenefisch, T. , Bonjer, K.-P. 1997: The stress field in the Rhinegraben area inferred from earthquake focal mechanisms and estimation of frictional parameters. Tectonophysics 275, 71-97.

Terakawa, T., Miller, S. A., Deichmann, N. 2012. High fluid pressure and triggered earthquakes in the enhanced geothermal system in Basel, Switzerland. Journal of Geophysical Research, 117, B07305, doi:10.1029/2011JB008980.

Ustaszewski, K., Schmid, S.M. 2007. Latest Pliocene to recent thick-skinned tectonics at the Upper Rhine Graben - Jura Mountains junction. Swiss Journal of Geosciences 100, 293-312.

Valley, B., Evans, K.F. 2009. Stress orientation to 5 km depth in the basement below Basel (Switzerland) from borehole failure analysis. Swiss Journal of Geosciences 102/3, DOI:10.1007/s00015-009-1335-z.

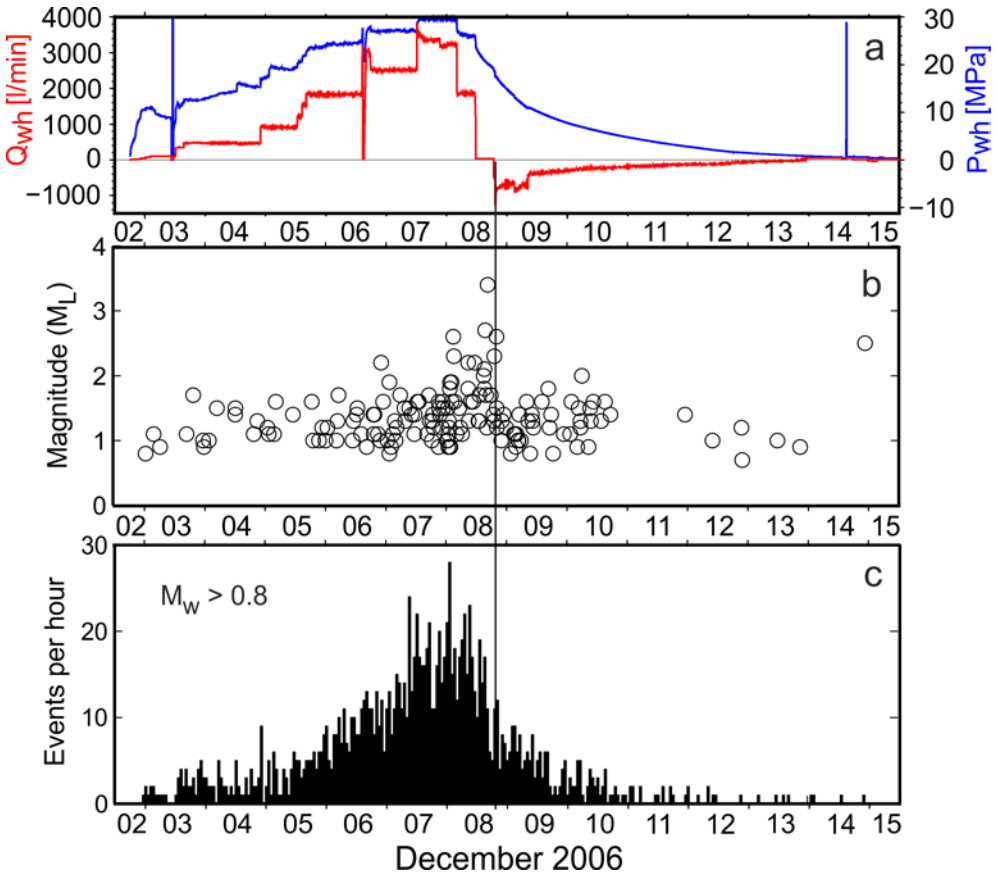

Figure 1: (a) Well-head pressure (blue) and injection rate (red) from the start of the stimulation until mid December 2006 (modified from Häring et al. 2008); (b) Local magnitudes (M_L) of the induced events recorded by the surface network of the Swiss Seismological Service; (c) Events per hour with moment magnitudes (M_w) greater than 0.8 recorded by the borehole network of Geothermal Explorers. The M_w of 0.8 is the estimated average magnitude of completeness over the given time period (Bachmann et al. 2011) and corresponds to an M_L of about 0 (Bethmann et al. 2011). The vertical line identifies the time when the well was opened and the water was allowed to flow back out of the well (the beginning of bleed-off).

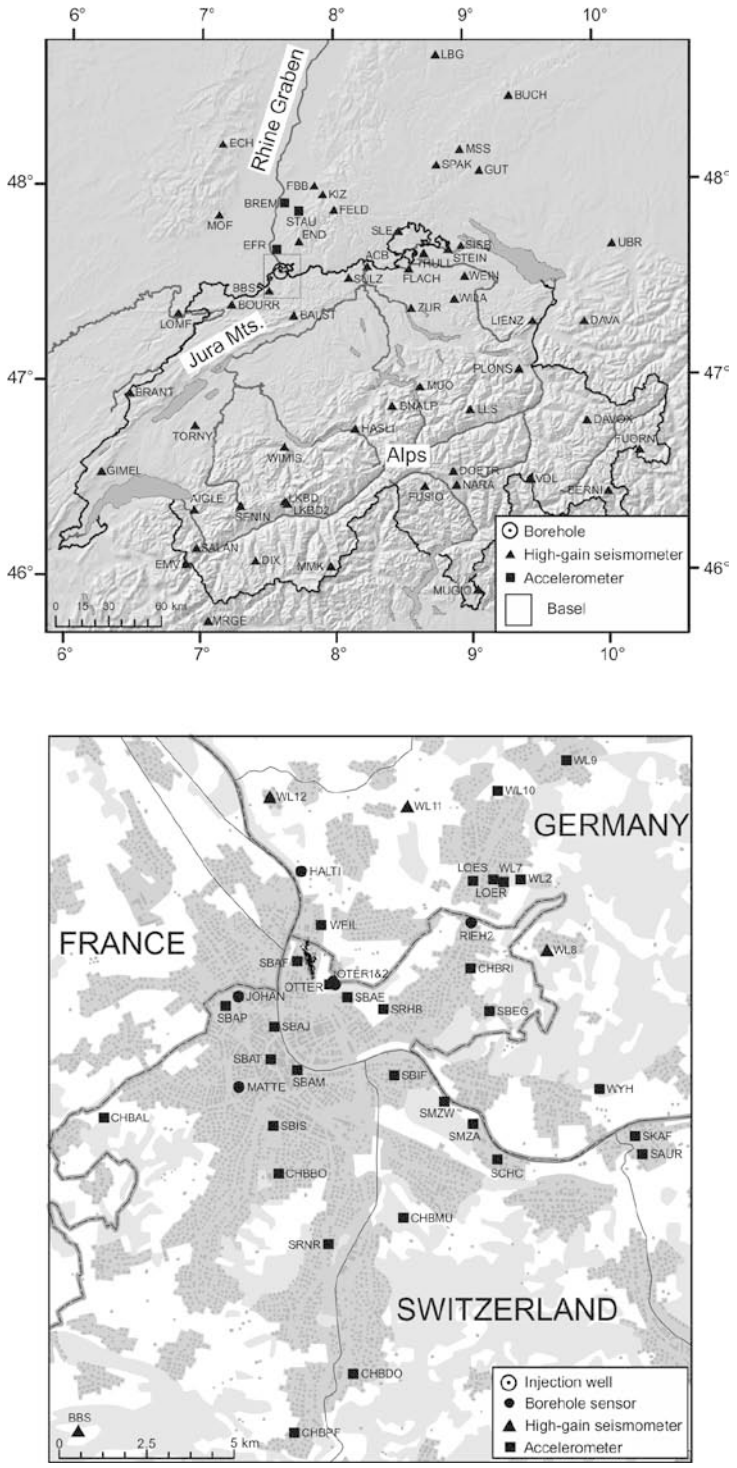

Figure 2. Top: Seismic stations in Switzerland and southern Germany that supplied data used for the fault-plane solutions of the induced seismicity in Basel. Bottom: Seismic stations in Basel and surroundings, during the stimulation in December 2006 and for about six months thereafter. The darker shaded areas correspond to the city of Basel and surrounding towns, while wood- and farmland are the light grey and white patches. The epicenters of the induced seismicity and the Basel injection well are located immediately east of station SBAF and in between stations WEIL and OTTER.

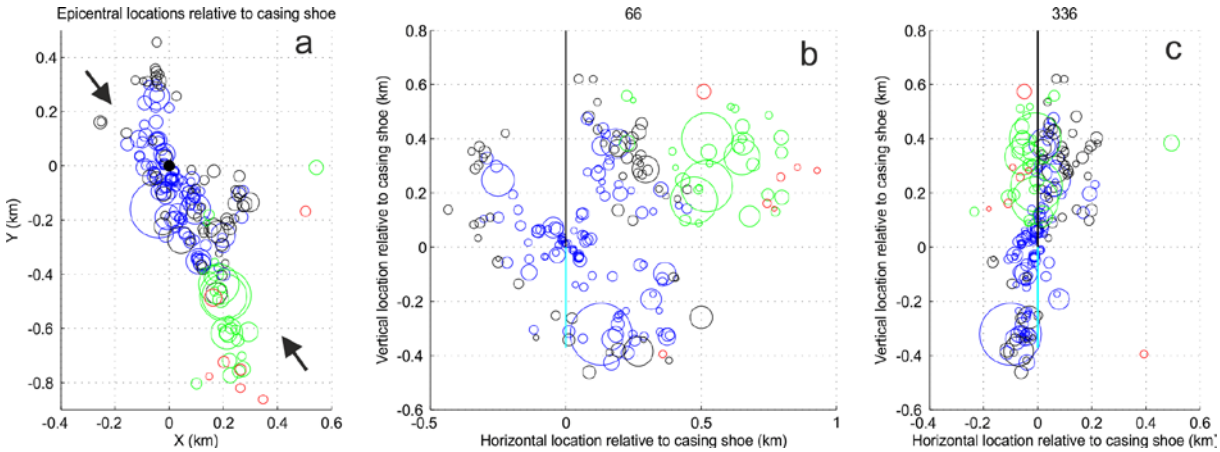

Figure 3. The master-event locations relative to the casing shoe (beginning of the open-hole section) of all events recorded by the regional networks, between Dec. 2nd, 2006 and June 29th, 2013: epicenter plot (a) and depth cross-sections parallel (b) and perpendicular (c) to the general trend of the epicenter alignment. In (a) the well is marked by the black dot (0,0); in (b) and (c) the cased section of the well is marked by the black vertical line and the open hole section by the cyan colored segment. The events are color coded as a function of time of occurrence: blue, the active stimulation phase from December 2nd to December 8th, 2006; black, the immediate post-stimulation period until December 31st; green, January 1st until November 30th, 2007; red, the seven events that occurred in 2010, 2012 and 2013. The size of each circle is proportional to the seismic moment of the event. The largest circle at a depth between -0.2 and -0.3 km represents the M_L 3.4 mainshock of December 8th, 2006. The arrows in panel (a) point in the direction of maximum horizontal compressive stress derived from wellbore failure measurements in the crystalline basement down to 5 km depth by Valley and Evans (2009).

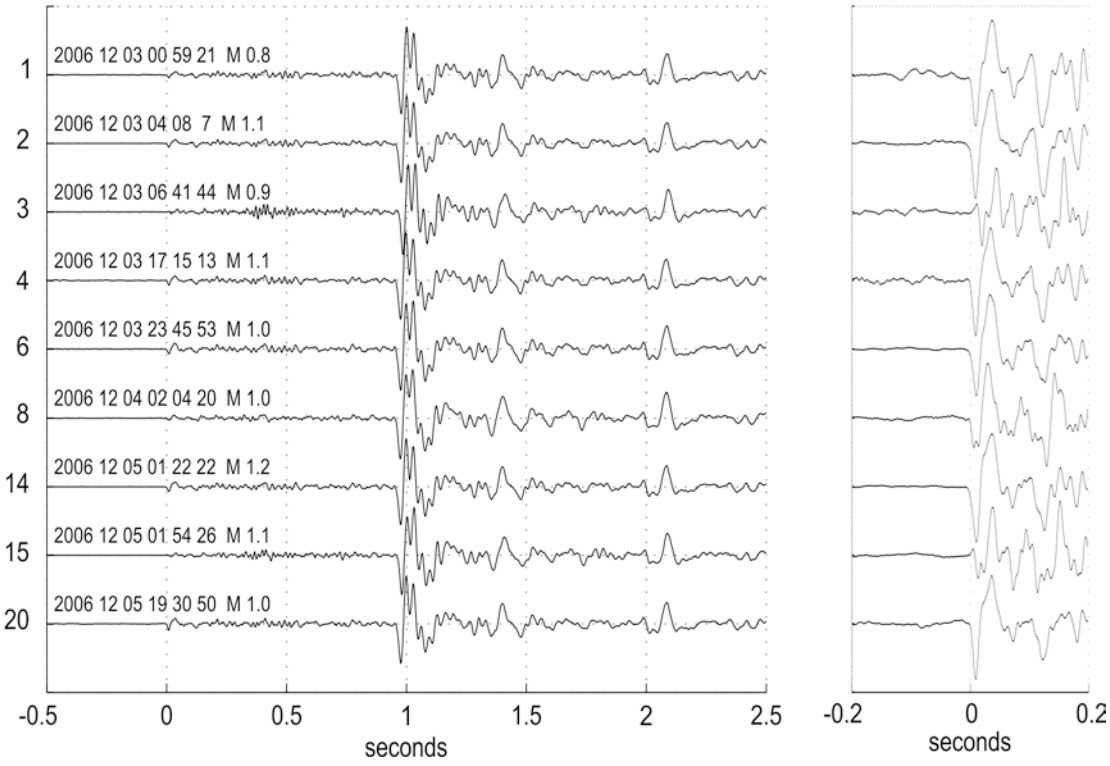

Figure 4. Example of seismograms (borehole station MATTE, channel B) of a family of similar events (Cluster 14/15), aligned at the P-wave onset. The ordinate is numbered with the event number. In the right-hand figure, note the polarity reversal of events 3 and 15 (emergent up in contrast to impulsive down), in spite of the high similarity of the S-phase – this occurs at stations that lie close to a nodal line on the focal sphere and is symptomatic of small differences in the focal mechanism.

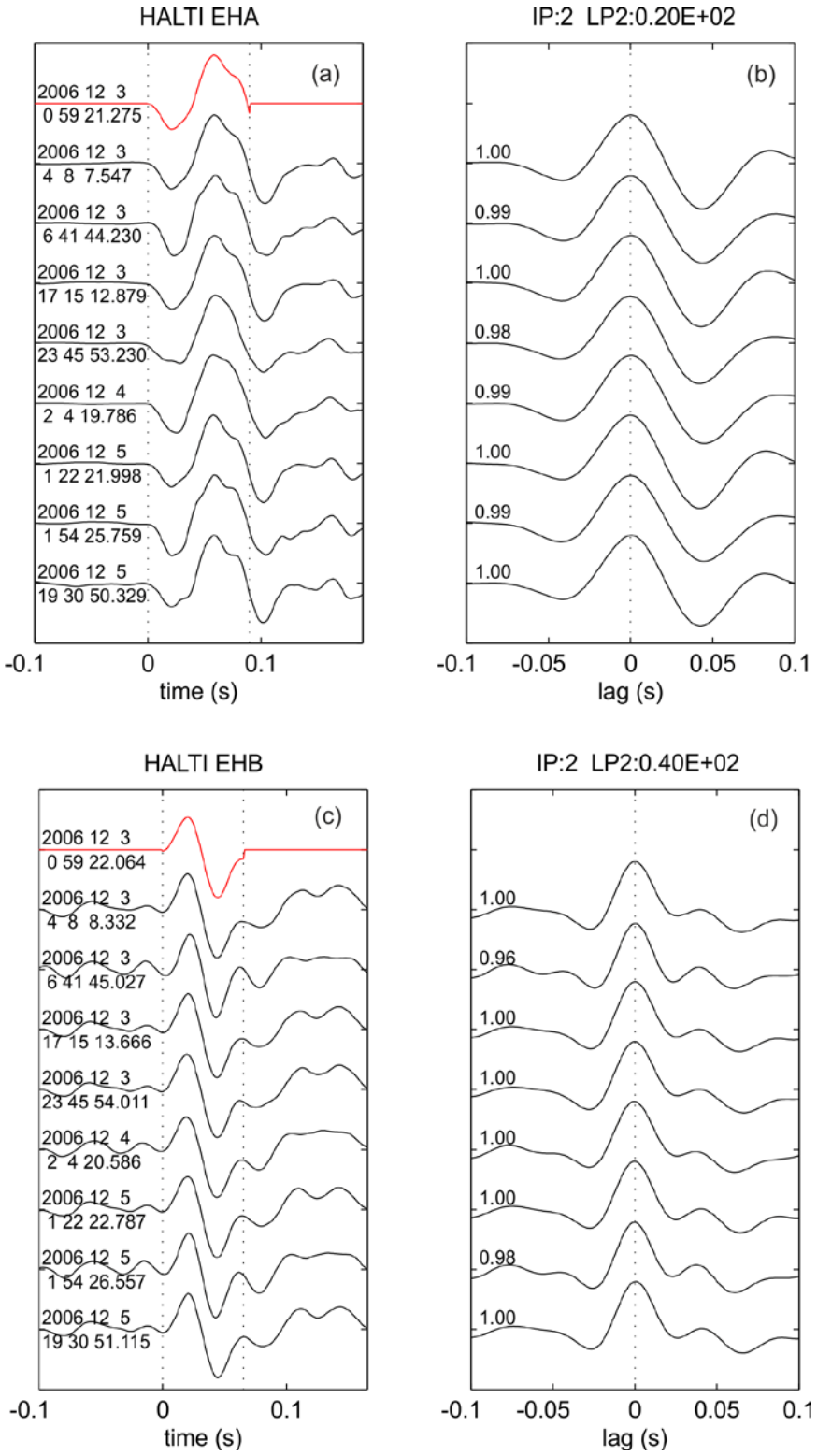

Figure 5. Example of a cross-correlation (Cluster 14, Station HALTI): (a) the P-phase and (c) the S-phase with date and time of each event; (b) and (d) show the corresponding cross-correlation functions and correlation coefficients. The red traces are the master-event and the vertical dotted lines in panels (a) and (c) mark the signal window used in the correlation.

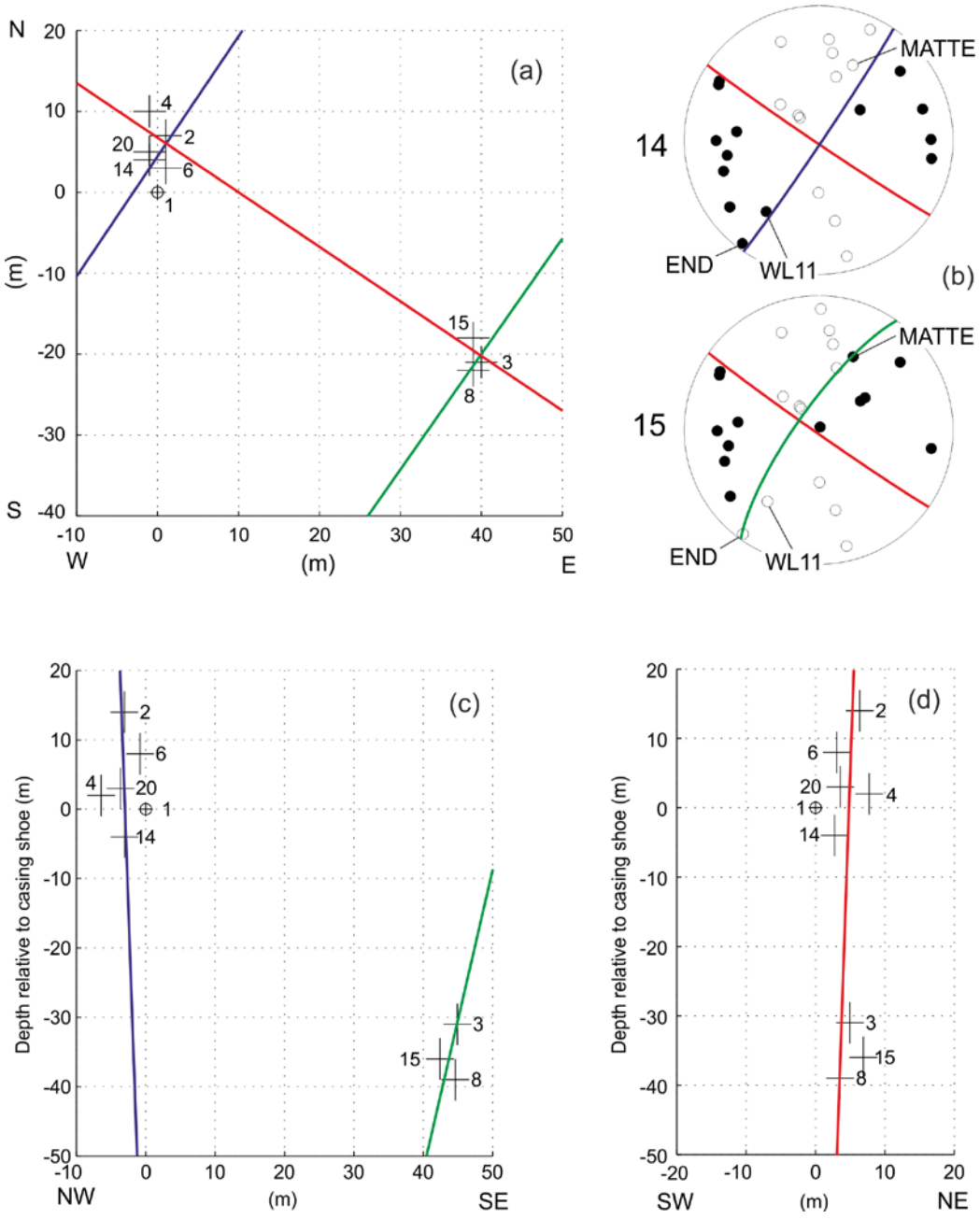

Figure 6. Relative hypocenter locations and focal mechanisms for Cluster 14/15: (a) epicenter map; (b) fault-plane solutions for events 14 and 15; (c) depth cross-section trending NW-SE; (d) depth cross-section trending SW-NE. The focal mechanisms of events 3 and 8 are similar to the one of event 15 and the others are identical to the mechanism of event 14. The size of the crosses corresponds to the relative location error (one standard deviation), and the numbers next to each cross is the event number in Table A.1. Note the polarity reversals at stations END, WL11 and MATTE, which constrain a different dip of the SW-NE striking nodal plane. The seismograms recorded at station MATTE are shown in Figure 4. The colored lines correspond to the traces of the corresponding nodal planes in the fault-plane solutions. Only the (red) NW-SE striking plane is common to both sub-clusters and thus is considered to represent the fault that ruptured in these nine similar events.

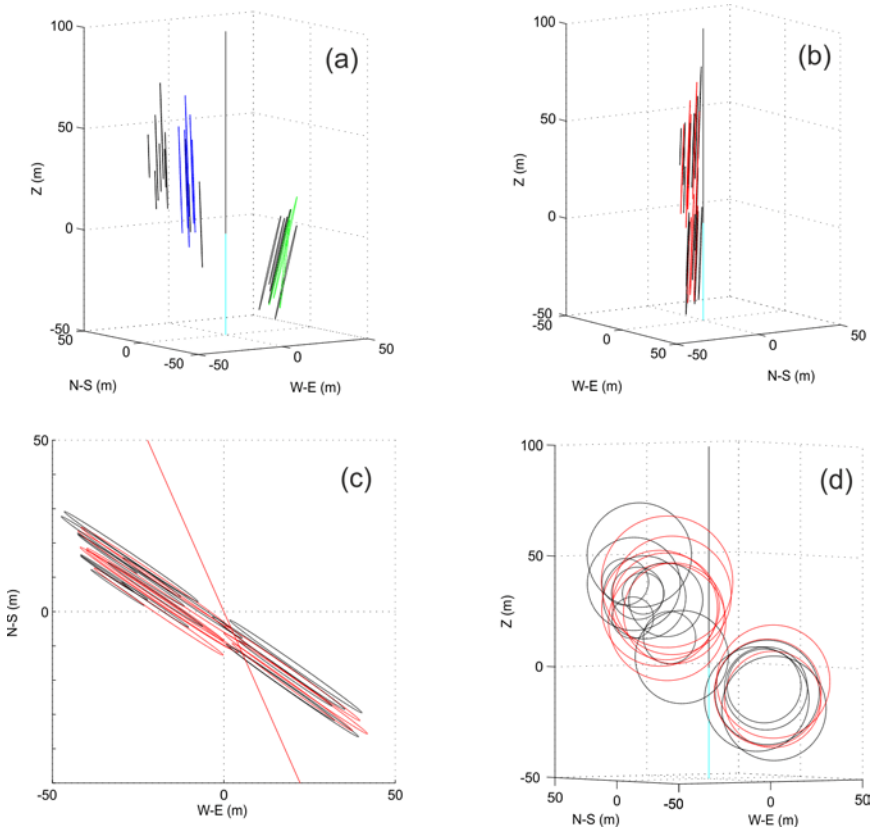

Figure 7. Perspective plots of the hypocenter locations relative to the casing shoe for Cluster 14/15. Panel (a) is the view towards NE (azimuth 34 degrees) and from an elevation of 10 degrees; the line segments show the dip and vertical rupture dimension of each event along the direction of the nodal planes that strike with 34 and 215-216 degrees: blue, sub-cluster 14, and green, sub-cluster 15 (as in Figure 6c); black, the events from Kraft & Deichmann (2013) recorded only by the borehole array. Panel (b) is like Panel (a) but viewed towards NW (azimuth 304 degrees) and with the line segments representing the nodal planes that strike with 124 degrees (as in Figure 6d). Panel (c) is a map view of Panel (b) with the red diagonal line representing the overall orientation of the seismic cloud shown in Figure 3a). Panel (d) is the view along the normal to the fault plane common to all events inferred from Panels (b) and (c). Each event is represented by a circular rupture patch with a size equal to the rupture dimension, estimated from the respective seismic moment and an assumed common stress drop of 3 MPa. Because of the chosen viewing angles in Panels (a), (b) and (c), the circles collapse into a line segment or a very narrow ellipse. The vertical lines in (a), (b) and (d) delineate the borehole (black, the cased section, and cyan, the open hole).

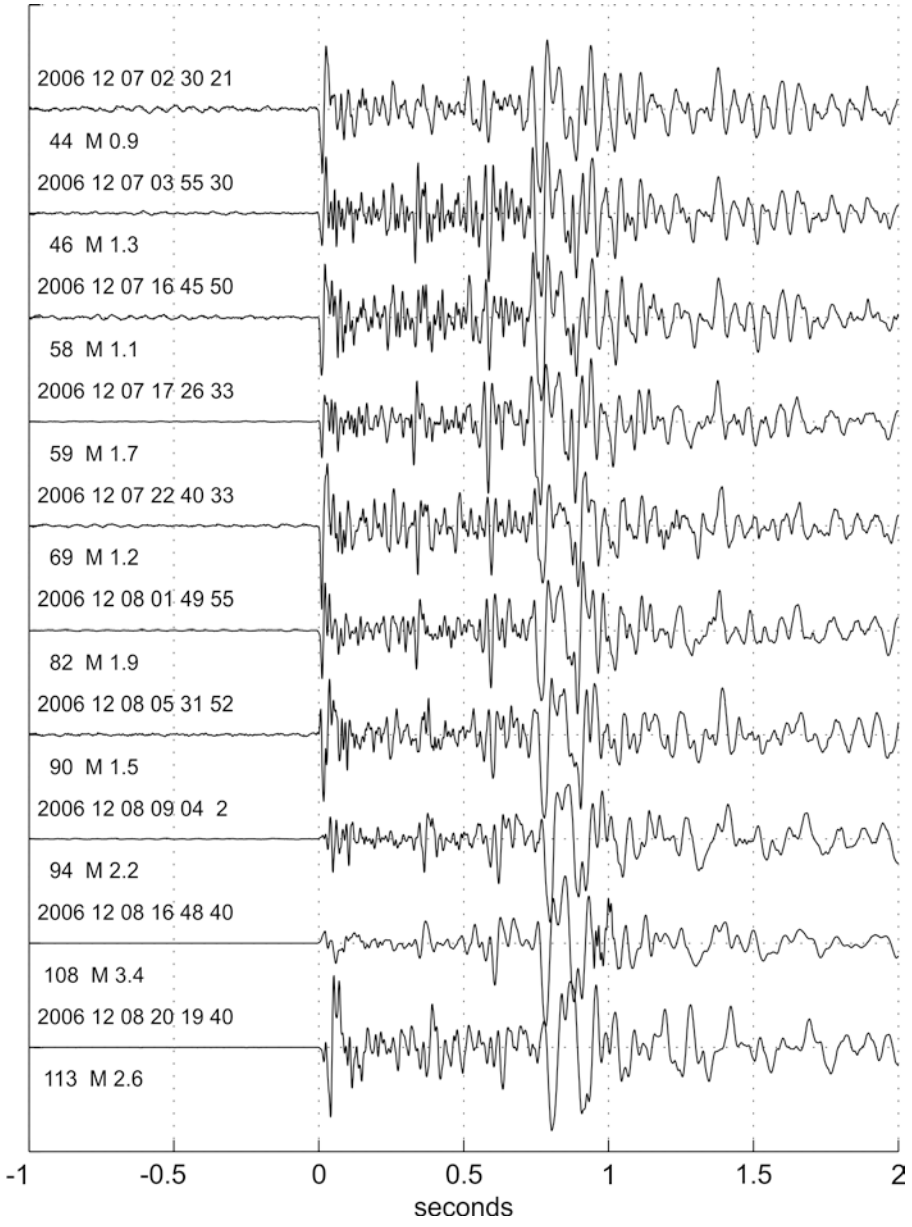

Figure 8. Cluster 82: Seismograms recorded by the borehole sensor at station JOHAN (channel B) of the 10 events detected by the surface network. This plot illustrates nicely both the waveform similarities (the S-phase and its coda) and the differences (polarity and impulsiveness of the P-phase) between the waveforms of the various events. Note the high similarity among the first six seismograms (from the top downwards).

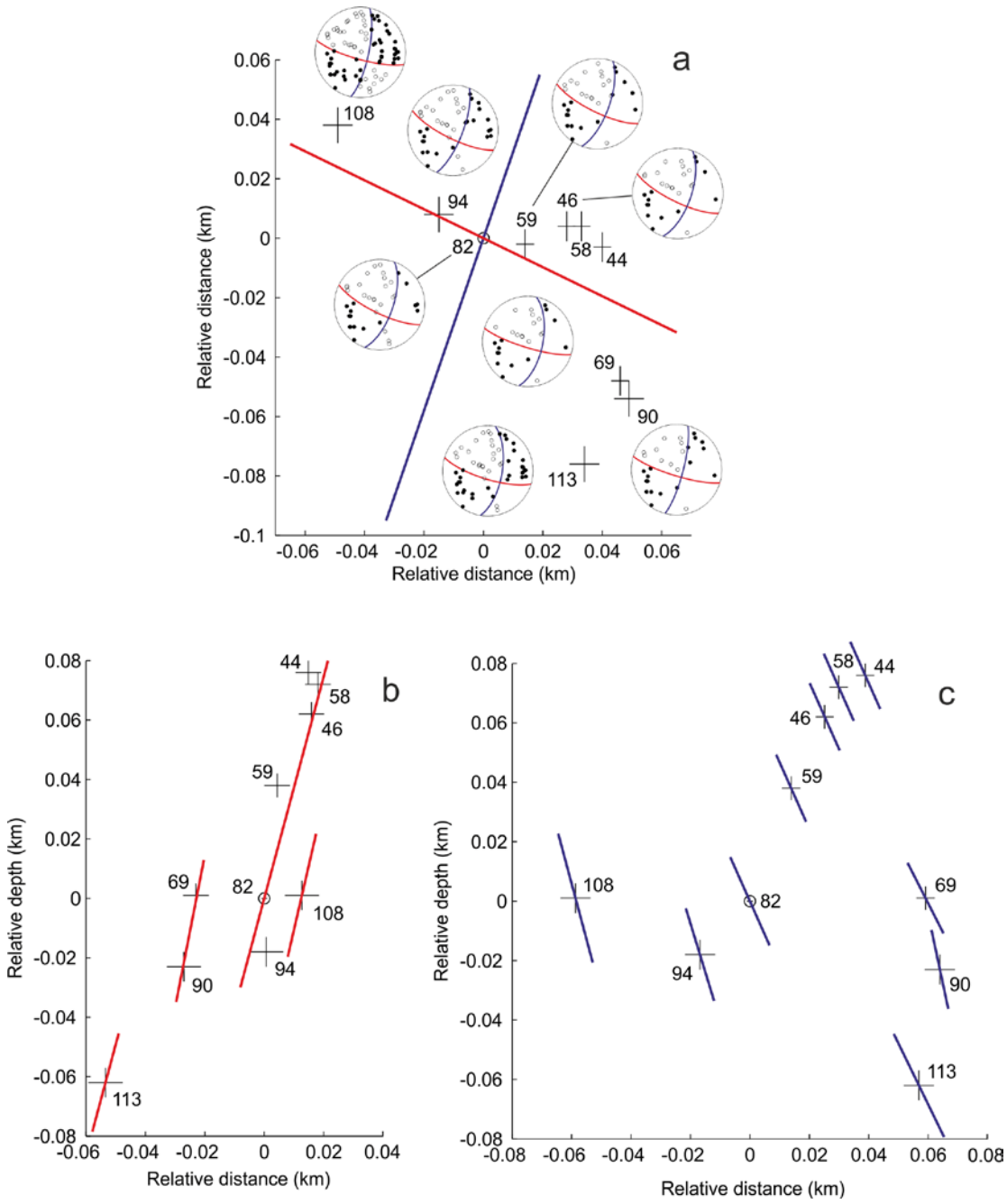

Figure 9. Cluster 82: event locations relative to the master-event (82) of the ten events detected by the surface network; the event numbers refer to Table A.1; (a) epicenters and the corresponding focal mechanisms (the mechanisms of events 44, 46, 58 and 82 are identical); (b) depth cross-section towards WNW, along strike of the red line in (a); (c) depth cross-section towards NNE along the blue line in (a). The size of the crosses is equal to the computed location uncertainty (one standard deviation). The line segments in (b) and (c) show the dip of the red or blue nodal planes; in (b) the strike and dip of the red nodal plane is identical for events 69 and 90 as well as for events 44, 46, 58, 59, 82 and 94. Viewed along the red nodal planes (b), the hypocenters can be grouped into a main cluster of six events, a subcluster of two events and two single events (108 and 113). Viewed along the blue nodal planes (c), none of the nodal planes are common to more than one event.

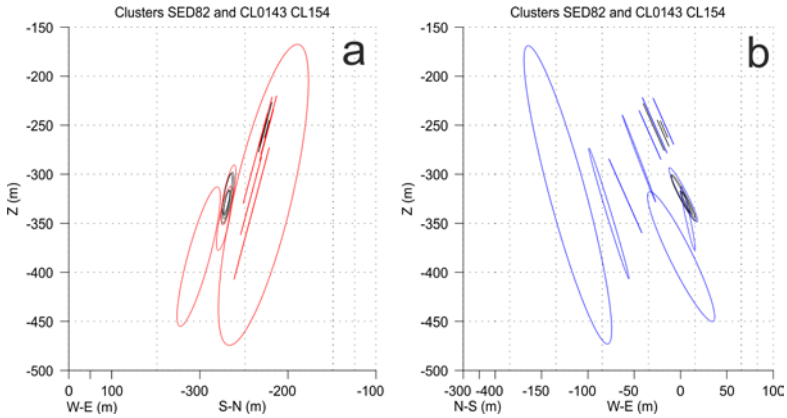

Figure 10. Cluster 82: (a) depth cross-section towards WNW, along strike of the red line in Figure 9a and (b) towards NNE along strike of the blue line in Figure 9a. Each line segment or ellipse corresponds to one of the events in the cluster and its size is equal to the rupture dimension of each event, assuming a stress drop of 3 MPa (30 bar). The black events were recorded only by the borehole network. The relative locations of the larger events are based on 30-31 phase correlations with assumed mean errors of 2-3 ms; mean residuals are 1-3 ms and standard deviations of the relative locations are 3-5 m in x, 5-6 m in y and 4-5 m in z.

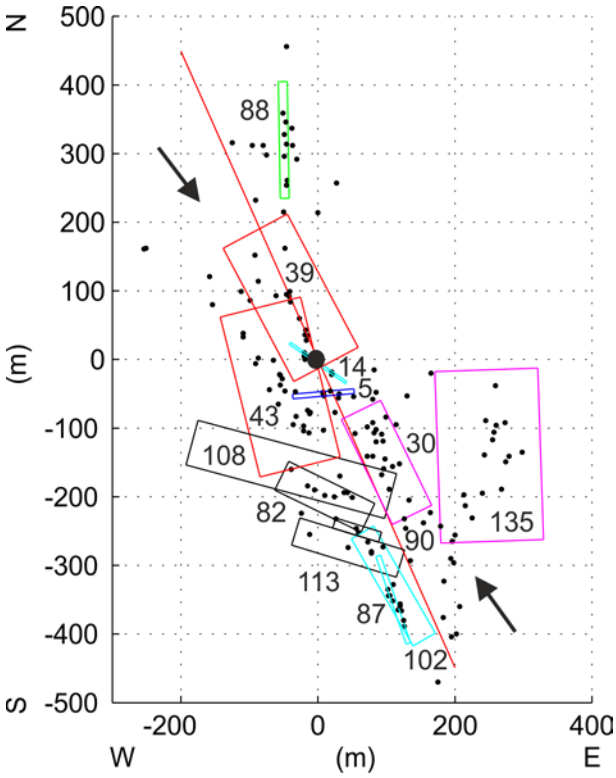

Figure 11. Map view of the identified fault planes. The black dots are the master-event locations shown in Figure 3 for the 165 events recorded in December 2006 by both the borehole and the surface networks. The different colors differentiate between the different faults as follows: normal faults (red), oblique strike-slip/normal fault (magenta), N-S strike-slip (green), E-W strike-slip (blue), approximately NW-SE strike-slip (cyan), M_L 3.4 mainshock cluster (black). The numbers next to the planes identify each cluster (the mainshock cluster is identified by four planes corresponding to events 82, 90, 108 and 113). The larger black dot corresponds to the location of the borehole and the red line shows the overall orientation of the seismic cloud. The arrows point in the direction of maximum horizontal compressive stress derived from wellbore failure measurements in the crystalline basement down to 5 km depth by Valley and Evans (2009).

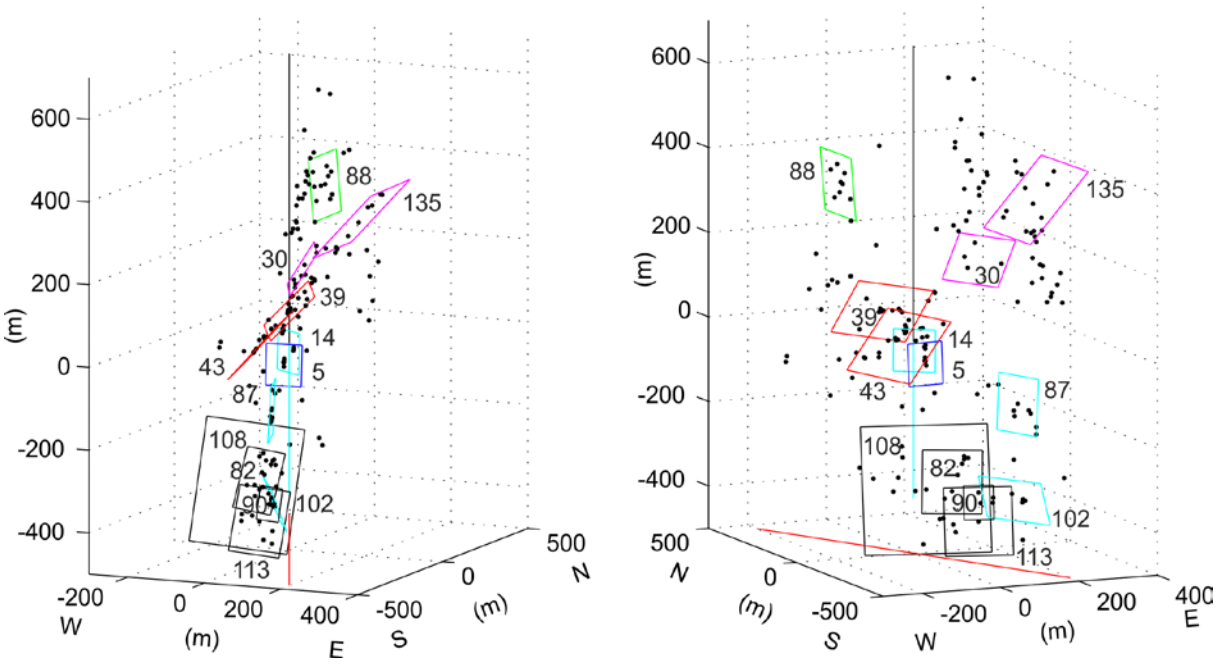

Figure 12. Perspective plots of the identified faults, viewed at 10 degrees from above and towards the NNW (azimuth 336 degrees, right) and towards the NNE (azimuth 24 degrees, right). The black dots are the master-event locations shown in Figure 3 for the 165 events recorded in December 2006 by both the borehole and the surface networks. The different colors differentiate between the different faults as follows: normal faults (red), oblique strike-slip/normal fault (magenta), N-S strike-slip (green), E-W strike-slip (blue), approximately NW-SE strike-slip (cyan), M_L 3.4 mainshock cluster (black). The numbers next to the planes identify each cluster (the mainshock cluster is identified by four planes corresponding to events 82, 90, 108 and 113). The vertical line denotes the location of the borehole (black, the cased section, and cyan, the open hole) and the red line shows the overall orientation of the seismic cloud.

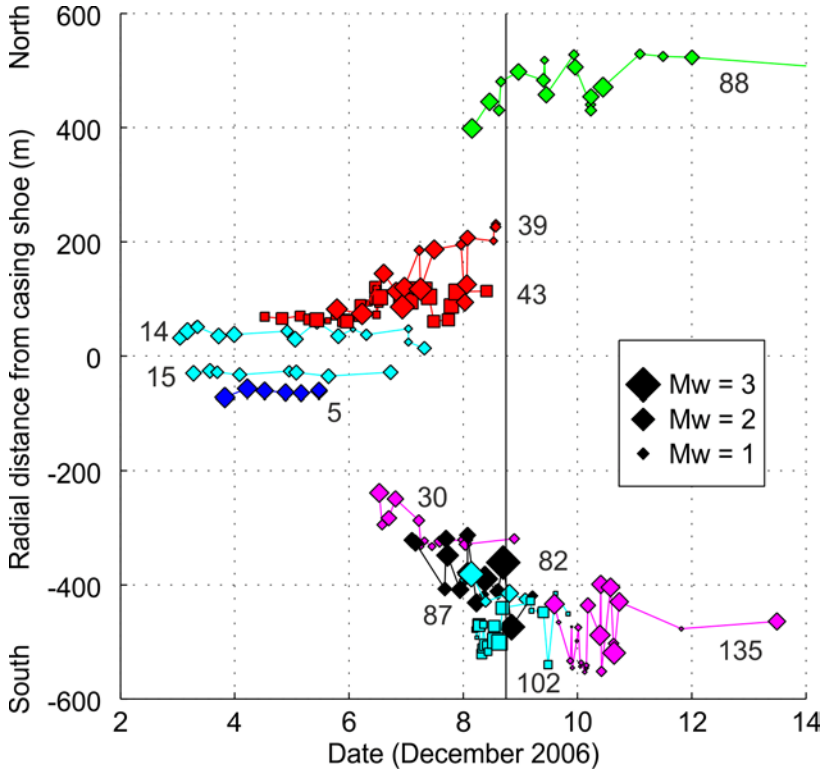

Figure 13. Evolution of the clusters analyzed in this study as a function of time and of radial distance from the casing shoe. The clusters are color coded as in Figures 11 and 12. The vertical line identifies the start of bleed-off.

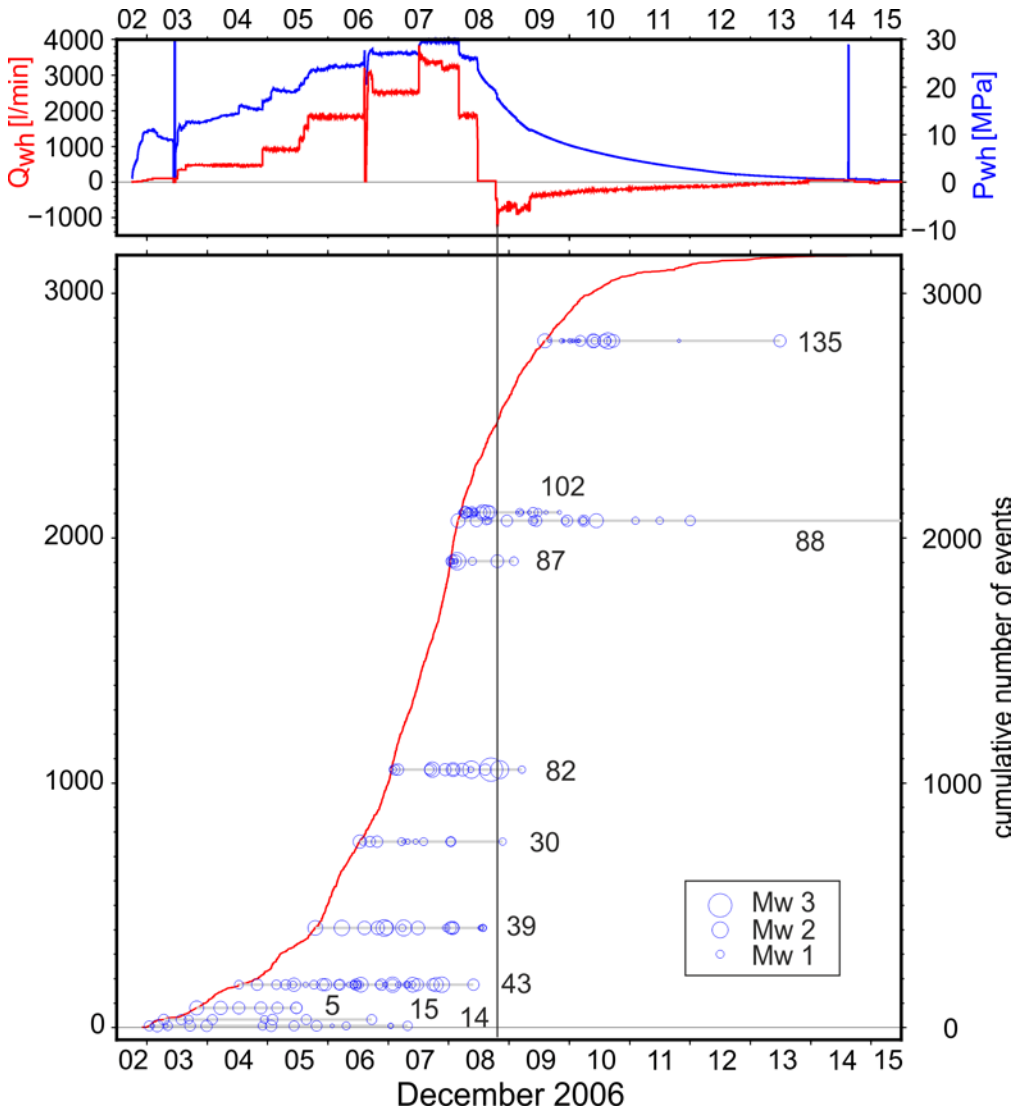

Figure 14. Top: Well-head pressure (blue) and injection rate (red) from the start of the stimulation until mid December 2006 (modified from Häring et al. 2008). Bottom: cumulative number of events located by the borehole array (red) and the temporal evolution of the clusters analyzed in this study (blue and numbered as in the previous figures). The vertical line identifies the beginning of bleed-off.

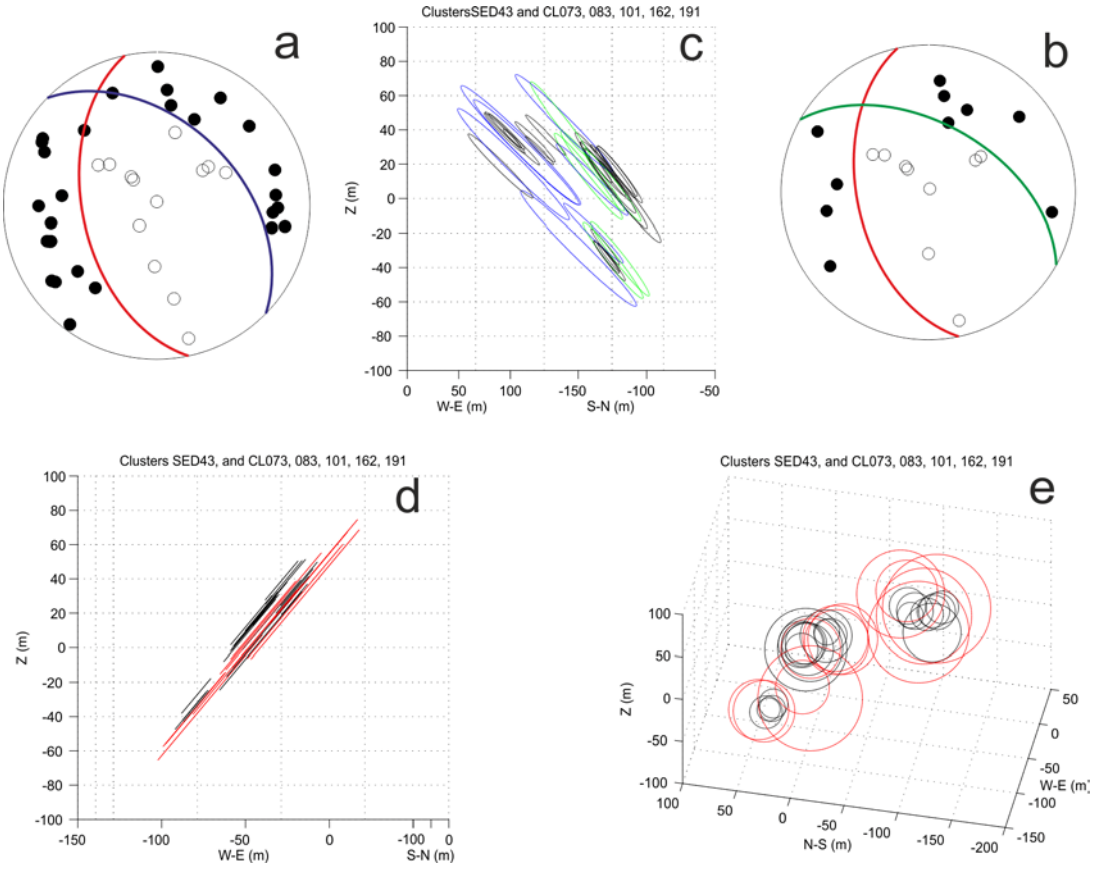

Figure A.1. Cluster 43: (a) focal mechanism of event 43; (b) focal mechanism of event 37; (c) depth cross-section viewed towards NW, more or less along strike of the blue and green nodal planes; (d) depth cross-section viewed toward NNW, along strike of the red nodal plane; (e) view from above along the normal to the red nodal plane. Each line segment, ellipse or circle corresponds to one of the events in the cluster and its size is equal to the rupture dimension of each event, assuming a stress drop of 3 MPa (30 bar). The black events were recorded only by the borehole network. The relative locations of the larger events are based on 14-24 phase correlations with assumed mean errors of 1-2 ms; mean residuals are 1-2 ms and standard deviations of the relative locations are 3-4 m in x, y and z.

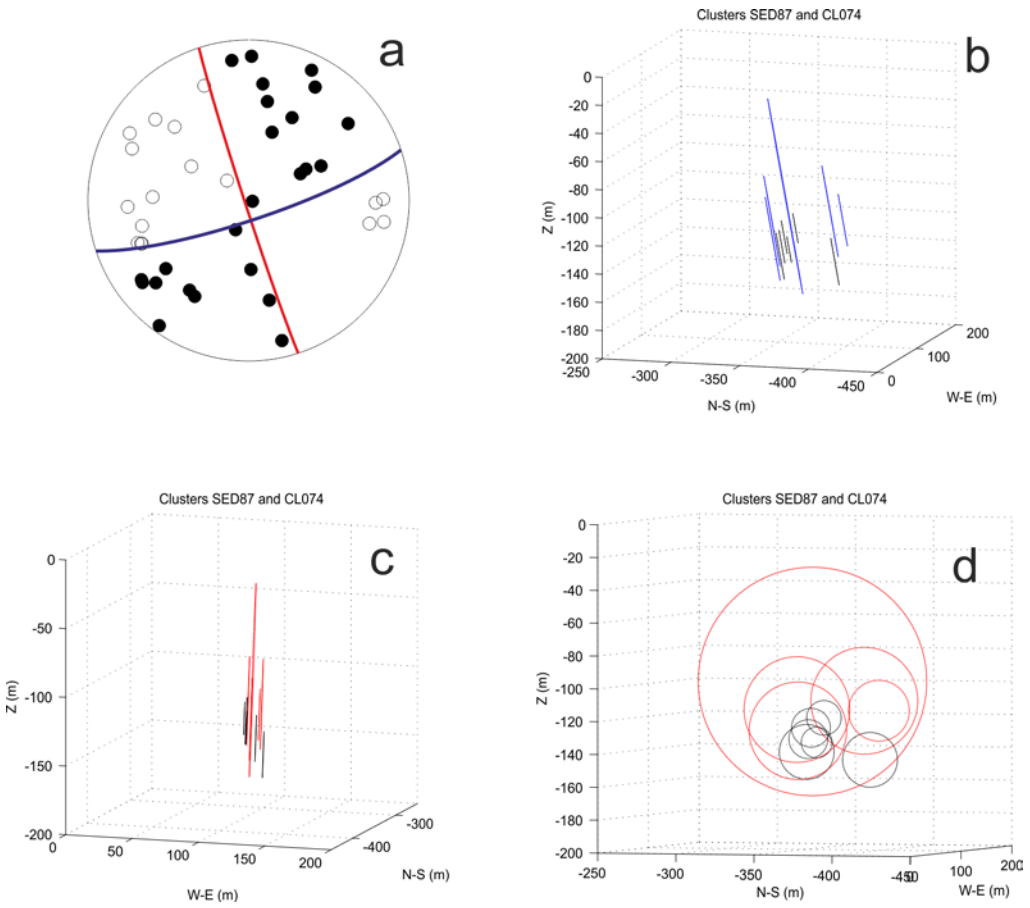

Figure A.2. Cluster 87: (a) focal mechanism of event 87; (b) perspective plot viewed towards ENE, along strike of the blue nodal plane; (c) perspective plot viewed towards NNW, along strike of the red nodal plane; (d) view along the normal to the red nodal planes. Each line segment or circle corresponds to one of the events in the cluster and its size is equal to the rupture dimension of each event, assuming a stress drop of 3 MPa (30 bar). The black events were recorded only by the borehole network. The relative locations of the larger events are based on 26-29 phase correlations with assumed mean errors of 2 ms; mean residuals are 1-2 ms and standard deviations of the relative locations are 4-5 m in x, y and z.

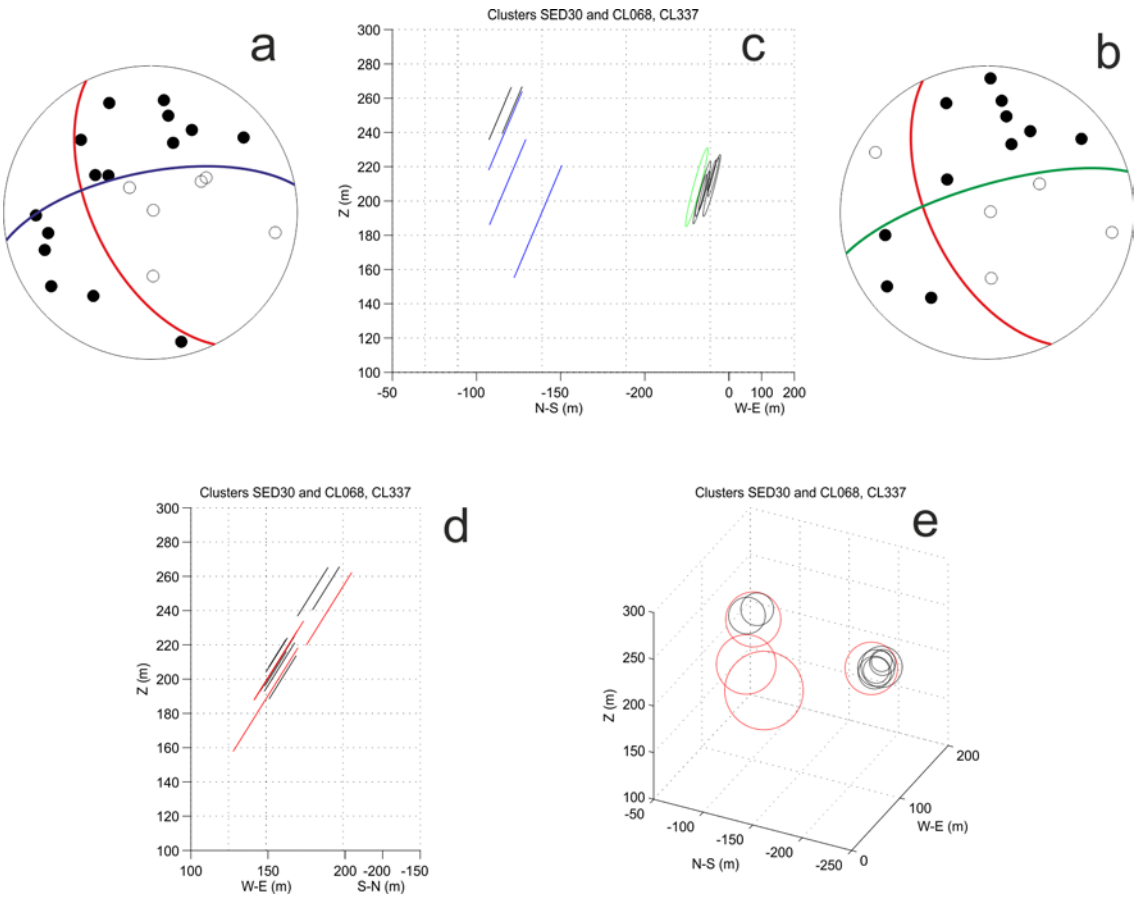

Figure A.3. Cluster 30: (a) focal mechanism of event 30; (b) focal mechanism of event 73; (c) depth cross-section viewed towards ENE, along strike of the blue nodal plane; (d) depth cross-section viewed toward NW, along strike of the red nodal plane; (e) view from above along the normal to the red nodal plane. Each line segment, ellipse or circle corresponds to one of the events in the cluster and its size is equal to the rupture dimension of each event, assuming a stress drop of 3 MPa (30 bar). The black events were recorded only by the borehole network. The relative locations of the larger events are based on 20 phase correlations with assumed mean errors of 2-3 ms; mean residuals are 1-2 ms and standard deviations of the relative locations are 5 m in x and y, and 6 m in z.

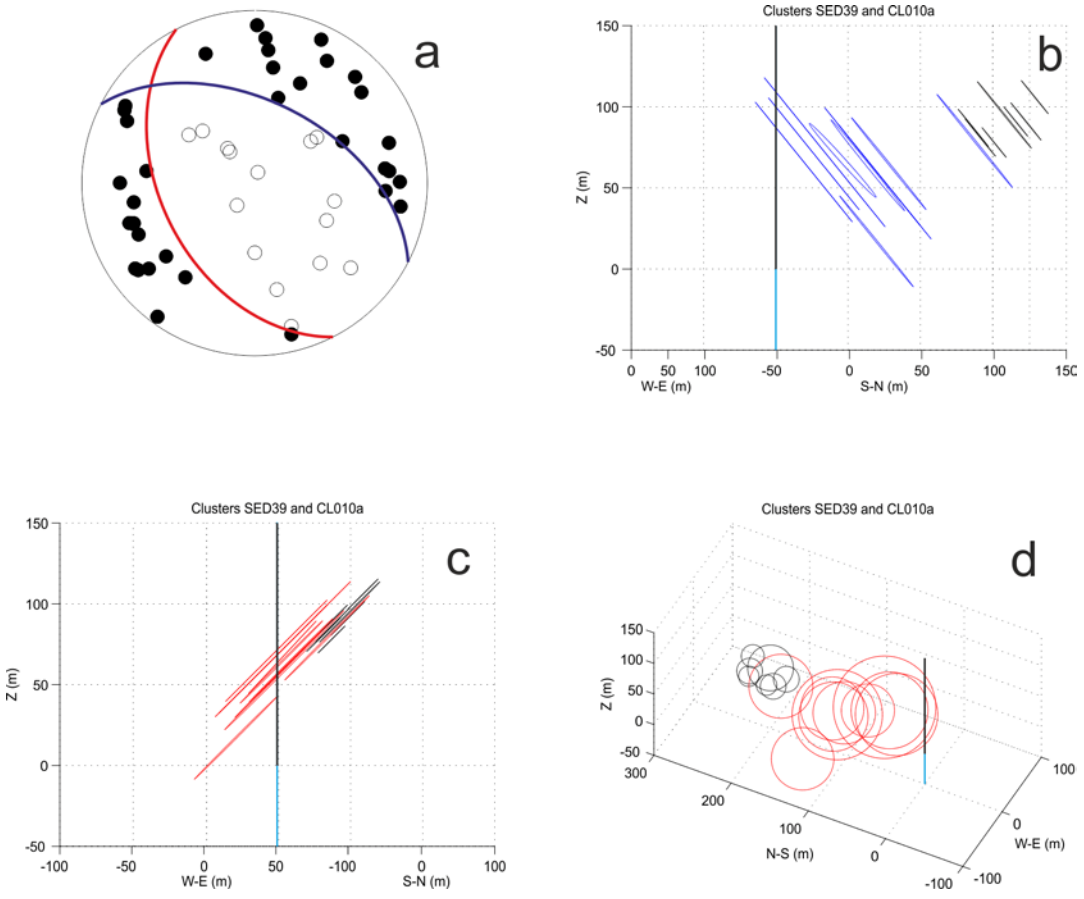

Figure A.4. Cluster 39: (a) focal mechanism of event 39; (b) depth cross-section viewed towards NW, along strike of the blue nodal plane; (c) depth cross-section viewed towards WNW, along strike of the red nodal plane; (d) view from above along the normal to the red nodal plane. The vertical lines denote the position of the injection well (casing in black, open hole in blue). Each line segment or circle corresponds to one of the events in the cluster and its size is equal to the rupture dimension of each event, assuming a stress drop of 3 MPa (30 bar). The black events were recorded only by the borehole network. The relative locations of the larger events are based on 21-24 phase correlations with assumed mean errors of 1-2 ms; mean residuals are 1-2 ms and standard deviations of the relative locations are 3 m in x and z, and 4 m in y.

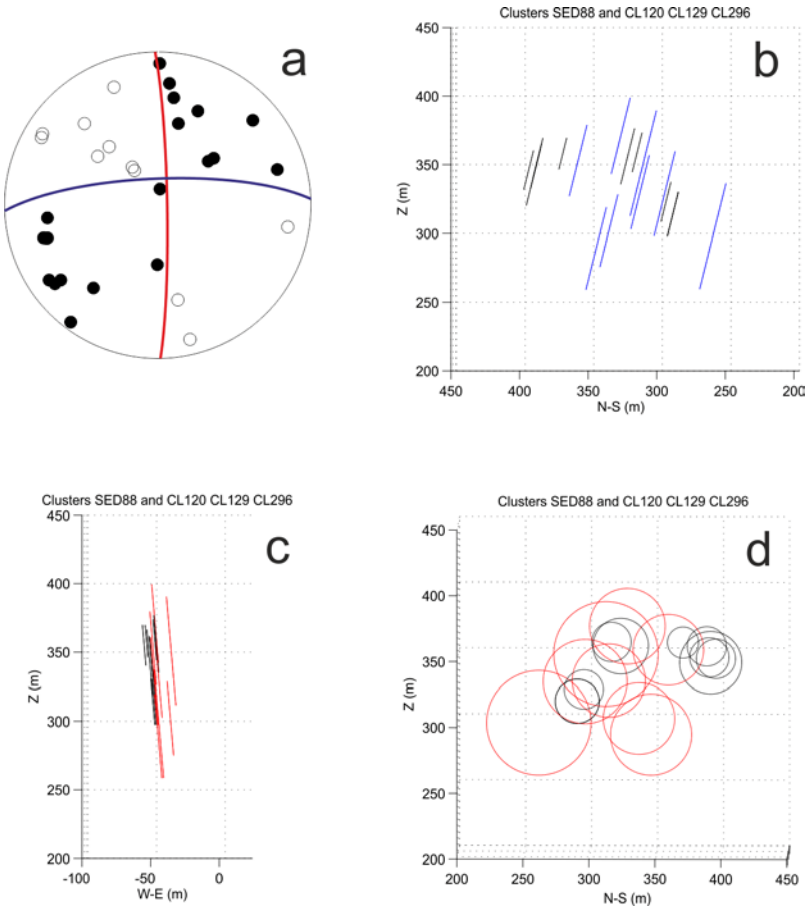

Figure A.5. Cluster 88: (a) focal mechanism of event 88; (b) depth cross-section viewed towards E, along strike of the blue nodal plane; (c) depth cross-section viewed towards N, along strike of the red nodal plane; (d) view along the normal to the red nodal plane. Each line segment or circle corresponds to one of the events in the cluster and its size is equal to the rupture dimension of each event, assuming a stress drop of 3 MPa (30 bar). The black events were recorded only by the borehole network. The relative locations of the larger events are based on 23-28 phase correlations with assumed mean errors of 1-2 ms; mean residuals are 1-2 ms and standard deviations of the relative locations are 3-4 m in x, y and z.

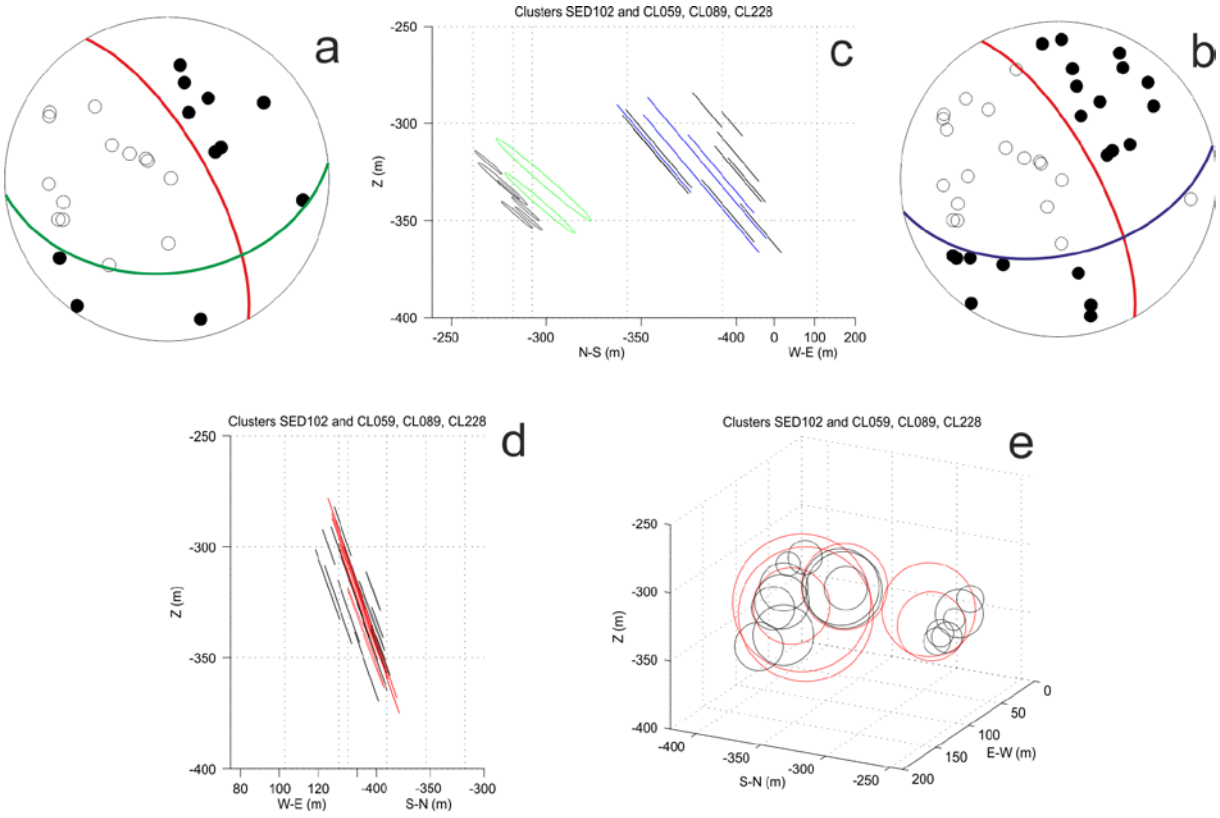

Figure A.6. Cluster 102: (a) focal mechanism of event 107; (b) focal mechanism of event 102; (c) depth cross-section viewed towards E, along strike of the blue nodal plane; (d) depth cross-section viewed toward NW, along strike of the red nodal plane; (e) view from above along the normal to the red nodal plane. Each line segment, ellipse or circle corresponds to one of the events in the cluster and its size is equal to the rupture dimension of each event, assuming a stress drop of 3 MPa (30 bar). The black events were recorded only by the borehole network. The relative locations of the larger events are based on 27-29 phase correlations with assumed mean errors of 1-2 ms; mean residuals are 1-2 ms and standard deviations of the relative locations are 3 m in x and y, and 3-4 m in z.

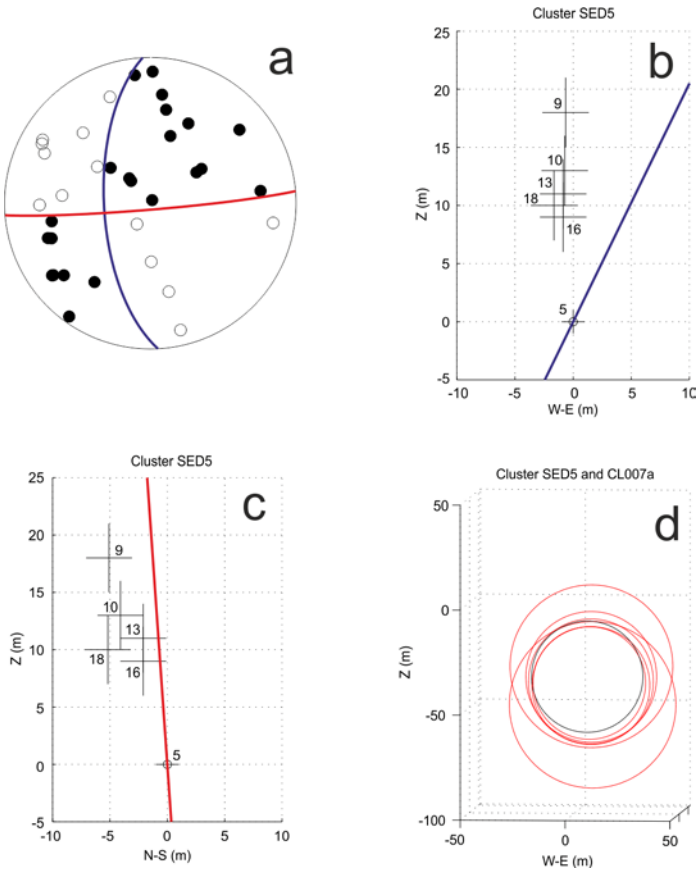

Figure A.7. Cluster 5: (a) focal mechanism of event 5; (b) depth cross-section viewed towards N, along strike of the blue nodal plane; (c) depth cross-section viewed towards E, along strike of the red nodal plane; (d) view along the normal to the red nodal plane. In (b) and (c), the hypocenter locations are relative to the master event (# 5) and the size of the crosses is equal to one standard deviation. In (d), each circle corresponds to one of the events in the cluster and its size is equal to the rupture dimension of each event, assuming a stress drop of 3 MPa (30 bar); the locations, in this plot, are relative to the casing shoe. The black event in (d) was recorded only by the borehole network. The relative locations of the larger events are based on 28-30 phase correlations with assumed mean errors of 1-2 ms; mean residuals are 1 ms and standard deviations of the relative locations are 2 m in x and y, and 3 m in z. In (b) and (c), the trace of the respective nodal plane is drawn through the master event. Based on the better fit between the hypocenter alignment and the trace of the (red) nodal plane (panel c), the E-W striking plane is judged to be the more likely fault to have been activated by this cluster.

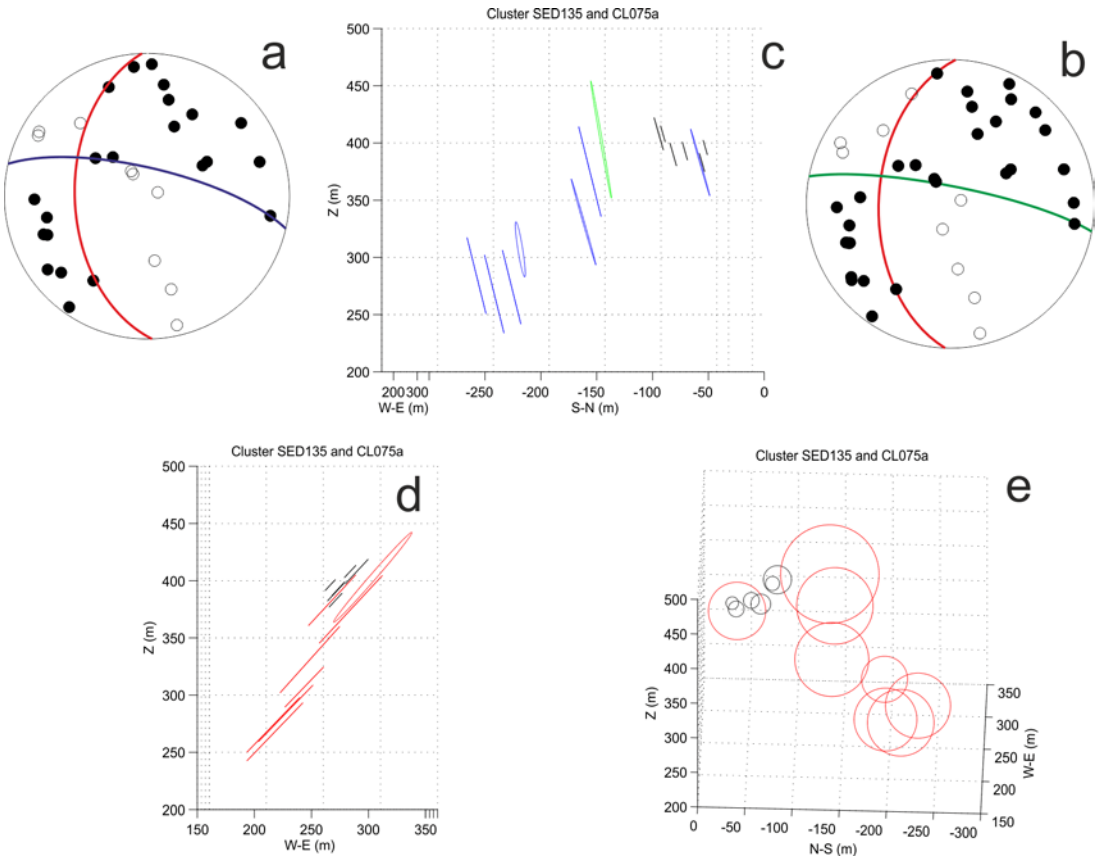

Figure A.8. Cluster 135: (a) focal mechanism of event 135; (b) focal mechanism of event 153; (c) depth cross-section viewed towards ESE, along strike of the blue and green nodal planes; (d) depth cross-section viewed towards N, along strike of the red nodal planes; (e) view along the normal to the red nodal planes. Each line segment, ellipse or circle corresponds to one of the events in the cluster and its size is equal to the rupture dimension of each event, assuming a stress drop of 3 MPa (30 bar). The black events were recorded only by the borehole network. The relative locations of the larger events are based on 22-27 phase correlations with assumed mean errors of 1-2 ms; mean residuals are 1-2 ms and standard deviations of the relative locations are 3-4 m in x and y, and 4 m in z.

Table A.1. List of the clusters analyzed in this report, with locations relative to the casing shoe (m), magnitudes and focal mechanism parameters (strike/dip/rake of the identified fault-plane) for each event (strike clockwise from North). All events with event-numbers below 200 were recorded by both the local borehole and the regional surface networks; their local magnitude (M_L) is based on the Wood-Anderson filtered amplitudes of the broad-band surface stations; their moment magnitude (M_w) was computed by Bethmann et al. (2011). The other events were recorded only by the borehole network; their M_W was computed by Geothermal Explorers (T. Spillmann, personal communication), as outlined in Dyer et al. (2008); their M_L is not known and has been set to -9. Focal mechanisms of the sub-clusters recorded only by the borehole network have been set equal to the focal mechanism of the event common to both the given sub-cluster and the cluster recorded by the surface stations.

Event	Date	Time (UTC)	X	Y	Z	MW	ML	Strike/Dip/Rake
Cluster 14								
1	2006 12	3 0 59 20.317	-19	0	25	1.27	0.8	124/88/-178
585	2006 12	3 1 59 13.252	-34	11	23	0.50	-9.	124/88/-178
2	2006 12	3 4 8 6.590	-18	7	39	1.50	1.1	124/88/-178
1041	2006 12	3 7 33 57.814	-34	17	39	0.60	-9.	124/88/-178
1051	2006 12	3 8 22 28.865	-30	16	38	1.20	-9.	124/88/-178
4	2006 12	3 17 15 11.923	-20	10	27	1.39	1.1	124/88/-178
6	2006 12	3 23 45 52.269	-18	3	33	1.41	1.0	124/88/-178
1888	2006 12	4 22 1 1.230	-27	12	32	1.10	-9.	124/88/-178
14	2006 12	5 1 22 21.039	-20	4	21	1.40	1.2	124/88/-178
2335	2006 12	5 10 32 54.708	-27	16	51	1.30	-9.	124/88/-178
20	2006 12	5 19 30 49.373	-20	5	28	1.32	1.0	124/88/-178
3318	2006 12	6 1 40 30.585	-31	7	34	0.50	-9.	124/88/-178
3766	2006 12	6 7 18 19.790	-20	5	31	1.00	-9.	124/88/-178
5534	2006 12	7 0 55 52.248	-32	10	34	0.70	-9.	124/88/-178
5536	2006 12	7 0 57 26.087	-20	2	14	0.70	-9.	124/88/-178
6334	2006 12	7 7 40 7.897	-12	4	5	1.20	-9.	124/88/-178
Cluster 15								
3	2006 12	3 6 41 43.264	21	-21	-6	1.37	0.9	125/88/ 167
1124	2006 12	3 13 34 38.418	16	-15	-14	1.30	-9.	125/88/ 167
1225	2006 12	3 16 39 51.954	17	-21	-9	1.10	-9.	125/88/ 167
8	2006 12	4 2 4 18.823	20	-22	-14	1.23	1.0	126/88/ 174
1920	2006 12	4 22 50 14.270	18	-18	-8	1.00	-9.	125/88/ 167
15	2006 12	5 1 54 24.796	20	-18	-11	1.32	1.1	125/88/ 167
2532	2006 12	5 15 25 44.021	20	-23	-18	1.30	-9.	125/88/ 167
4710	2006 12	6 17 29 45.368	21	-16	-11	1.30	-9.	125/88/ 167
Cluster 5								
5	2006 12	3 19 51 4.076	9	-53	-48	1.75	1.7	085/86/ 154
9	2006 12	4 5 17 56.011	8	-48	-30	1.73	1.5	085/86/ 154
10	2006 12	4 12 35 40.782	8	-49	-35	1.54	1.4	085/86/ 154
13	2006 12	4 21 20 16.153	8	-51	-37	1.50	1.3	085/86/ 154
16	2006 12	5 3 55 5.712	8	-51	-39	1.45	1.1	085/86/ 154
18	2006 12	5 11 25 55.708	7	-48	-38	1.41	1.4	085/86/ 154
2365	2006 12	5 11 26 29.684	6	-48	-35	1.40	-9.	085/86/ 154
Cluster 43								
1699	2006 12	4 12 37 18.376	-67	3	15	1.10	-9.	168/50/-054
12	2006 12	4 19 54 51.885	-65	-1	8	1.42	1.1	168/50/-054
2067	2006 12	5 3 28 13.291	-68	7	14	1.20	-9.	168/50/-054
2201	2006 12	5 7 15 31.587	-59	-14	20	1.30	-9.	168/50/-054

2312	2006	12	5	10	8	4.442	-58	-18	21	0.90	-9.	168/50/-054
2329	2006	12	5	10	29	57.567	-63	4	4	1.70	-9.	168/50/-054
2521	2006	12	5	15	7	12.945	-56	-14	22	0.70	-9.	168/50/-054
2728	2006	12	5	18	26	39.690	-69	6	16	1.10	-9.	168/50/-054
21	2006	12	5	21	50	28.377	-56	-22	16	1.50	1.0	168/50/-054
22	2006	12	5	23	6	24.609	-52	-28	13	1.56	1.2	168/50/-054
3527	2006	12	6	4	22	59.571	-69	1	10	1.30	-9.	168/50/-054
25	2006	12	6	4	46	51.413	-87	2	-20	1.33	1.0	168/50/-067
3862	2006	12	6	8	24	24.857	-24	-85	28	0.70	-9.	168/50/-067
4013	2006	12	6	10	18	1.441	-22	-100	30	0.90	-9.	168/50/-067
4028	2006	12	6	10	29	36.786	-23	-89	33	1.00	-9.	168/50/-067
28	2006	12	6	11	9	31.367	-109	38	-35	1.43	1.0	168/50/-054
4123	2006	12	6	11	32	22.360	-27	-107	39	0.90	-9.	168/50/-067
4127	2006	12	6	11	34	31.759	-71	6	10	0.90	-9.	168/50/-054
4236	2006	12	6	12	35	15.670	-22	-82	37	1.00	-9.	168/50/-067
31	2006	12	6	13	4	58.923	-21	-97	27	1.83	1.5	168/50/-067
5022	2006	12	6	20	30	6.684	-25	-110	38	1.00	-9.	168/50/-067
37	2006	12	6	21	12	52.176	-12	-79	46	1.45	1.2	168/50/-054
5287	2006	12	6	22	44	5.127	-108	29	-34	0.60	-9.	168/50/-054
42	2006	12	7	1	43	49.911	-109	33	-36	1.45	0.8	168/50/-054
43	2006	12	7	1	44	22.047	-91	-6	-29	1.91	1.9	168/50/-067
5898	2006	12	7	4	9	42.545	-106	25	-28	0.80	-9.	168/50/-054
6311	2006	12	7	7	27	30.453	-106	26	-34	0.70	-9.	168/50/-054
6313	2006	12	7	7	28	2.176	-110	31	-36	0.90	-9.	168/50/-054
6580	2006	12	7	9	23	23.567	-21	-114	40	0.90	-9.	168/50/-067
52	2006	12	7	9	40	50.587	-36	-95	20	1.88	1.5	168/50/-067
54	2006	12	7	11	38	41.838	-55	-23	11	1.49	1.1	168/50/-067
7908	2006	12	7	17	45	3.505	-63	0	6	1.50	-9.	168/50/-054
63	2006	12	7	19	2	25.759	-15	-74	44	1.76	1.4	168/50/-067
66	2006	12	7	21	16	54.898	-13	-107	31	1.94	1.6	168/50/-067
10453	2006	12	8	9	48	15.959	-33	-107	19	1.40	-9.	168/50/-067

Cluster 39

19	2006	12	5	18	56	0.105	-19	36	71	1.85	1.6	153/45/-063
27	2006	12	6	5	34	31.460	-17	28	66	1.91	1.7	153/45/-063
32	2006	12	6	14	34	3.269	-87	114	17	1.67	1.1	152/45/-063
36	2006	12	6	19	49	31.442	-40	84	64	1.67	1.4	152/45/-062
39	2006	12	6	22	27	0.905	-18	43	72	2.10	2.2	153/45/-063
40	2006	12	6	23	18	55.428	-46	95	58	1.76	1.6	152/45/-063
6065	2006	12	7	5	33	19.436	-42	158	87	0.90	-9.	152/45/-063
49	2006	12	7	6	3	44.796	-42	92	59	1.99	1.7	152/45/-063
55	2006	12	7	11	50	0.698	-48	162	79	1.69	1.4	152/45/-063
8759	2006	12	7	23	4	0.660	-54	169	81	0.90	-9.	152/45/-063
72	2006	12	8	0	41	33.193	-27	60	67	1.53	1.0	153/47/-067
78	2006	12	8	1	29	54.380	-41	99	65	1.68	1.2	152/45/-063
9231	2006	12	8	1	48	2.494	-41	179	95	1.40	-9.	152/45/-063
10723	2006	12	8	12	46	8.533	-53	178	78	0.70	-9.	152/45/-063
10740	2006	12	8	12	54	36.393	-61	197	91	0.70	-9.	152/45/-063
10844	2006	12	8	13	42	44.190	-43	201	106	0.80	-9.	152/45/-063
10845	2006	12	8	13	43	18.986	-53	200	91	0.90	-9.	152/45/-063

Cluster 30

30	2006	12	6	12	42	59.334	85	-120	188	1.66	1.4	154/58/-027
4341	2006	12	6	13	55	1.078	114	-99	253	0.90	-9.	154/58/-027
33	2006	12	6	16	44	28.369	114	-95	241	1.35	0.9	154/58/-027
35	2006	12	6	19	32	32.039	85	-102	211	1.42	1.1	154/58/-027
6046	2006	12	7	5	22	26.592	103	-94	251	1.00	-9.	154/58/-027
6155	2006	12	7	6	16	59.646	138	-213	215	0.50	-9.	154/58/-018
6333	2006	12	7	7	39	29.777	135	-209	206	0.70	-9.	154/58/-018
6812	2006	12	7	10	52	3.909	138	-214	214	0.70	-9.	154/58/-018
7320	2006	12	7	14	4	3.255	137	-208	207	1.00	-9.	154/58/-018
73	2006	12	8	0	52	14.475	133	-205	208	1.31	1.0	154/58/-018
9056	2006	12	8	0	52	21.472	138	-213	209	1.10	-9.	154/58/-018

11592	2006	12	8	21	25	51.278	138	-206	201	0.90	-9.	154/58/-018
Cluster 82												
5562	2006	12	7	1	12	33.817	50	-191	-249	0.50	-9.	116/75/-155
5649	2006	12	7	1	55	41.664	48	-194	-253	0.90	-9.	116/75/-155
44	2006	12	7	2	30	20.457	50	-201	-246	1.38	0.9	116/75/-155
46	2006	12	7	3	55	29.854	38	-194	-260	1.43	1.3	116/75/-155
7671	2006	12	7	16	17	59.787	53	-246	-320	1.20	-9.	107/79/-152
58	2006	12	7	16	45	49.887	43	-194	-250	1.54	1.1	116/75/-155
59	2006	12	7	17	26	32.229	24	-200	-284	1.91	1.7	116/75/-158
69	2006	12	7	22	40	32.731	56	-246	-321	1.54	1.2	107/79/-152
82	2006	12	8	1	49	54.050	10	-198	-322	1.79	1.9	116/75/-155
9244	2006	12	8	1	50	3.400	40	-188	-247	1.40	-9.	116/75/-155
90	2006	12	8	5	31	51.284	59	-252	-345	1.60	1.5	107/79/-168
10322	2006	12	8	8	47	35.845	58	-249	-329	0.80	-9.	107/79/-152
94	2006	12	8	9	4	1.060	-5	-190	-340	2.24	2.2	116/75/-162
10953	2006	12	8	14	34	53.013	56	-247	-324	1.40	-9.	107/79/-152
108	2006	12	8	16	48	39.176	-39	-160	-321	2.95	3.4	105/77/-165
113	2006	12	8	20	19	39.665	44	-274	-384	2.29	2.5	107/75/-153
12040	2006	12	9	5	5	35.519	60	-250	-331	0.90	-9.	107/79/-152
Cluster 87												
9038	2006	12	8	0	45	34.166	110	-348	-141	1.00	-9.	162/88/ 010
9081	2006	12	8	1	2	15.143	105	-356	-135	0.50	-9.	162/88/ 010
9100	2006	12	8	1	7	10.271	104	-351	-133	0.70	-9.	162/88/ 010
77	2006	12	8	1	21	59.367	105	-344	-128	1.50	1.3	162/88/ 010
9299	2006	12	8	2	8	10.805	103	-353	-126	0.70	-9.	162/88/ 010
85	2006	12	8	2	36	32.467	103	-344	-115	1.57	1.6	162/88/ 010
9431	2006	12	8	2	54	38.311	107	-360	-120	0.60	-9.	162/88/ 010
87	2006	12	8	3	24	3.546	109	-352	-98	2.24	2.3	162/88/ 010
10403	2006	12	8	9	25	23.888	127	-383	-146	1.00	-9.	162/88/ 010
111	2006	12	8	19	25	13.448	125	-380	-110	1.58	1.3	162/88/ 010
120	2006	12	9	1	58	54.507	126	-389	-116	1.09	0.8	162/88/ 010
Cluster 88												
88	2006	12	8	3	43	43.435	-45	261	298	1.75	1.6	359/85/ 014
97	2006	12	8	11	3	14.568	-49	296	329	1.56	1.6	359/85/ 014
11013	2006	12	8	15	1	42.641	-50	290	314	1.00	-9.	359/85/ 014
11108	2006	12	8	15	49	29.720	-49	316	359	0.90	-9.	359/85/ 014
118	2006	12	8	23	11	35.576	-49	328	371	1.47	1.4	359/85/ 014
12258	2006	12	9	9	41	9.241	-48	323	356	1.20	-9.	359/85/ 014
12278	2006	12	9	10	9	6.533	-56	370	358	0.70	-9.	359/85/ 014
134	2006	12	9	10	52	23.705	-46	314	330	1.44	1.2	359/85/ 014
12683	2006	12	9	22	30	2.820	-53	395	346	0.90	-9.	359/85/ 014
140	2006	12	9	23	3	12.798	-51	359	353	1.41	1.1	359/85/ 014
12844	2006	12	10	5	30	53.204	-49	295	323	0.90	-9.	359/85/ 014
12848	2006	12	10	5	36	41.828	-49	290	314	1.00	-9.	359/85/ 014
146	2006	12	10	5	39	57.197	-38	337	302	1.42	1.3	359/85/ 014
151	2006	12	10	10	45	3.159	-37	312	351	1.75	1.6	359/85/ 014
13099	2006	12	11	2	15	2.881	-58	388	355	0.90	-9.	359/85/ 014
13180	2006	12	11	11	59	28.538	-53	390	347	0.90	-9.	359/85/ 014
13255	2006	12	12	0	6	2.916	-54	391	343	1.30	-9.	359/85/ 014
163	2006	12	21	7	40	45.102	-47	346	289	1.53	1.4	359/85/ 014
Cluster 102												
9744	2006	12	8	4	54	34.431	111	-361	-293	0.70	-9.	331/71/-043
9860	2006	12	8	5	40	47.875	111	-374	-300	0.40	-9.	331/71/-043
92	2006	12	8	6	37	16.142	102	-335	-313	1.50	1.1	331/71/-043
9990	2006	12	8	6	37	21.134	104	-337	-313	1.40	-9.	331/71/-043
10169	2006	12	8	7	48	8.619	130	-368	-345	1.20	-9.	331/71/-043
10203	2006	12	8	8	0	3.390	117	-376	-326	1.10	-9.	331/71/-043
10266	2006	12	8	8	28	15.629	102	-334	-314	0.90	-9.	331/71/-043
95	2006	12	8	9	16	22.049	122	-366	-326	1.40	1.3	331/71/-043

10447	2006	12	8	9	47	16.219	112	-377	-317	1.00	-9.	331/71/-043
10539	2006	12	8	10	26	35.063	124	-379	-329	0.90	-9.	331/71/-043
10754	2006	12	8	13	0	53.852	101	-336	-316	1.40	-9.	331/71/-043
101	2006	12	8	13	30	29.832	120	-359	-323	1.91	1.7	331/71/-043
102	2006	12	8	15	12	51.864	120	-356	-331	1.89	2.0	331/71/-043
107	2006	12	8	16	29	26.471	78	-282	-329	1.58	1.2	330/70/-053
11956	2006	12	9	3	26	51.036	75	-264	-334	0.30	-9.	330/70/-053
11995	2006	12	9	4	16	51.925	71	-262	-331	1.00	-9.	330/70/-053
12014	2006	12	9	4	41	47.758	78	-268	-347	0.60	-9.	330/70/-053
12182	2006	12	9	8	6	0.519	80	-272	-344	0.50	-9.	330/70/-053
131	2006	12	9	9	39	35.794	78	-280	-341	1.31	0.8	330/70/-053
12332	2006	12	9	11	38	43.490	136	-384	-354	1.00	-9.	331/71/-043
12445	2006	12	9	14	47	6.384	68	-255	-320	0.50	-9.	330/70/-053
12613	2006	12	9	20	5	40.258	83	-273	-349	0.50	-9.	330/70/-053

Cluster 135

135	2006	12	9	14	17	39.641	243	-139	331	1.74	1.6	178/48/-022
12496	2006	12	9	16	6	47.560	262	-37	383	0.40	-9.	178/47/-022
12644	2006	12	9	20	58	0.057	289	-107	435	0.60	-9.	182/49/-013
12654	2006	12	9	21	33	32.968	257	-33	396	0.20	-9.	178/47/-022
12660	2006	12	9	21	48	59.481	297	-117	442	0.40	-9.	182/49/-013
12712	2006	12	9	23	44	50.264	276	-75	408	0.30	-9.	178/47/-022
12724	2006	12	10	0	20	13.209	263	-63	390	0.60	-9.	178/47/-022
12742	2006	12	10	1	10	31.390	286	-111	448	0.30	-9.	182/49/-013
12755	2006	12	10	1	32	0.614	286	-115	439	0.50	-9.	182/49/-013
12782	2006	12	10	3	1	52.430	298	-115	451	0.40	-9.	182/49/-013
12799	2006	12	10	3	44	10.033	294	-106	447	0.40	-9.	182/49/-013
12800	2006	12	10	3	44	51.092	287	-110	445	0.50	-9.	182/49/-013
143	2006	12	10	4	23	58.561	240	-195	307	1.33	0.9	178/46/-013
149	2006	12	10	9	28	7.728	279	-141	375	1.77	1.5	178/47/-019
150	2006	12	10	9	48	40.240	213	-197	274	1.60	1.3	178/46/-020
12912	2006	12	10	10	2	29.875	302	-122	445	0.90	-9.	182/49/-013
152	2006	12	10	13	53	14.344	215	-213	268	1.65	1.3	178/46/-020
12982	2006	12	10	15	9	52.067	282	-80	408	0.90	-9.	178/47/-022
153	2006	12	10	15	22	30.547	298	-135	403	1.99	1.6	182/49/-013
154	2006	12	10	17	30	31.241	225	-231	284	1.63	1.4	178/46/-020
13230	2006	12	11	19	37	17.819	265	-53	393	0.40	-9.	178/47/-022
158	2006	12	13	11	49	26.880	259	-38	383	1.52	1.0	178/47/-022

Stress tensor changes related to fluid injection at The Geysers geothermal field, California

Patricia Martínez-Garzón,[1] Marco Bohnhoff,[1,2] Grzegorz Kwiatek,[1] and Georg Dresen[1]

Received 25 March 2013; revised 25 March 2013; accepted 29 March 2013; published 7 June 2013.

[1] Studying variations of the stress field in reservoirs caused by massive fluid injection is important toward an improved understanding of geomechanical processes involved. We report on spatio-temporal variations of the local stress tensor orientation at The Geysers geothermal field, California. We apply two stress inversion methods with detailed uncertainty assessments using a selection of events recorded between 2007 and 2012. Our results clearly indicate variations in the orientation of the principal stress axes for the reservoir as a whole showing a normal faulting regime at the reservoir depth between 2 and 3.7 km bounded by a strike-slip regime above and below. Analyzing the temporal evolution of the stress tensor orientation for a prominent seismicity cluster we observe a clear correlation of changes in orientation for σ_{1-3} with the highest injection rates. These results suggest that temporal changes in the stress tensor orientation could contribute to characterize reservoirs during stimulation.
Citation: Martínez-Garzón, P., M. Bohnhoff, G. Kwiatek, and G. Dresen (2013), Stress tensor changes related to fluid injection at The Geysers geothermal field, California, *Geophys. Res. Lett.*, *40*, 2596–2601, doi:10.1002/grl.50438.

1. Introduction

[2] Determining and studying crustal stress field orientations by inverting earthquake focal mechanisms has proven to be a robust and effective tool to study fault mechanics along plate boundaries [e.g., *Hardebeck and Hauksson*, 2001; *Townend and Zoback*, 2001] or even spatiotemporal rotations of principal stresses related to major earthquakes [e.g., *Michael*, 1987a; *Bohnhoff et al*., 2006]. While stress rotations in most studies were in the order of 10–20° at best and thus close to the typical resolution limit of most data sets, recent $M \sim 9$ megathrust earthquakes showed larger stress rotations ($>20°$) clearly associated with the mainshock ruptures [*Hasegawa et al*., 2011; *Hardebeck*, 2012].

[3] Stress inversion techniques have also been applied to induced seismicity related to fluid injection into different types of reservoirs [*Oppenheimer*, 1986; *Feng and Lees*, 1998; *Sasaki and Kaieda*, 2002; *Bohnhoff et al*., 2004]. These studies have mainly focused on spatial analyses around the geothermal area and particularly on the variations in stress field orientation with depth.

[4] Spatio-temporal variations of the crustal stresses on the reservoir scale may be caused by massive fluid injections and extractions [*Segall and Fitzgerald*, 1998]. Detection of potential stress changes is important toward an improved understanding of the associated geomechanical processes at reservoir depth. However, an accurate and reliable determination of injection-induced changes in stress orientation is not trivial and requires dense local seismic networks allowing determining reliable and accurate focal mechanism data. For this reason, such observations are still few and a description of the stress field response of a reservoir where massive fluid injection is performed remains not fully understood.

[5] In this study, we investigate potential spatial and temporal variations of the stress field orientation at The Geysers (TG) geothermal area, which provides the largest existing data set of induced seismicity with ~500,000 events since the beginning of operation in the 1960s. We also selected this data set due to the great amount of local and regional seismic networks and stations available allowing calculating reliable focal mechanisms. First, we calculate the stress tensor orientation at different depths (local coordinate system) throughout TG. Second, we investigate a prominent cluster of induced seismicity within the reservoir and relate the stress inversion results to injection rates of the two nearby wells. Our main goal is to determine whether changes in the stress field can contribute to detect (or even monitor) potential changes in a reservoir due to fluid injection.

2. Data and Method

[6] We used the stress inversion software package SATSI developed by *Hardebeck and Michael* [2006]. SATSI is a linearized inversion scheme which uses focal mechanisms (strike/dip direction/dip angle) as input data. It allows for a spatial and/or temporal subdivision of the focal mechanism data set into smaller subareas. Then, a damped inversion method is applied to resolve the stress field orientation for each subarea taking into account the adjacent subareas to smooth the solution. Therefore, only strong heterogeneities of the stress tensor are left, while other variations, e.g., artifacts arising from data subdivision are smoothed. When using SATSI, we selected only seismic events with more than 10 high-quality first-motion polarities available (weight 0 as defined in *Klein* [2006]). Complementary, we also applied the MOTSI stress inversion method [*Abers and Gephart*, 2001]. MOTSI is a nonlinear scheme using first motion polarities as input data. Here, two nested grid searches are performed to identify the best-fitting stress orientations and focal mechanisms. The outer search tries a

[1]Section 3.2 Geomechanics and Rheology, GFZ German Research for Geosciences, Telegrafenberg, 14473 Potsdam, Germany.
[2]Free University Berlin, Institute of Geological Sciences, Berlin, Germany.

Corresponding author: P. Martínez-Garzón, Section 3.2 Geomechanics and Rheology, GFZ German Research for Geosciences, Telegrafenberg, 14473 Potsdam, Germany. (patricia@gfz-potsdam.de)

0094-8276/13/10.1002/grl.50438

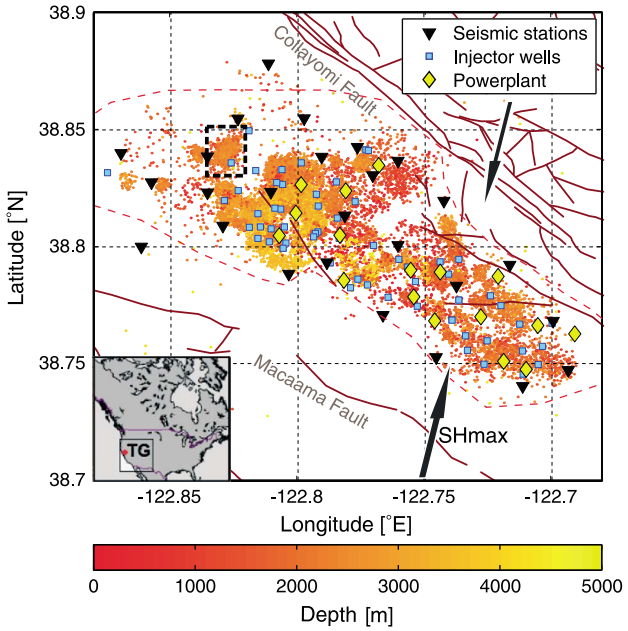

Figure 1. Spatial distribution of seismic events at The Geysers ($M >= 1$) from September 2007 to July 2012 (Data from NCEDC catalog). Hypocentral depth is color encoded. Selected cluster for temporal stress field variation analysis is surrounded with a black rectangle. Black triangles represent the local seismic network from LBNL. Yellow rhombs represent active powerplants, blue squares represent injection wells (not all wells from the field are plotted). Black arrows represent the direction of the regional stress field as described in *Oppenheimer* [1986] and *Provost and Houston* [2003]. Bottom-left corner: Overview on the location of TG in North America.

range of values for three stress directions and a relative stress magnitude $R = (\sigma_1 - \sigma_2/\sigma_1 - \sigma_3)$. Then, an inner grid search is conducted for each stress model and determines the focal mechanisms that best fit the first motions. To perform stress inversion with MOTSI we selected only events with a minimum of 20 high-quality first-motion polarities available (as recommended by *Abers and Gephart* [2001] to ensure correct results with this method). Outputs of both methods are the orientations of the principal stresses, σ_1, σ_2, σ_3, and a relative stress magnitude.

[7] To investigate the local stress tensor at TG we selected the hypocenter catalogue, fault plane solutions and first motion polarities as provided by Northern California Earthquake Data Center (NCEDC). We focus our study on the time period September 2007 to June 2012. The analyzed data set contained approx. 16,800 seismic events that occurred within TG area (Figure 1). They were recorded by a local seismic network operated by Lawrence Berkeley National Laboratory (LBNL), and by several regional permanent stations deployed at different distances around TG. The hypocenters were determined with the absolute location method HYPOINVERSE [*Klein*, 2002]. The local multilayered 1-D velocity model provided by *Eberhart-Phillips and Oppenheimer* [1984] is considered. Given the reasonably good azimuthal coverage of the seismic events and the large number of stations, the reported average horizontal location error for the NCEDC catalog calculated with HYPOINVERSE is 200 m and the vertical location error is 300 m.

[8] In a first step we searched for potential depth-dependent variations of the stress field orientation (Figure 2). For this part we selected seismic events with their epicenters distributed over the whole reservoir and sorted them according to the increasing depth. We performed a stress inversion of focal mechanisms using SATSI and a subset of first (shallowest) 150 events. Then, we moved by 100 events and repeated the inversion again using 150 events (i.e., the second subset contained 50 events overlapping with first one). This procedure (moving-depth window) was repeated until the last possible depth subset (containing the deepest 150 events). A few selected depth subsets are shown in Figures 2b and 2c, together with the corresponding results of stress inversion (Figure 2a). For comparison we also performed separate stress inversions using MOTSI.

[9] For the temporal analysis, we selected seismic data from a spatially constrained seismicity cluster located in the northwestern part of the reservoir (rectangle in Figure 1). In the direct vicinity of the cluster there are two wells for fluid injecting. The first well is used as a demonstration site for an Enhanced Geothermal System; there, injection resumed in November 2007. At the second well, injections started on April 2010. Gross amount of fluid injected is remarkably lower than in the first well, although both follow the same seasonal tendency (gross amount of fluid injected during winter months is higher than in summer months). During these injections, 742 earthquakes occurred. Their magnitudes vary between 1.0 and 3.1, and the majority of them are located at depths between 2000 and 3000 m. There is no first-order depth variation throughout the analyzed interval. If more than one possible focal mechanism was provided, we selected the one with the smallest misfit. The focal mechanism catalog includes a substantial variation in mechanisms allowing for a reliable estimation of stress field orientation. Sorting the events with time we formed subsets of 55 events and inverted moving windows with 10-event increments using the SATSI stress inversion. The number of events in one subset was selected to balance a tradeoff between the discrimination of different injection stages and the insurability of a certain variety of focal mechanisms. The required variety of focal mechanisms for each stress inversion was checked by inspection of the respective distribution of P and T axes.

[10] Because we aimed at detecting relatively small variations in the stress field orientation that could be close to the resolution limit of the methods applied, we performed complete uncertainty assessments for both used inversion methods. For SATSI we used bootstrap resampling method. Each fault plane solution taken into inversion was selected randomly from the two nodal planes available (i.e., we do not have a preference for one of the two permitted fault planes). For MOTSI the uncertainties were estimated applying a Bayesian technique. All inversion results shown in the following sections provide the best solution as well as the 95% confidence interval (2σ).

3. Results

3.1. Depth-Dependent Stress Field Changes

[11] Inverting subsets formed after hypocentral depth with the SATSI routine we find clear changes of the stress field orientation with depth (Figure 2a). At shallower level (down to $Z = 1000$ m) the σ_1 and σ_3 axes are oriented subhorizontal

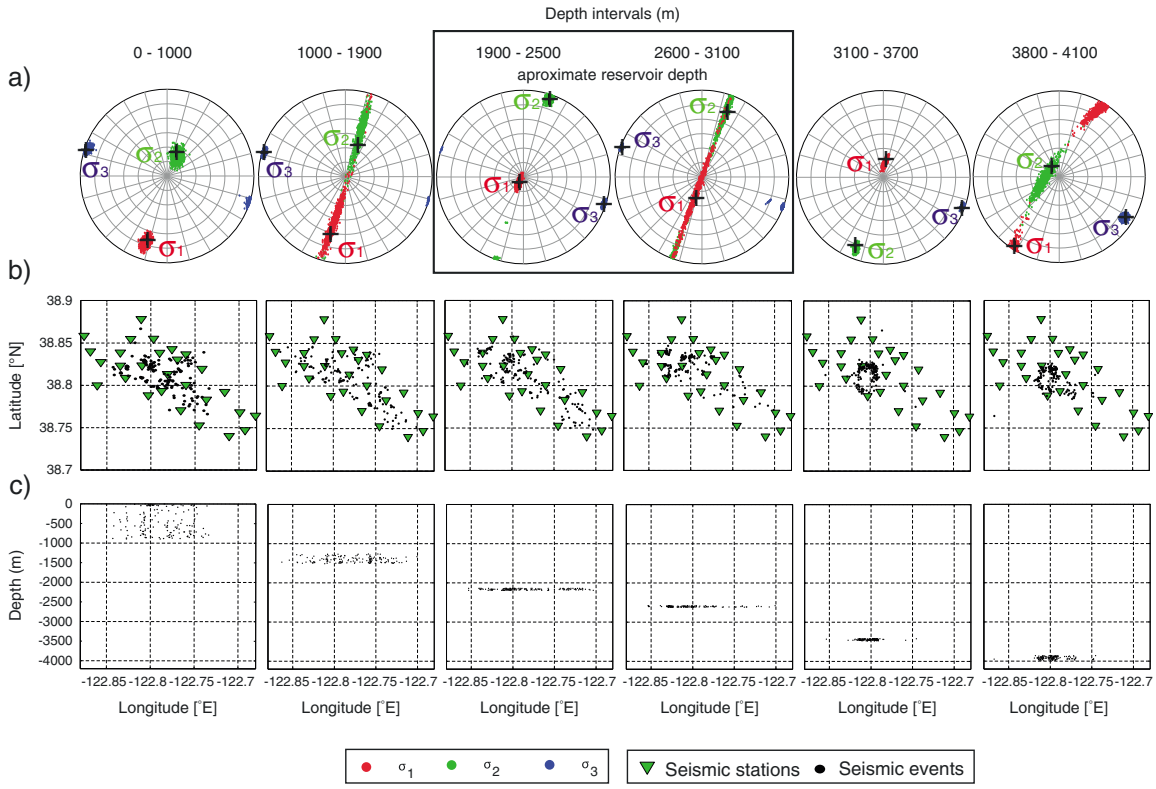

Figure 2. (a) Example of stress inversion results (lower hemisphere projection) representative for the average stress orientation of the total of inversions performed in each depth interval (depths in local coordinate system). Red, green and blue colors correspond to σ_1, σ_2, and σ_3 axes, respectively. Dots represent sampled bootstrap points framing the 95% confidence intervals. Black crosses mark the best stress orientation obtained from inversion. (b) Epicentral distribution of seismicity used in the corresponding inversion shown in Figure 2a. Green triangles represent seismic network from LBNL. (c) Seismic events from Figure 2b represented as a function of depth (note that as described in the text, several other stress inversions are performed, and therefore the seismic events plotted here are not representative of the total amount of seismicity but just for those event used in one particular inversion).

corresponding to a strike-slip regime. Between $Z = 1000$ m and $Z = 1900$ m, the position of the σ_1 and σ_2 axes is undefined considering plunges, indicating a transtensional stress regime. Between $Z = 1900$ m and $Z = 2500$ m, the σ_1 and σ_2 axes stabilize and σ_1 becomes vertical indicating a WSW/ENE-extensional normal faulting regime. Further below and down to $Z = 3800$ m changes to transtensional and normal faulting are repeated. Finally, at the deepest analyzed intervals $Z = 3800$ m to $Z = 4100$ m (below the geothermal reservoir) the σ_1 axis rotates back toward subhorizontal suggesting a strike-slip/transtensional regime as observed above the reservoir. As shown in Figures 2b and 2c for six selected depth intervals, the epicentral distribution of the seismic events considered for stress inversion is approximately homogeneous throughout the reservoir down to $Z = 2600$ m, while below this depth the hypocenters cluster in the central part of the reservoir delineating a circular structure [*Boyle et al.*, 2011]. The deepest seismicity is observed in the central and western part of the reservoir (cf. two right-most depth intervals presented in Figure 2). In all performed stress inversions the σ_3 axis is located subhorizontal pointing to N105°E. The trend of σ_1 and σ_2 remains stable at N15°E. Only for the deepest part of the reservoir the trend of σ_1 and σ_2 seems to be slightly rotated clockwise by 15°.

[12] The results from MOTSI generally follow those from SATSI described before with σ_1 and σ_3 being subhorizontally oriented in the shallower section. In contrast, the result for the deeper section includes a substantially steeper direction for σ_1 reflecting a strong normal faulting component. However, because the confidence intervals for σ_1 and σ_2 are partly overlapping the results indicate a transtensional stress regime at larger depth. This is also confirmed by the low values for the relative stress magnitude R obtained from both inversion routines.

3.2. Time-Dependent Stress Field Changes

[13] Analyzing the distribution of P and T axes of the 742 seismic events from the selected cluster suggests systematic variations during the investigated 5 year time period that can be easily correlated to injection rates (Figure 3a). The plunges of P axes before and after time periods with maximum injection rates are mainly distributed around the vertical direction. Remarkably, during the times of maximum flow rates P axes plunges decrease. We selected two time intervals framing the most prominent three peak injections (Intervals A and B, see black rectangles in Figure 3b) and performed a detailed time-dependent stress inversion analysis as described above using subsets of the data. The results confirm a clear and statistically significant relation between injection rates and changes in stress field orientation for all three principal stress axes (Figure 3c).

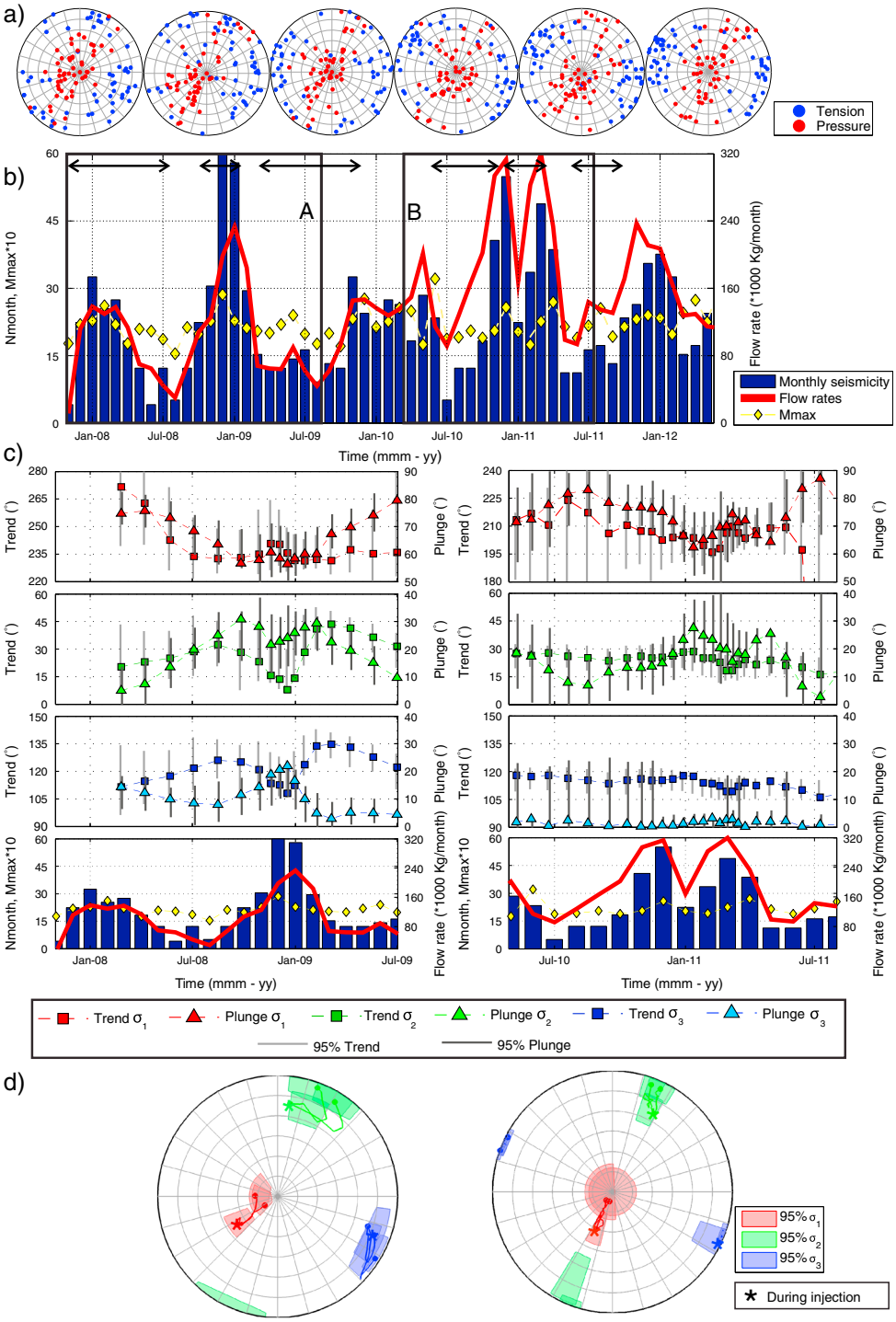

Figure 3. (a) Distribution of *P* and *T* axes of events used for stress inversions which contain seismic events from before, during and after the analyzed injections, respectively. The time frame covered in each plot is shown with the consecutive black horizontal arrows in Figure 3b. (b) Monthly seismicity rate from events from analyzed cluster (blue bars) from November 2007 to July 2012. Injection rates (gross amount injected/month) are plotted as a sum from both considered wells (solid red line). The maximum magnitude of each month is shown by a yellow rhomb. The black rectangles frame the two analyzed time intervals (A and B). (c) Results from the stress inversions performed during the time interval framed by black rectangles in Figure 3b. Each symbol represents one stress inversions which time average corresponds to the *X* coordinate. From top to bottom: Trend (squares) and plunge (triangles) of σ_1 (first plot – red), σ_2 (second plot – green) and σ_3 (third plot – blue). For these three graphics, light and dark gray vertical bars represent 95% confidence intervals of trend and plunge, respectively. Next plot contains a zoom from b) corresponding to the analyzed time intervals. (d) Variations of the stress field orientation during the selected time frames plotted in the lower hemisphere. Red: σ_1, Green: σ_2, Blue: σ_3. Solid lines: Trajectory described by the best solution. Semitransparent region: 95% confidence interval corresponding to three inversions before, during and after the performed inversions.

[14] The change in plunge of σ_1 is similar for all three injections. Prior to an injection, the σ_1 axis is close to vertical. Inversion of faulting mechanisms from seismic events that occurred during peak-injection rates results in a progressive decrease in the plunge of σ_1. Moreover, including seismic events from the time period after the injection peak, the σ_1 axis rotates back toward close to its initial vertical position. The change in the plunge of σ_1 is significant and varies between 15° and 20°.

[15] During interval A (peak-injection in December 2008), the plunges of the σ_2 and σ_3 axes also vary in accordance with injection rates. The plunge of σ_2 increases gradually and then during injection it slightly decreases by 15°. Similarly, the plunge of σ_3 gradually increases until the peak-injection and then decreases toward values from prior to the injection. For both σ_2 and σ_3 axes a counterclockwise and transient change in the axes trend is observed by about 25°. During interval B (peak injections in December 2010 and March 2011) the plunges of σ_1 and σ_2 show the most pronounced correlation with the gross amount of fluid injected. They show an inverse variation of approximately 20°. The plunge of σ_3 remains constant.

[16] There are two minor but important differences between the two analyzed periods: First, the time interval A shows variations in both trend and plunge of the three principal axes, while for the interval B no remarkable changes in trend are observed but the plunge of the σ_1 and σ_2 axes varies significantly. Second, during interval A the change in stress orientation is synchronous with fluid injection, whereas in interval B the stress changes appear slightly delayed.

4. Discussion and Conclusions

[17] Due to the high rate of seismicity at The Geysers geothermal field and the exceptionally good quality of the seismic data available, this data set provides a good opportunity to derive a better understanding on the effects of fluid injection on the stress state in the reservoir. In this study, stress inversion methods have been applied to two data subsets of induced seismicity. For the first case, the seismic events are distributed over the entire reservoir and we searched for potential variations of the stress tensor orientation with reservoir depth. For the second case, seismic events from a particular cluster of events were analyzed with regard to potential temporal variations in the orientation of the local stress field related to fluid injection in two wells. In both cases, the variations observed are significant considering 95% of confidence interval.

[18] Studies about the regional stress field of Northern and Central California indicate that the stress field around TG is consistent with a strike-slip regime with the direction of maximum horizontal compression being oriented N26°E, and thus inclined by 55° with respect to the regional strike of the San Andreas Fault system [*Provost and Houston*, 2003; *Hardebeck and Michael*, 2004]. No first-order spatial variations within TG have been reported [e.g., K. Boyle and M. Zoback, pers. comm., 2012]. In general, our analysis shows a combined strike-slip/normal faulting regime consistent with the known regional stress field in Northern California.

[19] Results from depth-dependent changes of the stress field orientation indicate a transition in the stress regime from strike slip above the reservoir to transtensional and normal at the reservoir level and finally transtensional and strike-slip below. This clear variation of the stress field orientation with depth is due to the flip of the plunges of the σ_1 and σ_2 axes, while their trend remains constant at N15°E. The changes observed in these axes are in accordance with changes in the value of the relative stress magnitude R, indicating that the magnitudes of σ_1 and σ_2 are less separated within the reservoir than outside.

[20] The cause of the changes in stress orientations observed with depth across the TG reservoir is still not well understood. A potential explanation could be related to the presence of fluids in the vapor-saturated reservoir level. The role of fluids modifying the stress field and the faulting regime has been already pointed out in earlier studies [e.g., *Hardebeck and Hauksson*, 1999; *Kato et al*., 2011]. In particular, *Segall and Fitzgerald* [1998] related a potential vertical variation of the stress state within the reservoir, above and below it to poroelastic effects related to reservoir depletion, i.e., on a time scale of decades. Specifically, the authors suggest that the horizontal stresses immediately above and below a reservoir are more compressive than within the reservoir. This is in qualitative agreement with the observed change in maximum compressive stress orientation from about horizontal above and below the reservoir to vertical within the reservoir. However, a quantitative assessment of interaction of stress rotation with variations in fluid pressure and depth does not yet exist for TG. Alternatively, the variations of the stress regimes with depth could also be related to the different geological formations within and above/below the reservoir. Particularly, the transition from graywacke sandstone to thermally altered graywacke sandstone where the temperature gradient is extremely high could affect the state of stress in the rocks, while a correlation between the average stress regime and the different geological layers remains imprecise due to the irregular high temperature layer at TG [*Calpine Corporation*, 2012].

[21] Although one of the assumptions for the inversion of fault plane solutions to determine the stress field orientation is a homogeneous stress field within the volume considered by the individual focal mechanism hypocenters [*Michael*, 1987b], we believe that the stress field at TG might have local spatial variations due to different injection and production sites and schedules. For this reason, the stress field orientations calculated in this part of the study provides an average of the expected different local stress field orientations throughout TG.

[22] In the second part of the study we analyzed potential temporal variations of the stress field orientation focusing on one particular spatially well-constrained seismicity cluster at the northwest of TG. Our results clearly show a systematic rotation of the principal stress axes during periods of massive fluid injection (Figure 3). This observation for itself is remarkable in that it allows using an observed stress field orientation as a proxy for a change in the geomechanical status of a (geothermal) reservoir, e.g., during stimulation through massive fluid injection. More interestingly, this correlation of stress field rotation and peak-injection rates is observed in all cases analyzed so far. On the other hand, the variation is more evident in the first remarkable injection performed in the investigated area (corresponding to interval A). This observation suggests that the effect of the stress perturbation due to the fluid injection might decrease over time with repeated injections. This might also be seen as an explanation for the delayed stress

change during the second peak-injection period. It is well known that the injection of fluid increases the pore pressure of the rock matrix and according to the rock failure criteria it facilitates the slip of the rocks. However, a complete geomechanical explanation of the stress tensor changes observed in our study leaves open several questions. The existence of local faults at TG NE/SW oriented is consistent with the direction of regional maximum horizontal stress. In response to the three injections considered in our study, the σ_1 axes are moving toward shallower plunges, while the trend is changing by a lesser extent and being in SW direction in first-order approximation. One potential explanation for the observed stress tensor perturbation, therefore, is that with the massive fluid injections, preexisting local faults and fractures well-oriented for the regional stress would be reactivated or weakened for a short interval during high injection rates. A second possibility might be related to the fact that the analyzed cluster of seismicity is the result of one of the few Enhanced Geothermal System project performed at TG involving massive fluid injection and thereby aiming at increasing the permeability of the reservoir. Therefore, the active stimulation of the low-permeable reservoir may imply hydro-fracturing. It is then possible that during the time periods with higher injection rates of cold water, new small fractures were created and might have opened. These small fractures would then be oriented in the direction of σ_{Hmax} (NE-SW) and their activation could also perturb the stress field in the observed way.

[23] **Acknowledgments.** We acknowledge funding within the Helmholtz-Alberta Initiative, from the Helmholtz foundation in the framework of the YIG "From microseismicity to large earthquakes" and from the EU-GEISER project. We acknowledge seismic data availability from North California Earthquake Data Centre and hydraulic parameters from Department of Conservation State of California. We thank Roland Gritto, Calpine Ltd. and Michèle Ickrath. We thank Volker Oye and an anonymous reviewer for their comments.

[24] The Editor thanks Volker Oye and an anonymous reviewer for their assistance in evaluating this paper.

References

Abers, G. A., and J. W. Gephart (2001), Direct inversion of earthquake first motions for both the stress tensor and focal mechanisms and application to southern California, *J. Geophys. Res.*, *106*, 26,523–26,540, doi:10.1029/2001JB000437.

Bohnhoff, M., S. Baisch, and H.-P. Harjes (2004), Fault mechanisms of induced seismicity at the super deep German Continental Deep Drilling Program (KTB) borehole and their relation to fault structure and stress field, *J. Geophys. Res.*, *109*, B02309, doi:10.1029/2003JB002528.

Bohnhoff, M., H. Grosser, and G. Dresen (2006), Strain partitioning and stress rotation at the North Anatolian Fault after the 1999 Izmit M_W= 7.4 earthquake, *Geophys. J. Int.*, *166*(1), 373–385, doi:10.1111/j.1365-246X.2006.03027.X.

Boyle, K., S. Jarpe, L. Hutchings, S. Saltiel, J. Peterson, and E. Majer (2011), Preliminary investigation of an aseismic "doughnut hole" region in the northwest Geysers, California, PROCEEDINGS, Thirty-Sixth Workshop on Geothermal Reservoir Engineering Stanford University, Stanford, California, January 31 - February 2, 2011 SGP-TR-191.

Calpine Corporation (2012), NW Geysers Enhanced Geothermal System Demonstration Project, *Update Report*, http://www.geysers.com/docs/11022012%20EGS_Community%20Update%20Presentation.pdf

Eberhart – Phillips, D., and D. Oppenheimer (1984), Induced Seismicity in The Geysers Geothermal Area, California, *J. Geophys. Res.*, *89*(B2), 1191–1207.

Feng, Q., and J. M. Lees (1998), Microseismicity, stress, and fracture in the Coso geothermal field, California, *Tectonophysics*, *289*, 221–238.

Hardebeck, J. L., and E. Hauksson (1999), Role of Fluids in Faulting Inferred from Stress Field Signatures, *Science*, *285*, 236, doi:10.1126/science.285.5425.236.

Hardebeck, J. L., and E. Hauksson (2001), Crustal stress field in southern California and its implications for fault mechanics, *J. Geophys. Res.*, *106*, 21,859–21,882.

Hardebeck, J. L., and A. J. Michael (2006), Damped regional-scale stress inversions: Methodology and examples for Southern California and the Coalinga aftershock sequence, *J. Geophys. Res.*, *111*, B11310, doi:10.1029/2005JB004144.

Hardebeck, J. L., and A. J. Michael (2004), Stress orientations at intermediate angles to the San Andreas Fault, California, *J. Geophys. Res.*, *109*, B11303, doi:10.1029/2004JB003239.

Hardebeck, J. (2012), Coseismic and postseismic stress rotation due to great subduction zone earthquakes, *Geophys. Res. Lett.*, *39*, L21313, doi:10.1029/2012GL053438.

Hasegawa, A., K. Yoshida, and T. Okada (2011), Nearly complete stress drop in the 2011 Mw 9.0 off the Pacific coast of Tohoku earthquake, *Earth Planets Space*, *63*(7), 703–707, doi:10.5047/eps.2011.06.007.

Kato, A., et al. (2011), Anomalous depth dependency of the stress field in the 2007 NotoHanto, Japan, earthquake: Potential involvement of a deep fluid reservoir, *Geophys. Res. Lett.*, *38*, L06306, doi:10.1029/2010GL046413.

Klein, F. W. (2002), User's Guide to HYPOINVERSE-2000, a Fortran Program to Solve for Earthquake Locations and Magnitudes, Open file report. URL: http://geopubs.wr.usgs.gov/open-file/of02-171/

Klein, F. W. (2006), Y2000 shadow format and NCSN data codes. Open file report, URL: NCEDC, http://www.ncedc.org/ftp/pub/doc/ncsn/shadow2000.pdf

Michael, A. J. (1987a), Stress Rotation during the Coalinga Aftershock Sequence, *J. Geophys. Res.*, *92*, 7963–7979.

Michael, A. J. (1987b), Use of focal mechanisms to determine stress: a control study, *J. Geophys. Res.*, *92*, 357–368.

Oppenheimer, D. (1986), Extensional tectonics at The Geysers Geothermal Area, California, *J. Geophys. Res.*, *91*, 11,463–11,476.

Provost, A. S., and H. Houston (2003), Stress orientation in northern and central California: Evidence for the evolution of frictional strength along the San Andreas plate boundary system, *J. Geophys. Res.*, *108*(B3), 2175, doi:10.1029/2001JB001123.

Sasaki, S., and H. Kaieda (2002), Determination of stress state from local mechanisms of microseismic events induced during hydraulic injection at the Hijiori Hot Dry Rock site, *Pure Appl. Geophys.*, *159*, 489–516.

Segall, P., and S. D. Fitzgerald (1998), A note on induced stress changes in hydrocarbon and geothermal reservoirs, *Tectonophysics*, *289*, 117–128.

Townend, J., and M. D. Zoback (2001), Implications of earthquake focal mechanisms for the frictional strength of the San Andreas fault system, *Geol. Soc. Spec. Publ. London*, *186*, 13–21, doi:10.1144/GSL.SP.2001.186.01.02.

Geophysical Journal International

Geophys. J. Int. (2013) doi: 10.1093/gji/ggt301

Geophysical Journal International Advance Access published August 28, 2013

Fatigue hydraulic fracturing by cyclic reservoir treatment enhances permeability and reduces induced seismicity

Arno Zang, Jeoung Seok Yoon, Ove Stephansson and Oliver Heidbach

GFZ German Research Centre for Geosciences, Section 2.6 Seismic Hazard and Stress Field, Telegrafenberg, D-14473 Potsdam, Germany.
E-mail: zang@gfz-potsdam.de

Accepted 2013 July 23. Received 2013 July 22; in original form 2013 March 18

SUMMARY

The occurrence of induced seismic events during hydraulic fracturing of reservoirs to enhance permeability is an unavoidable process. Due to the increased public concern with respect to the risks imposed by induced seismicity, however, the development of a soft stimulation method is needed creating higher permeability with less induced seismicity. We use a discrete element model of naturally fractured rock with pore fluid flow algorithm in order to analyse two scenarios of high-pressure fluid injection (hydraulic fracturing) at depth and associated induced seismicity. The ratio of pumped-in energy to released seismic energy is in agreement with field data. Our results suggest that cyclic reservoir treatment is a safer alternative to conventional hydraulic fracture stimulation as both, the total number of induced events as well as the occurrence of larger magnitude events are lowered. This work is motivated by results of laboratory triaxial indenter tests on granite rock samples where continuous loading leads to a wide fracture process zone while cyclic treatment with frequent starting and stopping of loading fatigues the rock, resulting in smaller damage volume and more persistent fracture growth.

Key words: Geomechanics; Fracture and flow; Seismicity and tectonics.

1 INTRODUCTION

Hydraulic stimulation of rock mass at depth is an essential component to enhance permeability in the development of hydrocarbon and geothermal reservoirs (MIT Report 2006; Majer *et al.* 2007). An unavoidable by-product of hydraulic stimulation, however, is the generation of induced seismic events (Suckale 2009) which became a major concern in particular for geothermal sites near densely populated areas (Deichmann & Gardini 2009). The stimulation of the geothermal site in the suburb of Basel in Switzerland for example, induced a seismic event with moment magnitude, M_w 3.2 which finally stopped the project. This event was, in particular in Europe, the nucleus of an on-going discussion on induced seismicity not only for hydraulic fracturing (HF) at geothermal sites, but also for the potential risk of induced seismicity in general (Giardini 2009).

Since then, several approaches were proposed that potentially lower the occurrence probability of induced seismic events (Bommer *et al.* 2006; Shapiro *et al.* 2010; Barth *et al.* 2013). These approaches have in common that they are based on a recorded catalogue of induced seismicity and thus can only be applied in real-time during the stimulation. Furthermore, since the recorded seismicity is analysed with either empirical laws (Bachmann *et al.* 2012) or with a point source of constant or increasing pressure (Dinske & Shapiro 2013), these approaches cannot provide a priori practical recommendations to the reservoir engineer of how to perform the stimulation experiment in order to lower the released seismic energy and enhance permeability at the same time.

To overcome these problems, one can use hydro-mechanical coupled, discrete element models which not only help to understand the mechanics of fluid-induced seismicity, provide insights on the relationship between seismicity, stress field, damage pattern and propagating fluid front (Zhao & Young 2011), but also have *a priori* predictive power. Therefore, we propose to use the forward hydro-mechanical coupled model with discrete element-fracture network of Yoon *et al.* (2013). This model is able to (1) simulate injection in fractured reservoirs with arbitrary fluid injection pressure schemes, (2) propagate mode I (tensile) and mode II (shear) fractures, and (3) generate fluid-induced seismicity catalogues. This model allows testing of different stimulation scenarios with the same initial conditions in terms of rock properties and *in situ* stress. In particular, cyclic stimulation is tested versus the established, continuous stimulation where the injection pressure is increased in steps (e.g. Evans *et al.* 2005). During cyclic treatment fluid injection is stopped frequently to allow for relaxation of peak stress at the fracture tip (2-D)/front (3-D).

The motivation for testing cyclic stimulation is derived from laboratory triaxial indenter tests of granite cores (Zang *et al.* 1998, 2002). These tests indicate that displacement-controlled loading,

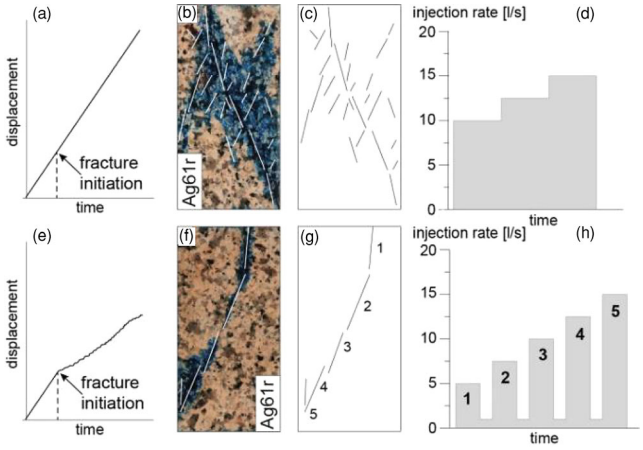

Figure 1. (a) Loading curve, (b) result and (c) interpretation of a laboratory triaxial indenter test on granite cores where loading is kept constant (Zang *et al.* 1998). (b, c) Fractures impregnated with blue epoxy dye, develop over a wide zone. (d) This is interpreted as an analogue of continuous stimulation with monotonic increase of injection rate. (e–g) Loading is crack-rate-controlled and leads to frequent stop of the displacement (Zang *et al.* 2002). (f, g) The fracture zone is much narrower. (h) We translate this as cyclic stimulation where fluid injection is stopped frequently in order to allow the peak stresses at the fracture tip to relax.

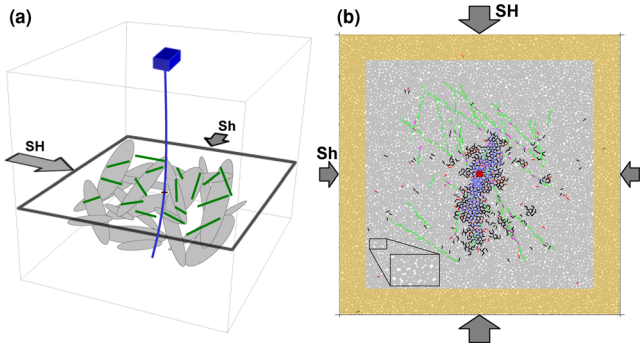

Figure 2. (a) 3-D schematic view of fluid injection in naturally fractured geothermal reservoir. Injection well (*blue*) and traces (*green*) of penny shaped cracks (*grey*) on horizontal cross section at specific depth. (b) Simulated 2-D reservoir model (2 km × 2 km) with discrete elements (*grey disks*) and pre-existing fractures (*green bars*) subjected to anisotropic stresses ($S_H = 75$ MPa, $S_h = 60$ MPa). Fluid injected at the model centre (*red dot*) diffuses by the pressure gradient. Pore pressure build up (*blue dots*) changes the stress state at the particle contacts and results in Mode I and Mode II failures of rock matrix (parallel bond failure, *black and red bars*) and of pre-existing discrete fractures (smooth joint bond failure, *blue and pink bars*). In shaded area near model boundary, high viscous damping is applied to exclude reflection of the seismic waves.

i.e. the monotonic increase of load with time (Figs 1a–c, Zang *et al.* 1998) generates a wider fracture process zone with more acoustic emissions count (seismic energy) as compared to cyclic loading, i.e. constant loading interrupted with multiple stopping phases of no further deformation (Figs 1e–g, crack-rate controlled tests, Zang *et al.* 2002) which results in a narrow zone of tensile and shear fractures (Zang *et al.* 2000). In the former test, the fracture process is controlled by the short adaption times of peak stresses that prevent the locating of the optimum growth path at the fracture tip/front. In the latter test, the frequent starting and stopping of loading fatigues the rock, resulting in smaller damage volume and more persistent fracture growth (Figs 1e–g). We translate the results of these laboratory tests into two different stimulation schemes. The first (Figs 1a–c) with monotonically increase of load resembles the continuous scheme where fluid injection rate is increased in steps (Fig. 1d). The second one (Figs 1e–g) we name cyclic stimulation where fluid injection rate is also increasing, but interrupted frequently with low fluid injection rate intervals (Fig. 1h).

2 SYNTHETIC CRYSTALLINE GEOTHERMAL RESERVOIR MODEL

A 3-D schematic view of the fluid injection in naturally fractured geothermal reservoir and horizontal cross section at specific target depth is shown in Fig. 2(a). In the 2-D simulated reservoir section (2 km × 2 km in size, Fig. 2b), the intact rock matrix part is represented using enhanced parallel bond model of the software PFC2D (Itasca 2012). The discrete elements are 20–30 m in diameter and the particle ensemble has strength, stiffness and deformation characteristics calibrated against Soultz-sous-Forêts granites. The pre-existing fractures are simulated by a smooth joint contact model (Fig. 2b). The mechanical property data of the embedded discrete fractures are taken from crystalline rock at Forsmark Sweden (Hökmark *et al.* 2010). A hydro-mechanical coupling scheme is implemented that enables fluid flow driven bond breakages in mode I (tensile) and mode II (shear) failure, following the Mohr-Coulomb criterion. The applied *in situ* stresses are those at 4 km depth ($S_H = 75$, $S_h = 60$ MPa) in Soultz-sous-Forêts (Cornet *et al.* 2007, their eq. 1a–c). Bond breakage results in seismic energy radiation from which seismic source information is retrieved, e.g. magnitude and focal mechanisms of mode I+II failure of rock matrix (Hazzard & Young 2002, 2004; Zhao & Young 2011; Yoon *et al.* 2012) and mode I+II failure of pre-existing joints (Yoon *et al.* 2013). Along the model boundaries a ∼150 m wide zone is assigned with high viscous damping properties to model energy absorption (Fig. 2b). This concept is taken to exclude side effects on bond breakages coming from reflected kinetic seismic wave energy at the model boundaries. During fluid injection in the centre of the model, the onset of tensile and shear fractures of intact rock (enhanced parallel bonds) and pre-existing joints (smooth joint contacts) are governed by Mohr-Coulomb failure criterion (e.g. Labuz & Zang 2012). More details of the model and parameters can be found in the supplementary material.

3 STIMULATION SCENARIOS AND FLUID-INDUCED SEISMICITY

In Fig. 3, we present the results of the two stimulation scenarios analysed. The left-hand side row (Figs 3a–e) shows the continuous stimulation where the flow rate is increased in three steps over 6 hr (10 l s^{-1} for the first 2 hr, 12.5 l s^{-1} for the next 2 hr and 15 l s^{-1} for the last 2 hr; Fig. 3a). The corresponding fluid pressure at the injection point is normalized to the fracture breakdown pressure (FBP) that is estimated from the classical HF theory (e.g. Zang & Stephansson 2010, their eq. 7.3), see Fig. 3(a) red line. Early seismic events occur when FBP is reached (Figs 3a and b). The 2-D nature of the model limits direct comparison with 3-D field injection tests, such as fluid injection rate and total fluid volume. Moment magnitudes (M_w) of induced seismic events are computed from mode I and mode II failures in the model reservoir. The related

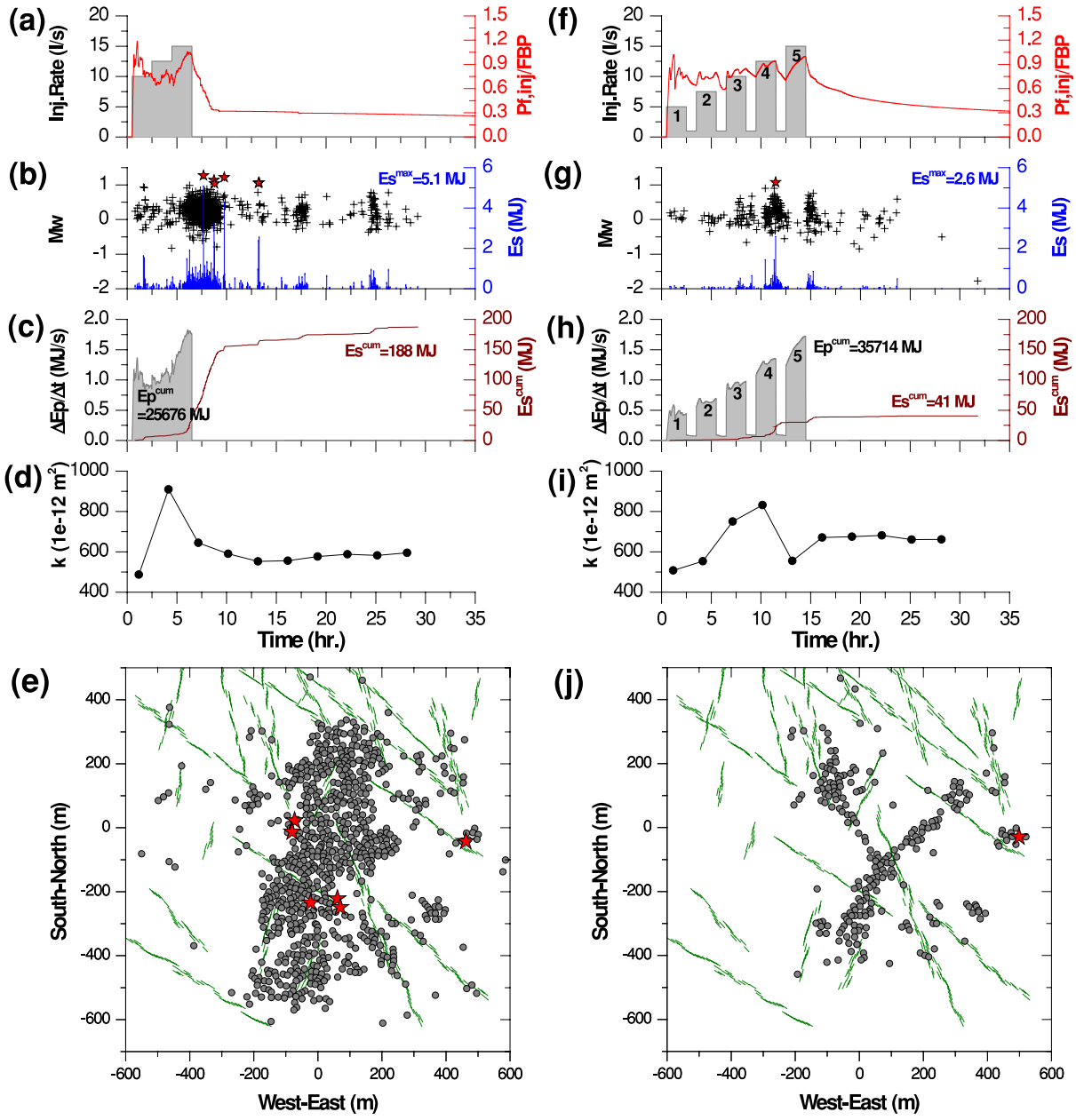

Figure 3. Results of continuous, step-wise fluid injection (a–e), and cyclic injection (f–j). Time variation of (a, f) injection rate (l s^{-1}), normalized fluid pressure at injection point, $P_{f,inj}$/ FBP; (b,g) Moment magnitude (M_w) and radiated seismic energy, E_s (MJ) of the induced events, E_s^{max} is the maximum E_s of a single event; (c, h) Time variation of rate of pumped-in hydraulic energy, E_p (MJ) and cumulative radiated seismic energy, E_s^{cum} (MJ). Shaded area represents total amount of pumped-in energy, E_p^{cum} (MJ); (d, i) Fracture permeability, k (Darcy, 1e-12 m^2) computed from the average hydraulic apertures of the induced events ($e_{avg}^2/12$); (e, j) Spatial distribution induced seismicity. Stars are induced events with moment magnitude, $M_w > 1.0$ which are indicated also in (b, g).

radiated seismic energy (E_s) presented in Fig. 3(b) is calculated from moment magnitudes using the relation

$$\log_{10}(E_s) = 4.8 + 1.5M_w \quad (1)$$

from Gutenberg & Richter (1956) and Kanamori (1977). As observed in field experiments the peak seismic activity coincides with the termination of fluid injection (Dorbath *et al.* 2009). Sometimes, larger magnitude events occur in the post-shut-in phase (Baisch *et al.* 2010). In Fig. 3(c), the time variation of hydraulic pumped-in energy rate ($\Delta E_p/\Delta t$) and the cumulative seismic radiated energy (E_s^{cum}) is shown. At the time fluid injection terminated, the total pumped-in energy is 25 676 MJ while the seismic radiated energy generated is only 45 MJ in the model reservoir. Most of the induced seismic energy is released in the time interval after the fluid pressure at the injection point has dropped (Fig. 3c, time 6.5 to 8.5 hr). In this interval, the cumulative value of radiated seismic energy increases from 45 MJ to 150 MJ, the latter value accounts for 80 per cent of the total value (188 MJ). Computation of seismic moment magnitude, seismic energy and permeability is described in the Supporting Information.

In Fig. 3(d), the permeability evolution with time is shown computed from average hydraulic aperture of induced fracture events. After a prominent peak in permeability during the stimulation the value remains after shut-in at around 590 Darcy (10^{-12} m^2). Fig. 3(e)

shows the spatial distribution of all induced seismic events displayed in Fig. 3(b). In analogy to the result of the laboratory rock tests (Fig. 1, upper row) the induced seismicity affects a wider area and six events with $M_w > 1.0$ are detected (red stars in Figs 3b and e). In total, 785 induced events are observed; 643 of these occur after the shut-in of fluid injection.

The right-hand side column of Fig. 3 shows results of the cyclic stimulation scenario where fluid flow rate is also increasing with time, but interrupted frequently (Figs 3f–j). The flow rate is lowered to a residual value of $1\,l\,s^{-1}$ before each step-wise increase from $5\,l\,s^{-1}$ initial to $15\,l\,s^{-1}$ final value (Fig. 3f). Most seismic activity is related to the pre-shut-in period of the stimulation before the fluid pressure at the injection point decays exponentially (Figs 3f and g). The largest magnitude induced seismic event occurs at the end of the fourth cycle (Fig. 3g, time 11.5 hr). The time variation of energy partition for cyclic stimulation is presented in Fig. 3(h). Even though the total cumulative pumped-in energy value is higher after the cyclic injection (35 714 MJ) as compared to the continuous, step-wise injection (25 676 MJ), the cumulative seismic energy released in cyclic stimulation (Fig. 3h, 41 MJ) is only a fraction (22 per cent) of the corresponding value in continuous fluid stimulation (Fig. 3c, 188 MJ). The faster relaxation of fluid pressure after shut-in of the continuous injection (Fig. 3b), results in a denser cluster of induced events with larger crack apertures for fluid path ways.

The increase in permeability during cyclic treatment (Fig. 3i) is not as steep as for the continuous step-wise fluid injection (Fig. 3d), but at the end of the treatment the remaining value of 660 Darcy is slightly higher compared to the value of 590 Darcy after continuous injection (Fig. 3d). Fig. 3(j) shows the spatial distribution of all induced seismic events of the cyclic injection displayed in Fig. 3(g). In analogy to the result of the laboratory tests (Fig. 1, lower row) the induced seismicity affects a substantially smaller area and only one event with $M_w > 1.0$ is detected (red star in Figs 3g and j). The cyclic injection generates an Y-shape seismicity pattern with early events close to the injection point (Figs 3g and j). The branching of the fracture propagating towards North occurs parallel and conjugate to the pre-existing fracture network. Fracture growth towards South is almost parallel to the maximum compressive stress orientation. The cyclic injection generates very few post-shut-in events in particular for induced events with higher magnitudes (Fig. 3g). In total, only 244 induced events are observed in cyclic injection, from which 76 occur in the post-shut-in phase.

4 HYDRAULIC VERSUS SEISMIC RADIATED ENERGY

In Table 1, we summarize the main characteristics of the two simulated injection scenarios. While in the continuous, step-wise injection scenario 270 m^3 of fluid is pumped into the model reservoir, the cyclic testing involves injecting 374 m^3. The total pumped-in hydraulic energy (E_p) after the continuous injection is 25 676 MJ and 35 714 MJ after the cyclic injection. Only 244 induced events are observed during cyclic stimulation while 785 induced events are generated in the continuous injection scenario. The maximum occurrence rate of induced events drops to about half the value from continuous to cyclic injection. The cumulative seismic radiated energy (E_s^{cum}) in the continuous and cyclic injections is 188 and 41 MJ, respectively. This means that about 0.1 per cent of the E_p has been converted into E_s in the cyclic injection, while seven times more was generated in the continuous injection. Therefore, we interpret

Table 1. Model results from sequential/continuous and fatigue/cyclic fluid injection.

	Sequential	Cyclic	Change (per cent)
Hydraulics			
Hydraulic injected volume (m^3)	270	374	+38
Total pumped-in energy, E_p (MJ)	25 676	35 714	+39
Induced seismicity			
Total number of induced events	785	244	−70
Max. number of event occurrence (/min)	2.8	1.7	−61
Cumulative seismic energy, E_s^{cum} (MJ)	188	41	−78
Single event energy, E_s^{max} (MJ)	5.1	2.6	−51
Efficiency ratio, E_s^{cum}/E_p (per cent)	0.73	0.11	−85
Fracture permeability			
Maximum avg. value (Darcy)	910	830	−10
Residual avg. value (Darcy)	590	660	+12

that the cyclic treatment is a softer stimulation strategy (in terms of seismic energy radiated) as compared to the continuous, step-wise increase of the flow rate used in geothermal field operation thus far.

The permeability enhancement for both injection scenarios is documented in comparable average residual values at the end of the model runs. Due to the nature of cyclic treatment, peak and residual values are reached at a later stage as compared to the continuous injection case. Based on our result from laboratory testing on granite and interpretation (Fig. 1), the underlying process operating *in situ* can be compared with the concept of fatigue fracturing in material sciences. Fatigue is the progressive and localized structural damage that occurs when a material is subjected to cyclic loading. During cyclic loading, the nominal maximum stress values are less than the ultimate tensile stress limit, and may be below the yield stress limit of the material. Thus, the cyclic treatment (Figs 3f–j) seems to generate a kind of larger scale fatigue hydraulic fracturing (FHF) process which leads to permeability increase as observed in conventional HF with the advantage to convert less pumped-in energy into unwanted induced seismic radiated energy. This interpretation describes the short-term (hours, days) effect of cyclic hydraulic treatment on larger scale rock fractures (length ∼100 to 500 m) as opposed to long-term (weeks, years), chemical processes operating at fracture tips (grain scale), so-called subcritical crack growth (e.g. Nara *et al.* 2013). However, we note that this observation can be overprinted by silent hydro-shears and aseismic deformation operating in naturally fractures of stimulated reservoirs.

In Fig. 4, induced seismic radiated energy (E_s) versus pumped-in hydraulic energy (E_p) from the simulations obtained in this numerical study is compared with field data. We use data from European geothermal sites in Bad Urach, Basel and Soultz-sous-Forêts (Fig. 4, red squares with numbers) and data from Canadian shale gas fracturing (Fig. 4, blue circles). Squares denote that the E_s is calculated using only the largest induced event (M_w^{max}), whereas circles indicate cumulative values for E_s of all induced events during stimulation. We convert the local magnitude M_L to the moment magnitude M_W using the empirical relation

$$M_w = 0.0376M_L^2 + 0.646M_L + 0.53 \quad (2)$$

of Grünthal *et al.* (2009). Fig. 4 shows that both, fatigue cyclic and continuous step-wise injection generate a degree of efficiency (E_s/E_p in per cent) that is in agreement with field observations (about

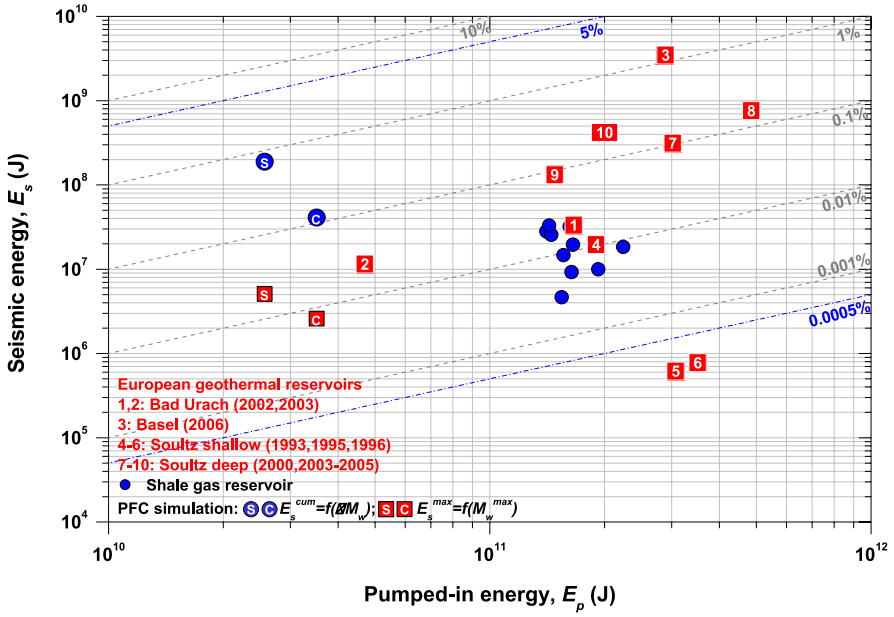

Figure 4. Relation between total pumped-in energy (E_p) and total radiated seismic energy (E_s). *Red squares with numbers* indicate calculations for European geothermal fields that are based on the largest event only. *Blue circles* indicate calculations from shale gas reservoirs that are based on all induced events (Boroumand & Dave 2012). For comparison the results of the two stimulation models are shown for both calculation procedures of the released seismic energy (S and C for step-wise continuous and cyclic, respectively). Dashed lines are degree of seismic efficiency, i.e. the ratio of seismic to pumped-in energy in percentage values. Data points (1–10) are computed from field data listed in Baisch & Vörös (2009).

0.01 per cent in shale gas fracturing, and up to about 1 per cent in geothermal).

5 CONCLUSIONS

We use a hydro-mechanical model to investigate different injection scenarios in order to test which stimulation is efficient in terms of permeability enhancement, but lowers the radiated seismic energy. Our 2-D model is capable of generating induced seismic event catalogues from tensile and shear fractures of different stimulation scenarios. The model results reproduce key observations in geothermal fields. The extension of the seismic cloud is in the orientation of maximum horizontal stress, the peak seismicity is associated with abrupt changes of injection rate and larger magnitude events occur in the post-shut-in phase. The ratio of pumped-in energy versus seismic energy radiated is in the order of field data.

Based on our findings of the damage pattern in laboratory tested granite, we propose a kind of larger scale (∼100 m) FHF process operating *in situ* during cyclic treatment of rock mass. The cyclic injection scheme has a degree of efficiency of radiated seismic energy with respect to the pumped-in energy of about 0.1 per cent while in conventional, continuous flow rate injection this ratio is seven times larger. The idea seems promising to be applied in the field not only for geothermal, but also for other energy technologies [CO_2 sequestration, oil and (shale) gas] where minimization of induced seismicity is needed.

ACKNOWLEDGEMENTS

This work was supported by GEISER (Geothermal Engineering Integrating Mitigation of Induced SEismicity in Reservoirs), European Commission project No. 241321–2. We kindly acknowledge the permission of Stefan Baisch (Q-con Geothermal Reservoir Engineering, Bad Bergzabern, Germany) to use field data from the Basel SERIANEX study.

REFERENCES

Bachmann, C.E., Wiemer, S., Goertz-Allmann, B.P. & Woessner, J., 2012. Influence of pore-pressure on the event-size distribution of induced earthquakes, *Geophys. Res. Lett.,* **39,** L09302, doi:10.1029/2012GL051480.

Baisch, S. & Vörös, R., 2009. Induced seismicity, *Technical Report* SERIANEX, AP3000, Appendix 2, pp. 56–59.

Baisch, S., Vörös, R., Rothert, E., Stang, H., Jung, R. & Schellschmidt, R., 2010. A numerical model for fluid injection induced seismicity at Soultz-sous-Forêts, *Int. J. Rock. Mech. Min. Sci.,* **47,** 405–413.

Barth, A., Wenzel, F. & Langenbruch, C., 2013. Probability of earthquake occurrence and magnitude estimation in the post shut-in phase of geothermal projects, *J. Seismol.,* **17**(1), 5–11.

Bommer, J.J., Oates, S., Cepeda, J.M., Lindholm, C., Bird, J., Torres, R., Marroquín, G. & Rivas, J., 2006. Control of hazard due to seismicity induced by a hot fractured rock geothermal project, *Eng. Geol.,* **83,** 287–306.

Boroumand, N. & Dave, W., 2012. Comparing energy calculations: hydraulic fracturing and microseismic monitoring, *GeoConvention: Vision,* 2012 May 14–18, Calgary, Alberta, Canada.

Cornet, F.H., Bérard, T. & Bourouis, S., 2007. How close to failure is a granitic rock mass at a 5 km depth? *Int. J. Rock. Mech. Min. Sci.,* **44,** 47–66.

Deichmann, N. & Gardini, D., 2009. Earthquakes induced by the stimulation of enhanced geothermal system below Basel (Switzerland), *Seism. Res. Let.,* **80**(5), 784–798.

Dinske, C. & Shapiro, S., 2013. Seismotectonic state of reservoirs inferred from magnitude distributions of fluid-induced seismicity, *J. Seismol.,* **17**(1), 13–25.

Dorbath, L., Cuenot, N., Genter, A. & Frogneux, M., 2009. Seismic response of the fractured and faulted granite of Soultz-sous-Forêts (France) to 5 km deep massive water injections, *Geophys. J. Int.,* **177,** 653–675.

Evans, K.F. *et al.*, 2005. Microseismicity and permeability enhancement of hydrogeologic structures during massive fluid injections into granite at 3 km depth at the Soultz HDR site, *Geophys. J. Int.,* **160,** 388–412.

Giardini, D., 2009. Geothermal quake risk must be faced, *Nature,* **426,** 848–849.

Grünthal, G., Wahlström, R. & Stromeyer, D., 2009. The unified catalogue of earthquakes in central, northern, and northwestern Europe (CENEC)—updated and expanded to the last millennium, *J. Seismol.,* **13**(4), 517–541.

Gutenberg, B. & Richter, C.F., 1956. Earthquake magnitude, intensity, energy and acceleration (second paper), *Bull. seism. Soc. Amer.,* **46,** 105–145.

Hazzard, J.F. & Young, R.P., 2002. Moment tensors and micromechanical models, *Tectonophysics,* **356,** 181–197.

Hazzard, J.F. & Young, R.P., 2004. Dynamic modeling of induced seismicity, *Int. J. Rock. Mech. Min. Sci.,* **41,** 1365–1376.

Hökmark, H., Lönnqvist, M. & Fälth, B., 2010, *THM-issues in repository rock—thermal, mechanical, thermo-mechanical and hydro-mechanical evolution of the rock at the Forsmark and Laxemar sites,* Swedish Nuclear Fuel and Waste Management Co, *Technical Report SKB TR-10–23*.

Itasca, 2012. *Technical Memorandum—5.0 Parallel Bond Enhancement,* PFC2D Particle Flow Code in 2 Dimensions: Theory and Background.

Kanamori, H., 1977. The energy release in great earthquakes, *J. geophys. Res.,* **82**(20) 2981–2987.

Labuz, J.F. & Zang, A., 2012. Mohr-Coulomb failure criterion, *Rock Mech. Rock Eng.,* **45,** 975–979.

Majer, E.L., Baria, R., Stark, M., Oates, S., Bommer, J., Smith, B. & Asanuma, H., 2007. Induced seismicity associated with enhanced geothermal systems, *Geothermics,* **36,** 185–222.

MIT Report, 2006. *The Future of Geothermal Energy: Impact of Enhanced Geothermal Systems (EGS) on the United States in the 21st Century,* Massachusetts Institute of Technology, 209 pp. Available at: www1.eere.energy.gov/geothermal/egs_technology.html (last accessed 7 August 2013).

Nara, Y., Yamanaka, H., Oe, Y. & Kaneko, K., 2013. Influence of temperature and water on subcritical crack growth parameters and long-term strength of igneous rocks, *Geophys. J. Int.,* **193,** 47–60.

Shapiro, S.A., Dinske, C. & Langenbruch, C., 2010. Seismogenic index and magnitude probability of earthquakes induced during reservoir stimulations, *Leading Edge,* **29**(3), 304–309.

Suckale, J., 2009. Induced seismicity in hydrocarbon fields, *Advances Geophys.,* **51,** 55–106.

Yoon, J.-S., Zang, A. & Stephansson, O., 2012. Simulating fracture and friction of Aue granite under confined asymmetric compressive test using clumped particle model, *Int. J. Rock. Mech. Min. Sci.,* **49,** 68–83.

Yoon, J.-S., Zang, A. & Stephansson, O., 2013. Hydro-mechanical coupled discrete element modeling of geothermal reservoir stimulation and induced seismicity, in *Clean Energy Systems in the Subsurface: Production, Storage and Conversion*, pp. 221–231, eds Hou, M.Z., Xie, H. & Were, P., Springer-Verlag.

Zang, A. & Stephansson, O., 2010. *Stress Field of the Earth's Crust,* Springer Science + Business Media B.V..

Zang, A., Stanchits, S. & Dresen, G., 2002. Acoustic emission controlled triaxial rock fracture and friction tests, in *Structural Integrity and Fracture,* pp. 289–294, eds Dyskin, A.V., Hu, X. & Sahouryeh, E., Swets & Zeitlinger.

Zang, A., Wagner, F.C., Stanchits, S., Janssen, C. & Dresen, G., 2000. Fracture process zone in granite. *J. geophys. Res.,* **105**(B10), 23 651–23 661.

Zang, A., Wagner, C., Stanchits, S., Dresen, G., Andresen, R. & Haidekker, M.A., 1998. Source analysis of acoustic emissions in Aue granite cores under symmetric and asymmetric compressive loads, *Geophys. J. Int.,* **135,** 1113–1130.

Zhao, X. & Young, R.P., 2011. Numerical modelling of seismicity induced by fluid injection in naturally fractured reservoirs, *Geophysics,* **76**(6), WC167–WC180.

SUPPORTING INFORMATION

Additional Supporting Information may be found in the online version of this article:

Supplementary material for Fig. 2.
Supplementary material for Fig. 3 (http://gji.oxfordjournals.org/lookup/suppl/doi:10.1093/gji/ggt301/-/DC1).

Please note: Oxford University Press are not responsible for the content or functionality of any supporting materials supplied by the authors. Any queries (other than missing material) should be directed to the corresponding author for the article.